High resolution spectroscopy of molecules of astrophysical interest and radio astronomical observations of star forming regions.

Johanna Chantzos

München 2020

High resolution spectroscopy of molecules of astrophysical interest and radio astronomical observations of star forming regions.

Johanna Chantzos

Dissertation
an der Fakultät für Physik
der Ludwig–Maximilians–Universität
München

vorgelegt von
Johanna Chantzos
aus Thessaloniki, Griechenland

München, den 03.02.2020

Erstgutachter: Prof. Dr. Paola Caselli
Zweitgutachter: Prof. Dr. Hans Böhringer
Tag der mündlichen Prüfung: 19.03.2020

Contents

List of Figures

List of Tables

Zusammenfassung

Die vorliegende Abschlussarbeit enthüllt wichtige astrochemische Prozesse in Sternentstehungsgebieten niedriger Masse durch die Anwendung von drei grundlegenden Hilfsmitteln: *astronomische Beobachtungen*, *Labormessungen* und *theoretische Modelle*. Diese Arbeit konzentriert sich insbesondere auf die frühen Phasen der Sternentstehung: diffuse und lichtdurchlässige Wolken, sternlose/prästellare Kerne und Protosterne der Klasse 0. Die chemischen und physikalischen Eigenschaften dieser Quellen werden durch radioastronomische Beobachtungen der molekularen Emissions- und Absorptionslinien aufgedeckt. Darüber hinaus werden Labormessungen mit zwei verschiedenen Experimenten durchgeführt, um die Rotationsspektren astrophysikalisch relevanter Moleküle in der Gasphase zu messen. Schließlich wird ein chemisches Modell für eine zuverlässige Vorhersage der Molekülhäufigkeiten in den beobachteten Quellen verwendet, das ergänzende Informationen zu den astronomischen Beobachtungen liefert.

Im ersten Teil dieser Arbeit untersuche ich die molekulare Deuteriumanreicherung in Richtung dichter Kerne auf der Grundlage von Beobachtungen mit dem 30m-Teleskop IRAM. Es ist bekannt, dass der Deuteriumanteil zu prästellaren Kernen hin zunimmt, die kurz vor der Geburt eines Protosterns stehen. Er wird daher als wichtiger evolutionärer Indikator für die frühen Stadien der Sternentstehung verwendet. Hierbei untersuche ich den Deuterierungsgrad von c-C_3H_2 in sternlosen/prästellaren und protostellaren Kernen der Klasse 0 in Richtung der Taurus und Perseus Komplexe. Insbesondere untersuche ich die Korrelation zwischen dem Deuterierungsgrad c-C_3HD/c-C_3H_2 und der Staubtemperatur, der H_2 Säulendichte sowie dem CO-Abreicherungsfaktor. Ich zeige, dass der Deuterierungsgrad von c-C_3H_2 in etwa 10% beträgt und innerhalb aller beobachteten Quellen übereinstimmt, mit Ausnahme des jüngsten Protosterns HH211, der den höchsten Deuterierungsgrad besaß ($\sim$ 23%). Dies könnte von einer kürzlich erfolgten Verdampfung prästellarer Eisschichten stammen, die in c-C_3HD angereichert sind, was darauf hindeutet, dass eine zusätzliche Deuterierung von c-C_3H_2 auf Staubkörnern stattfindet.

Der zweite Teil der Arbeit präsentiert die spektroskopische Untersuchung der Radikale HCCO (Ketenyl) und DCCO, sowie des protonierten Carbonylsulfids $HSCO^+$ im (Sub)-millimeterbereich. Alle Moleküle wurden in einer elektrischen Gasentladung erzeugt und in einer Hochvakuumkammer stabilisiert. Die Messungen von HCCO und seinem deuterierten Gegenstück wurden mit einer Absorptionszelle (CASAC) im Frequenzbereich von 170 bis 650 GHz durchgeführt. Für jedes Isotopolog habe ich mehr als 100 Rotationslinien aufgenommen. Im Rahmen dieser Arbeit habe ich ebenfalls zum Aufbau eines neuen Exper-

iments, dem Überschalldüsen-Experiment, beigetragen. Dieser Versuchsaufbau ermöglicht die Erzeugung eines kalten und nahezu kollisionsfreihen Molekularstrahls durch die adiabatische Expansion eines ausgewählten Gasgemisches in eine Hochvakuumkammer. Die erreichten Temperaturen (bis hinunter zu etwa 5 K) und niedrigen Dichten innerhalb des Strahls bieten perfekte Bedingungen, um instabile Moleküle (wie z.B. Radikale und Ionen) zu untersuchen. Die ersten Messungen mit diesem Experiment wurden am Ion $HSCO^+$ zwischen 274 bis 373 GHz durchgeführt. Durch den neuen Datensatz der oben genannten Moleküle konnten die spektroskopischen Molekülparameter signifikant besser und präzise Rotationskonstanten bis hin zu hoher Ordnung bestimmt werden. Die daraus resultierenden Linienkataloge enthalten hochpräzise Frequenzen von HCCO, DCCO und $HSCO^+$, die eine sichere radioastronomische Suche dieser Moleküle im (sub)mm-Wellenlängenbereich ermöglichen.

Im letzten Teil meiner Arbeit habe ich die interstellare Phosphorchemie in Richtung diffuser/lichtdurchlässiger Wolken untersucht. Angesichts der wenigen bisher verfügbaren Nachweise sind die Bildungs- und Zersetzungswege P-haltiger Moleküle im ISM noch weitgehend umstritten. Die Untersuchung diffuser/lichtdurchlässiger Wolken hilft uns, einen wesentlichen Parameter in unserem chemischen Modell einzuschränken, nämlich den Grad der Phosphorabreicherung. Hierbei konzentriere ich mich auf eine markante Sichtlinie in Richtung des lichtstarken Quasars B0355+508, die bis zu fünf diffuse/lichtdurchlässige Wolken enthält. Der Nachweis der Moleküle HNC, CN, $C^{34}S$ und ^{13}CO schränkt die physikalischen Eigenschaften der beobachteten Quellen zusätzlich ein. Anhand dieser Einschränkungen untersuche ich mit unserem chemischen Gas-Staub-Modell die wichtigsten Erzeugungs- und Zersetzungsmechanismen von P-haltigen Molekülen und die daraus resultierenden Häufigkeiten. Nach unserem Modell erreichen P-haltige Moleküle (wie HCP, CP, PN und PO) nachweisbare Mengen eher in Richtung lichtdurchlässiger als in Richtung diffuser Wolken, wo sie stärker von der interstellaren Strahlung abgeschirmt sind.

Abstract

The present thesis unveils important astrochemical processes towards low-mass star forming regions by using three main tools: *astronomical observations, laboratory measurements* and *theoretical models*. This work focuses in particular on the early phases of star formation: diffuse and translucent clouds, starless/pre-stellar cores and Class 0 protostars. The chemical and physical properties of these sources are revealed through radioastronomical observations of molecular emission and absorption lines. Furthermore, laboratory measurements are performed with two different experiments in order to measure the rotational spectra of astrophysically relevevant molecules in the gas phase. Finally, a chemical model is used for a reliable prediction of the molecular abundances in the observed sources, providing complementary information to the astronomical observations.

In the first part of this thesis I studied molecular deuterium enhancement towards dense cores based on observations with the IRAM 30m telescope. The deuterium fraction is known to increase towards pre-stellar cores, right before the birth of a protostar, and is therefore used as an important evolutionary tracer of the early stages of star formation. Here, I investigate the deuteration level of c-C_3H_2 within starless/pre-stellar and Class 0 protostellar cores towards the Taurus and Perseus complexes. In particular, I examine the correlation between the deuteration level c-C_3HD/c-C_3H_2 and the dust temperature, the H_2 column density as well as the CO depletion factor. I show that the deuterium fraction of c-C_3H_2 is consistent with $\sim$ 10% among all observed sources, except for the youngest protostar HH211 that showed the highest deuteration level of $\sim$ 23%. This could be inherited from a recent evaporation of pre-stellar ices that contain enhanced c-C_3HD, suggesting that additional deuteration of c-C_3H_2 is happening on dust grains.

The second part of the thesis presents the spectroscopic study on the radicals HCCO (ketenyl) and DCCO as well as the protonated carbonyl sulfide $HSCO^+$ in the (sub)millimeter regime. All species were produced in an electric gas discharge and stabilized in a high-vacuum cell. The measurements of HCCO and its deuterated counterpart were done with our CAS Absorption Cell (CASAC) between 170 and 650 GHz. For each isotopologue I recorded more than 100 rotational lines. Within the framework of this thesis I also contributed to the technical realization of a new experiment, called the Supersonic Jet Experiment. This experimental set up allows the production of a cold and nearly collision-free molecular beam via the adiabatic expansion of a selected gas mixture into a high-vacuum chamber. The achieved temperatures (down to $\sim$5 K) and low densities within the jet provide us with the perfect conditions to study unstable species (i.e. radicals and ions).

The first measurements conducted with this experiment were done on the molecular ion $HSCO^+$ between 274 and 373 GHz. The new set of measured lines of the aforementioned species considerably improved the determination of their spectral molecular parameters, with high-order rotational constants being significantly constrained. The resulting catalogues of lines contain highly precise frequencies of HCCO, DCCO and $HSCO^+$, allowing a confident radioastronomical search of these molecules in the (sub)mm frequency range.

In the last part of my thesis I studied the interstellar phosphorus chemistry towards diffuse/translucent clouds. Given the small number of available detections so far, the formation and destruction routes of P-bearing species in the ISM are still largely debatable. Studying diffuse/translucent clouds helps us constrain an essential parameter in our chemical model, namely the depletion level of phosphorus. Here, I focus on a prominent line of sight towards the strong quasar B0355+508 that incorporates up to five diffuse/translucent clouds. Detections of the species HNC, CN, $C^{34}S$ and ^{13}CO put additional constraints on the physical properties of the observed sources. With these constraints as a guide, I explore with our gas-grain chemical model the main formation and destruction mechanisms of P-bearing molecules and their resulting abundances. According to our model, P-bearing molecules (like HCP, CP, PN and PO) reach detectable amounts towards translucent rather than diffuse clouds, where there is a stronger shielding from the interstellar radiation.

Chapter 1

Introduction

1.1 Astrochemistry

In the early 40's scientists were able to identify the first molecules in the Interstellar Medium (ISM): CH, CH^+ and CN. These detections were the starting point of a new and exciting research field called Astrochemistry. The growing interest in the chemical complexity of the ISM has led astrochemists to detect more than 180 interstellar molecules so far. These observations aim to answer essential questions like: how are molecules formed and excited in the ISM? What do these molecules reveal about the physical properties and dynamics of a source? How does the interstellar chemistry change with the evolution of a star-forming region? And, to which extent is the chemical complexity on Earth inherited from the early phases of star formation? Interstellar molecules vary greatly in size from simple diatomic species such as OH and CO, up to large complex organic molecules (COMs)[1], like the pure carbon fullerenes C_{60} and C_{70}. A large fraction of these interstellar molecules are chemically reactive species, i.e. free radicals and molecular ions, which can survive for a long time in space due to the low densities and temperatures. The existence of several ionic species like H_3^+, HCO^+ and C_4H^- indicates that interstellar gas is in the form of a weakly ionized plasma. These ions initiate essential chemical processes and significantly enhance the interstellar chemical complexity.

Depending on its mass, geometry and electronic structure every molecule has its own unique spectrum; in other words, every molecule will absorb and emit radiation at very specific energies (or frequencies), that correspond exactly to the energy difference between two discrete energy levels. The magnitude of this energy difference will determine whether it is an electronic, vibrational or rotational transition. Electronic transitions require large energies ($> 1\,\mathrm{eV}$) and therefore lie in the optical and UV range, while vibrational and rotational transitions are less energetic, and lie in the infrared and millimeter range, respectively. In order to cover this broad range of frequencies and be able to observe all three kinds of transitions, astronomers need different observational facilities: the *Hubble Space Telescope* (HST) has been the leading telescope for recording optical, UV- and near-

[1] In astronomy complex organic molecules are defined as organic molecules with at least six atoms.

infrared radiation, soon to be replaced by the *James Webb Space Telescope* (JWST) that will provide even higher angular resolution and sensitivity at the mid-infrared wavelengths. Powerful ground-based telescopes for the millimeter and submillimeter range with broadband detectors are the IRAM 30m telescope operated by the *Institute for Radio Astronomy in Millimeter range* (IRAM) as well as the *Atacama Large Millimeter/submillimeter Array* (ALMA). The IRAM 30m telescope is a single dish telescope located at an altitude of $\sim$ 3000 m and operating at 3, 2, 1 and 0.9 mm. ALMA is an interferometer located at even higher altitude ($\sim$ 5000 m), that consists of 66 antennas (with a 12- and 7-meter diameter), providing a high spatial resolution as well as an extended spectral coverage from 31 to 1000 GHz. Finally, one of the most prominent telescopes for observations in the submillimeter and far-infrared regime is the *Stratospheric Observatory For Infrared Astronomy* (SOFIA), which is the largest airborne telescope in the world; it can fly up to an altitude of 12 km, avoiding most of the water vapor in the atmosphere that absorbs radiation in the infrared regime. The new generation of interferometers is providing astronomers the necessary angular resolution to explore the atmospheres of exoplanets, the mass-accretion and jets in young stellar objects, the evolution of protoplanetary disks, the motion of binary stars and many other objects and processes relevant for both Astrochemistry and Astrophysics. Apart from ALMA, other significant interferometers are the Karl G. Jansky *Very Large Array* (VLA) in Socorro, the *NOrthern Extended Millimeter Array* (NOEMA) in Plateau de Bure and the *Very Large Telescope* (VLT) in Cerro Paranal. In fact, a new instrument implemented at the VLT called GRAVITY has revolutionized interferometric imaging, offering an astrometric precision in the micro-arcsecond regime and an image resolution of a few milli-arcsecond.

Following the collection of observational data, astronomers need to identify the recorded spectral lines and assign them to the molecular carrier. The information on highly accurate molecular spectra is provided by laboratory scientists by using various spectroscopic techniques such as: frequency modulation absorption spectroscopy, Fourier transform microwave spectroscopy, which is often coupled with the chirped-pulse technique, cavity ring-down spectroscopy and the THz time domain spectroscopy [van Dishoeck, 2017]. One of the challenges for gas-phase spectroscopy is to produce reactive species (like radicals and ions) under extreme conditions (high voltages/temperatures) and subsequently stabilize them in a high-vacuum environment. Ideally, molecules are cooled down to a temperature of a few Kelvin by producing a cold, supersonic molecular beam [Lattanzi et al., 2018, McCarthy et al., 2015, McCarthy and Thaddeus, 2007]. That way the rotational spectra are simplified and the low-energy levels are strongly occupied, leading to enhanced line intensities. The (sub)mm frequencies and line strengths of rotational transitions of gas-phase molecules of astrophysical or atmospheric interest are listed in databases such as the *Jet Propulsion Laboratory catalog* (JPL)[2] [Pickett et al., 1998] and the *Cologne Database for Molecular Spectroscopy* (CDMS)[3] [Endres et al., 2016]. Line catalogues of vibrational transitions in the infrared regime are included in the databases HITRAN [Rothman et al., 2009] and

[2]https://spec.jpl.nasa.gov
[3]https://cdms.astro.uni-koeln.de

EXOMOL [Tennyson et al., 2016]. Apart from gas-phase molecules, solid species have also been detected in space in the form of ices, that are deposited on top of the cold surfaces of dust particles. These icy mantles consist mainly of water along with other molecules like CO_2 and CO, whose spectra have been observed in the infrared regime. Advanced laboratory experiments [Giuliano et al., 2019] have been developed to analyze the optical and chemical properties of astrophysically-relevant ices by depositing ice layers on a substrate, whose temperature is kept down to a few Kelvin through the implementation of a cryostat. In addition to ice deposition, other processes relevant in the ISM, such as photo- and thermal desorption, or irradiation with high energy particles/electrons are studied as well [Öberg, 2016]. Using this information together with observations, astrochemists are able to unveil the contribution of dust particles and their icy mantles to the interstellar chemistry.

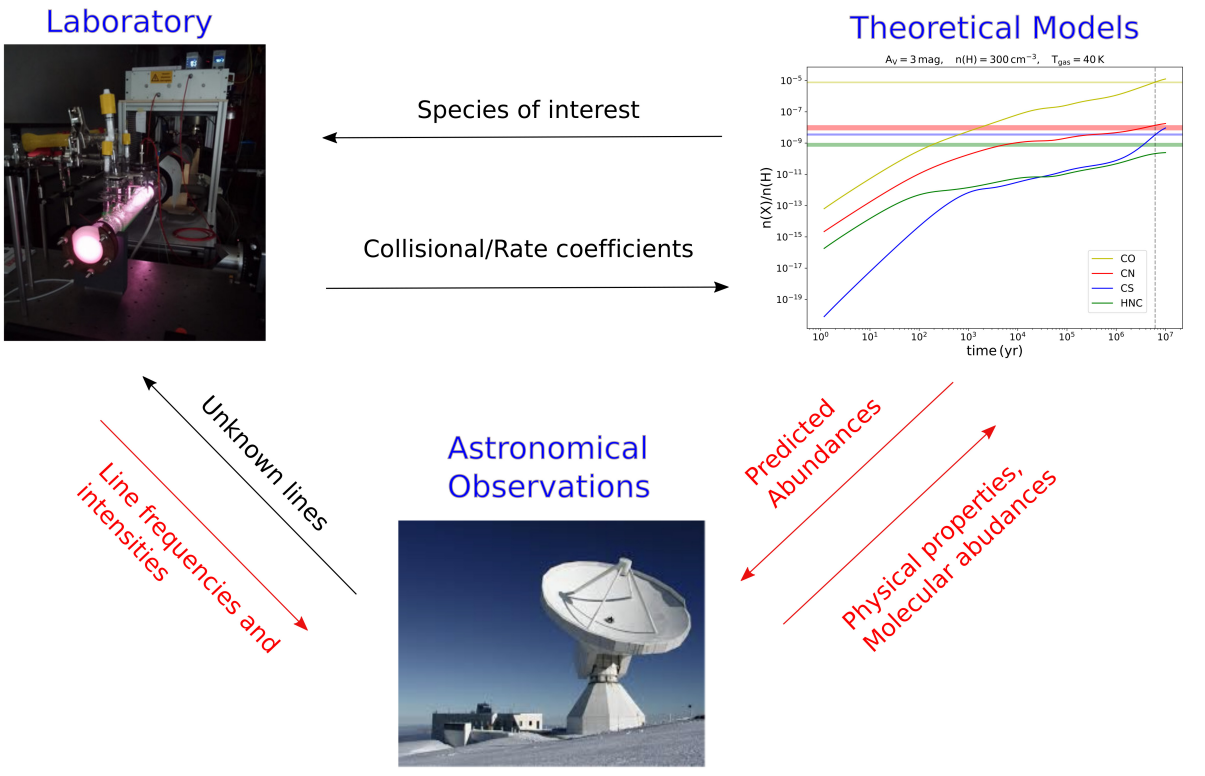

Figure 1.1: Depiction of the interacting fields of astrochemistry: activities connecting observations, laboratory and theory. The highlighted text emphasizes the contribution of the present thesis.

Theoretical work is also essential in astrochemistry in order to understand the chemical and physical properties of an observed source and to make reliable predictions for future observations and measurements. A chemical model is a large network of two-body chemical

reactions that involve the formation and destruction of chemical bonds, as well as their rearrangement (such as radiative association, photodissociation, ion-molecule, neutral-neutral reactions and etc.). Typical gas-grain models take into account the accretion/desorption processes of molecules to/from dust grains and regulate the surface mobility of depleted species that determines the probability of molecular formation on grains. The numerical integration of a system of ordinary differential equations (ODE), which contains chemical rate equations for gas-phase and surface reactions, gives as a result the time dependent fractional abundances of the investigated species. As the number of detected molecules in the ISM continued to grow, the necessity of chemical databases soon became clear. The two most prominent databases nowadays that contain an extensive collection of chemical (gas-phase and surface) reactions along with their rate coefficients are the *KInetic Database for Astrochemistry* (KIDA)[4] [Wakelam et al., 2015a] and the *UMIST Database for Astrochemistry* (UDfA)[5] [McElroy et al., 2013]. Apart from chemical models, astrochemists work with dynamical models as well, in order to understand the physical processes and dynamics of an observed source. The results of both chemical and physical models lead to a full picture of the chemical composition of an astronomical object as a function of its physical properties (such as density and temperature).

As the above discussion indicates, astrochemisty involves the constant interaction between three main areas: (a) **Astronomical observations** (b) **Laboratory Measurements** and (c) **Theoretical Models**. This interdisciplinary structure of astrochemistry is illustrated in Fig. 1.1, and in particular the contribution of the present thesis is highlighted in red: Through our spectroscopic studies in the laboratory we provide highly accurate rest frequencies of astrophysically relevant species that allow their radioastronomical search in the ISM. Based on our observational data we derive molecular abundances which are then compared to the values predicted by our chemical model. This comparison puts additional constraints on the physical properties of the observed sources. Given these constraints, our model provides us with reliable predictions of molecular abundances that serve as a guide for future radioastronomical observations.

Before we treat in detail the projects of the present thesis, we will first introduce basic concepts from astrochemistry and radioastronomy as well as rotational spectroscopy.

[4]http://kida.obs.u-bordeaux1.fr

[5]http://udfa.ajmarkwick.net/index.php?mode=species

1.2 Low-mass star formation

The vast space between stars is filled with gas and dust and is described as the Interstellar Medium (ISM). The gas is a mixture of atoms, molecules and charged particles, that accounts for 99% of the total mass, while the remaining 1% consists of dust grains. The gas in the ISM is composed of 70% hydrogen (H), 28% helium (He) and 2% heavier elements. Based on the chemical state of hydrogen (ionized, atomic, molecular), the ISM can be divided into five different phases: (1) molecular clouds, (2) the cold neutral medium (CNM), (3) the warm neutral medium (WNM), (4) the warm ionized medium (WIM) and (5) the hot ionized medium (HIM). The above five states can vary significantly in temperature and density, ranging from cold, dense conditions with $T \sim 10-20\,\mathrm{K}$ and $n(\mathrm{H}) > 100\,\mathrm{cm}^{-3}$, to hot plasmas with temperatures of $\sim 10^6\,\mathrm{K}$ and low densities of $\sim 10^{-2}\,\mathrm{cm}^{-3}$. These physical conditions are decisive for the ionisation state of hydrogen, that can either be fully in H_2 form (molecular clouds), mostly in neutral atomic form (CNM, WNM), or completely ionized (HIM) [Tielens, 2005].

This work focuses predominantly on the study of molecular clouds, that represent just 1% of the total volume of the ISM. Densities below $\sim 100\,\mathrm{cm}^{-3}$ mark the regime of diffuse atomic gas, that is part of the CNM. Due to the very low densities, diffuse atomic clouds are fully exposed to the interstellar radiation, which subequently leads to strong photodissociation- and ionization. Hydrogen is in its neutral atomic form (H I) and all other species, such as C and Si, with ionization potentials smaller than that of hydrogen are almost fully ionized. The temperature ranges between 30 and 100 K and the molecular fraction of hydrogen is less than 10%. Diffuse molecular clouds represent the transition phase from atomic to molecular gas, in which the densities lie higher ($n(\mathrm{H}) = 100 - 500\,\mathrm{cm}^{-3}$) and the fraction of molecular hydrogen becomes significant (> 0.1), due to a stronger H_2 self-shielding from the interstellar radiation. However, the UV irradiation is still high enough to ionize C or dissociate most of the CO. So-called translucent clouds with even higher densities of $n(\mathrm{H}) = 500-5000\,\mathrm{cm}^{-3}$ can provide efficient protection from interstellar radiation, enabling the transition from C^+ to C and partly CO [Snow and McCall, 2006].

At densities of $n(\mathrm{H}) > 10^4\,\mathrm{cm}^{-3}$ carbon is found almost entirely in its molecular form (CO) and the gas temperature drops down to 10 K. This type of cloud is referred to as dense, dark or molecular cloud (typical size ~ 2 pc) and it appears as a dark spot in the sky, obscuring the visible light from background stars. This is due to the fact that dust grains efficiently absorb the interstellar UV radiation and re-emit the energy in the far-infrared as black-body emission. Within an extended molecular cloud, smaller and denser sub-structures of the size of ~ 0.1 pc can be formed through external instabilities, such as turbulence, or through gravitational contraction. Such self-gravitating dense cores are stable when the gravitational potential energy is balanced by the kinetic energy of the gas pressure (Virial-Theorem). In order for the gravitation to overcome the gas pressure, the dense clump needs to reach a critical mass called Jeans-Mass, which is given by the following expression:

$$M_{\mathrm{J}} = \Big(\frac{5k_BT}{G\mu m(\mathrm{H})}\Big)^{3/2}\Big(\frac{3}{4\pi n(\mathrm{H})}\Big)^{1/2}, \tag{1.1}$$

where k_{B} is the Boltzmann constant, T the temperature, G the gravitational constant, μ the mean molecular weight, $m(\mathrm{H})$ the mass of atomic hydrogen and $n(\mathrm{H})$ the number density of total hydrogen nuclei. The cores that are dense and massive enough to undergo gravitational collapse ($M > M_J$) are known as pre-stellar cores. It is evident from Eq. 1.1 that the colder and the denser the core is, the smaller the Jeans-Mass, and therefore the easier it is for the gravitational collapse to take place. For typical dense-core conditions ($T \approx 10\,\mathrm{K}$, $n(\mathrm{H}) = 10^4\,\mathrm{cm}^{-3}$, $\mu = 2.4$) the Jeans-Mass is equal to 5 solar masses ($M_J \approx 5M_\odot$). The collapse is isothermal as long as the released gravitational potential energy can be radiated away efficiently. This is done mainly in two ways: (1) dust grains absorb the excessive energy, heat-up and finally re-emit this energy in the infrared and (2) molecules (mainly CO) are collisionally excited and eventually return to the ground state via radiative decay or collisional de-excitation. These cooling mechanisms keep the collapse in its initial stages isothermal. However, as the density increases ($\geq 10^{10}\,\mathrm{cm}^{-3}$, Larson [1969]) the cloud becomes optically thick, trapping the energy that is released during the collapse, and the core starts to heat up. An enhanced temperature is increasing the Jeans-Mass, so that further collapse is hindered and a first hydrostatic core is formed (with a temperature of $\sim 100\,\mathrm{K}$ and a size of ~ 5 AU). The temperature continues to rise until the H_2 gas is dissociated. The energy that was initially stabilizing the core is now missing; this initiates a second collapse leading to the formation of a so-called protostar. The accreting central object is surrounded by a protostellar envelope that absorbs the radiation released by the infalling material and re-emits strong thermal radiation in the far-infrared (emission peak is at $\sim 100\,\mu$m). At this evolutionary stage the object is defined as a Class 0 protostar in which most of the mass is still embedded in the envelope. At the end of the Class I stage almost all the material has been accreted and a thick circumstellar disk remains emitting strongly in the mid-infrared (emission peak at $24\,\mu$m). In the Class II stage the envelope has fully dissipated allowing the emission from the central protostar in the optical range to be observed (along with the infrared emission from the disk). The protostar has reached temperatures high enough to initiate deuterium fusion in the nucleus, turning the central core into a pre-main sequence star. Finally, in the Class III phase the disk has almost entirely disappeared with the remnant called debris disk. The observed light originates now mostly from the central star, which has reached its final mass. Once hydrogen fusion starts in the nucleus, the central core becomes a main-sequence star [Klessen and Glover, 2016, Stahler and Palla, 2008]. Figure 1.2 shows the evolutionary stages of the low-mass star formation process.

The above process applies to the low-mass star formation, that leads to stars with masses below $8M_\odot$[6]. High-mass star formation on the other hand, happens faster as hydrogen fusion starts while the envelope is still collapsing and results in the formation of massive stars or multiple star systems. However, this will not be treated in more detail, as

[6]Stars with $2M_\odot < M < 8M_\odot$ are called "intermediate-mass stars".

it is beyond the scope of this thesis.

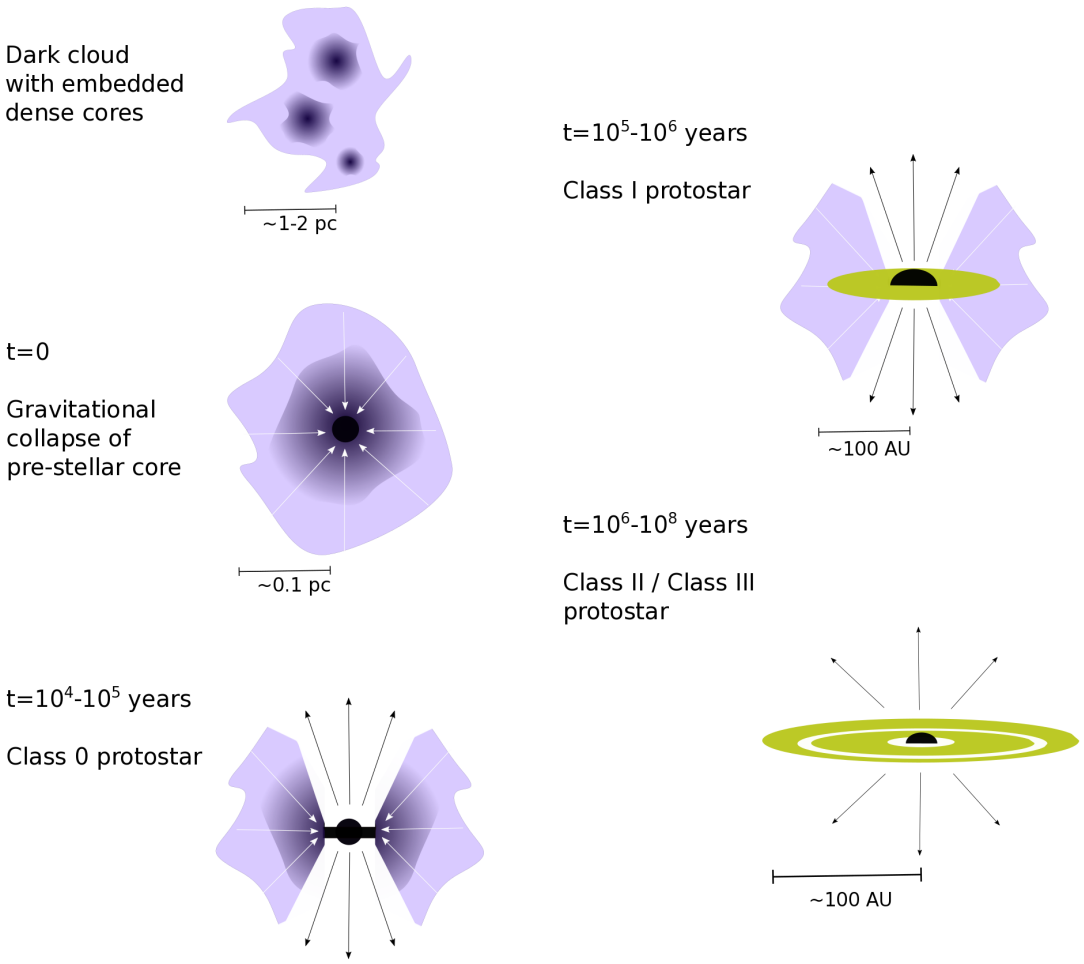

Figure 1.2: Illustration of the main phases of the low-mass star formation. This figure was inspired by Klessen and Glover [2016].

1.3 Astrochemical processes

The following chapter is based mainly on the books Tielens [2005] and Yamamoto [2017].

The majority of the molecules detected so far in the ISM has been identified towards molecular clouds. Within these clouds molecular formation takes place in the gas phase and/or on the surfaces of small dust grains. Dust particles are solid compounds that are made mainly out of silicate and carbonaceous material with typical sizes of 0.005-1μm [Mathis et al., 1977]. Despite their small contribution to the total ISM mass, dust particles play an essential role in the interstellar chemistry, since they serve as efficient coolants of interstellar gas and catalysts for important chemical reactions. The interplay between gas-phase and grain-surface reactions and the chemical complexity seen towards star-forming regions are driven by various physical parameters, such as heating and cooling processes or the irradiation with UV photons and cosmic rays. In the following discussion we will explore the main astrochemical processes in both gas- and solid phase and their connection to the evolutionary stages of a star-forming region.

1.3.1 Gas-phase chemistry

The gas-phase reactions that take place in the ISM can lead to bond formation, bond breaking and bond rearrangement. Radiative association and associative detachment reactions lead to bond formation, while photodissociation, dissociation via cosmic rays and collisions as well as dissociative recombination cause the species to fragment into smaller compounds. Finally, processes like ion-molecule, neutral-neutral and charge-transfer reactions are responsible for rearranging the chemical bonds. The different kind of reactions in the gas phase are summarized in Table 1.1:

Table 1.1: Astrochemical gas-phase reactions along with their reaction rates.

Category	Type of reaction	Reaction	Typical rate coefficient ($cm^3\,s^{-1}$)
Bond formation	Radiative association	$A + B \rightarrow AB + h\nu$	$10^{-17} - 10^{-14}$
	Associative detachment	$A^- + B \rightarrow AB + e^-$	$\sim 10^{-9}$
Bond breaking	Photodissociation	$AB + h\nu \rightarrow A + B$	$10^{-10} - 10^{-8}$ [a]
	Dissociative recombination	$A^+ + e^- \rightarrow C + D$	$10^{-7} - 10^{-6}$
Rearrangement	Ion-molecule reaction	$A^+ + B \rightarrow C^+ + D$	$10^{-9} - 10^{-8}$
	Charge-transfer reaction	$A^+ + B \rightarrow A + B^+$	$\sim 10^{-9}$
	Neutral-neutral reaction	$A + B \rightarrow C + D$	$10^{-11} - 10^{-9}$

[a] The rate coefficient of photodissociation reactions is given in s^{-1}.

The intrinsic velocity k of a bimolecular reaction between species A and B is given by:

$$-\frac{dn(\mathrm{A})}{dt} = -\frac{dn(\mathrm{B})}{dt} = kn(\mathrm{A})n(\mathrm{B}), \tag{1.2}$$

where $n(\mathrm{X})$ denotes the density of species X. Since densities are expressed in cm^{-3} the formation/destruction rate k is given in units of $\mathrm{cm}^3\,\mathrm{s}^{-1}$, unless it is an unimolecular reaction and k is expressed in s^{-1}.

In case of **radiative association**, two species (neutral or ionic) react with each other to form a single product, which is internally excited due to the energy and linear momentum conservation. Within high density environments the product can be de-excited and stabilized through further collision with a third body. However, interstellar gas has extremely low densities compared to typical terrestrial ones; even towards dense clouds with densities of $10^6\,\mathrm{cm}^{-3}$, the collision frequency is very low ($\sim 5\times10^{-4}\,\mathrm{s}^{-1}$), making collisional de-excitation quite unlikely. Stabilization can happen instead with the emission of a photon, when the resulting product returns to the ground state through an allowed electronic transition. The molecule can be de-excited also through vibrational relaxation, and thus emitting in the infrared, although this process is much slower. Typical rate constants for radiative association are $10^{-17} - 10^{-14}\,\mathrm{cm}^3\,\mathrm{s}^{-1}$ but can be as high as $10^{-9}\,\mathrm{cm}^3\,\mathrm{s}^{-1}$ for large, polyatomic species. During an **associative detachment process**, an anionic species reacts with a neutral one, which finally leads to the detachment of an electron. This process can be quite fast with $k \sim 10^{-9}\,\mathrm{cm}^3\,\mathrm{s}^{-1}$, but requires the presence of anions, which have not been widely detected in the ISM. In fact, the only negative ions that have been identified so far towards molecular clouds are $\mathrm{C_6H^-}$, $\mathrm{C_8H^-}$ and $\mathrm{C_4H^-}$ [McCarthy et al., 2006, Brünken et al., 2007, Sakai et al., 2010]. Due to their large electron affinities, these carbon-chain molecules are expected to be formed mostly through radiative electron-attachment reactions: $\mathrm{C_nH} + \mathrm{e^-} \rightarrow \mathrm{C_nH^-} + \mathrm{h}\nu$.

The interstellar radiation field in the ultaviolet regime has been estimated to be equal to $\sim 10^8$ ultraviolet (UV) photons $\mathrm{cm}^{-2}\,\mathrm{s}^{-1}$ [Habing, 1968, Draine, 1978]. Photons with energies larger than 13.6 eV are absorbed by atomic hydrogen at the outer layers of a cloud and therefore do not contribute to the chemistry. Since typical bonding energies of molecules lie between 5 and 10 eV, the UV **photodissociation** is a dominant process for bond breaking in the ISM, showing typical photodissociation rates of $10^{-8} - 10^{-10}\,\mathrm{s}^{-1}$. Following the irradiation and absorption of UV photons, fragmentation happens mostly through the transition of the molecule to the continuum of an excited electronic state. In case of $\mathrm{H_2}$, photodissociation occurs when the excited molecule relaxes back to the ground state but ends up in its vibrational continuum. Towards diffuse and translucent clouds the chemistry is heavily influenced by photodissociation, as the densities are low $\sim 100 - 5000\,\mathrm{cm}^{-3}$, and thus the UV photons can easily penetrate the diffuse gas. Denser sources on the other hand, such as pre-stellar cores, can efficiently shield the internal regions of the source due to the high density of hydrogen gas and dust grains. The latter effectively absorb UV photons (see Section 1.4.1) and following their increase in temperature, re-emit thermal emission in the infrared, to which dust is mostly transparent. In this case, the

photodissociation rate $k_{\rm pd}$ is given by

$$k_{\rm pd} = a \exp(-bA_V), \tag{1.3}$$

where a is the unshielded rate and A_V is the visual extinction due to absorption and scattering processes on dust particles. Apart from dust, molecular hydrogen gas also contributes to the attenuation of UV radiation in dense clouds: when the column density of H_2 is higher than $\sim 10^{14}\,\mathrm{cm}^{-2}$, the medium becomes optically thick to the absorption lines of H_2 in the UV (the Lyman and Werner transitions), leading to the so-called self-shielding effect. In this case, the photodissociation rate is given by the H_2 column density as a function of depth within the cloud.

Unlike UV photons, cosmic rays can be energetic enough (> MeV per nucleon) to permeat even the interiors of a dense cloud. Cosmic rays originate from supernovae, active galactic nuclei and gamma-ray bursts and consist of 84% protons, 14% alpha particles and 2% electrons. Ionization processes induced by direct impact with cosmic rays can release highly energetic electrons that excite H_2 (also H), which subsequently returns to the ground state through radiative decay. The emission of secondary photons from molecular or atomic hydrogen means that there is a permanent UV source present, even towards the densest parts of a core. The mean photon intensity produced locally by cosmic rays is estimated to be equal to $\simeq 10^4\,\mathrm{photons\,cm^{-2}\,s^{-1}}$, which however depends on the grain properties and the energy distribution of cosmic rays [Shen et al., 2004].

Another process that leads to bond breaking of interstellar molecules is the **dissociative recombination reaction**. Here, a cation reacts with an electron, which leads to the production of a highly excited neutral species. Since collisional de-excitation is very unlikely, and when radiative decay is not allowed, the resulting product will release the excessive energy by dissociating and breaking into smaller compounds. These kind of reactions are fast, as they have large cross-sections (due to the strong electrostatic attraction between the cation and the electron). Thus, the corresponding rate constants are large too (up to $\sim 10^{-6}\,\mathrm{cm^3\,s^{-1}}$).

During the early phases of star formation, the temperatures are very low with $\sim 10\,\mathrm{K}$ being typical for pre-stellar cores and $\sim 100\,\mathrm{K}$ characteristic for the diffuse atomic gas. Under these conditions there is very little energy available for colliding species to overcome the activation barrier and finally react with each other. For this reason, the main driver of gas-phase interstellar chemistry are **ion-molecule reactions**: these type of reactions occur fast, as the ion induces a dipole moment to the neutral reaction partner, and hence overcomes any activation barrier energy due to the long-range attractive force. When the involved neutral species has a permanent dipole moment, the reaction takes place even faster and the total rate is described as follows:

$$k_{\rm dip} = 2\pi e \Big[\Big(\frac{\alpha}{\mu}\Big)^{1/2} + \mu_D \Big(\frac{2}{\pi \mu k_B T}\Big)^{1/2} \Big], \tag{1.4}$$

where μ is the reduced mass, α the polarizibilty, e the electron charge, μ_D the dipole moment of the neutral molecule and k_B the Boltzmann constant. The first term of Eq. 1.4

is known as the Langevin rate, which gives the reaction rate in case of an induced-dipole interaction. The presence of a permanent dipole moment contributes to an increased rate: low temperatures and strong dipoles can lead to reaction rates of up to $10^{-7}\,\mathrm{cm^3\,s^{-1}}$. In a **charge-transfer reaction** an electron is exchanged from a neutral atom or molecule to an ion, followed by a possible dissociation of the resulting (molecular) ion. These kind of processes can take place at large distances between the reactants (up to ~ 10 Å) and can show relatively high reaction rates of up to $10^{-9}\,\mathrm{cm^3\,s^{-1}}$. Charge-exchange reactions can lead to the formation of various cations, such as C^+ and O^+ and thus enhance the chemical complexity within molecular clouds.

Neutral-neutral reactions involve an activation barrier energy in order to achieve the bond breaking and rearrangement. Such reactions are relevant in warm environments, like the hot central core of a protostar. In cold sources on the other hand, such as pre-stellar cores, the only neutral-neutral reactions that can take place are the ones involving radicals that have at least one unpaired valence electron and are thus highly reactive[7]. Reaction rates of this type of processes are expressed in a modified form of the Arrhenius-equation:

$$k_{\mathrm{neut}} = \alpha(T/300)^{\beta}\exp(-\gamma/k_B T). \tag{1.5}$$

Here, the rate coeffiecient α has the same unit as the total reaction rate k_{neut} ($\mathrm{cm^3\,s^{-1}}$), while β is just a numerical factor. The coefficient γ describes the activation energy and is given in K.

As already mentioned above, the main driving force of interstellar gas-phase chemistry are ion-molecule reactions that are barrierless and can take place also at very low temperatures ($\sim 10\,\mathrm{K}$). The rich ion-molecule chemistry on the other hand, is a result of the ionization processes triggered mostly by the highly energetic cosmic rays; especially towards dense clouds that efficiently attenuate UV radiation, cosmic rays are the main source of ionization. The most prominent example is the cosmic-ray ionization of H_2 that produces H_2^+. Once formed, H_2^+ reacts with H_2 and forms H_3^+. This cation is the most important molecule in astrochemistry: since it is an ionic species, it can easily react with other atoms and molecules, serving as a proton-donor. This initiates several other chemical processes and eventually increases the molecular complexity seen in star forming regions. For example, the reaction of H_3^+ with atomic carbon is the starting point of hydrocarbon chemistry through the following reaction path:

$$\mathrm{C} \xrightarrow{\mathrm{H_3^+}} \mathrm{CH^+} \xrightarrow{\mathrm{H_2}} \mathrm{CH_2^+} \xrightarrow{\mathrm{H_2}} \mathrm{CH_3^+} \xrightarrow{\mathrm{e^-}} \mathrm{CH, CH_2}. \tag{1.6}$$

CH_3^+ can also react with O and form HCO^+, which in turn is the most important precursor for CO, the second most abundant molecule in the ISM.

The primary **cosmic-ray ionization rate** $\zeta(\mathrm{CR})$ can be determined based on observations of H_3^+ in diffuse clouds. Considering electron recombination as the main loss route

[7]Recent studies [Shannon et al., 2013] have shown that the reaction rate between a radical and a neutral species at interstellar temperatures is even higher than expected due to quantum tunneling through the activation energy barrier.

for H_3^+, the ζ(CR) can be described as:

$$\zeta(\mathrm{CR}) = \frac{k_\mathrm{e}\, n(e)\, n(\mathrm{H}_3^+)}{2.3\, n(\mathrm{H}_2)}, \tag{1.7}$$

where the numerical factor takes into account secondary ionization. Assuming that we have a uniform cloud in which the electrons originate from the ionization of atomic carbon and considering an electron recombination coefficient k_e of $10^{-6}\, T^{-0.45}$, will lead to the following expression for ζ(CR):

$$\zeta(\mathrm{CR}) = 7 \times 10^{-8} \frac{N(\mathrm{C}^+)\, N(\mathrm{H}_3^+)}{N(\mathrm{H}_2)\, L} = 7 \times 10^{-16} \Big(\frac{\mathrm{pc}}{L}\Big). \tag{1.8}$$

Here, the density has been replaced by the expression of the column density N(X) using the relation: $N(\mathrm{X}) = n(\mathrm{X}) \times L$, with L being the pathlength of the source. Typical sizes of diffuse clouds ($L \sim (2-3)\,\mathrm{pc}$) result to a ζ(CR) of $(2-3) \times 10^{-16}\,\mathrm{s}^{-1}$. However, when considering observations of H_3^+ towards dense clouds, the estimated cosmic-ray ionization rate is lower with $\zeta(\mathrm{CR}) = (1-3) \times 10^{-17}\,\mathrm{s}^{-1}$. This indicates that a denser environment provides a stronger protection from cosmic rays and thus shows a lower ionization fraction. The total ionization rate $k_\mathrm{CR,i}$ of a species i including also secondary ionization is expressed as:

$$k_\mathrm{CR,i} = A_i\, \zeta(\mathrm{CR}). \tag{1.9}$$

The factor A_i depends on the integrated cross section across the relevant ionization spectrum [Heays et al., 2017]. Chemical databases commonly refer to the primary cosmic-ray ionization rate of H_2, which is twice as high as the corresponding value for atomic hydrogen.

1.3.2 Grain-surface chemistry

The most abundant molecule in the ISM is H_2, which can be formed in the gas phase via the radiative association reaction of two H atoms: $\mathrm{H} + \mathrm{H} \rightarrow \mathrm{H}_2 + \mathrm{h}\nu$. However, this process is extremely slow ($\leq 10^{-23}\,\mathrm{cm}^3\,\mathrm{s}^{-1}$), as the radiative decay in a homonuclear molecule like H_2 is highly forbidden. This is a clear indication that the only way for H_2 to form efficiently in the ISM, is on the surface of dust grains: the excessive energy that is released during the H_2 formation is absorbed by dust grains that act as a third body. This makes the presence of dust grains vital to the interstellar chemistry. Once H_2 is formed, a large number of reactions is triggered through the formation of H_3^+, as mentioned already in Section 1.3.1. But how are dust particles formed in the first place? When an old, dying star reaches the end of its hydrogen fusion stage, it begins to eject its outer layers, that consist of heavy particles such as SiO, SiC and TiO. These molecules eventually condense in the cool atmosphere of the evolved star and become the seeds of dust grains. As time evolves, the grains become larger and convert into amorphous structures made of sillicate and/or carbonaceous material. Their typical size is $\sim 0.1\,\mu$m, although they can grow

up to a few cm towards dense cores and circumstellar disks. At the low temperatures of dense cores, gas-phase molecules freeze-out on the grain-surfaces forming layers of ice that contain predominantly water, CO, CO_2, CH_3OH and H_2CO. Fig. 1.3 shows an infrared spectrum taken towards the W33A massive young star by Gibb et al. [2000]. Here, several absorption features are visible that originate either from the silicate core of the grain (broad absorption lines), or the icy species on the grain-surface (like H_2O, CO and etc.).

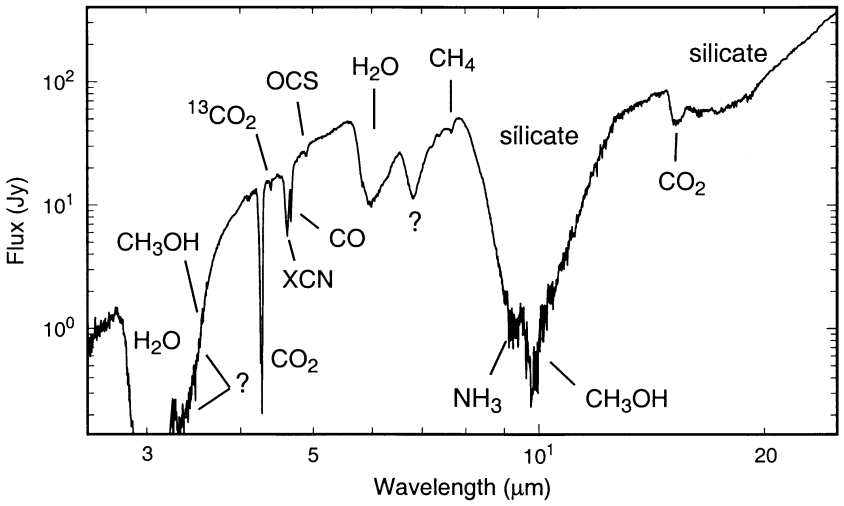

Figure 1.3: Infrared spectrum of the dust-embedded W33A young stellar object [Gibb et al., 2000].

Dust-grain chemistry mainly involves the deposition of species on grain-surfaces, known as accretion, the surface mobility of the accreted species and finally the ejection of the grains-species back to the gas-phase, called desorption (see Fig. 1.4). In the following paragraphs we will discuss these mechanisms in more detail.

When a gas-phase species is coming close to a grain-surface it experiences attractive Van-der-Waals forces, that originate from the mutually induced dipole moment between the approaching molecule and the atoms of the grain-surface. The probability of a species to accrete onto the surface (also known as sticking coefficient) depends on the thermal energy of the accreting molecule, the phonon energy of the grain-lattice as well as the interaction energy between molecule and grain. At typical temperatures of pre-stellar cores ($10 - 20\,\mathrm{K}$) the sticking probability of most species has been estimated to be 1, except for atomic hydrogen, whose sticking coefficient amounts to 0.8 at 10 K. The location of the accreted species on a dust grain is called adsorption or surface site. Depending on the binding/desorption energy E_D, i.e. depth of the potential well, surface sites are distinguished between the so-called physisorbed sites with well depths of 0.01-0.2 eV and the chemisorbed sites with an energy depth of $\sim 1\,\mathrm{eV}$. Chemisorbed sites have strongly bound molecules that share electrons with the atoms of the grain-lattice. Based on experimental

studies done on olivine dust grains [8], the surface density has been estimated to be $2 \times 10^{14}\,\mathrm{sites\,cm^{-2}}$, which results to $\approx 3 \times 10^5$ sites per grain [Biham et al., 2001].

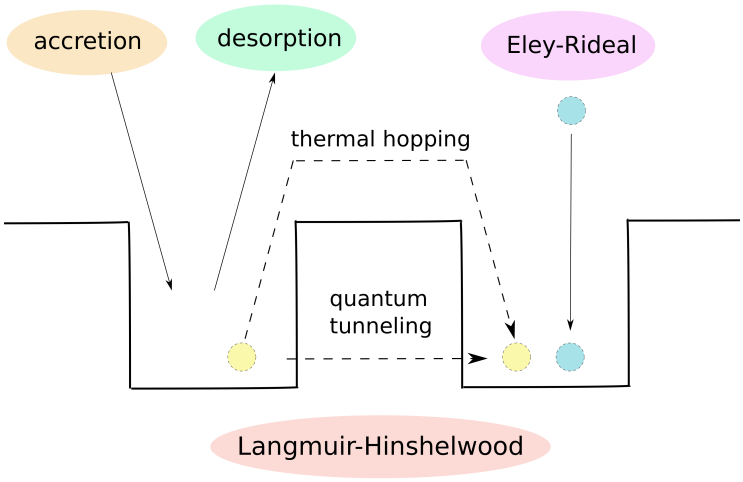

Figure 1.4: Depiction of the main chemical processes (accretion, desorption, surface migration) taking place on grain-surfaces.

As depicted in Fig. 1.4, reactions on grains can happen in two ways: (1) adsorbed species move through the surface, until they meet and eventually react with each other, known as the Langmuir-Hinshelwood mechanism or (2) gas-phase species impact the dust grain and react directly with already adsorbed molecules without being accreted on the surface first; this is the so-called Eley-Rideal mechanism. For the first mechanism to occur at low temperatures, at least one of the reactants has to be a physisorbed species, or in other words, weakly bound to the surface. A chemisorbed species on the other hand, is not capable of diffusive motion through the surface and can therefore react with another species only through the Eley-Rideal mechanism.

The Langmuir-Hinshelwood process is considered to be the most probable mechanism for surface chemistry. Especially towards diffuse clouds, where the dust grains are not covered by icy mantels, the probability of a gas-phase H-atom to find and react with another H-atom already accreted on a grain-surface is very small. According to the formalism proposed by Hasegawa et al. [1992], diffusive surface chemistry can take place either via quantum tunneling of light species through potential barriers or via thermal hopping. If we assume a rectangular potential barrier of height E_b and width a, light species (H, D and H_2) can tunnel through that energy barrier in a time τ_{qt}:

[8] olivine is a polycrystalline silicate thats consists of Mg_2SiO_4 and Fe_2SiO_4.

$$\tau_{\rm qt} = {\nu_0}^{-1} \exp\left[\frac{2a}{\hbar}(2mE_b)^{1/2}\right], \tag{1.10}$$

where m is the mass of the accreted species ν_0 is the vibrational frequency of the species within the grain lattice. Typical timescales for atomic hydrogen scanning with a barrier width of $a = 1$ Å, Eq. 1.10 are $\tau_{\rm qt} \sim 10^{-4}$ s. If the temperatures are high enough, accreted species can overcome the energy barrier by "hopping" from one surface site to another. The thermal hopping timescale is expressed as:

$$\tau_{\rm th} = {\nu_0}^{-1} \exp(E_b/k_B T_{\rm dust}). \tag{1.11}$$

At a dust temperature of 10 K the thermal hopping timescale for H can be as short as $\tau_{\rm th} \sim 10^{-3}$ s, suggesting that quantum tunneling happens faster at low temperatures. The decisive factor for the surface mobility is determined by the energy ratio E_b/E_D. A large potential height E_b will decrease the probability of quantum tunneling and thus only thermal hopping will play an essential role. Based on previous work [Hasegawa et al., 1992, Ruffle and Herbst, 2000, Vasyunin and Herbst, 2013a] the most common values adopted for the E_b/E_D ratio are: 0.30, 0.50 and 0.77. For the latter two cases the quantum tunneling is expected to be negligible due to the long resulting timescales (see Eq. 1.10).

One way for grain-species to be ejected back to the gas phase is via thermal desorption. This process happens when the dust temperature reaches the sublimation temperature of the accreted species, which mostly depends on its desorption energy E_D. The thermal desorption rate is described as

$$k_{\rm ev} = \nu_0 \exp(-E_D/k_B T_{\rm dust}). \tag{1.12}$$

Due to the low existing temperatures towards dense molecular clouds, the observed abundances of gas-phase molecules can only be explained if non-thermal desorption processes are taken into account. One of these happens upon irradiation of the grains by interstellar UV photons, also known as photodesorption. Recent experimental studies [Fayolle et al., 2013, Dupuy et al., 2017] have shown that photodesorption occurs through the electronic excitation of the accreted molecules, which can lead to two possible outcomes: (1) the excited species release the UV radiation when returning to the ground state, which then causes other molecules of the grain-lattice to rearrange and subsequently desorb. In this case the photodesorption yield (defined as number of desorbed molecules per UV photon) strongly correlates with the efficiency of the energy redistribution between the excited species and the grain surface [Fayolle et al., 2013]; (2) the excited molecules dissociate upon UV irradiation, which introduces new ways of ejecting grain species to the gas phase. For example, in case of the O_2 photodissociation, the resulting oxygen atoms can meet on the grain and react with each other to form molecular oxygen, which releases its excessive energy via desorption (exothermic recombination). Another option is that molecular oxygen

is ejected to the gas phase following its collision with a mobile oxygen atom (kick-out by atomic oxygen). Finally, an oxygen atom can react with accreted O_2 and form O_3, which can lead to the formation of excited O_2 upon photolysis (photoinduced dissociation of O_3). Typical values for photodesorption yields range from 10^{-2} to 10^{-5} molecules/UV photon. Good estimates have been done for H_2O, O_2, CH_4 and CO ices with a photodesorption efficiency of $\sim 10^{-3}$ molecules/UV photon.

Non-thermal desorption can also be induced by the irradiation of cosmic rays. In this case, cosmic rays will transfer energy to a dust grain, which will in turn heat up, leading to the desorption of volatile accreted species. A study by Hasegawa and Herbst [1993] has shown that the impact by a heavy cosmic ray (like Fe) of 20-70 MeV per nucleon will increase the dust temperature up to ~ 70 K, causing some molecules to desorb, but not complex ones like CH_3OH that are more strongly bound to the surface. Nevertheless, this kind of non-thermal desorption has proven to be very slow and is relevant only on large timescales ($t \geq 10^6$ yr) for species like CO [Hasegawa and Herbst, 1993].

Finally, another non-thermal desorption process essential for interstellar chemistry is the reactive desorption, in which the excited product of an exothermic reaction is desorbed from the surface due to its excessive energy. The reactive desorption rate is only poorly constrained, as it has been experimentally determined just for H_2 so far [Katz et al., 1999]. Recent theoretical studies [Garrod et al., 2007, Vasyunin and Herbst, 2013b] have adopted for the reactive desorption efficiency values of 1% and 10%, that were able to reproduce the observed abundances of several complex organic molecules (like CH_3OH, CH_3OCH_3) towards cold cores.

1.3.3 Gas-grain chemical network

Taking into account the chemical processes described above, one can construct a large chemical network of all known reactions in the gas and solid phase that can serve as an input information for chemical models. Such models are based on a numerical code, that solves differential equations for the abundance of each species and has the following form:

$$\frac{dn_i(\text{gas})}{dt} = \sum_{lm} k_{lm} n_l n_m - n_i \sum_s k_{is} n_s - r_i^{\text{acc}} n_i + r_i^{\text{des}}, \tag{1.13}$$

$$\frac{dn_i(\text{grain})}{dt} = \sum_{lm} k_{lm} n_l n_m - n_i \sum_s k_{is} n_s + r_i^{\text{acc}} n_i - r_i^{\text{des}}, \tag{1.14}$$

where Eq. 1.13 and Eq. 1.14 describe the time evolution of abundances of gas-phase and grain-surface species, respectively. The first term in the above equations stands for the sum of all bimolecular reactions that lead to the formation of species i, while the second sum contains all co-reactants of species i. The last two terms give the change in abundance due to accretion and desorption to/from dust grains. This set of differential equations, also

known as chemical rate equations, is integrated over time upon certain physical consitions, such as a given density, temperature, and a cosmic-ray ionization rate, as well as a set of initial elemental abundances. The result of this numerical integration are time-dependent chemical abundances of the involved species with respect to the total number of hydrogen nuclei. In this thesis we are using a chemical code that was developed by Vasyunin and Herbst [2013a], and contains over 600 species whose abundances are regulated by over 6000 gas-phase reactions and 200 grain-surface processes. More information on this can be found in Chapter 5.

An alternative option to the deterministic approach is the application of a stochastic method, such as the Monte Carlo approach, which instead of chemical abundances is calculating the probability of a chemical system to be in a certain state within the phase space at a given time. Previous studies [Vasyunin et al., 2009, Vasyunin and Herbst, 2013a] have shown that the Monte Carlo method has proven to be suitable for reproducing well the stochastic nature of surface processes, requires however extensive computer power, and is thus not always preferred.

1.4 Observational studies

The following chapter is based mainly on the references Mangum and Shirley [2015] and Yamamoto [2017].

1.4.1 Radiative transfer equation

One of the most important relations in astrochemistry is the radiative tranfser equation. This equation describes the absorption, emission and scattering processes that take place when light propagates through a medium and is described by the following expression:

$$\frac{dI_\nu}{ds} = -\rho\kappa_\nu I_\nu + j_\nu, \tag{1.15}$$

where ν is the frequency of the passing light, I_ν the specific intensity (W/m^2/sr/Hz), s the propagation path and κ_ν is the opacity (cm^{2}g^{-1}), which expresses the effective surface area for extinction per unit mass of interstellar material. In addition, ρ is the total gas density (g cm^{-3}) and j_ν describes the emissivity (W/m^3/sr/Hz). The product $\rho\kappa_\nu$ gives the absorption coefficient in cm^{-1}. The above equation indicates that when radiation passes through the medium it reduces by $\rho\kappa_\nu I_\nu ds$ (due to absorption), while it can also increase by $j_\nu ds$ due to emission coming from the host medium. Since the actual propagation length s is usually unknown, it is customary to use instead a new quantity called the optical depth, τ_ν:

$$d\tau_\nu = \rho\kappa_\nu ds. \tag{1.16}$$

This changes Eq. 1.15 to:

$$dI_\nu = -I_\nu d\tau_\nu + S_\nu d\tau_\nu, \tag{1.17}$$

where we introduce $S_\nu = \frac{j_\nu}{\rho\kappa_\nu}$ known as the source function. Multiplying both sides of Eq. 1.17 by e^{τ_ν} followed by integration from $\tau_\nu = 0$ and $I_\nu = I_\nu(0)$ we obtain:

$$I_\nu = I_\nu(0)e^{-\tau_\nu} + \int_0^{\tau_\nu} \exp[-(\tau_\nu - \tau')]S_\nu d\tau'. \tag{1.18}$$

Eq. 1.18 describes the measured intensity I_ν as the sum of what remains from the background intensity after being attenuated by the host gas ($I_\nu(0)e^{-\tau_\nu}$) plus the emission ($S_\nu d\tau'$) from the medium itself being also attenuated by absorption along the remaining path to the observer ($\exp[-(\tau_\nu - \tau')]$). Radiation cannot penetrate regions with a large optical depth ($\tau_\nu \gg 1$); in these cases the medium is said to be "optically thick". Therefore if the interior of an object has $\tau_\nu \gg 1$, we only see the emission coming from the outer layers or the surface of the object.

The above equation can be further simplified by assuming Local Thermodynamic Equilibrium (LTE). In general, a global equilibrium can only be considered for closed systems, which is not the case for a radiative system, such as a star forming region. A system is said to be in LTE when the following conditions are valid:

- The velocity distribution of a sample of particles is given by the Maxwell-Distribution.
- The energy level population in a molecule is described by the Boltzmann-Distribution.
- Radiative balance is achieved at a specific frequency ν with $S_\nu = B_\nu(T_{\rm ex})$.

The excitation temperature $T_{\rm ex}$ is a measure of the level population of a molecule and is assumed to be uniform throughout the entire medium. At LTE the kinetic, excitation and radiative temperature are all in equilibrium with each other ($T_{\rm kin} \approx T_{\rm ex} \approx T_{\rm rad}$)[9]. In the following discussion we will explore what conditions produce an emission or an absorption molecular line when considering a **gas-phase medium**. Integration of Eq. 1.18 leads to:

$$I_\nu = I_\nu(0)e^{-\tau_\nu} + B_\nu(T_{\rm ex})(1 - e^{-\tau_\nu}) \tag{1.19}$$

There are four cases that best describe what Eq. 1.19 implies:

- The gas is optically thin ($\tau_\nu \ll 1$) and the background intensity is insignificant ($I_\nu(0) \to 0$). If we perform a Taylor-Expansion of the exponent in Eq. 1.19 we obtain:
  $I_\nu = \tau_\nu B_\nu(T_{\rm ex})$
  This result indicates that if the radiation frequency matches the transition frequency of a specific molecule in the host gas, then the absorption coefficient $\rho\kappa_\nu$ becomes large and we record an emission line.

[9] $T_{\rm kin}$ describes the kinetic temperature of the gas particles and $T_{\rm rad}$ stands for the radiative temperature of a blackbody.

- The gas is optically thick ($\tau_\nu \gg 1$) and the background intensity is negligible ($I_\nu(0) \to 0$). This leads to:
  $I_\nu = B_\nu(T_{\rm ex})$
  In this case the emitted radiation resembles a black body spectrum.

- The gas is optically thin ($\tau_\nu \ll 1$) and the background intensity is significant:
  $I_\nu = I_\nu(0) - \tau_\nu(I_\nu(0) - B_\nu(T_{\rm ex}))$
  This leads to further two sub-cases:

  - if $I_\nu(0) < B_\nu(T_{\rm ex})$ we will record an emission line (overlapping with a background spectrum).

  - if $I_\nu(0) > B_\nu(T_{\rm ex})$ we will obtain an absorption line.

- The gas is optically thick ($\tau_\nu \gg 1$) and the background intensity is significant:
  $I_\nu = B_\nu(T_{\rm ex})$
  This gives the same result as the second case.

In order to obtain the intensity that only originates from the molecule itself, one has to remove from the total measured intensity I_ν the background intensity $I_\nu(0)$ as done in the following:

$$\begin{aligned}\Delta I_\nu &= I_\nu - I_\nu(0) \\ &= I_\nu(0)\exp(-\tau_\nu) + B_\nu(T_{\rm ex})[1-\exp(-\tau_\nu)] - I_\nu(0) \\ &= [B_\nu(T_{\rm ex}) - B_\nu(T_{\rm bg})][1-\exp(-\tau_\nu)],\end{aligned} \tag{1.20}$$

where we used $B_\nu(T_{\rm bg}) = I_\nu(0)$ with $T_{\rm bg}$ being the background temperature. It is common to replace the specific intensity I_ν by a quantity known as the Rayleigh-Jeans temperature $J_\nu(T)$ that expresses the blackbody radiation in terms of a temperature:

$$J_\nu(T) = \Big(\frac{h\nu}{k_B}\Big)(e^{\frac{h\nu}{k_B T}} - 1)^{-1}, \tag{1.21}$$

which in turn is related to the blackbody radiation field B_ν as:

$$\frac{c^2}{2k_B\nu^2}B_\nu(T) = J_\nu(T). \tag{1.22}$$

Considering the above relations, we can write the radiative transfer equation in the following final form:

$$T_R = [J_\nu(T_{\rm ex}) - J_\nu(T_{\rm bg})][1-\exp(-\tau_\nu)], \tag{1.23}$$

where the so-called source radiation temperature T_R is defined as $T_R = \frac{c^2}{2k_B\nu^2}\Delta I_\nu$.

An essential quantity that is used frequently in observational studies in order to derive the physical properties of a source, such as densities, molecular abundances and the kinetic gas temperature, is the column density. This quantity gives the number of molecules per unit area along the line of sight. The column density of molecules in the upper energy state u is given by integrating the volume density n_u over the pathlength ds:

$$N_u = \int n_u ds. \tag{1.24}$$

The column density N_u and the optical depth τ_ν are related to each other as[10]:

$$N_u = \frac{3h}{8\pi^3|\mu_{lu}|^2}\left[\exp\left(\frac{h\nu}{k_B T}\right) - 1\right]^{-1} \int \tau_\nu dv, \tag{1.25}$$

where the Doppler conversion $\frac{d\nu}{\nu} = \frac{dv}{c}$ has been considered. The quantity $|\mu_{lu}|^2$ describes the dipole matrix element of a transition with an upper and a lower energy state u and l, respectively. The total molecular column density N_{tot} gives the total number of molecules in all possible states and is related to N_u through the following expression:

$$\frac{N_{tot}}{N_u} = \frac{Q_{rot}}{g_u} \exp\left(\frac{E_u}{k_B T_{\rm ex}}\right). \tag{1.26}$$

The quantity Q_{rot} is known as the rotational partition function and describes the statistical sum of all rotational energy states in a molecule. The degeneracy factor of the upper state u is given by g_u. Through the substitution of Eq. 1.25 in Eq. 1.26 we obtain for N_{tot}:

$$N_{tot} = \frac{3h}{8\pi^3|\mu_{lu}|^2}\frac{Q_{rot}}{g_u} \exp\left(\frac{E_u}{k_B T_{\rm ex}}\right) \times \left[\exp\left(\frac{h\nu}{k_B T}\right) - 1\right]^{-1} \int \tau_\nu dv. \tag{1.27}$$

In this thesis we study the molecular emission lines towards dense cores as well as molecular absorption lines towards diffuse/translucent clouds. In both cases, the observed gas is considered to be optically thin ($\tau_\nu \ll 1$) to the investigated molecular transitions, meaning that the molecular line intensity ΔI_ν (as shown above) is equal to $\tau_\nu(B_\nu(T_{\rm ex}) - I_\nu(0))$. In terms of T_R we retrieve for the optically thin approximation:

$$T_R = \tau_\nu[J_\nu(T_{\rm ex}) - J_\nu(T_{\rm bg})], \tag{1.28}$$

and the column density becomes:

$$N_{tot}^{thin} = \frac{3h}{8\pi^3|\mu_{lu}|^2}\frac{Q_{rot}}{g_u} \exp\left(\frac{E_u}{k_B T_{\rm ex}}\right) \times \left[\exp\left(\frac{h\nu}{k_B T}\right) - 1\right]^{-1} \frac{1}{[J_\nu(T_{\rm ex}) - J_\nu(T_{\rm bg})]} \int T_R dv. \tag{1.29}$$

[10] for the full derivation see Mangum and Shirley [2015]

Observations provide us with the factor $\int T_R dv$, which is the integrated intensity, or in other words, the area covered underneath a spectral line.

What happens if we also take into account **dust particles** in our host medium? Dust grains interact efficiently with radiation whose wavelength is similar to the size of the grains. Since grains are sub-micron in size with typical radii of $\sim 0.1\,\mu$m, the extinction due to absorption and scattering is much higher for short wavelengths (the UV- and in the optical regime) than towards long wavelengths, indicating that dust particles are mostly transparent to radiation in the millimeter and the far-infrared range. The heating of the dust grains up to $\sim 10-90$ K through the absorption of UV photons leads to the emission of thermal radiation lying in the far-infrared (30-300 μm) that will pass through the source mostly unhindered; this represents the most efficient cooling mechanism in the ISM. In general, the extinction at visual wavelentghs ($\sim$ 5500 Å) is defined as $A_V = 1.086 \times \tau_\nu$, with τ_ν being the optical depth of the dust. Since the host medium towards dense clouds is optically thin to the thermal dust emission, we obtain also here from the radiative transfer equation: $I_\nu = \tau_\nu B_\nu(T_{\rm dust})$. The density ρ of a dense cloud can be written as a function of the density of molecular hydrogen as $\rho = \mu_{\rm H_2}\, m({\rm H})\, n({\rm H_2})$. Following this, we retrieve for the optical depth τ_ν after integrating along the line of sight:

$$\tau_\nu = \kappa_\nu \mu_{\rm H_2} m({\rm H}) \int n({\rm H_2}) ds = \kappa_\nu \mu_{\rm H_2} m({\rm H}) N_{\rm H_2}, \tag{1.30}$$

where $N_{\rm H_2}$ gives the column density of molecular hydrogen. Previous studies [Hildebrand, 1983] have shown that the dust opacity κ_ν can be described by a power-law in the millimeter range:

$$\kappa_\nu = \kappa_{\nu_0} \Big(\frac{\nu}{\nu_0}\Big)^\beta, \tag{1.31}$$

with β being a parameter depending on the properties of the dust grains, called spectral index. Typical values are $\beta \approx 1-2$ between 30 μm and 1 mm. β has been found to be small towards dense cores and circumstellar disks, but closer to 2 within molecular and diffuse clouds [Schnee and Goodman, 2005]. Under consideration of Eq. 1.30 and Eq. 1.31 the dust emission can be expressed as:

$$I_\nu = \kappa_{\nu_0} \Big(\frac{\nu}{\nu_0}\Big)^\beta \mu_{\rm H_2} m({\rm H}) N_{\rm H_2} B_\nu(T_{\rm dust}) \tag{1.32}$$

Eq. 1.32 allows us to determine $N_{\rm H_2}$ of the observed dense cloud by fitting the spectral energy distribution (SED) to the thermal emission of dust grains in the mm-range.

1.4.2 Deuterium fractionation

Deuterium was formed along with H and He during the early phases of the Universe and its cosmic abundance D/H is estimated to be $\sim 2\times10^{-5}$. D-atoms are thought to be destroyed in the inner parts of stars, which explains why the deuterium abundance is lower towards the Galactic center, that shows a high star formation rate. However, towards dense objects,

such as pre-stellar and protostellar cores, the abundance ratios of deuterated molecules with respect to the associated normal species can reach very high levels ($> 10\%$), suggesting that there must be chemical processes in play that enhance the total deuteration level. The key molecule for initiating deuterium fractionation is H_3^+. Once formed, H_3^+ can exchange a proton with a deuteron through the exothermic reaction:

$$H_3^+ + HD \rightleftharpoons H_2D^+ + H_2 + 230\,K. \tag{1.33}$$

At low temperatures of pre-stellar cores ($< 20\,K$), the above reaction proceeds from left to right, increasing the abundance of H_2D^+. This molecule can then easily tranfer its deuteron to other species through further reactions, such as:

$$H_2D^+ + N_2 \rightarrow N_2D^+ + H_2 \quad \text{or} \tag{1.34}$$

$$H_2D^+ + CO \rightarrow DCO^+ + H_2 \tag{1.35}$$

Further deuteration leads to the formation of the doubly and triply deuterated species D_2H^+ and D_3^+. The spin symmetry of H_2 is also crucial for the deuterium fractionation. Ortho- (parallel nuclear spins) and para- (anti-parallel nuclear spins) H_2 is formed on dust grains showing a statistical ratio of 3:1, with ortho-H_2 lying energetically higher than para-H_2 (lowest energy level is $\sim 175\,K$). If the abundance of ortho-H_2 increases, the activation barrier of the inverse reaction of Eq. 1.33 can be overcome and subsequently decrease the H_2D^+ abundance. However, previous studies [Sipilä et al., 2013] have shown that proton-exchange reactions in the gas phase, that convert ortho- to para-H_2 are favoured at low temperatures of pre-stellar cores, enhancing the abundance of the less energetic para-H_2. Another factor that affects the deuteration level is the depletion level of CO from the gas phase, which is described as the ratio of the CO abundance in the local ISM (undepleted) to the observed CO abundance. At high densities, CO molecules (and other neutral species like atomic O) freeze-out on the surfaces of dust grains forming icy mantles. Having less CO available in the gas-phase means that the destruction rate of H_3^+ and H_2D^+ through their reaction with CO is decreased, and finally the deuteration level increases.

The physical properties of pre-stellar cores change from the core center to the edge of the object: towards the outer layers, densities are still low $< 10^4\,cm^{-3}$ and the UV radiation can easily penetrate the medium; photochemistry (like photodissociation and ionization) plays here a major role in the formation and destruction of molecules. In the so-called dark-cloud zone the environment becomes denser, the visual extinctions larger ($A_V > 4\,mag$) and the main driver of the chemistry are molecule-ion reactions. Towards the central core ($\sim 7000\,AU$), the density becomes even higher than a few $10^4\,cm^{-3}$, which leads to a significant shielding from the interstellar radiation; the visual extinction reaches very large values of $\geq 50\,mag$. This region is known as the deuteration zone, where the

deuteration process becomes the most efficient: temperatures drop down to $\sim 7-10\,\mathrm{K}$, and $\sim 90\%$ of the CO molecules are frozen-out on dust grain surfaces. The largest deuteration within pre-stellar cores has been observed in N_2H^+ with $N_2D^+/N_2H^+ = 0.1-0.7$, followed by ammonia with $NH_2D/NH_3 = 0.1-0.4$ and formaldehyde, $D_2CO/H_2CO = 0.01-0.1$ (see Ceccarelli et al. [2014] and references therein). High deuteration levels of certain molecules (such as methanol and formaldehyde) can be explained if we consider additional deuterium enrichment taking place in grains. The dissociative recombination of H_2D^+, D_2H^+ and D_3^+ leads to an enhanced D/H ratio of atomic gas (high abundance of D-atoms in the gas phase). Due to high densities and low temperatures, deuterium atoms (along with other species) freeze-out on dust grains and subsequently scan the surface of the icy mantles (but slower than hydrogen due to the higher mass) till they find another reaction partner. Water, for example, is mainly formed and deuterated on the grain surfaces by adding H and D atoms to atomic O, O_2 and O_3. The depleted species can eventually evaporate from the cold surfaces of grains via non-thermal desorption mechanisms (such as photodesorption) [Ceccarelli et al., 2014]. The regions of low, medium and high deuterium fractionation towards the pre-stellar core L1544 are shown in the left panel of Fig. 1.5, while the right panel summarizes the main steps of deuteration processes towards cold cores.

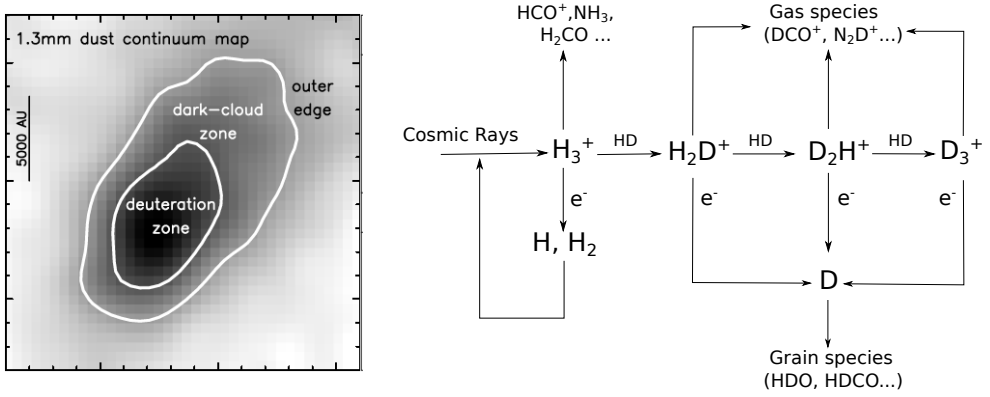

Figure 1.5: *Left panel:* Dust continuum emission of the pre-stellar core L1544 recorded at 1.3 mm, depicted in grey scale [Ceccarelli et al., 2014]. The transitions from the outer-edge to the dark zone and finally to the deuteration zone are marked by white contours. *Right panel:* Main steps of deuterium fractionation processes towards cold cores (see text for explanation).

The highest deuteration levels have been measured so far towards Class 0 protostars, where also large abundances of doubly and triply deuterated molecules have been detected. As already mentioned in Section 1.2, Class 0 protostars are the youngest protostars with a hot central core (temperatures of $\sim 100 - 120$ K), surrounded by an outer, colder envelope. The high temperatures towards the center lead to the thermal desorption of the deuterated species that were frozen onto the dust grains during the pre-stellar core phase: the enriched deuteration observed here is mainly inherited from the pre-stellar ices. This

is also supported by the fact that Class 0 protostars are short-lived ($10^4 - 10^5$ yrs). The reasons for the high deuteration levels towards the cold envelope are the same as for the pre-stellar cores. Here, the grain species originating from the past remain accreted on the grain surfaces.

From the above considerations it is evident that deuterium fractionation is strongly correlated with the physical conditions of the source: low temperatures favour the production of H_2D^+ and high densities lead to efficient freeze-out of CO (and other species). Therefore, the deuteration level of a molecule can reveal information about the evolutionary stage of an observed source. In addition to single deuteration, one can also study the D/D_2 abundance ratio of molecules; this helps us understand better the formation and destruction routes of deuterated species and put additional constraints on chemical models. Since the deuteration level in the gas phase is expected to increase with time via successive reactions with H_2D^+ and eventually reach a stationary value, the determination of both single and double deuteration can be used as a chemical clock and constrain the age of the core.

In this thesis we study the single and double deuteration of c-C_3H_2 towards starless/pre-stellar cores and Class 0 protostars. This molecule provides two main advantages: it is quite abundant in space and also has the possibility of double deuteration. The most prominent evolutionary tracer so far has been N_2H^+. This species has proven to be more resistant to depletion than carbon-bearing species, and thus being able to trace the denser, central parts of the core, while c-C_3H_2 is believed to trace the outer layers of the core, which are less dense and more exposed to UV radiation. The study of the c-C_3H_2 deuteration can reveal possible differences between the deuteration of carbon- and nitrogen-bearing species. In addition, since c-C_3H_2 is strongly affected by depletion, comparing its deuteration level towards pre-stellar cores and young protostars can unveil possible deuteration processes on dust grains happening in the pre-stellar core phase, right before the ignition of a protostar. More information on the deuteration of c-C_3H_2 in star forming regions can be found in Chapter 2.

1.4.3 Radioastronomy

Ground-based telescopes can only record parts of the electromagnetic spectrum that pass through the atmosphere without being absorbed or scattered. Based on the transmittance of the Earth's atmosphere, one of these spectral windows lies in the visible regime and covers the range from 300 to 900 nm; this light can be used to probe electronic transitions. Furthermore, the atmosphere is partially transparent to two spectral windows in the infrared, that span from 1 to 5 μm and from 8 to 14 μm, corresponding to vibrational molecular transitions. Another partially "observable" window lies in the microwave and millimeter regime and ranges from 0.6 to 8 mm, which is suitable for studying rotational transitions. Finally, a radio-wave window from 5 cm to 10 m is accessible as well, and can be used for example to observe the 21 cm line of atomic hydrogen. Since the present thesis aims to study molecular rotational transitions that lie in the millimeter range, the perfect observational tool is a radio telescope. For this work in particular, we have used the IRAM 30m single dish telescope, that is located at the Pico Veleta peak in Spain, at an altitude

of 2850 m, operating between 70 and 370 GHz. With a diameter of 30 m and a surface accuracy of 55 μm, the IRAM 30m telescope is one of the most powerful and sensitive observational facilities, suitable for observing cold matter that radiates predominantly in the millimeter range.

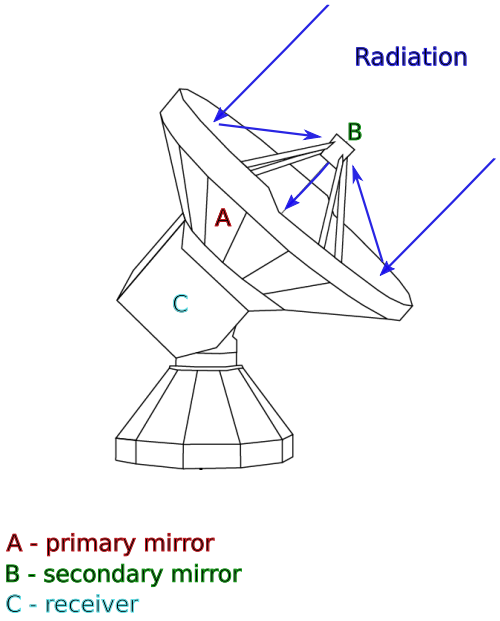

Figure 1.6: Main components of the IRAM 30m telescope, labeled as A, B and C.

A typical single dish radio telescope consists mainly of an antenna and a receiver, as shown in Fig. 1.6. The signal from the sky is collected by a parabolic antenna, also known as the primary reflector, and is subsequently focused on a secondary mirror, or sub-reflector, which finally passes the signal to the detectors/receivers. The detector's signal is then processed and analyzed by a spectrometer/backend. The IRAM 30m telescope in particular is built in a so-called Nasmyth configuration with a hyperbolic secondary reflector and an additional flat mirror that focuses the radiation on the receiver. Due to diffraction taking place at the primary antenna, the beam pattern of the telescope consists of a main beam that contains most of the incoming signal intensity, and the side lobes, which are axisymmetric to the beam pattern surrounding the main lobe. The more intensity is concentrated in the main beam, the less power is lost through the side lobes. The half power beam width (HPBW) of the main lobe gives the angular resolution of the telescope, which at a given wavelength λ and a telescope diameter D is described as HPBW $\sim \lambda/D$. For example, at a frequency of 345 GHz, the beam size of the IRAM 30 telescope is $\sim 7''$, while a frequency of 115 GHz corresponds to a $\sim 21''$ beam. The intensity scale of a radioastronomical observation is often given in K, and is expressed as antenna temperature T_{A}: this quantity is not a physical temperature but is a measure of the incident energy flux collected by the primary antenna at the direction of the observing

source. The system temperature $T_{\rm sys}$ on the other hand, is a measure of the noise generated by the electronics and the sky. Following the data collection, astronomers calibrate the recorded spectra, which involves converting the intensity scale into antenna temperature, and correcting for any atmospheric and instrumental losses.

The observational data for this thesis were recorded by using as a frontend the Eight MIxer Receiver (EMIR) that operates in the 3, 2, 1.3 and 0.9 mm range. Depending on their center frequency in GHz these bands are characterized as E090, E150, E230, and E330. Every band has two orthogonal linear polarization channels that are tuned to the same frequency. In addition, each EMIR band is equipped with dual sideband mixers (2SB), that generate an output signal of two sidebands, described as Lower Sideband (LSB) and Upper Sideband (USB). The available frequency bandwidth per sideband and polarization is 8 GHz, leading to a maximum frequency coverage of 32 GHz. In this work we have used the E090 band that corresponds to the 3 mm atmospheric window and can cover the frequency range from 73 to 117 GHz. The receiver was connected to a Fourier Transform Spectrometer (FTS) backend that achieved a frequency resolution of 50 kHz. Based on the above configuration we report in Chapter 2 observations of the main isotopologue c-C_3H_2, the singly and doubly deuterated species c-C_3HD and c-C_3D_2 as well as the isotopologue c-$H^{13}CC_2H$, where one ^{13}C is off the principal axis of the molecule. In Chapter 5 we aim for the phosphorus-bearing molecules HCP, CP, PN, and PO in the 3 mm range as well.

1.5 Rotational spectroscopy of transient molecules

The following chapter is based mainly on the books Yamada and Winnerwisser [2011], Hirota [1985] and Townes and Schawlow [1955].

A large fraction of the molecules detected in the ISM are radicals or ions, which are predominantly short-lived under terrestrial conditions due to their high reactivity. However, in space these species can exist for long times as "stable" species as a result of the low interstellar densities and temperatures. Radicals and ions have been the object of extensive laboratory study, that aims to record and analyze their rotational spectra in order to make their identification in the ISM possible. The spectrum of a transient molecule with at least one unpaired electron exhibits special spectral features known as the fine and hyperfine structure; this will be discussed in detail in the following paragraphs along with some basic theoretical aspects from rotational spectroscopy. In addition, we will introduce the main experimental technique for producing reactive species as well as the spectral acquisition method and the spectral analysis applied in this work.

1.5.1 The rigidly rotating molecule

The rotation of a molecule can be well approximated by the rotational motion of a rigid rotor, in which the internuclear distance stays constant. The Hamilton operator $\hat{H}_{rot}$ that describes the rotational energy of the molecule is then given by:

$$\hat{J}^2\Psi\left(\vartheta,\varphi\right)=\hbar^2 J\left(J+1\right)\Psi\left(\vartheta,\varphi\right)\quad\Rightarrow\quad\hat{H}_{rot}=\frac{\left|\hat{J}^2\right|}{2I}=\frac{\hbar^2 J\left(J+1\right)}{2I}. \tag{1.36}$$

The angular momentum operator is expressed as $\hat{J}$, the wavefunction is denoted with Ψ, while J describes the rotational quantum number and I the moment of inertia with respect to the rotating axis. In case of a linear molecule the rotation along the molecular axis is not allowed, as the corresponding moment of inertia I is zero, and thus the rotational energy would be infinitely large following Eq. 1.36. The above expression can be simplified by introducing a new quantity known as the rotational constant, B, which is given as:

$$B=\frac{\hbar^2}{2hcI}\left[\mathrm{cm}^{-1}\right]\quad\Rightarrow\quad\frac{E_J^{\mathrm{rot}}}{hc}=BJ\left(J+1\right)\left[\mathrm{cm}^{-1}\right]. \tag{1.37}$$

The rotational constant B is structure dependent as it is a function of I. A pure rotational transition can take place only if the molecule has a permanent dipole moment, that will couple with the electromagnetic field. The calculation of the transition moment intergral (see Eq. 1.50) with consideration of the symmetries of the rotational wave functions leads to the following selection rule for a rotational transition in a linear molecule:

$$\Delta J=\pm 1, \tag{1.38}$$

As a consequence, the resulting transition frequencies are equal to:

$$\nu = \frac{E_{J+1} - E_J}{hc} = 2B(J+1). \tag{1.39}$$

This means that the rotational spectrum of a linear molecule is a series of equidistant lines, separated by $2B$ as shown in Fig. 1.7.

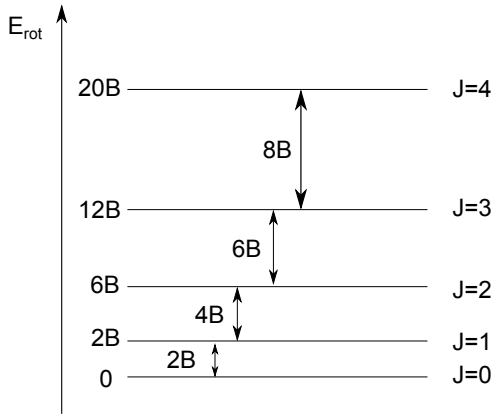

Figure 1.7: Scheme of the rotational energy levels of a linear molecule, approximated as a rigid rotor.

In case of a non-linear molecule there are three different rotor types based on their moments of inertia I_a, I_b, I_c along the principal axes a, b and c, respectively:

- spherical top: $I_c = I_b = I_a$
- symmetric top (two out of three moments of inertia are equal to each other)
  prolate: $I_c = I_b > I_a$
  oblate: $I_c > I_b = I_a$
- asymmetric top: $I_c > I_b > I_a$

For a symmetric top the axis with the smallest or largest moment of inertia is referred to as symmetry or figure axis. The rotation of the molecule around the symmetry axis by an angle $2\pi/n$ gives an unchanged distribution of atoms in space, and the molecule is said to have an n-fold symmetric axis. In the following we will explore further the rotational spectra of a symmetric and asymmetric top. The general expression for the zero-order Hamiltonian is:

$$\hat{H}_{rot} = \frac{\hat{J}_a^2}{2I_a} + \frac{\hat{J}_b^2}{2I_b} + \frac{\hat{J}_c^2}{2I_c}. \tag{1.40}$$

If we consider an oblate symmetric top ($I_c > I_b = I_a$) and apply the relation $\hat{J}^2 = \hat{J}_a^2 + \hat{J}_b^2 + \hat{J}_c^2$, the Hamiltonian can be written as:

$$\hat{H}_{rot} = (\frac{1}{2I_c} - \frac{1}{2I_b})\hat{J}_c^2 + \frac{\hat{J}^2}{2I_b}. \tag{1.41}$$

The operators $(\hat{J}_a, \hat{J}_b, \hat{J}_c)$ describe the components of the angular momentum with respect to the molecule-fixed axes (abc). In analogy, we can define the operators $(\hat{J}_X, \hat{J}_Y, \hat{J}_Z)$ with respect to the laboratory-fixed axes (XYZ). Since $\hat{H}_{rot}$ commutes with $\hat{J}^2$, $\hat{J}_c$ and $\hat{J}_Z$ we can choose a basis set of $\Psi(\theta, \phi) = |Jkm\rangle$, that contains eigenfunctions to all three operators, ($\hat{J}^2$, $\hat{J}_c$ and $\hat{J}_Z$). This makes it possible to solve the Schrödinger Equation with the Hamiltonian given in 1.41. With $\hat{J}^2 |Jkm\rangle = \hbar^2 J(J+1) |Jkm\rangle$, $\hat{J}_c |Jkm\rangle = \hbar K_c |Jkm\rangle$ and $\hat{J}_Z |Jkm\rangle = \hbar M |Jkm\rangle$, we obtain the following expression for the rotational energy levels $E_{rot}^{ob}(J, K_c)$ for an oblate symmetric top:

$$E_{rot}^{ob}(J, K_c) = \frac{\hbar^2 J(J+1)}{2I_b} + (\frac{\hbar^2}{2I_c} - \frac{\hbar^2}{2I_b})K_c^2 \equiv BJ(J+1) + (C-B)K_c^2, \tag{1.42}$$

with B and C being the rotational constants with respect to the axes b and c. The quantity K_c describes the projection of the angular momentum J on the symmetry axis c (with respect to the molecule-fixed coordinate system) with $K_c = -J, -J+1, ..., J-1, J$. If $K_c = 0$ the energy levels are those of a linear molecule. Since the eigenvalue $E_{rot}^{ob}(J, K_c)$ depends on the square of K_c, the right-handed and left-handed rotation results to the same energy. This indicates that every eigenstate is double degenerate, also known as K degeneracy. In a similar way, one can determine the rotational energy levels of a prolate symmetric top $E_{rot}^{pro}(J, K_a)$:

$$E_{rot}^{pro}(J, K_a) = \frac{\hbar^2 J(J+1)}{2I_b} + (\frac{\hbar^2}{2I_a} - \frac{\hbar^2}{2I_b})K_a^2 \equiv BJ(J+1) + (A-B)K_a^2, \tag{1.43}$$

where A is the rotational constant with respect to the a principal axis. For a prolate molecule the rotational energy increases (for a given J) with increasing K since $(A-B) > 0$, while in case of an oblate top the energy decreases with K through $(C-B) < 0$.

Due to the geometry of a symmetric top, the electric dipole moment is aligned only along the symmetry axis of the molecule. Since there is no component of the dipole moment perpendicular to the symmetry axis, there is also no torque exerted along this axis due to the electric field associated with radiation, meaning that the component of the angular momentum along the figure axis is not changing during a transition. As a consequence, the selection rule for the rotational transition within a symmetric top is $\Delta K = 0$ together with $\Delta J = 0, \pm 1$.

For an asymmetric top, the Hamiltonian cannot be further simplified as it was done for the symmetric rotor in Eq. 1.41, since $I_a \neq I_b \neq I_c$, suggesting that there is no analytical solution for the Schrödinger Equation. However, an approximation can be done by expanding the rotational wavefunction of an asymmetric top in terms of the symmetric

top eigenfunctions:

$$\Psi_{\mathrm{rot},(J,m)} = \sum_{k=-J}^{J} c_k^{(J,m)} \, |Jkm\rangle \tag{1.44}$$

The level of asymmetry is often given by the so-called Ray-parameter κ:

$$\kappa = \frac{2B - A - C}{A - C} \tag{1.45}$$

For $\kappa = +1$ we obtain the oblate limit ($A = B$), while $\kappa = -1$ stands for the prolate limit ($B = C$). Plotting the energies of an asymmetric top as a function of B gives a correlation diagramm, as depicted in Fig. 1.8. Every curve connects the prolate with the oblate limit, indicating that any nearly-prolate asymmetric top correlates with a prolate symmetric top level with a certain K_a value, and similarly, a nearly-oblate asymmetric top can be well approximated by an oblate symmetric rotor with a defined value of K_c. It is also evident from Fig. 1.8 that for a given J, there are $2J + 1$ different energies. As a consequence, two energy curves cannot cross, otherwise there would be just $2J$ energy levels, which is not feasible. Due to this non-crossing rule, the highest energy of the prolate rotor, with $K_a = J$, correlates with highest level of the oblate top with $K_c = 0$, while the lowest energy of the prolate top $K_a = 0$ stands in correlation with the lowest energy of the oblate rotor with $K_c = J$ [Yamada and Winnerwisser, 2011]. Each rotational level is given by $K_a + K_c = J$ or $K_a + K_c = J + 1$.

In contrary to the symmetric top, an asymmetric top can show a dipole moment along every principal axis (μ_a, μ_b and μ_c). Each non-vanishing dipole moment component will result to its own set of selection rules for the pseudo quantum numbers K_a and K_c (see Table 1.2):

Table 1.2: Selection rules for asymmetric top molecules.

Transition	Dipole moment component	ΔK_a [a]	ΔK_c [a]
a-type	$\mu_a \neq 0$	$0, (\pm 2, \pm 4, ...)$	$\pm 1, (\pm 3, \pm 5, ...)$
b-type	$\mu_b \neq 0$	$\pm 1, (\pm 3, \pm 5, ...)$	$\pm 1, (\pm 3, \pm 5, ...)$
c-type	$\mu_c \neq 0$	$\pm 1, (\pm 3, \pm 5, ...)$	$0, (\pm 2, \pm 4, ...)$

[a] The transitions in the brackets are much weaker than the main ones.

The rotation of a molecule can cause the internuclear distance to increase due to centrifugal forces, which generates additional energy terms in Eq. 1.42 and 1.43. The level of centrifugal distortion within a molecule does not depend on whether the angular rotation is clockwise or counterclockwise. Therefore, the change in rotational energy is a function of only the even powers of angular momentum. For an asymmetric top the centrifugal

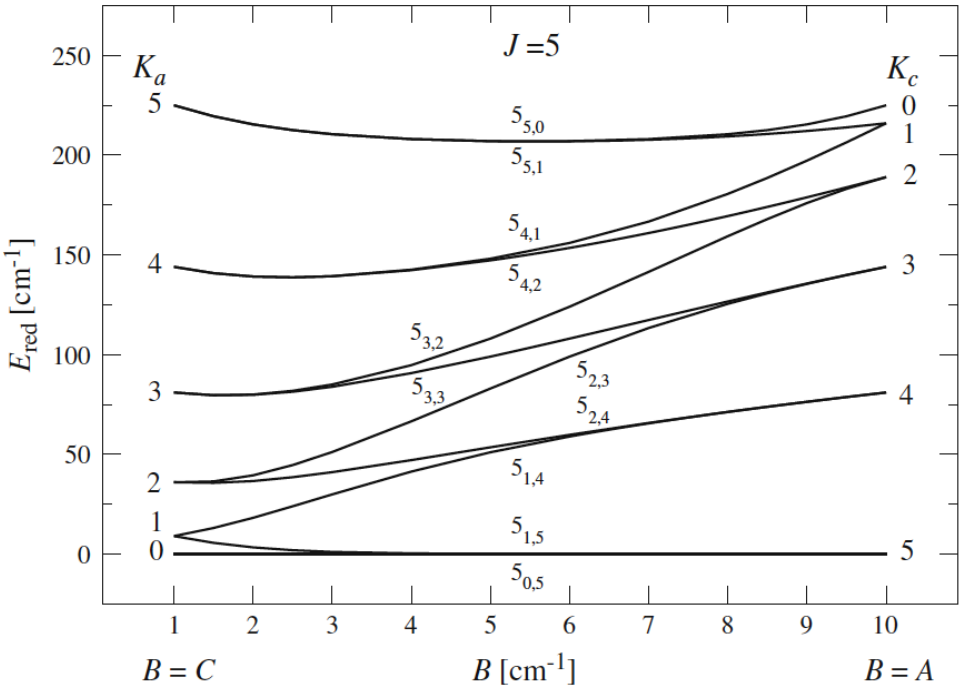

Figure 1.8: Scheme of the energy levels of an asymmetric molecule, plotted for $J = 5$, with the constant B varying continuously from C (prolate limit) to A (oblate limit) [Yamada and Winnerwisser, 2011].

distortion can be included by expanding the rotational operator $\hat{J}$ in the following way:

$$\begin{aligned}\hat{H}_{rot}^{(A)} &= A\hat{J}_z^2 + \frac{1}{2}(B+C)(\hat{J}^2 - \hat{J}_z^2) + \frac{1}{4}(B-C)(\hat{J}_+^2 + \hat{J}_-^2) \\ &- \Delta_J \hat{J}^4 - \Delta_{JK}\hat{J}^2\hat{J}_z^2 - \Delta_K \hat{J}_z^4 + \Phi_J J^6 + \Phi_{JK}\hat{J}^4\hat{J}_z^2 + \Phi_{KJ}\hat{J}^2\hat{J}_z^4 + \Phi_K J_z^6 \\ &- \frac{1}{2}[\delta_J \hat{J}^2 + \delta_K \hat{J}_z^2 - \phi_J \hat{J}^4 - \phi_{JK}\hat{J}^2\hat{J}_z^2 - \phi_K \hat{J}_z^4, (\hat{J}_+)^2 + (\hat{J}_-)^2]_+ \end{aligned} \tag{1.46}$$

This expression is known as the Watson's A-reduced Hamiltionian, proposed by Watson [1977], where $\hat{J}_\pm = \hat{J}_x \pm i\hat{J}_y$ and $[\hat{A}, \hat{B}]_+$ is the plus commutator $\hat{A}\hat{B} + \hat{B}\hat{A}$. The parameters $\Delta_J, \Delta_{JK}, \Delta_K, \delta_J$ and δ_K are the so-called quartic centrifugal distortion constants, whereas $\Phi_J, \Phi_{JK}, \Phi_{KJ}, \Phi_K, \phi_J, \phi_{JK}$ and ϕ_K are the sextic ones. For a more precise reproduction of the energy levels, one can expand the rotational operator to even higher orders (octic, decadic, and so on). There is another reduction of the Hamiltonian called S-reduction, that is appropriate for describing the rotational energy and the centrifugal distortion of a

nearly-prolate or nearly-oblate asymmetric top:

$$\begin{aligned}\hat{H}_{rot}^{(S)} &= A\hat{J}_z^2 + \frac{1}{2}(B+C)(\hat{J}^2 - \hat{J}_z^2) + \frac{1}{4}(B-C)(\hat{J}_+^2 + \hat{J}_-^2) \\ &- D_J\hat{J}^4 - D_{JK}\hat{J}^2\hat{J}_z^2 - D_K\hat{J}_z^4 + H_J J^6 + H_{JK}\hat{J}^4\hat{J}_z^2 + H_{KJ}\hat{J}^2\hat{J}_z^4 + H_K J_z^6 \\ &+ (d_1\hat{J}^2 + h_1\hat{J}^4)(\hat{J}_+^2 + \hat{J}_-^2) + (d_2 + h_2\hat{J}^2)(\hat{J}_+^4 + \hat{J}_-^4) + h_3(\hat{J}_+^6 + \hat{J}_-^6). \end{aligned} \tag{1.47}$$

Here, the quartic centrifugal distortion parameters are given by D_J, D_K, D_{JK}, d_1 and d_2, while the sextic order is expressed through the constants $H_J, H_{JK}, H_{KJ}, H_K, h_1, h_2$ and h_3. According to Watson [1977], the A- and S-reduction give similar results, however, the constants mentioned above tend to be more strongly correlated in case of the A-reduced form.

1.5.2 Line width and line intensity

A spectral line is never a perfect monochromatic line but shows a certain width around the center frequency due to three main physical processes. The natural linewidth results from the limited lifetime of a specific energy level and the associated energy uncertainty (Heisenberg's uncertaintly principle, $\Delta E \cdot \Delta\tau \geq \hbar$). Another type of line broadening is the so-called Doppler broadening. Due to the thermal motion of gas species, each molecule absorbs and emits radiation at frequencies slightly shifted from the actual transition frequency because of the resulting Doppler effect. Assuming a Maxwell-Boltzmann velocity distribution, the Doppler broadening $\Delta\nu_D$ is described by

$$\Delta\nu_D = 7.1 \cdot 10^{-7}\sqrt{\frac{T}{M}}\nu_0, \tag{1.48}$$

where ν_0 is the transition frequency, T is the temperature in Kelvin and M is the mass of the molecule in atomic mass units (amu). For example, at a frequency of 300 GHz and room temperature, the Doppler broadening of a molecule with a mass of 37 amu is $\Delta\nu_D = 0.6\,\mathrm{MHz}$. This would require a spectrometer with a spectral resolution of $R = \frac{\Delta\nu}{\nu_0} \sim 10^{-6}$. Pressure broadening on the other hand, is significant especially at high pressures and it arises mostly from collisions between molecules. Such a collision can interrupt the absorption or emission process of a molecule, and thus shorten the lifetime of the corresponding energy level. This creates an even larger uncertainty in the associated energy and in turn a larger line width. The pressure broadening $\Delta\nu_P$ is expressed as

$$\Delta\nu_P = \frac{\sqrt{8}\sigma}{\sqrt{Mk_BT\pi}} \cdot p, \tag{1.49}$$

with σ as the cross section between two colliding molecules.

The line intensity is determined by the product of the transition probability P_{ul} and the population difference Δp between a lower and an upper energy state. The intrinsic probability P_{ul} is estimated via

$$P_{ul} = |\langle\psi_u|\,\hat{\mu}\,|\psi_l\rangle|^2, \tag{1.50}$$

where ψ_u, ψ_l are the corresponding rotational wavefunctions and $\hat{\mu}$ is the dipole moment operator. This shows that the presence of a permanent dipole moment is required in order for a rotational transition to take place. The population p_u of a given state u at a temperature T is described by the Boltzmann distribution, as already shown in Eq. 1.25. The application of the Boltzmann distribution is justified when a (local) thermodynamic equilibrium is given (see Section 1.4.1).

1.5.3 Fine and hyperfine structures

A radical is a molecule that has one or more unpaired electrons, which leads to additional splittings in its rotational spectrum, known as fine and hyperfine structures. The fine structure results from the coupling of the electron spin angular momentum $\hat{S}$ with the electron orbital angular momentum $\hat{L}$ and the molecular rotation. Furthermore, if a molecule contains at least one nucleus with a nonzero nuclear spin, the nuclear spin angular momentum $\hat{I}$ couples with $\hat{S}$ and/or $\hat{L}$ leading to the formation of magnetic hyperfine structures. In the following paragraphs we will explore further the details of the fine and hyperfine structure.

The electron spin angular momentum $\hat{S}$ has the eigenvalues $S = 0, 1/2, 1, ...$ that determine if the electronic state is a singlet, doublet, triplet state and so on. The electron orbital angular momentum $\hat{L}$ is not well determined (Heisenberg's uncertainty principle), but its projection on the molecular axis $\hat{L}_z$ is well defined and conserved with the eigenvalue Λ. Depending on $\Lambda = 0, \pm1, \pm2, \pm3, ...$ the molecular state can be specified as $\Sigma, \Pi, \Delta, \Phi, ...$, respectively. A common notation for a full description of the molecular state is ${}^{2S+1}\Lambda_{sym}$, with $sym = u, g$. The letters u and g stand for the symmetry of a molecular state towards a center of inversion. The electronic state can be additionally characterized with a $+$ or $-$, that determines the symmetry with respect to a reflection towards a plane containing the internuclear axis. There are two main cases of angular momentum coupling that are known as Hund's case (a) and (b). In Hund's case (a) the orbital and spin angular momentum are both strongly coupled with the molecular axis, so that their projections $\hat{L}_z$, $\hat{S}_z$ and their eigenvalues Λ and Σ are well defined. Thus, along the molecular axis there is an angular momentum $\hat{\Omega}$ with the eigenvalue $\Omega = \Lambda + \Sigma$. Finally, the angular momentum caused by the rotation of the molecule $\hat{R}$ couples with $\hat{\Omega}$, that leads to the total angular momentum $\hat{J}$. In Hund's case (b) on the other hand, the electron spin is not strongly coupled to the molecular axis because of the weak spin-orbit interaction, so that Σ is no longer defined. Consequently, the rotational angular momentum interacts with $\hat{L}_z$ to generate $\hat{N}$, which in turn adds to $\hat{S}$, to form the total angular momentum $\hat{J}$:

$$\hat{J} = \hat{N} + \hat{S} \tag{1.51}$$

Thus, the quantum number J can take following values: $J = N+S, N+S-1, ..., |N-S|$. Fig. 1.9 illustrates the main coupling shemes for Hund's case (a) and (b). For the Hund's

case (b) one can define the spin-rotation Hamiltonian as:

$$\hat{H}_{\mathrm{SR}} = (1/2)\sum_{\alpha,\beta}\epsilon_{\alpha,\beta}(\hat{N}_\alpha\hat{S}_\beta + \hat{S}_\beta\hat{N}_\alpha), \tag{1.52}$$

where $\epsilon_{\alpha,\beta}$ denotes the spin-rotation tensor and α, β run separately over the molecule-fixed coordinates a, b and c. In analogy to the A- and S-reduced rotational Hamiltonian shown in Eq. 1.46 and Eq. 1.47, one can introduce the quartic spin-rotation Hamiltonian, or in other words, the centrifugal distortion of the spin-rotation interaction [Brown and Sears, 1979]. In this case, the corresponding S-reduction is given by:

$$\begin{aligned}\hat{H}^{(4)}_{\mathrm{SR}} = D^S_N\hat{N}^2(\hat{N}\hat{S}) + \frac{1}{2}D^S_{NK}(\hat{N}^2\hat{N}_z\hat{S}_z + \hat{N}_z\hat{S}_z\hat{N}^2) + D^S_{KN}\hat{N}^2_z(\hat{N}\hat{S}) + \hat{D}^S_K\hat{N}^3_z\hat{S}_z \\ +d^S_1(\hat{N}^2_+ + \hat{N}^2_-)(\hat{N}\hat{S}) + d^S_2(\hat{N}^3_+\hat{S}_+\hat{N}^3_-\hat{S}_-).\end{aligned} \tag{1.53}$$

The six constants listed above (from D^S_N to d^S_2) are analogous to the quartic centrifugal distortion parameters applied for the S-reduced rotational Hamiltionian (see Eq. 1.47). Another fine structure interaction is the so-called spin-spin coupling, which occurs only for molecules with more than one unpaired electron. Here, the dipole-dipole interaction between the different electron spins is generating an additional perturbation to the energy given as:

$$\hat{H}_{\mathrm{SS}} = \lambda\frac{2}{3}(3\hat{S}^2_z - \hat{S}^2). \tag{1.54}$$

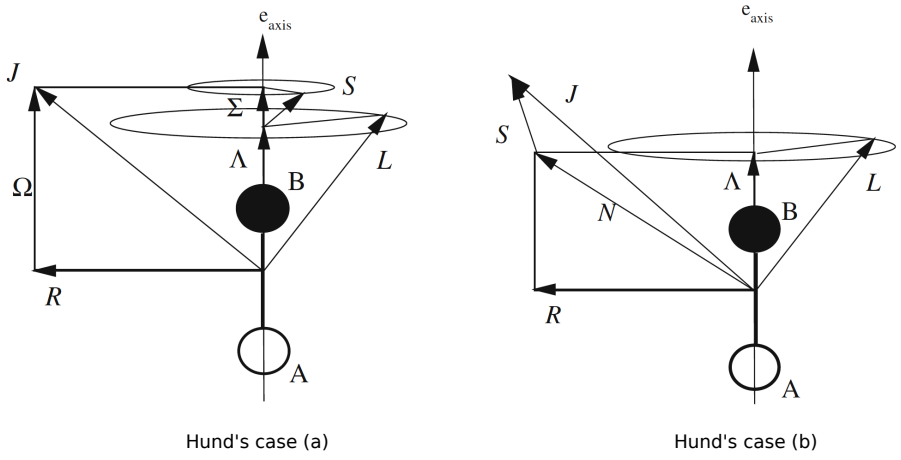

Figure 1.9: Vector diagramms of the two cases of angular momentum coupling in a radical with the nuclei A, B and a molecular axis expressed as e_{axis} [Yamada and Winnerwisser, 2011].

The most important hyperfine interaction for open-shell molecules is the magnetic coupling between the unpaired electron and nuclear spins within the molecule. In particular, the

nuclear angular momentum $\hat{I}$ couples with the total angular momentum $\hat{J}$, leading to a further splitting of the energy levels into the hyperfine structure, described as $\hat{F}$:

$$\hat{F} = \hat{J} + \hat{I} \tag{1.55}$$

The magnetic hyperfine interactions can be summarized as:

$$\hat{H}_{\mathrm{HF}} = a(\hat{I} \cdot \hat{L}) + b_F(\hat{I} \cdot \hat{S}) + c(\hat{I}_z\hat{S}_z - \hat{I} \cdot \hat{S}/3), \tag{1.56}$$

where the first term describes the nuclear spin-orbit coupling, the second term, known as the Fermi-contact interaction, stands for the coupling between the electron and nucleus spin, and finally, the third term describes the contribution of the electron spin and nucleus spin dipole-dipole interaction. In addition, there is the nucleus spin-rotation interaction, which is analogous to the electron spin-rotation coupling:

$$\hat{H}_{\mathrm{NSR}} = (1/2)\sum_{\alpha,\beta} C_{\alpha,\beta}(\hat{N}_\alpha\hat{I}_\beta + \hat{I}_\beta\hat{N}_\alpha). \tag{1.57}$$

Apart from the magnetic hyperfine interaction there is also the electrostatic coupling between the quadrupole field of a nucleus (spin larger than $1/2$) and the electric field generated by the surrounding electrons. This type of interaction can be essential to both open-shell and closed-shell molecules and the corresponding Hamiltonian is given by following expression:

$$\hat{H}_Q = \frac{1}{2}eQq_J\Big[3(\hat{I} \cdot \hat{J})^2 + \frac{3}{2}\hat{I} \cdot \hat{J} - \hat{I}^2\hat{J}^2]/[I(2I-1)J(2J-1)\Big], \tag{1.58}$$

where eQ stands for the nuclear quadrupol field and $q_J = \left(\frac{\partial^2 V}{\partial z_J^2}\right)$ is the electric field gradient caused by the surrounding electrons, indicative of the asymmetric charge distribution around the nucleus.

1.5.4 The Renner-Teller effect

In a degenerate electronic state ($\Lambda > 0$) of a linear molecule, the vibrational angular momentum, which is induced by a degenerate bending vibrational mode is coupled with the electronic angular momentum, leading to additional splitting of the electronic state. In particular, the projection of the vibrational angular momentum on the molecular axis denoted with l couples with Λ and leads to the vibronic angular momentum K given by $K = |\pm\Lambda \pm l|$. This way the degeneracy is removed and the vibrational potential function is split into two parts, that collapse with each other when the molecule is in a linear configuration. In fact, this type of vibronic coupling is seen also in our work within the investigated radical HCCO (ketenyl), in which the hydrogen nucleus is bent away from the nearly linear backbone CCO. As a consequence, the electronic state $^2\Pi_\mathrm{u}$ is split into two further states that are stabilized in a non-linear ($^2A'$, ground state) and linear

configuration ($^2A''$, excited state), that lie energetically close to each other ($\sim 1700\,\mathrm{K}$), and thus permitting HCCO to easily overcome the barrier between bent and linear state (*quasi-linearity*). More details on the Renner-Teller Effect and the resulting energy perturbation towards HCCO can be found in Chapter 3.

1.5.5 DC-discharge

The challenge of studying unstable species such as radicals and ions in the laboratory is their production and stabilization under extreme physical conditions. One of the most common ways of generating transient molecules in the laboratory is the application of an electric gas discharge. The basic concept of electric gas discharges is the ignition of a plasma formed when electric current passes through a gas. Technically this is achieved by using two electrodes, one at each end of the absorption gas cell, and applying a high voltage of several hundreds of volts. Within this plasma, processes like ionization and bond breaking of the mixed gas-components can initialize further chemical reactions that lead to the formation of the desired radical or ion. In this work in particular we implement a low-pressure Direct Current (DC) discharge (application of a DC voltage). Depending on the flowing current, there are three main types of DC discharge that are illustrated in Fig. 1.11: the *Townsend dark*, the *glow* and the *arc discharge*.

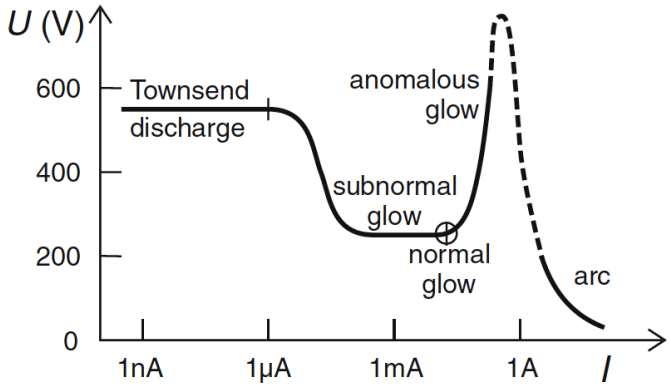

Figure 1.10: Depiction of the main discharge regimes upon gradual reduction of the circuit's resistance [Piel, 2010].

As an example, we start with a high voltage of 600 V combined with a resistor connected in series with a value of 1 MΩ. The electrons already present in the probing gas will accelerate in the electric field and eventually collide with other species, so that additional electrons will be emitted via ionization. This regime is known as the *Townsend dark discharge*, in which the resulting discharge current equals a few μA. If we decrease the resistance in the circuit, the current increases and a so-called *sub-normal glow* develops that covers partially the cathode surface. The increase in current is caused by positive ions that

upon impact with the cathode release secondary electrons, raising the flowing current up to the mA-regime. This mode shows a lower discharge voltage that is approximately constant over $I \approx (0.1 - 10)\,\mathrm{mA}$, till the glow has completely covered the cathode. At this point we have reached the *normal glow discharge*, which shows several glowing regions within the absorption cell. A further reduction of the resistance will raise again the discharge current, forming the anomalous glow discharge, followed finally by the *arc discharge*, that will cause the current to increase up to several Amperes. Here, the electrons leave the heated cathode via thermionic or field emission [Piel, 2010].

In the present thesis we produce our unstable species of interest within a glow discharge. This type of discharge will show alternating luminous and dark spaces as a result of the charge and energy distribution within the plasma (see Fig. 1.11). Starting from the cathode, the first region to find is the so-called *Aston dark space*. Here, the secondary electrons that were emitted through the impact of positive ions with the cathode are still low in energy and cannot excite or ionize other species. However, thanks to the applied electric field, these electrons will gain enough energy and consequently excite other species. These excited molecules and/or atoms eventually return to their ground electronic state by emitting light, making this region glow (thus the name *cathode glow*). After having obtained even higher energies the flowing electrons will mostly ionize instead of exciting other species. This results into the *cathode dark space*, where a large number of electrons is emitted but not any additional light. The large electron density is followed by an increased recombination of electrons with cations, forming the most luminous region of the discharge called the *negative glow*. This regime shows a weak electric field, but is one of the main sources of ions due to the high electron density. The cathodic part ends in the *Faraday Dark Space*, where the electrons slow down (due to collisions) and gradually lose their energy. The anodic part consists mainly of the *positive column* and a transition regime to the anode (*anode glow* and *anode dark space*). Even though the positive column shows a lower electron density than the negative glow, it leads to an effective ion production, as it occupies the largest part of the cell. In this thesis however, we are increasing the length of the electron-rich negative glow, by applying a longitudinal magnetic field, as it was done in [De Lucia et al., 1983]. This study showed that the magnetic field confines the ionizing electrons into a narrow beam, which in turn considerably increases the positive ion production, with an enhanced ion signal intensity of up to two orders of magnitude.

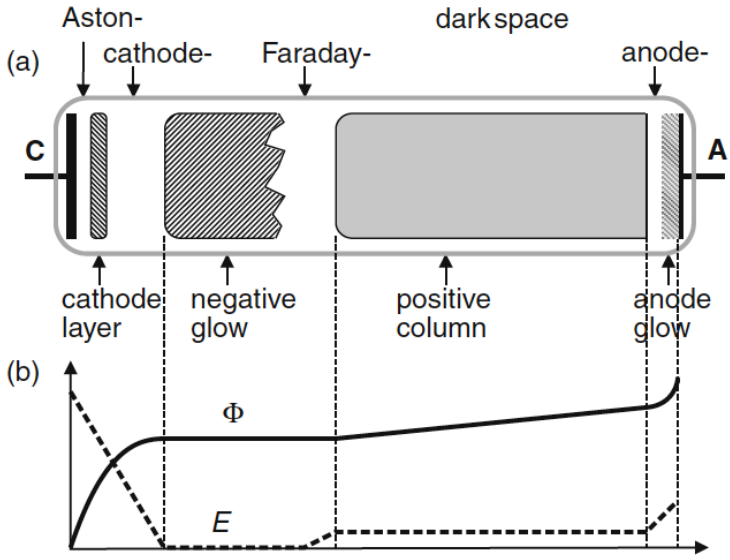

Figure 1.11: (a) Regions of the DC glow discharge. The negative glow and the positive column are the main sources of ion production. (b) Distribution of the electric potential Φ and the axial electric field E within a glow discharge. The largest drop in voltage is seen towards the cathodic part. The negative glow shows very low fields (nearly zero), while the positive column shows a higher and nearly-constant electric field [Piel, 2010].

1.5.6 Spectral acquisition method

The spectroscopic method we apply for recording the absorption spectra of our investigated species is the frequency modulation, which can be expressed as

$$\omega = \omega_0 + a \cdot \cos(\Omega t), \tag{1.59}$$

where ω_0 is the carrier frequency, Ω is the modulation frequency, a is the modulation width and ω is the frequency of the resulting modulated signal. The quantity a describes the change in the carrier frequency ω_0 through the modulation. For example, if $\omega_0 = 100$ kHz and $a = 40$ kHz, the frequency of the carrier signal will change between 60 and 140 kHz. The pace of this frequency change is given by the modulation frequency Ω. The corresponding absorbing intensity is described by [Demtröder, 2010]:

$$I_{abs}(\omega) = I_{abs}(\omega_0 + a \cdot \cos(\Omega t)). \tag{1.60}$$

Following Eq. 1.60, a Taylor expansion of $I_{abs}(\omega)$ at ω_0 is then given by:

$$I_{abs}(\omega) = I_{abs}(\omega_0) + \sum_{n=1}^{\infty} \frac{a^n}{n!} \cos^n(\Omega t) \left(\frac{d^n I_{abs}(\omega)}{d\omega^n}\right)_{\omega_0}. \tag{1.61}$$

According to the Lambert-Beer-Law, the absorbing intensity I_{abs} depends on the absorption coefficient $\alpha(\omega)$ through:

$$I_{abs}(\omega) = I_0[1 - \exp(-\alpha(\omega) \cdot N \cdot L)] \approx I_0 \cdot \alpha(\omega) \cdot N \cdot L, \tag{1.62}$$

with I_0 being the incoming intensity, L the length of the absorption cell and N the concentration of the absorbing molecules. This means, that the n^{th}-derivative of the absorbing intensity I_{abs} is equal to:

$$(\frac{d^n I_{abs}(\omega)}{d\omega^n})_{\omega_0} = I_0 N L (\frac{d^n \alpha(\omega)}{d\omega^n})_{\omega_0}. \tag{1.63}$$

If we include Eq. 1.63 in Eq. 1.61, the intensity of the modulated signal can be expressed as [Demtröder, 2010]:

$$I_{abs}(\omega) = I_{abs}(\omega_0) + I_0 N L \sum_{n=1}^{\infty} \frac{a^n}{n!} \cos^n(\Omega t)(\frac{d^n \alpha(\omega)}{d\omega^n})_{\omega_0}. \tag{1.64}$$

This can be approximated as:

$$\begin{aligned} I_{abs}(\omega) \;=\; & I_{abs}(\omega_0) \\ & + a I_0 N L (\frac{d^1 \alpha(\omega)}{d\omega^1})_{\omega_0} \cos(\Omega t) \\ & + \frac{a^2}{2} I_0 N L (\frac{d^2 \alpha(\omega)}{d\omega^2})_{\omega_0} \cos(2\Omega t) \\ & + \frac{a^3}{6} I_0 N L (\frac{d^3 \alpha(\omega)}{d\omega^3})_{\omega_0} \cos(3\Omega t) + ... \end{aligned} \tag{1.65}$$

The first term describes the intensity of the non-modulated signal. The remaining terms oscillate with the single, double and triple modulation frequency Ω and correspond to the first, second and third derivation of the absorption spectrum. In other words, the frequency modulation is creating infinitely many harmonics of the modulation frequency (Ω, 2Ω, 3Ω, 4Ω, etc.), that can be individually selected and amplified.

The so-called demodulation of the signal involves multiplying (mixing) the detected (modulated) signal with a reference signal whose frequency is either equal to or a multiple of the modulation frequency (depending on which component we want to obtain). In the following we show as an example the first-order demodulation. Here, the modulated signal I_{abs} is multiplied with $I_{ref} = \cos(\Omega t + \phi)$:

$$\begin{aligned} I_{abs}(\omega) \cdot I_{ref} &= [I_{abs}(\omega_0) + a I_0 N L (\frac{d^1 \alpha(\omega)}{d\omega^1})_{\omega_0} \cos(\Omega t) + ...] \cdot \cos(\Omega t + \phi) \\ &= I_{abs}(\omega_0) \cdot \cos(\Omega t + \phi) + a I_0 N L (\frac{d^1 \alpha(\omega)}{d\omega^1})_{\omega_0} \cdot \cos(\Omega t) \cdot \cos(\Omega t + \phi) + ... \end{aligned} \tag{1.66}$$

The different pathways for the detected and reference signal result to a phase shift ϕ between the two. If we apply the trigonometric relation $\cos a \cdot \cos b = \frac{1}{2}\cos(a+b) + \frac{1}{2}\cos(a-b)$ on the second term of Eq. 1.66 we obtain the following expression:

$$\begin{aligned} I_{abs}(\omega) \cdot I_{ref} &= I_{abs}(\omega_0) \cdot \cos(\Omega t + \phi) \\ &+ \frac{1}{2} a I_0 N L \left(\frac{d^1\alpha(\omega)}{d\omega^1}\right)_{\omega_0} \cdot \cos(2\Omega t + \phi) \\ &+ \frac{1}{2} a I_0 N L \left(\frac{d^1\alpha(\omega)}{d\omega^1}\right)_{\omega_0} \cdot \cos(\phi) + ... \end{aligned} \tag{1.67}$$

The output signal $I_{abs}(\omega) \cdot I_{ref}$ is then passing through a low-pass filter, that filters out all the high-frequency components except for the following term [Demtröder, 2010]:

$$I_{abs}(\omega) \cdot I_{ref} = a I_0 N L \left(\frac{d^1\alpha(\omega)}{d\omega^1}\right)_{\omega_0} \cdot \cos(\phi). \tag{1.68}$$

This means that the final outcome is a DC-signal, that corresponds to the first derivative of the absorption line and is proportional to the phase shift ϕ between $I_{abs}(\omega)$ and I_{ref}. This kind of modulation is also called $1f$ modulation. Similarly, for a $2f$ modulation the reference signal oscillates with twice the modulation frequency, and the resulting signal contains the second derivative of the absorption spectrum. The $1f$ modulation is removing constant baselines, while the $2f$ modulation also removes baselines that increase or decrease linearly in time. In general, the main advantage of the modulation technique is the fact that most noise contribution that is also mixed with the reference signal, is in the end being filtered out, leading to very sensitive, low-noise spectra. In addition, typical flicker noise or $1/f$ noise in electronic devices is substantially reduced when the modulation frequency is large enough.

The demodulation process as well as the application of the low-pass filter is done by the so-called lock-in amplifier. The low-pass filter is integrating the mixed signal $I_{abs}(\omega) \cdot I_{ref}$ over several micro- or milliseconds, in order to clear away all the noise features. Hence, the higher the time constant of the filter, the lower the noise. The phase shift ϕ between the two mixing signals can be adjusted in a way that the resulting output signal has maximum intensity.

1.5.7 Spectral analysis

In this thesis we perform rotational spectroscopy in the (sub)mm range on the radical HCCO and its deuterated counterpart DCCO as well as the protonated species $HSCO^+$. Both species are produced within a DC gas discharge and studied in a high-vacuum environment that is additionaly cooled down through liquid nitrogen or via the production of a cold molecular beam (see Chapter 3 and 4). That way, we reduce the line broadening and stabilize the reactive species within the cell. After collecting the molecular line frequencies in the lab, we apply the proper rotational Hamiltonian, in order to assign quantum states to the measured lines. The most common program for this purpose is SPFIT that

was developed by Herbert M. Pickett and is fitting experimental data with a specific set of rotational constants. The main output file of this fitting routine gives all the needed information concerning the fit:

- the updated rotational constants and their uncertainties for every iteration as well as the variation of each constant with respect to the previous iteration.

- a list of the experimental frequencies and the assumed experimental uncertainty along with the assigned quantum numbers.

- the predicted frequencies calculated by the last set of rotational parameters and the residual between measured and calculated frequency.

- a global weighted σ_{rms}, which is a measure for the "goodness" of the fit and is defined as:

$$\sigma_{rms} = \sqrt{\frac{\sum_i (\frac{\delta_i}{err})^2}{N}}, \tag{1.69}$$

  where δ are the residuals weighted by the given experimental uncertainty *"err"* and N is the total number of transitions applied in the fit.

- a correlation matrix for each iteration, that describes how strongly correlated two certain rotational parameters are.

Finally, the SPCAT program is producing a catalogue file that includes the entire molecular line spectrum based on the parameters derived from the fitting software SPFIT.

1.6 This thesis

The next chapters will present in detail my scientific results from the astronomical observations, laboratory measurements and theoretical modeling that were performed within the framework of this thesis. A short summary on the content of each chapter is given below:

In **Chapter 2** I study the deuteration level of c-C_3H_2 within starless, pre-stellar and protostellar cores in the Taurus and Perseus Complexes. In particular, I examine how the deuteration level, given by the column density ratio $N(c\text{-}C_3HD)/N(c\text{-}C_3H_2)$, correlates with important evolutionary indicators, like the dust temperature, the H_2 column density and the CO depletion factor. I will show that the deuterium fraction of c-C_3H_2 is for all the observed sources consistent with $\sim 10\%$ within error bars and comparable to that of

N_2H^+. However, the highest deuteration level is found towards the youngest protostar HH211. This suggests additional deuteration processes of c-C_3H_2 taking place on dust grains during the pre-stellar core phase.

In **Chapter 3** I describe our laboratory measurements on ketenyl (HCCO) and its deuterated counterpart DCCO in the millimeter and submillimeter range, that were performed with our frequency modulation absorption spectrometer (CAS Absorption Cell, CASAC). Here I will show that the new recorded rotational lines of each isotopologue considerably improves the spectral fit, which results to highly accurate rest-frequencies for both HCCO and DCCO in the (sub)mm range. A detection of HCCO towards the prestellar core L1544 shows that ketenyl peaks towards the region where c-C_3H_2 peaks, indicating that a hydrocarbon-based chemistry leads to an effective HCCO formation. This agrees well with our results from our gas-grain chemical model.

In **Chapter 4** I present the technical realization of our new Supersonic Jet Experiment. This set up allows the production of a cold molecular beam through a supersonic, adiabatic expansion of a gas sample into a high-vacuum chamber. The low temperatures ($\sim 5-10\,\mathrm{K}$) and densities within the jet stabilize reactive species (like radicals and ions) and make them available from spectroscopic studies. Our first measurements were performed on the protonated species $HSCO^+$ between 274 and 373 GHz. The new measured lines result to a highly precise spectral analysis, thus allowing future astronomical observations of the yet non-detected $HSCO^+$ in the (sub)mm range.

In **Chapter 5** I study the interstellar phosphorus chemistry towards diffuse and translucent clouds. Detections of the species HNC, CN, $C^{34}S$ and ^{13}CO towards diffuse/translucent clouds along the line of sight to the strong quasar B0355+508 gave us new physical constraints for the observed sources. Based on these constraints I make reliable predictions for the abundances of P-bearing molecules. I will show that parameters such as the visual extinction A_V and the cosmic-ray ionization rate ζ(CR) dramatically affect the abundances of all P-bearing species, indicating that P-chemistry leads to detectable amounts of molecular species towards the more shielded and denser translucent clouds.

In **Chapter 6** I give a summary of the main results produced by the present thesis as well as an outlook concerning future observations and lab measurements.

Chapter 2

A study of the *c*-C_3HD/*c*-C_3H_2 ratio in low-mass star forming regions

The content of this chapter was published in the *The Astrophysical Journal*.

2.1 Abstract

We use the deuteration of *c*-C_3H_2 to probe the physical parameters of starless and protostellar cores, related to their evolutionary states, and compare it to the N_2H^+-deuteration in order to study possible differences between the deuteration of C- and N-bearing species. We observed the main species *c*-C_3H_2, the singly and doubly deuterated species *c*-C_3HD and *c*-C_3D_2, as well as the isotopologue *c*-$H^{13}CC_2H$ toward 10 starless cores and 5 protostars in the Taurus and Perseus Complexes. We examined the correlation between the $N(c\text{-}C_3HD)/N(c\text{-}C_3H_2)$ ratio and the dust temperature along with the H_2 column density and the CO depletion factor. The resulting $N(c\text{-}C_3HD)/N(c\text{-}C_3H_2)$ ratio is within the error bars consistent with 10% in all starless cores with detected *c*-C_3HD. This also accounts for the protostars except for the source HH211, where we measure a high deuteration level of 23%. The deuteration of N_2H^+ follows the same trend but is considerably higher in the dynamically evolved core L1544. We find no significant correlation between the deuteration of *c*-C_3H_2 and the CO depletion factor among the starless and the protostellar cores. Toward the protostellar cores the coolest objects show the largest deuterium fraction in *c*-C_3H_2. We show that the deuteration of *c*-C_3H_2 can trace the early phases of star formation and is comparable to that of N_2H^+. However, the largest *c*-C_3H_2 deuteration level is found toward protostellar cores, suggesting that while *c*-C_3H_2 is mainly frozen onto dust grains in the central regions of starless cores, active deuteration is taking place on ice.

2.2 Introduction

During the early stages of star formation, self-gravitating starless cores begin to contract ($n_H > 10^4\,cm^{-3}$) and to cool down to a few Kelvin ($T < 10$ K). Under these conditions, the deuteration of molecules is considerably increasing. H_2D^+ is the main deuterium provider for most molecules in dense cores and is formed from the following deuteron-proton reaction [Millar et al., 1989]:

$$H_3^+ + HD \rightleftharpoons H_2D^+ + H_2 + 230\,K. \tag{2.1}$$

This reaction is exothermic and proceeds mostly in the forward direction at temperatures lower than 30 K, increasing the abundance of H_2D^+. The abundance of H_2D^+ also depends on the ortho-to-para-H_2 ratio. The backward direction of reaction 2.1 is endothermic if the reactants H_2D^+ and H_2 are mostly in the para form [Pagani et al., 1992]. An important process in these environments is the freeze-out of molecules onto dust grains. Previous studies have shown that CO depletes heavily toward the center of cores [Willacy et al., 1998, Caselli et al., 1999, Bacmann et al., 2003, Crapsi et al., 2005, Pagani et al., 2007]. Since CO destroys H_3^+ and H_2D^+, its depletion from the gas phase leads to a further enhancement of the total deuteration level [Dalgarno and Lepp, 1984]. As the starless core continues to contract, it eventually becomes a pre-stellar core, defined as being a self-gravitating core [Ward-Thompson et al., 1999] with signs of contraction motions and high levels of CO freeze-out and deuteration [Crapsi et al., 2005]. Pre-stellar cores are a sub-sample of starless cores, i.e. the most dynamically evolved and destined to form one or more protostars. Once the protostar is formed, the central regions of the contracting core warm up and the whole core starts to become affected by the outflow driven by the young stellar object. This causes CO to desorb and also increases the backward rate of reaction 2.1, leading finally to a decrease of the total deuteration degree. In summary, the increase and decrease of molecular deuteration is sensitive to the evolutionary stage in the star formation process and is an excellent tool to trace the early stages of star formation.

Species that can be used as evolutionary tracers of high-density and low-temperature gas must have the possibility of deuteration and should be abundant in space. One molecule that has been proven to be a very good evolutionary tracer is diazenylium, N_2H^+ [Crapsi et al., 2005, Emprechtinger et al., 2009, Friesen et al., 2013, Punanova et al., 2016]. It has been shown that the deuteration of N_2H^+ correlates tightly with important evolutionary indicators, such as the dust temperature, the CO depletion factor and the central column density of H_2. In addition, the emission maps of N_2H^+ strongly follow the dust emission maps, indicating that N_2H^+ is less depleted than C-bearing molecules at higher densities [Bergin et al., 2001, Tafalla et al., 2002]. This makes N_2H^+ a very good tracer of the deuteration level in central regions of dense cores. The resistance of N_2H^+ to depletion has been ascribed by previous studies [Flower et al., 2006, Le Gal et al., 2014] to the fact that nitrogen in the ISM is mainly in atomic form, and N atoms could stay in the gas phase longer because of their lower sticking probabilities and the slow process which transforms N into N_2.

Following the detection of c-C_3H_2 in the laboratory [Thaddeus et al., 1985], a number of U-lines observed by Thaddeus et al. [1981] were able to be identified as c-C_3H_2 transitions. After its first detection, cyclopropenylidene has been observed in various sources, like cold dark clouds, diffuse clouds, circumstellar envelopes, planetary nebulae etc. [e.g. Benson et al., 1998, Spezzano et al., 2013, and references therein]. Due to the high abundance of the normal species, also the singly deuterated species c-C_3HD and the isotopologue c-$H^{13}CC_2H$ have been observed in various sources in the past 30 years. For example, c-C_3HD was detected toward L1498 [Bell et al., 1988], TMC-1C and L1544 [Spezzano et al., 2013] as well as TMC-1 [Turner, 2001] in the Taurus Molecular Cloud.

After the first laboratory measurement of the doubly deuterated species by Spezzano et al. [2012], c-C_3D_2 was detected in the ISM for the first time toward the starless cores TMC-1C and L1544 with a high signal-to-noise-ratio [Spezzano et al., 2013]. The observed single and double deuteration in these two sources could be reproduced by a chemical model including only gas-phase reactions [Aikawa et al., 2012]. The possibility of double deuteration and its gas-phase chemistry makes c-C_3H_2 a useful probe for the deuteration processes taking place only in the gas phase. A study of the c-C_3H_2-deuteration as an evolutionary indicator will give complementary information to the deuteration of N_2H^+, and reveal possible differences between the deuteration of C- and N-bearing species in the gas phase. In fact, unlike N_2H^+, c-C_3H_2 is believed to be an early-type molecule [Herbst and Leung, 1989] in terms of cloud evolution and can therefore trace the early stages of star formation; in particular, in L1544, c-C_3H_2 preferentially traces the side of the core more exposed to the interstellar radiation field, where the chemistry is continually rejuvenated by the photodissociation of CO [Spezzano et al., 2016]. However, c-C_3H_2 is also affected by freeze-out or chemical depletion, as it does not trace the central regions of starless cores [e.g. Spezzano et al., 2017]. It is therefore important to compare the deuteration of this molecule in starless and protostellar cores, in order to investigate the level of deuteration in different stages of low-mass star formation. This can give us insights on possible deuteration processes taking place on grain surfaces during the cold and dense phases just before the switch-on of the protostar.

In this work we present single pointing observations of c-C_3H_2, the singly and doubly deuterated species, c-C_3HD and c-C_3D_2, as well as the isotopologue c-$H^{13}CC_2H$ toward 10 starless cores and 5 protostars in the Taurus and Perseus Molecular Cloud Complexes. In Section 2.3 we summarize the details concerning the observations. Section 5.4 describes the calculation of the single and double deuteration of c-C_3H_2 as well as the comparison between the deuterium fraction of N_2H^+ and c-C_3H_2. In Section 5.4 we also describe the correlation between the deuteration level of c-C_3H_2 and important evolutionary indicators (dust temperature, CO depletion level and central column density of H_2). The conclusions are summarized in Section 2.5.

2.3 Observations

The observations were done at the IRAM 30m telescope located at Pico Veleta (Spain) toward 10 starless cores and 5 protostellar cores in Taurus and Perseus. A summary of the observed objects, their coordinates and their distances is reported in Table 2.1. These sources lie all in our Galactic vicinity and represent different stages of star formation, from starless cores, to more evolved pre-stellar cores and young Class 0 protostars. Previous observations of these sources showed a significant deuteration of N_2H^+ which correlates with evolutionary indicators, such as the dust temperature, the CO depletion and central column density of H_2 [Crapsi et al., 2005, Emprechtinger et al., 2009]. A special case in our sample of sources is L1521F. Even though some studies [Crapsi et al., 2005] describe this source as an evolved pre-stellar core, successive work [Bourke et al., 2006, Takahashi et al., 2013] has proven that L1521F shows an infrared source and a compact continuum millimeter emission which indicates the existence of a protostar. The detection of a small outflow and a low bolometric luminosity (0.034-0.07 $L_\odot$) suggests that this source is a so-called Very Low Luminosity Object (hereafter VeLLO) which could be a very young protostellar source or a protostar at its minimum of activity, if episodic accretion is at work [e.g. Visser et al., 2015].
The observations were carried out with the EMIR receiver using the E090 configuration (3mm atmospheric window). Each sub-band covered a frequency range of 1.8 GHz, leading to a total spectral coverage of 7.2 GHz. All four EMIR sub-bands were connected to the Fast Fourier Transform Spectrometer with a frequency resolution of 50 kHz. Frequency switching was performed with a frequency throw of ±3.9 MHz. Telescope pointing was checked every 2 hr on Mercury and was accurate to 3″-4″. The intensity of the obtained spectra was given in antenna temperature units, T_A^*. The antenna temperature T_A^* was converted to the main beam temperature T_{mb} by using the relation $T_{mb} = \frac{F_{eff}}{B_{eff}} \cdot T_A^*$.

In both samples we observed the main isotopologue c-C_3H_2, the singly and doubly deuterated species c-C_3HD and c-C_3D_2 as well as the isotopologue c-$H^{13}CC_2H$ with one ^{13}C being off the principal axis of the molecule. Table 3.1 summarizes the observed species, the spectroscopic parameters and telescope settings at the corresponding frequencies: E_{up} describes the upper state energy and A_{ul} is the Einstein coefficient of the corresponding transition. The upper state degeneracy is given by g_u. The parameters B_{eff} and θ_{MB} describe the main beam efficiency and the main beam size of the telescope at a given frequency, respectively. The system temperature T_{sys} is given in K. The forward efficiency, F_{eff}, is in the observing frequency range equal to 95%.

2.4 Results

In the Appendix A (Figures A.1- A.16) we show the observed spectra toward all sources. The $3_{2,2} - 3_{1,3}$ transition of c-C_3H_2 at 84.727 GHz was detected in all starless and pre-stellar cores except for L1400K, L1517B and L1512. The same line of c-C_3H_2 was also detected in all protostars except for L1448IRS2. The c-C_3HD ($3_{0,3} - 2_{1,2}$) and c-$H^{13}CC_2H$ ($2_{1,2} - 1_{0,1}$)

Table 2.1: Observed sources with their corresponding coordinates and estimated distances. Here we also include the well studied objects L1544 and IRAS16293-2422.

Source	Object	R.A J2000.0	Decl. J2000.0	Distance (pc)	References [a]
L1495	starless core	04 14 08.2	+28 08 16	140	2
L1495B	starless core	04 18 05.1	+28 22 22	140	1
L1495AN	starless core	04 18 31.8	+28 27 30	140	1
L1495AS	starless core	04 18 41.8	+28 23 50	140	1
L1400K	starless core	04 30 52.1	+54 51 55	140	2
L1400A	starless core	04 30 56.8	+54 52 36	140	1
CB23	starless core	04 43 27.7	+29 39 11	140	1
L1517B	starless core	04 55 18.8	+30 38 04	140	1
L1512	starless core	05 04 09.7	+32 43 09	140	1
TMC2	pre-stellar core [b]	04 32 48.7	+24 25 12	140	1
L1544	pre-stellar core [b]	05 04 17.2	+25 10 43	140	3
L1521F	protostellar core	04 28 39.8	+26 51 35	140	1
Per 5	protostellar core	03 29 51.6	+31 39 03	220	4
IRAS03282	protostellar core	03 31 21.0	+30 45 30	220	4
HH211	protostellar core	03 43 56.8	+32 00 50	220	4
L1448IRS2	protostellar core	03 25 22.4	+30 45 12	220	4
IRAS16293	protostellar core	16 32 22.6	-24 28 33	120	5

[a] (1) Lee et al. [2001]; (2) Tafalla et al. [2002]; (3) Ward-Thompson et al. [1999]; (4) Cernis [1990]; (5) Caux et al. [2011].

[b] The definition of a pre-stellar core is based on the work of Crapsi et al. [2005].

emission was detected in all starless, pre-stellar and protostellar cores with a very high S/N; the strongest lines have a S/N ratio of 25 and 40, respectively. The $3_{1,3} - 2_{0,2}$ transition of c-C_3D_2 at 97.761 GHz was found at a high S/N level (the strongest line was detected at a 27σ level) in the following starless and pre-stellar cores: L1495AN, L1512, L1517B, TMC2 and L1544. In case of the protostellar cores, c-C_3D_2 was detected in four sources: Per5, HH211, L1521F and IRAS16293-2422 with S/N levels ranging from 7.8 to 13.5.

2.4.1 Calculation of the column densities and the deuteration level

The data reduction and analysis was done using the GILDAS[1] software [Pety, 2005]. In order to substract the baseline caused mainly by the frequency switching mode, high-order

[1] http://www.iram.fr/IRAMFR/GILDAS

Table 2.2: Transition parameters of the observed species and telescope settings.

Species	Transitions J_{K_a,K_c}	Frequency (GHz)	Ref. [a]	E_{up} (K)	A_{ul} ($10^{-5}s^{-1}$)	g_u	B_{eff} (%)	θ_{MB} ($''$)	T_{sys} (K)
c-C_3H_2	$3_{2,2}-3_{1,3}$	84.727	1	16.14	1.04	7	81	29	80-120
c-C_3HD	$3_{0,3}-2_{1,2}$	104.187	2	10.85	3.95	21	79	25	90-151
c-C_3HD	$2_{1,1}-1_{1,0}$	95.994	2	7.56	0.45	15	80	27	99-114
c-$H^{13}CC_2H$	$2_{1,2}-1_{0,1}$	84.185	2	6.33	2.17	10	81	29	80-116
c-C_3D_2	$3_{0,3}-2_{1,2}$	94.371	3	9.85	3.37	21	80	27	82-123
c-C_3D_2	$3_{1,3}-2_{0,2}$	97.761	3	9.88	3.87	42	80	26	79-119
c-C_3D_2	$2_{2,1}-1_{1,0}$	108.654	3	7.90	4.79	15	78	24	96-105

[a] (1) Thaddeus et al. [1985]; (2) Bogey et al. [1987]; (3) Spezzano et al. [2012]

polynomials were fitted. Each line was fitted by using the standard CLASS gaussian fitting method. The total column density was calculated by using the expression for optically thin transitions:

$$N_{tot} = \frac{8\pi k_B W \nu^2}{A_{ul} h c^3} \cdot \frac{J(T_{ex})}{J(T_{ex}) - J(T_{bg})} \cdot \frac{Q_{rot}(T_{ex})}{g_u e^{-\frac{E_{up}}{k_B T_{ex}}}}, \tag{2.2}$$

where $W = \frac{\sqrt{\pi}\Delta v T_{mb}}{2\sqrt{\ln(2)}}$ is the integrated intensity of the line, with Δv being the linewidth (FWHM) [Caselli et al., 2002]. $J(T) = (\frac{h\nu}{k_B})(e^{\frac{h\nu}{k_B T}} - 1)^{-1}$ is the Rayleigh-Jeans temperature in K, k_B is the Boltzmann constant, ν is the transition frequency, c is the speed of light, and h is the Planck constant. The partition function of a molecule at a given excitation temperature T_{ex} is given by Q_{rot}. T_{bg} is the cosmic background temperature (2.7 K). For a further extension of our sample we also included in this study the pre-stellar core L1544 [Spezzano et al., 2013] as well as the Class 0 protostar IRAS16293-2422 (hereafter IRAS16293) [Caux et al., 2011]. In Tables 2.3 and 2.4 we summarize the detected lines in every source and the line properties which were derived from Gaussian fits. The sources CB23, L1495AN, L1495B, Per5, HH211, L1448IRS2, IRAS03282 and IRAS16293 show differences in the linewidth between the main isotopologue and the isotopic variants ranging in the 0.1-0.5 km/s interval. These differences do not exhibit any clear trend and are poorly constrained with errors varying from 36% to 94%. Such discrepancies are likely to be produced by the high noise levels of these latter observations and by the coarse sampling of the line profiles (channel spacing is 0.167 km/s).

Table 2.3: Observed lines in the starless core sample. The line properties are derived from Gaussian fits.

Source/Molecule	Frequency (GHz)	$T_{\rm mb}$ (K)	rms (mK)	W (K km s^{-1})	$v_{\rm LSR}$ (km s^{-1})	Δv (km s^{-1})
CB23						
c-C_3H_2	84.727	0.05	11	0.017 ± 0.004	6.018 ± 0.037	0.333 ± 0.088
c-C_3HD	104.187	0.23	9	0.056 ± 0.002	6.015 ± 0.005	0.229 ± 0.010
c-$H^{13}CC_2H$	84.185	0.13	3	0.024 ± 0.001	5.987 ± 0.003	0.174 ± 0.017
c-C_3D_2	97.761	< 0.02	7	< 0.004		
L1400A						
c-C_3H_2	84.727	0.07	8	0.019 ± 0.002	3.355 ± 0.020	0.246 ± 0.030
c-C_3HD	104.187	0.13	8	0.036 ± 0.002	3.348 ± 0.008	0.263 ± 0.021
c-$H^{13}CC_2H$	84.185	0.06	2	0.020 ± 0.001	3.287 ± 0.006	0.334 ± 0.014
L1400K						
c-$H^{13}CC_2H$	84.185	0.06	9	0.018 ± 0.002	3.178 ± 0.023	0.268 ± 0.048
c-C_3HD	104.187	< 0.04	15	< 0.01		
L1495						
c-C_3H_2	84.727	0.06	4	0.015 ± 0.001	6.779 ± 0.012	0.244 ± 0.035
c-C_3HD	104.187	0.13	10	0.038 ± 0.002	6.768 ± 0.010	0.269 ± 0.025
c-$H^{13}CC_2H$	84.185	0.07	14	0.021 ± 0.005	6.726 ± 0.036	0.281 ± 0.088
L1495AN						
c-C_3H_2	84.727	0.17	14	0.062 ± 0.006	7.259 ± 0.014	0.344 ± 0.039
c-C_3HD	104.187	0.43	22	0.138 ± 0.007	7.275 ± 0.007	0.304 ± 0.019
c-$H^{13}CC_2H$	84.185	0.22	10	0.075 ± 0.004	7.261 ± 0.007	0.329 ± 0.019
c-C_3D_2	97.761	0.04	6	0.011 ± 0.001	7.208 ± 0.020	0.236 ± 0.044
L1495AS						
c-C_3H_2	84.727	0.08	8	0.028 ± 0.004	7.302 ± 0.019	0.353 ± 0.046
c-C_3HD	104.187	0.15	9	0.046 ± 0.002	7.281 ± 0.008	0.280 ± 0.018
c-$H^{13}CC_2H$	84.185	0.09	8	0.025 ± 0.002	7.229 ± 0.015	0.254 ± 0.022
L1495B						
c-C_3H_2	84.727	0.04	8	0.020 ± 0.004	6.655 ± 0.038	0.460 ± 0.086
c-C_3HD	104.187	0.13	16	0.054 ± 0.006	6.635 ± 0.022	0.403 ± 0.048
c-$H^{13}CC_2H$	84.185	0.06	7	0.018 ± 0.002	6.582 ± 0.020	0.300 ± 0.045
L1512						
c-C_3HD	104.187	0.30	19	0.067 ± 0.005	7.095 ± 0.009	0.204 ± 0.015
c-$H^{13}CC_2H$	84.185	0.15	8	0.033 ± 0.002	7.058 ± 0.012	0.211 ± 0.015
c-C_3D_2	97.761	0.03	3	0.008 ± 0.001	7.075 ± 0.017	0.293 ± 0.038
L1517B						
c-C_3HD	104.187	0.30	14	0.068 ± 0.004	5.778 ± 0.007	0.249 ± 0.017
c-$H^{13}CC_2H$	84.185	0.10	11	0.029 ± 0.004	5.751 ± 0.018	0.279 ± 0.031
c-C_3D_2	97.761	0.05	8	0.014 ± 0.002	5.777 ± 0.024	0.266 ± 0.054
c-C_3D_2	94.371	0.05	8	0.013 ± 0.002	5.854 ± 0.025	0.271 ± 0.053
TMC2						
c-C_3H_2	84.727	0.16	18	0.061 ± 0.007	6.192 ± 0.020	0.365 ± 0.047
c-C_3HD	104.187	0.53	24	0.184 ± 0.007	6.217 ± 0.007	0.325 ± 0.016
c-$H^{13}CC_2H$	84.185	0.16	9	0.065 ± 0.004	6.132 ± 0.010	0.374 ± 0.024
c-C_3D_2	97.761	0.10	4	0.030 ± 0.001	6.237 ± 0.005	0.283 ± 0.012
c-C_3D_2	94.371	0.05	5	0.018 ± 0.001	6.258 ± 0.014	0.330 ± 0.040
c-C_3D_2	108.654	0.03	7	0.012 ± 0.002	6.262 ± 0.036	0.355 ± 0.107
L1544 [a]						
c-C_3H_2	84.727	0.21	10	0.10 ± 0.01	7.210 ± 0.008	0.46 ± 0.01
c-C_3HD	104.187	0.48	10	0.238 ± 0.004	7.181 ± 0.004	0.468 ± 0.009
c-C_3HD	95.994	0.13	10	0.065 ± 0.003	7.17 ± 0.01	0.48 ± 0.03
c-$H^{13}CC_2H$	84.185	0.19	10	0.093 ± 0.003	7.154 ± 0.008	0.44 ± 0.02
c-C_3D_2	97.761	0.13	5	0.059 ± 0.002	7.181 ± 0.007	0.43 ± 0.02
c-C_3D_2	94.371	0.07	5	0.032 ± 0.002	7.20 ± 0.01	0.45 ± 0.03
c-C_3D_2	108.654	0.04	5	0.023 ± 0.002	7.17 ± 0.02	0.54 ± 0.05

[a] The values for L1544 were taken from Spezzano et al. [2013].

Table 2.4: Observed lines in the protostellar core sample. The line properties are derived from Gaussian fits.

Source/Molecule	Frequency (GHz)	T_{mb} (K)	rms (mK)	W (K km s^{-1})	v_{LSR} (km s^{-1})	Δv (km s^{-1})
Per5						
c-C_3H_2	84.727	0.09	9	0.050 ± 0.004	8.102 ± 0.021	0.529 ± 0.051
c-C_3HD	104.187	0.27	21	0.116 ± 0.007	8.174 ± 0.013	0.401 ± 0.032
c-$H^{13}CC_2H$	84.185	0.09	6	0.035 ± 0.002	8.171 ± 0.012	0.362 ± 0.026
c-C_3D_2	97.761	0.09	11	0.029 ± 0.004	8.215 ± 0.021	0.318 ± 0.050
HH211						
c-C_3H_2	84.727	0.10	7	0.051 ± 0.002	9.089 ± 0.013	0.461 ± 0.029
c-C_3HD	104.187	0.35	14	0.163 ± 0.005	9.097 ± 0.007	0.432 ± 0.018
c-$H^{13}CC_2H$	84.185	0.05	5	0.022 ± 0.002	9.100 ± 0.019	0.403 ± 0.045
c-C_3D_2	97.761	0.10	7	0.037 ± 0.002	9.102 ± 0.012	0.361 ± 0.032
L1448IRS2						
c-C_3HD	104.187	0.20	13	0.105 ± 0.005	4.084 ± 0.011	0.479 ± 0.027
c-$H^{13}CC_2H$	84.185	0.05	6	0.037 ± 0.004	3.977 ± 0.032	0.690 ± 0.082
IRAS03282						
c-C_3H_2	84.727	0.02	5	0.020 ± 0.002	7.002 ± 0.062	0.933 ± 0.155
c-C_3HD	104.187	0.12	9	0.064 ± 0.004	6.863 ± 0.015	0.517 ± 0.034
c-$H^{13}CC_2H$	84.185	0.03	5	0.013 ± 0.002	6.812 ± 0.035	0.414 ± 0.072
L1521F						
c-C_3H_2	84.727	0.22	6	0.086 ± 0.002	6.407 ± 0.005	0.366 ± 0.010
c-C_3HD	104.187	0.33	17	0.144 ± 0.006	6.433 ± 0.009	0.410 ± 0.018
c-$H^{13}CC_2H$	84.185	0.18	12	0.077 ± 0.005	6.365 ± 0.013	0.404 ± 0.028
c-C_3D_2	97.761	0.05	6	0.018 ± 0.002	6.477 ± 0.020	0.360 ± 0.063
IRAS16293						
c-C_3H_2	84.727	0.09	3	0.183 ± 0.006	4.303 ± 0.034	2.011 ± 0.077
c-C_3HD	104.187	0.17	6	0.280 ± 0.012	4.235 ± 0.031	1.573 ± 0.080
c-C_3HD	95.994	0.03	2	0.053 ± 0.004	4.026 ± 0.059	1.914 ± 0.147
c-$H^{13}CC_2H$	84.185	0.03	3	0.089 ± 0.008	3.889 ± 0.108	2.394 ± 0.237
c-C_3D_2	94.371	0.03	4	0.059 ± 0.010	4.342 ± 0.158	1.952 ± 0.375
c-C_3D_2	97.761	0.03	3	0.049 ± 0.006	4.281 ± 0.097	1.516 ± 0.196

For the calculation of the total column densities of c-C_3H_2 and its isotopologues we assumed the same excitation temperature T_{ex} that has been used in the same sources by Crapsi et al. [2005] and Emprechtinger et al. [2009] for N_2H^+.[2] We also used the same excitation temperature for the deuterated and the ^{13}C species. The effect of underestimating the excitation temperature of the main and the deuterated species by 1 K changes the deuteration level $N(c\text{-}C_3HD)/N(c\text{-}C_3H_2)$ up to 30%. In case of L1544 we use the T_{ex} derived in Gerin et al. [1987], where detections of c-C_3H_2 and its deuterated counterpart are reported. In particular, there were three transitions of c-C_3HD at 19.419, 79.812 and 104.187 GHz detected in L1544 which gave a T_{ex} of 5 ± 2 K. An optically thick transition of c-C_3H_2 detected at 85.339 GHz provided a T_{ex} of 6 K. This excitation temperature is, within the errors, equal to that found in N_2H^+(1-0) and N_2D^+(2-1) toward the same source

[2]The critical density of c-C_3H_2 ($3_{2,2}-3_{1,3}$) lies a factor of 12.7 higher than the critical density of N_2H^+(1-0) at 30 K [Chandra and Kegel, 2000, Schöier et al., 2005]. We cannot compare the critical densities of the above transitions at lower temperatures, since the collisional rate of the c-C_3H_2 ($3_{2,2}-3_{1,3}$) transition is unknown below 30 K.

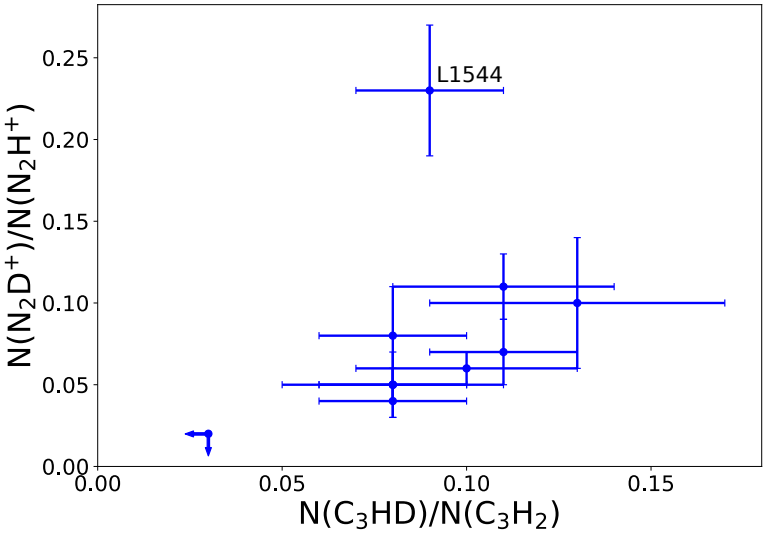

Figure 2.1: Deuterium fraction of c-C_3H_2 and N_2H^+ in 11 starless cores located in the Taurus Complex. The deuteration level of N_2H^+ was calculated in previous work [Crapsi et al., 2005]. The arrows indicate the upper limits for the estimated c-C_3H_2 and N_2H^+ deuterium fraction in the source L1400K.

[Crapsi et al., 2005]. Due to the large error of T_{ex} for c-C_3HD, we use for the main and the deuterated species a T_{ex} of 6 K.

Since c-$H^{13}CC_2H$ has been detected in every source, we used the total column density of c-$H^{13}CC_2H$ to derive $N(c\text{-}C_3H_2)$ by considering a $^{12}C/^{13}C$ ratio of 77 [Wilson and Rood, 1994]. This gives us the additional advantage of avoiding ambiguities due to the optical depth of the main species. The carbon isotope ratio has been determined in several sources, from different molecular species and can vary up to a factor of 2 [Wilson and Rood, 1994]. This means that the derived $N(c\text{-}C_3H_2)$ suffers from an uncertainty of a factor of 2. The assumed ortho to para ratio of c-C_3H_2 and c-C_3D_2 is 3 and 2, respectively. Table 2.5 and Table 2.6 show the derived column densities for every species in each starless core and protostar, respectively. The error for the column densities was calculated by propagating the uncertainty on the integrated intensity, W, including the 1σ statistical error as well as 10% calibration uncertainty. The column densities for the singly and doubly deuterated species were calculated from the c-C_3HD ($3_{0,3} - 2_{1,2}$) and c-C_3D_2 ($3_{1,3} - 2_{0,2}$) transitions.

Figure 2.1 shows the deuterium fraction for each species in every starless core. Here one can clearly see that the deuteration for both c-C_3H_2 and N_2H^+ follows a similar trend and is of the same magnitude, except for the most dynamically evolved object, the pre-stellar core L1544. The deuteration of c-C_3H_2 is in all sources within the 1σ uncertainty consistent with 10%, except for L1400K where the c-C_3HD column density was estimated to be less than $0.26 \times 10^{12}\,\mathrm{cm}^{-2}$, which resulted in a 3σ upper limit for the $N(c\text{-}C_3HD)/N(c\text{-}C_3H_2)$ ratio of 0.03. All these sources except for TMC2 and L1544 have been identified in Crapsi

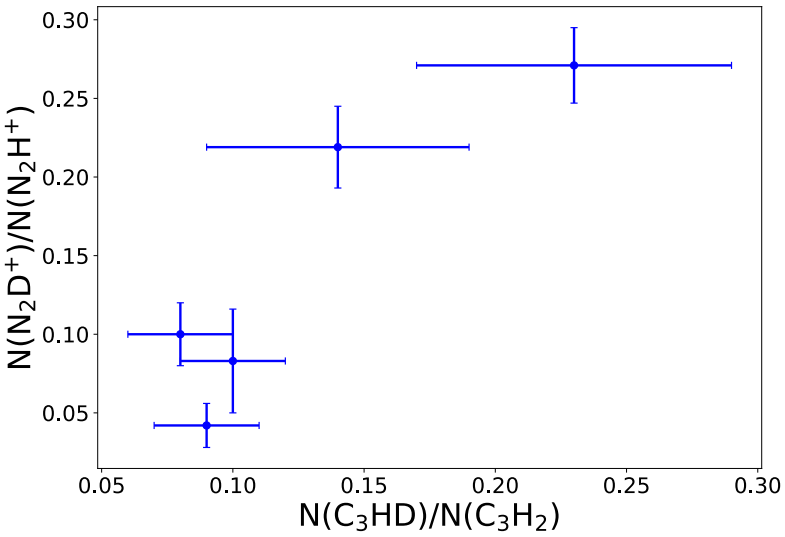

Figure 2.2: Deuterium fraction of c-C_3H_2 and N_2H^+ in 4 protostellar cores in the Perseus Complex and one protostellar core (L1521F) in the Taurus Complex. The deuteration level of N_2H^+ was calculated in previous work done by Emprechtinger et al. (2009).

et al. [2005] as less evolved starless cores, having, among other properties, a deuteration degree $\leq$0.1 which is also in our case fulfilled (in the source L1495B the deuterium fraction can still be within the errors less than or equal to 0.1). L1544 is the only source where the deuteration of N_2H^+ is larger than the one of c-C_3H_2, showing a significant discrepancy of a factor of 2.6. One possible explanation for this can be found in the formation route of N_2H^+. The progenitor of N_2H^+ is N_2 which is formed via neutral-neutral reactions: $N + C \rightarrow CN$ and $CN + N \rightarrow N_2$ [Pineau des Forets et al., 1990, Le Gal et al., 2014]. Carbon-bearing molecules like c-C_3H_2 on the other hand are formed faster through sequential ion-neutral reactions. For this reason, N_2H^+ is believed to be a late-type molecule, becoming highly abundant in evolved cores, such as L1544. Furthermore, N_2H^+ is more resistant to depletion and survives in the gas phase longer than C-bearing molecules, thus tracing regions where the deuterium fractionation is more efficient because of the large amount of freeze out of neutral species (such as CO and O) which participate in the destruction of the H_3^+ deuterated isotopologues [Dalgarno and Lepp, 1984].

The abundance of the doubly deuterated species with respect to the normal species is 0.4-1.5%. These values are comparable to those calculated by Spezzano et al. [2013] in TMC-1C and L1544. The ratios $N(c\text{-}C_3HD)/N(c\text{-}C_3H_2)$ and $N(c\text{-}C_3D_2)/N(c\text{-}C_3HD)$ are quite similar in all starless and pre-stellar cores. This suggests that c-C_3H_2 and c-C_3HD follow the same deuteration route and are not affected by the dynamical evolution of the dense core, as already pointed out in Spezzano et al. [2013]. In the source CB23 we find a marginal detection of c-C_3D_2 and therefore derive a 3σ upper limit for the column density. The abundance ratios $N(c\text{-}C_3HD)/N(c\text{-}C_3H_2)$, $N(c\text{-}C_3D_2)/N(c\text{-}C_3H_2)$

and $N(c\text{-}C_3D_2)/N(c\text{-}C_3HD)$ among the starless core sample are listed in Table 2.7.

Table 2.5: Column densities of the species c-C_3H_2, c-C_3HD, c-C_3D_2 and c-$H^{13}CC_2H$ in the 11 starless cores within the Taurus Molecular Cloud Complex.

Starless Core	$N(c\text{-}C_3H_2)$ $(10^{12}\,\mathrm{cm}^{-2})$	N $(c\text{-}C_3HD)$ $(10^{12}\,\mathrm{cm}^{-2})$	$N(c\text{-}H^{13}CC_2H)$ $(10^{12}\,\mathrm{cm}^{-2})$	$N(c\text{-}C_3D_2)$ $(10^{12}\,\mathrm{cm}^{-2})$
CB23	10.9 ± 1.2	1.15 ± 0.13	0.28 ± 0.03	< 0.07
L1400A	9.1 ± 1.1	0.74 ± 0.09	0.24 ± 0.03	-
L1400K	8.0 ± 1.3	< 0.26	0.21 ± 0.03	-
L1495	8.6 ± 2.1	0.66 ± 0.08	0.22 ± 0.06	-
L1495AN	31.7 ± 3.5	2.50 ± 0.28	0.82 ± 0.09	0.13 ± 0.02
L1495AS	11.4 ± 1.6	0.94 ± 0.11	0.30 ± 0.04	-
L1495B	7.5 ± 1.2	0.94 ± 0.14	0.20 ± 0.03	-
L1512	13.2 ± 1.6	1.09 ± 0.13	0.34 ± 0.04	0.08 ± 0.02
L1517B	12.2 ± 1.9	1.23 ± 0.14	0.32 ± 0.05	0.16 ± 0.03
TMC2	25.9 ± 2.9	2.94 ± 0.32	0.67 ± 0.08	0.31 ± 0.03
L1544	34.9 ± 3.7	3.18 ± 0.32	0.91 ± 0.10	0.53 ± 0.06

- no data available

Table 2.6: Column densities of the species c-C_3H_2, c-C_3HD, c-C_3D_2 and c-$H^{13}CC_2H$ in the 6 protostars. The protostars Per 5, HH211, L1448IRS2 and IRAS03282 belong to the Perseus Complex, L1521F lies in the Taurus Complex while IRAS16293 is part of the Ophiuchus Complex.

Protostellar Core	$N(c\text{-}C_3H_2)$ $(10^{12}\,\mathrm{cm}^{-2})$	$N(c\text{-}C_3HD)$ $(10^{12}\,\mathrm{cm}^{-2})$	$N(c\text{-}H^{13}CC_2H)$ $(10^{12}\,\mathrm{cm}^{-2})$	$N(c\text{-}C_3D_2)$ $(10^{12}\,\mathrm{cm}^{-2})$
Per5	14.2 ± 1.7	1.4 ± 0.16	0.37 ± 0.04	0.24 ± 0.04
HH211	8.5 ± 1.2	1.9 ± 0.20	0.22 ± 0.03	0.30 ± 0.04
L1448IRS2	13.9 ± 1.9	1.3 ± 0.14	0.36 ± 0.05	-
IRAS03282	5.1 ± 1.1	0.7 ± 0.09	0.13 ± 0.03	-
IRAS16293	36.4 ± 5.0	3.6 ± 0.39	0.95 ± 0.13	0.43 ± 0.07
L1521F	31.5 ± 3.7	2.4 ± 0.26	0.82 ± 0.10	0.20 ± 0.03

- no data available

Table 2.7: Column density ratios of the deuterated species c-C_3HD, c-C_3D_2 with respect to the main species in the starless core sample.

Starless Core	$N(c\text{-}C_3HD)/N(c\text{-}C_3H_2)$	$N(c\text{-}C_3D_2)/N(c\text{-}C_3H_2)$	$N(c\text{-}C_3D_2)/N(c\text{-}C_3HD)$
CB23	0.11 ± 0.02	< 0.006	< 0.06
L1400A	0.08 ± 0.02	-	-
L1400K	< 0.03	-	-
L1495	0.08 ± 0.03	-	-
L1495AN	0.08 ± 0.02	0.004 ± 0.001	0.05 ± 0.01
L1495AS	0.08 ± 0.02	-	-
L1495B	0.13 ± 0.04	-	-
L1512	0.08 ± 0.02	0.006 ± 0.002	0.08 ± 0.02
L1517B	0.10 ± 0.03	0.013 ± 0.005	0.13 ± 0.04
TMC2	0.11 ± 0.03	0.012 ± 0.003	0.10 ± 0.02
L1544	0.09 ± 0.02	0.015 ± 0.003	0.17 ± 0.03

- no data available

Also in the observed protostars the deuteration for both species is similar, as we can clearly see in Figure 2.2. The deuterium fraction peaks in HH211, reaching 23% in case of c-C_3H_2 and 27% in case of N_2H^+ which is also the highest estimated deuteration among all observed protostellar and starless cores. The abundance ratio $N(c\text{-}C_3HD)/N(c\text{-}C_3H_2)$ is within the error bars equal to 10%, with the exception of HH211, where the average deuteration level is 0.23 ± 0.06. These results are similar to the $N(c\text{-}C_3D_2)/N(c\text{-}C_3HD)$ ratio, that ranges from 5% to 17%. Finally, the abundance of the doubly deuterated species with respect to the main isotopologue varies between 0.6% and 3.6%. The single and double deuteration level of c-C_3H_2 in every protostellar core is summarized in Table 2.8.

In case of IRAS16293, we derived the deuteration of c-C_3H_2 and its isotopologues, as well as the depletion factor of CO by using the publicly available data from TIMASSS [Caux et al., 2011]. For the calculation of the c-C_3H_2 column density and its isotopologues, we assumed a T_{ex} of 8.9 K for the main and the ^{13}C species, and a T_{ex} of 6.3 K for the deuterated counterparts, as it was derived in Majumdar et al. [2017]. The $N(c\text{-}C_3HD)/N(c\text{-}C_3H_2)$ ratio in IRAS16293 calculated in this work is 0.10 ± 0.02. This is comparable to the deuteration of 14% determined in Majumdar et al. [2017] within the uncertainties.

2.4.2 Correlation between deuteration and CO depletion factor

In a cold and dense cloud, molecules in the gas phase tend to collide and freeze-out onto dust grains, leading to a gradual decrease of their gas-phase abundance. Molecules are bound on grains through Van der Waals forces [Garrod et al., 2007], meaning that species with a non-zero dipole moment, such as CS as well as CO, will be strongly bound on grain surfaces at the low temperatures typical of starless cores; thus, they deplete from the gas phase by significant amounts. Deuteration is expected to correlate with the CO depletion factor, since CO destroys H_2D^+ [Dalgarno and Lepp, 1984]. Previous studies have proven

Table 2.8: Column density ratios of the deuterated species c-C_3HD, c-C_3D_2 with respect to the main species in the protostellar core sample.

Protostellar Core	$N(c\text{-}C_3HD)/N(c\text{-}C_3H_2)$	$N(c\text{-}C_3D_2)/N(c\text{-}C_3H_2)$	$N(c\text{-}C_3D_2)/N(c\text{-}C_3HD)$
Per5	0.10 ± 0.02	0.017 ± 0.005	0.18 ± 0.05
HH211	0.23 ± 0.06	0.036 ± 0.009	0.16 ± 0.04
L1448IRS2	0.09 ± 0.02	-	-
IRAS03282	0.14 ± 0.05	-	-
IRAS16293	0.10 ± 0.02	0.012 ± 0.003	0.12 ± 0.03
L1521F	0.08 ± 0.02	0.006 ± 0.002	0.08 ± 0.02

- no data available

that the deuterium fraction of N_2H^+ correlates strongly with the degree of CO depletion [Caselli et al., 2002, Crapsi et al., 2005, Emprechtinger et al., 2009]. The level of depletion is usually expressed as depletion factor f_d and is given by:

$$f_d(\mathrm{CO}) = \frac{X_{ref}(\mathrm{CO})}{X(\mathrm{CO})}, \tag{2.3}$$

where $X_{ref}(\mathrm{CO})$ is the reference abundance of CO in the local ISM and $X(\mathrm{CO})$ is the observed CO abundance [e.g. Emprechtinger et al., 2009].

Figure 2.3 shows the $N(c\text{-}C_3HD)/N(c\text{-}C_3H_2)$ and the $N(N_2D^+)/N(N_2H^+)$ ratio versus the CO depletion factor for the starless core sample. The depletion factors for the sources L1544, TMC2, L1495, L1517B were taken from Crapsi et al. [2005]. In order to search for a statistical correlation between $N(c\text{-}C_3HD)/N(c\text{-}C_3H_2)$ and $f_d(\mathrm{CO})$ we have applied the Kendall's τ and the Spearman's ρ rank correlation tests. The Kendall's rank test gives $\tau = 0.33$ with a significance p of 0.49 and the Spearman's rank test gives $\rho = 0.40$ with $p = 0.60$, indicating that there is no correlation between the c-C_3H_2 deuteration and the CO depletion factor within the starless core sample. In case of the N_2H^+ deuteration, however, we note a significant jump toward the pre-stellar core L1544. As already mentioned in §5.4, this indicates that N_2H^+ is less affected by depletion than c-C_3H_2 and traces the deuteration level in the highest density regions of the core; in fact the N_2H^+ abundance also increases where CO is significantly frozen, as CO destroys N_2H^+ to form HCO^+.

The correlation between $N(c\text{-}C_3HD)/N(c\text{-}C_3H_2)$ and the CO depletion factor in the observed protostars is shown in Figure 2.4. The depletion factors for the sources HH211, IRAS03282, L1448IRS2 and Per5 were taken from Emprechtinger et al. (2009), while the depletion factor for L1521F is reported in Crapsi et al. (2005). For the CO depletion level in IRAS16293 we used the spectral properties of the $C^{18}O$ (1-0) transition given in Caux et al. [2011] to calculate the column density of $C^{18}O$, as it was done in Emprechtinger et al. [2009]. Here we use $X_{ref}(C^{16}O) = 9.5 \times 10^{-5}$ [Frerking et al., 1982] to allow fair comparison with Emprechtinger et al. [2009], although other values for $X_{ref}(C^{16}O)$ can be found in the

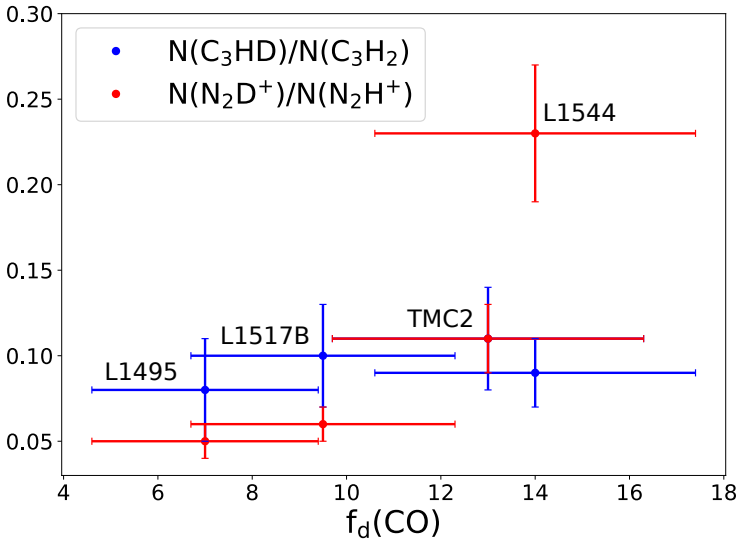

Figure 2.3: Deuterium fraction of c-C_3H_2 and N_2H^+ as a function of the CO depletion factor in the starless cores L1495, L1517B, TMC2 and L1544.

literature [Wannier, 1980, Lacy et al., 1994]. We use the relation $X(C^{16}O)/X(C^{18}O) = 560$ [Wilson and Rood, 1994] such that:

$$X(C^{16}O) = \frac{N_{tot}(C^{18}O) \cdot 560}{N(H_2)}. \tag{2.4}$$

The excitation temperature of $C^{18}O$ was set equal to 43 K which is the dust temperature for IRAS16293 [Schöier et al., 2002]. At this temperature no CO depletion is expected. However, the $C^{18}O$ column density is an average along the line of sight, which apart from the warm central regions, also includes the cold envelope, where CO can be significantly frozen [e.g. Brünken et al., 2014]. The hydrogen column density $N(H_2)$ was derived by using the Herschel/SPIRE image of IRAS16293 at 250, 350 and 500 μm. These data are publicly available and can be downloaded from the Herschel Science Archive (HSA) [3]. For more information concerning the data reduction, see §2.4.3. The resulting $N(H_2)$ of $1.0 \times 10^{23}\,\mathrm{cm}^{-2}$ is the mean value of column densities within a beam of 40". Following Equation C.1, the depletion factor for IRAS16293 is equal to:

$$f_d(\mathrm{CO}) = 0.7 \pm 0.2. \tag{2.5}$$

This value is consistent with the low f_d(CO) values measured by Punanova et al. [2016] in various sources toward ρ Ophiuchus. The fact that f_d(CO) is lower than 1 suggests that the adopted $X_{ref}(C^{16}O)$ is underestimated by a factor of 2-3. Moreover, one has to keep in

[3] www.cosmos.esa.int/web/herschel/science-archive

mind that the $C^{18}O$ (1-0) emission was observed within 22″, while the estimation of $N(H_2)$ was done within a 40″ beam. This indicates that the derived depletion factor should be considered as a lower limit.

Figure 2.4 shows no clear trend between the deuteration of c-C_3H_2 and the CO depletion among the protostellar cores. This is also confirmed by the Kendall's rank test that gives $\tau = 0.32$ with a significance p of 0.45 as well as by the Spearman's rank test that results to $\rho = 0.56$ with $p = 0.32$ (without considering the protostar L1521F). The source L1521F deviates strongly from the rest of the sources, having a significant depletion factor of 15 and simultaneously showing a low c-C_3H_2 deuteration of 8%. These values are comparable to those found in L1544, where the CO depletion factor is 14 [Crapsi et al., 2005] and the deuteration of c-C_3H_2 is 9%. The peculiarity of L1521F has been proven already in previous works, where the central column density $N(H_2)$ is high ($13.5 \times 10^{22}\,\mathrm{cm}^{-2}$) despite the low N_2H^+ deuteration [being a factor of 2 lower than in L1544; Crapsi et al., 2004, 2005].

The large CO depletion factor and low deuteration both in N_2H^+ and c-C_3H_2 in L1521F, could be a signature of episodic accretion of the central protostar. Since L1521F has been classified as a VeLLO [Bourke et al., 2006, Takahashi et al., 2013] it may be in a quiescent phase, following an accretion burst event. During such a burst, CO is expected to return in the gas phase [Visser et al., 2015], thus reducing the deuterium fraction. After the burst, the fast cooling of the dust could quickly lead to CO freeze out, with short time scales of the order of $10^9/\mathrm{n_H}\,\mathrm{yr}$, where n_H is the total number density of hydrogen nuclei [e.g. Caselli et al., 1999], while the deuteration of gas-phase molecules is a slower process, especially if during the burst the ortho-to-para H_2 ratio (sensitive to the temperature) increases to values larger than 1% [e.g. Flower et al., 2006, Kong et al., 2015]. However, the exact physical and chemical conditons of L1521F are beyond the scope of this work and it is clear that further observations are needed to prove this point.

2.4.3 Correlation between deuteration and H_2 column density

As already pointed out in §2.4.2, an increase in volume density toward the core centre is expected to correlate with an increase in deuteration, because of the consequently larger CO freeze-out rates, as long as the temperature remains below 20 K. For this reason we examine how the estimated deuteration of c-C_3H_2 in the starless and the pre-stellar cores correlates with the central column density of molecular hydrogen. For the $N(H_2)$ calculation we use the Herschel/SPIRE image of the Taurus Complex at 250, 350 and 500 μm, taken during the Herschel Gould Belt Survey [André et al., 2010].

A modified blackbody radiation is fitted to each pixel, using an emissivity spectral index $\beta = 1.5$ and a dust emissivity coefficient $\kappa_{250\mu\mathrm{m}} = 0.1\,\mathrm{g}^{-1}\,\mathrm{cm}^2$ [Hildebrand, 1983]. The data reduction involves smoothing the 250 μm and 350 μm images to the resolution of the 500 μm image and resampling all images to the same grid. From this fitting procedure we obtain the central column density $N(H_2)$ as well as the dust temperature T_Dust for every pixel. The resulting $N(H_2)$ is the mean value of column densities in a 40″ beam. For the error estimation we take into account calibration uncertainties of 7% according to

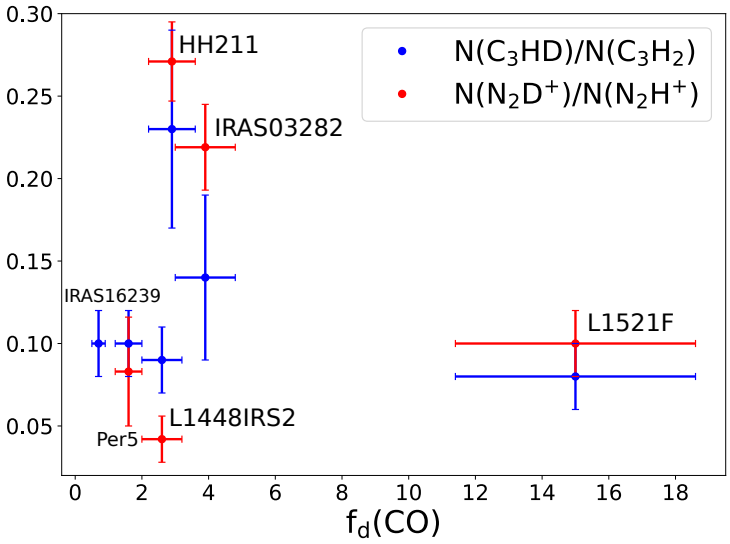

Figure 2.4: Deuterium fraction of c-C_3H_2 and N_2H^+ as a function of CO depletion factor for the protostellar core sample. The deuterium fraction of N_2H^+ and the CO depletion factors were taken from Emprechtinger et al. [2009], while the $N(N_2D^+)/N(N_2H^+)$ ratio and f_d(CO) for L1521F was given in Crapsi et al. [2005].

the SPIRE manual (see Appendix A.3). In Table 2.9 we summarize the resulting column densities and their uncertainties. The estimated $N(H_2)$ values are up to a factor of 3 smaller than the ones calculated in Crapsi et al. [2005] at the 1.2 mm dust continuum peak. This results from the different beam sizes used, 40″ vs 11″, so that the highest density parts of the central cores [such as L1544, with central densities of $\sim 10^6$ cm^{-3} within a 1000 AU in radius; see Keto and Caselli, 2010] are diluted within the *Herschel* beam.
Figure 2.5 shows the correlation between $N(c\text{-}C_3HD)/N(c\text{-}C_3H_2)$ and $N(H_2)$ for the starless core sample. We also included the $N(N_2D^+)/N(N_2H^+)$ ratio, calculated in Crapsi et al. [2005] for a direct comparison. The cores L1400K and L1400A were not part of this study, since there were no SPIRE images of these sources available.

No correlation is found between the deuteration level of both species and $N(H_2)$ among the starless cores. However, in L1544, we recognize a substantial increase in the deuteration of N_2H^+, as it was already visible in Figure 2.1. In Crapsi et al. [2005] there are three additional evolved pre-stellar cores (L183, L429 and L694-2), that show enhanced N_2H^+ deuteration with increasing $N(H_2)$. This indicates that indeed N_2H^+ is a late-type molecule and stays in the gas phase at high densities, while c-C_3H_2 is possibly depleted in the central regions, thus it stops tracing the central zone of the core where high levels of deuterium fractions are present. This is in agreement with our current understanding of the chemistry of c-C_3H_2, and its distribution across the pre-stellar core L1544 [Sipilä et al., 2016, see Figure A.17 in Appendix A.2].

Another way of testing this theory is to examine parameters that are related to the

Table 2.9: $N(H_2)$ values for the starless core sample, derived from the Herschel/SPIRE images, within a 40″ beam (this work), as well as the ones derived from the 1.2 mm continuum emission within a 11″ beam [Crapsi et al., 2005].

Starless Core	$N(H_2)$[a] (10^{21} cm^{-2})	$N(H_2)$[b] (10^{21} cm^{-2})
L1495	8.3 ± 1.6	31 ± 10
L1495B	10.1 ± 2.0	
L1495AN	15.1 ± 2.7	
L1495AS	22.1 ± 4.1	
TMC2	18.9 ± 3.3	60 ± 12
L1544	27.9 ± 5.1	94 ± 16
L1512	8.6 ± 1.6	
L1517B	11.5 ± 2.3	37 ± 10
CB23	8.5 ± 1.6	

[a] This work
[b] Crapsi et al. [2005]

kinematic of the gas, such as the width of the detected lines. Figure 2.6 shows the correlation between the observed linewidth, Δv_{obs}, of c-C_3H_2 ($3_{2,2} - 3_{1,3}$) and of N_2H^+ (1-0) among the starless and protostellar core sample. Thermal, turbulent and systematic motions contribute to the total Δv_{obs}. Thermal broadening does not play a substantial role, since the thermal linewidth of c-C_3H_2 is just 0.11 km s^{-1} at 10 K (and 0.13 km s^{-1} for N_2H^+). As we can clearly see in Figure 2.6, the observed c-C_3H_2 line has a larger width in most of the cores (except for L1495 and L1495AN, where the observed linewidths are approximately the same).

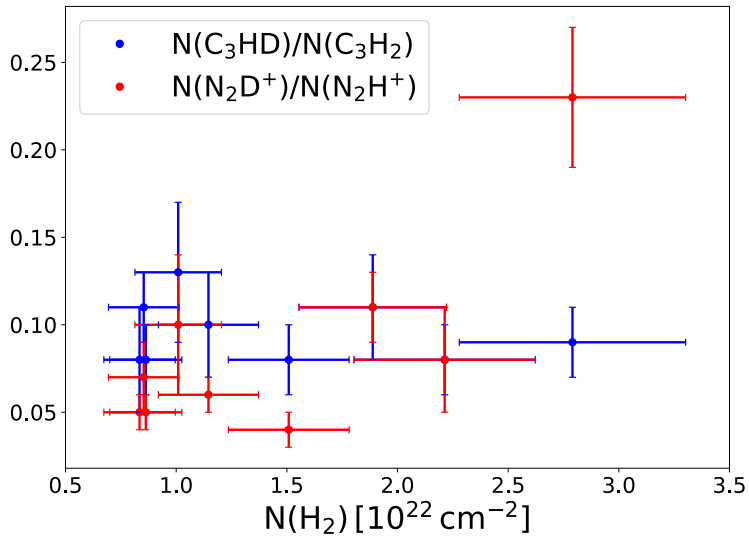

Figure 2.5: Deuterium fraction of c-C_3H_2 (blue dots) and N_2H^+ (red dots) as a function of central column density of H_2, measured with *Herschel* in the starless and pre-stellar core sample. The deuteration of N_2H^+ was calculated in Crapsi et al. [2005].

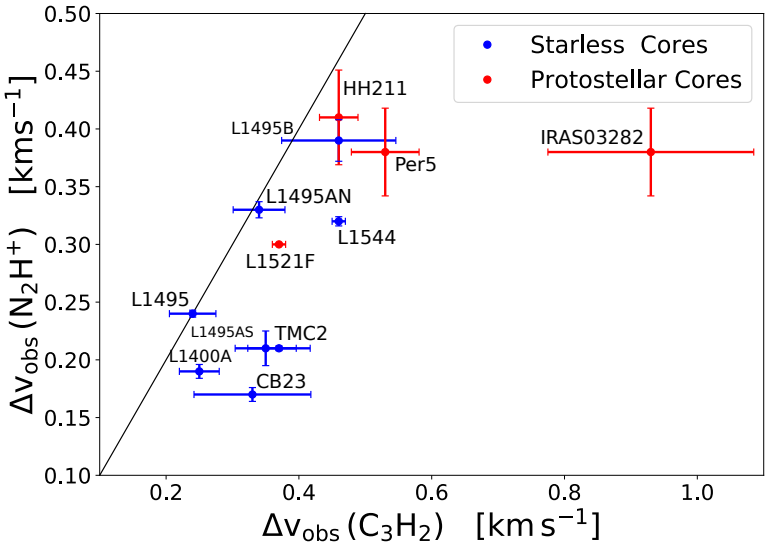

Figure 2.6: Observed linewidth of N_2H^+ [Crapsi et al., 2005, Emprechtinger et al., 2009] compared to that of c-C_3H_2 (this work) in the starless and protostellar core sample. The dashed line represents the 1:1 ratio.

This suggests that c-C_3H_2 traces a different region than N_2H^+, where turbulent or

systematic (i.e. rotation, infall or outflows in protostellar objects) motion dominates. In both starless and protostellar core samples we see the same trend by studying the linewidth of c-H^{13}CC$_2$H ($2_{1,2} - 1_{0,1}$) instead, suggesting that the optical depth broadening of c-C$_3$H$_2$ ($3_{2,2} - 3_{1,3}$) is negligible.

2.4.4 Correlation between deuteration and dust temperature

During the protostellar phase, the core starts to warm up the surrounding material leading to desorption of CO from dust grains. Moreover, the energetic ouflows by protostars can also contribute to the release of CO molecules in the gas phase via sputtering or grain-grain collisions [e.g. Caselli et al., 1997, Jiménez-Serra et al., 2008]. Back in the gas phase, CO can react and destroy H_2D^+, reducing the total deuteration in molecules. In addition, reaction 2.1 can proceed at high temperatures also in the backward direction, leading to a further reduction of H_2D^+. Therefore, one expects an anticorrelation between the deuteration and the dust temperature [e.g. Ladd et al., 1991, Myers and Ladd, 1993] of a protostar, as it has already been confirmed in previous works [Emprechtinger et al., 2009, Fontani et al., 2011]. In Figure 2.7 we plot the deuterium fraction of c-C$_3$H$_2$ against $T_{\rm Dust}$ in the protostellar core sample. The values for the $T_{\rm Dust}$ were taken from Emprechtinger et al. [2009]. As in §2.4.2, also here we include the protostar IRAS16293 [Schöier et al., 2002]. Figure 2.7 shows a clear anticorrelation between deuteration and $T_{\rm Dust}$, when excluding L1521F, that has a Kendall's τ coefficient of -0.74 with a significance p of 0.08 and a Spearman's ρ coefficient of -0.82 with a significance p of 0.09. The abundance ratio $N(c\text{-}C_3HD)/N(c\text{-}C_3H_2)$ peaks in the coldest source, HH211 at 23%, and decreases toward the warmer sources down to 8%.

The young source HH211 could be an example of a protostar where the accretion burst has recently happened and/or where ices have been recently evaporated. If this is the case, one way to interpret the large deuteration of c-C$_3$H$_2$ is the release of large amount of deuterated (and non-deuterated) c-C$_3$H$_2$ from the ices into the gas phase. Furthermore, this could imply significant deuteration of c-C$_3$H$_2$ on the surface of dust grains, maybe due to hydrogen-deuterium exchange reactions known to happen for other molecules, such as CH$_3$OH during the preceding cold pre-stellar phase [Parise et al., 2006, e.g.]. [4]

The result for L1521F deviates considerably from the rest of the sources. The dust temperature for L1521F ($T_{\rm Dust} = 9 \pm 2$ K) was taken from Kirk et al. [2005]. As already highlighted in §2.4.2, L1521F hosts a VeLLO which could be a protostar in very early stages of evolution and/or an example of low activity in protostellar evolution characterized by episodic accretion. This could explain the mismatch between the physical (low $T_{\rm Dust}$) and chemical conditions (low deuteration).

[4] Recent experiments of D-H exchanges carried out by Faure et al. [2015] suggest that D-H exchanges are made possible by hydrogen bonds between the hydroxyl functional groups of methanol and water ice. This makes it unlikely that such a process could work for c-C$_3$H$_2$, although experimental and theoretical work is needed to rule out this hypothesis.

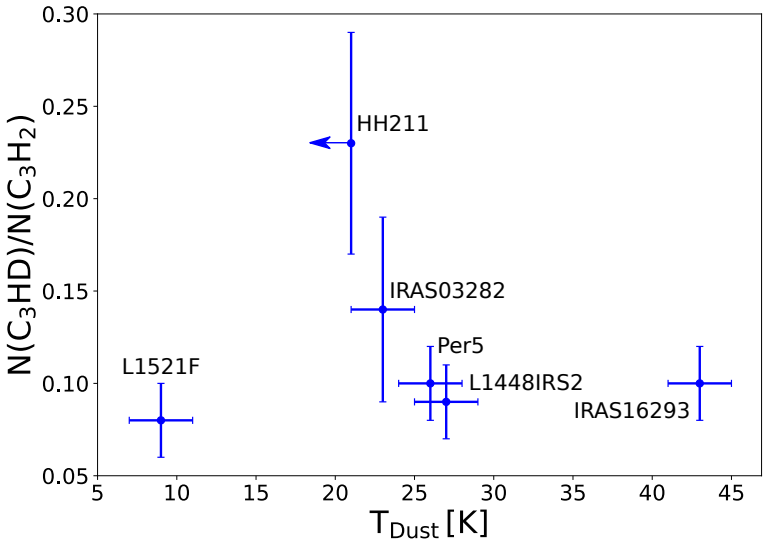

Figure 2.7: Deuterium fraction of c-C_3H_2 as a function of dust temperature $T_{\rm Dust}$ in the protostellar core sample, including the VeLLO L1521F.

2.5 Conclusions

In this work we presented single pointing observations of c-C_3H_2, the singly and doubly deuterated species, c-C_3HD and c-C_3D_2 as well as the isotopologue c-$H^{13}CC_2H$ toward 10 starless cores and 5 protostellar cores in the Taurus and the Perseus Complexes. The pre-stellar core L1544 and the protostellar core IRAS16293 were also included in our study. We calculated the deuterium fractionation $N(c\text{-}C_3HD)/N(c\text{-}C_3H_2)$ and studied its correlation with the CO depletion factor, the dust temperature and the H_2 column density toward the core centre. We also examined the differences between the deuteration of C- and N-bearing molecules. Here is a summary of our main conclusions:

- The ratio $N(c\text{-}C_3HD)/N(c\text{-}C_3H_2)$ is within the error bars equal to 10% in all starless and pre-stellar cores, where c-C_3HD has been detected. This also accounts for the protostars except for the source HH211 where we measure a high deuteration level of (23 ± 6)%. The $N(c\text{-}C_3D_2)/N(c\text{-}C_3H_2)$ ratio ranges from 0.4 to 1.5% in starless and pre-stellar cores, and from 0.6 to 3.6% among the protostellar cores. The deuteration of c-C_3H_2 and N_2H^+ follows the same trend in both samples. However, in case of the evolved pre-stellar core L1544, the deuteration of N_2H^+ is significantly higher (factor of 2.6) compared to the $N(c\text{-}C_3HD)/N(c\text{-}C_3H_2)$ ratio. This can be understood by the well-known fact that N_2H^+ remains in the gas phase even at densities of about $10^6\,{\rm cm}^{-3}$, where the C-bearing molecules (including c-C_3H_2 and its deuterated forms) are highly frozen and where deuterium fractionation proceeds fast, thanks to the large abundances of the deuterated H_3^+ isotopologues.

- Among the starless cores, we find no correlation between the deuteration of *c*-C_3H_2 and the CO depletion factor or the central H_2 column density (measured with *Herschel*). However, the N_2H^+ deuteration substantially increases toward L1544, which is the most evolved source within the starless core sample. This indicates that N_2H^+ traces the central dense core, unlike *c*-C_3H_2, which is more likely tracing an outer shell, surrounding the dense region of the pre-stellar core. This theory is also favoured by the fact that the observed linewidth of the *c*-C_3H_2 emission is larger than that of the N_2H^+ emission among the starless and the protostellar cores. As a consequence, the information resulting from observing *c*-C_3H_2 and N_2H^+ is complementary because they bring insights on different regions of the core.

- Among the protostellar cores, there is a tight anticorrelation between the deuteration of *c*-C_3H_2 and the dust temperature ($\tau = -0.74$ and $\rho = -0.82$), with the exception of L1521F. The $N(c\text{-}C_3HD)/N(c\text{-}C_3H_2)$ ratio drops with increasing $T_{\rm Dust}$, reaching the maximum value of 0.23 in the coolest source HH211 ($T_{\rm Dust} < 21$ K) and decreasing toward the warmest sources, down to a deuteration level of 0.08. The *c*-C_3H_2 deuteration does not correlate with the CO depletion factor within the protostellar core sample. L1521F differs substantially from the rest of the sources, showing in both species, *c*-C_3H_2 and N_2H^+, a low deuteration and at the same time a high depletion factor of 15 (see comment below for explanation).

- The high *c*-C_3H_2 deuteration of the youngest source HH211, might be the result of a recent evaporation of *c*-C_3H_2 and *c*-C_3HD, coming from a recent accretion burst. The timescale must be short enough to avoid the enhanced abundance of CO in the gas phase to significantly alter the *c*-C_3H_2 abundance and deuterium fraction. As similarly large values are not seen in the pre-stellar phase, deuteration processes taking place also on dust grains would be a possible scenario for the observed high deuteration of *c*-C_3H_2 in this young protostar.

- The source L1521F shows a peculiar behaviour, having a low deuteration of 0.08 in spite of a significant CO depletion factor ($f_d(\mathrm{CO}) = 15 \pm 3.6$) and a low dust temperature ($T_{\rm Dust} = 9 \pm 2$ K). The peculiarity of this source has been highlighted in other studies as well [Crapsi et al., 2005, 2004]. L1521F could be an episodically accreting low-mass protostar in a quiescent phase [Bourke et al., 2006, Takahashi et al., 2013]. The fact that it shows a low deuteration and dust temperature, while having a high CO depletion, might imply that after a recent burst, which heated dust and gas, the ortho-to-para-H_2 ratio possibly increased, thus slowing down the deuteration process in the now cold envelope.

Chapter 3

Rotational spectroscopy of the HCCO and DCCO radicals in the millimeter and submillimeter range

The content of this chapter was published in *Astronomy & Astrophysics Journal*.

3.1 Abstract

The ketenyl radical, HCCO, has recently been detected in the ISM for the first time. Further astronomical detections of HCCO will help us understand its gas-grain chemistry, and subsequently revise the oxygen-bearing chemistry towards dark clouds. Moreover, its deuterated counterpart, DCCO, has never been observed in the ISM. HCCO and DCCO still lack a broad spectroscopic investigation, although they exhibit a significant astrophysical relevance. In this work we aim to measure the pure rotational spectra of the ground state of HCCO and DCCO in the millimeter and submillimeter region, considerably extending the frequency range covered by previous studies. The spectral acquisition was performed using a frequency-modulation absorption spectrometer between 170 and 650 GHz. The radicals were produced in a low-density plasma generated from a select mixture of gaseous precursors. For each isotopologue we were able to detect and assign more than 100 rotational lines. The new lines have significantly enhanced the previous data set allowing the determination of highly precise rotational and centrifugal distortion parameters. In our analysis we have taken into account the interaction between the ground electronic state and a low-lying excited state (Renner-Teller pair) which enables the prediction and assignment of rotational transitions with K_a up to 4. The present set of spectroscopic parameters provides highly accurate, millimeter and submillimeter rest-frequencies of HCCO and DCCO for future astronomical observations. We also show that towards the pre-stellar core L1544, ketenyl peaks in the region where c-C_3H_2 peaks, suggesting that HCCO follows a predominant hydrocarbon chemistry, as already proposed by recent gas-grain chemical

models.

3.2 Introduction

The evolution of organic molecules from dark clouds to planetary systems is of fundamental importance to shed light on the astrochemical heritage of life on Earth [Caselli and Ceccarelli, 2012]. However, interstellar organic chemistry is still not fully understood [Herbst and van Dishoeck, 2009]. Complex organic species (hereafter COMs) have been widely detected in hot cores embedded in high-mass star forming regions [Cummins et al., 1986, Blake et al., 1987], and low-mass hot corinos [Cazaux et al., 2003, Bottinelli et al., 2004]. Their formation towards warm sources is well reproduced by the so-called "warm-up scenario" [Garrod and Herbst, 2006, Garrod, 2008], wherein COMs form on the surface of dust grains through radical-radical reactions and are eventually ejected to the gas-phase via thermal desorption during the warm-up phase of the protostar. Organic species, such as CH_3OCH_3, H_2CCO and CH_3OCHO have been detected also in cold, pre-stellar cores [Cernicharo et al., 2012, Bacmann et al., 2012, Vastel et al., 2014, Jiménez-Serra et al., 2016] but need other formation processes to justify their presence in the gas phase, since there is no rise in temperature toward a starless or a pre-stellar core ($T < 20\,K$). Pre-stellar cores are the initial phase of star formation right before gravitational collapse sets in, which ultimately leads to the birth of a protostar.

So far, there have been several chemical models [Vasyunin and Herbst, 2013a, Reboussin et al., 2014, Ruaud et al., 2015, Chang and Herbst, 2016] that try to reproduce the observed abundances of COMs toward pre-stellar cores. All of them include grain-surface reactions and non-thermal desorption processes. One of these studies was carried out by Vasyunin et al. [2017], in which organic species are formed on dust grains through ion-molecule as well as radiative association reactions, and released in the gas phase through reactive desorption. With a multilayer treatment of ice chemistry and a special approach to reactive desorption based on experimental studies of Minissale et al. [2016], the authors were able to reproduce the abundance of many COMs, like CH_3OH and $HCOOCH_3$, toward the pre-stellar core L1544. Recent work by Shingledecker et al. [2018] has shown that taking into account cosmic-ray proton bombardment of icy dust grain mantles in gas-grain chemical models also boost the formation of some COMs. Despite the progress that has been made in the last few years, there are still some important pieces of the puzzle missing to understand the interstellar organic chemistry taking place in dark clouds.

One of the missing pieces in oxygen-bearing chemistry has been ketenyl, HCCO, a possible building block of oxygen-containing COMs. HCCO was detected for the first time in two sources, Lupus-1A and L483 by Agúndez et al. [2015]. After including all known formation and destruction reactions of HCCO from the literature and the chemical databases, it was found that the main formation mechanism for HCCO is the reaction between OH and C_2H. Nevertheless, a discrepancy of three orders of magnitude between the observed and the predicted HCCO abundance implies that there is an effective formation mechanism of HCCO still unknown and which can compete against its depletion by reactions with neutral atoms

[Agúndez et al., 2015]. Previous studies [Hudson and Loeffler, 2013, Maity et al., 2014] had shown that ketene, H_2CCO, can be formed in ices after UV and electron irradiation, representing a possible formation path for HCCO as an intermediate product. In Wakelam et al. [2015b], the rate coefficient of the main HCCO formation pathway was increased by almost an order of magnitude based on the comparison to similar reactions. In doing so, their chemical model was able to reproduce the observed abundances of HCCO towards the sources Lupus-1A and L483. However, the reaction of interest, $OH + C_2H \rightarrow HCCO + H$, has never been studied before, neither theoretically nor experimentally, and there remains a large uncertainty behind HCCO chemistry. From the above considerations, it is evident that further observations are needed to revise the gas-grain chemistry of HCCO. Moreover, deuterated ketenyl, DCCO, has never been detected in the ISM and its spectral line catalog is not yet available in the online databases. The interstellar detection of DCCO would give information about possible deuteration routes of HCCO, and put more constraints on current gas-grain chemical models.

The laboratory spectrum of HCCO was first measured by photoionisation mass spectroscopy [Jones and Bayes, 1972] targeting the reactions

$$C_2H_2 + O \rightarrow HCCO + H \tag{3.1}$$
$$\rightarrow CH_2 + CO. \tag{3.2}$$

where channel (1) is more than two times faster than reaction (2) throughout a broad range of temperatures [Michael and Wagner, 1990]. Follow-up work was done by Endo and Hirota [1987], where pure rotational lines of HCCO ($N = 15 - 18$) and DCCO ($N = 17 - 20$) were measured in the 320-390 GHz range. Their analysis showed a considerable interaction between the ground state and a low-lying excited state (Renner-Teller pair), which leads to a strong perturbation of the spin-rotation splitting. In another work done by Ohshima and Endo [1993], HCCO was studied in the microwave spectral region in a supersonic jet expansion. In particular, the fine and hyperfine components of the $N = 1 - 0$ transition were measured at around 21 GHz, enabling the determination of the hyperfine coupling constants ascribed to the hydrogen nucleus. A further study by Szalay et al. [1996] involved the ab initio calculations of rotational constants, equilibrium geometries and excitation energies of the ground and excited electronic states of HCCO. Their results are in good agreement with the values obtained from the microwave and millimeter measurements.

In this work we have recorded the pure rotational spectra of HCCO and DCCO between 170 and 650 GHz, extending substantially the frequency range compared to the previous studies mentioned above. More than 100 lines were recorded and assigned for each isotopologue, reducing the errors of the rotational and centrifugal distortion constants down by a factor of ~ 40. With this new data set we are able to provide highly accurate rest-frequencies for future astronomical millimeter observations.

3.3 Laboratory Experiments

In the present work, the rotational spectra were taken with the frequency-modulation mm/sub-mm Absorption Cell spectrometer developed at the Center for Astrochemical Studies (CASAC) in Garching. A full description of the experiment can be found in Bizzocchi et al. [2017]. This instrument consists of an absoprtion cell made of a Pyrex tube (3 m long and 5 cm in diameter), which serves as the main flow cell. Each end is equipped with one stainless steel electrode in order to apply a high voltage and ignite a discharge, creating a plasma from the appropriate mixture of gaseous precursors. To stabilize the plasma and minimize the collisions between the species, the outer walls of the cell are cooled with liquid nitrogen.

As a radiation source we use an active multiplier chain (Virginia Diodes, Inc.) which is coupled to a synthesizer (Keysight E8257D) operating at centimeter wavelengths. By applying additional frequency multipliers, the radiation source can cover continuously the 82-1100 GHz frequency range. High phase accuracy is achieved by phase locking the synthesizer with an external 10 MHz rubidium clock (Stanford Research Systems). For the detection of the molecular signal we use a liquid-He-cooled InSb hot electron bolometer (QMC Instruments Ltd.). The signal is frequency-modulated with a sine wave of 15 kHz, while the output detector signal is demodulated at $2f$ (where f denotes the modulation frequency) by a lock-in amplifier (Standford Research Systems SR830), meaning that we record the second derivative of the actual absorption line.

HCCO and DCCO were produced by a DC high-voltage plasma ($\sim 11\,\mathrm{mA}$, $\sim 0.6\,\mathrm{kV}$) of a 2:1 mixture of O_2 and C_2H_2/C_2D_2 diluted in a buffer gas of Ar (total pressure $\sim 28\,\mathrm{mTorr}$). The freezing point of acetylene C_2H_2 provides a lower limit of the cooling temperature of the cell at around 190 K.

3.4 Results and data analysis

HCCO and DCCO have a $^2A''$ ground electronic state with one unpaired electron at the carbon nucleus, showing paramagnetic nature [1]. Both species show a rich rotational spectrum with fine (spin-rotation interaction) and hyperfine structure (H/D nuclear spin). In addition, the ground state rotational constants determined in Endo and Hirota [1987] led to inertia defects of 0.155(15) and 0.120(4) amu Å for HCCO and DCCO, respectively, confirming the planarity of the species. The dipole moment along the a axis has been determined by Szalay et al. [1996] to be 1.59 D and by Jerosimić [2007] to be 1.68 D. We have adopted the second value for the predictions of the line intensities. The total dipole moment is only marginally larger than its a component. We detected 114 and 138 new lines for HCCO and DCCO, respectively. These are a-type rotational transitions, with N ranging from 8 to 27 for HCCO and with $N = 9 - 33$ for DCCO with a maximum K_a of 4. We have modeled the frequency-modulated absorption lines using an in-house code that

[1] The ketenyl radical is a quasilinear molecule in the ground state with an ∠HCC angle of 135° and a ∠CCO angle of 169° [Szalay et al., 1996].

implements the $2f$ Voigt profiles presented by Dore [2003]. The estimated accuracy on the central frequency depends on the signal-to-noise ratio, the line width and the baseline (mainly caused by standing waves formed between the two windows placed at each end of the absorption cell), and ranges between 25-75 kHz by our estimates. In Figure 5.3 we show plots of HCCO and DCCO lines, as well as the corresponding fitted profiles.

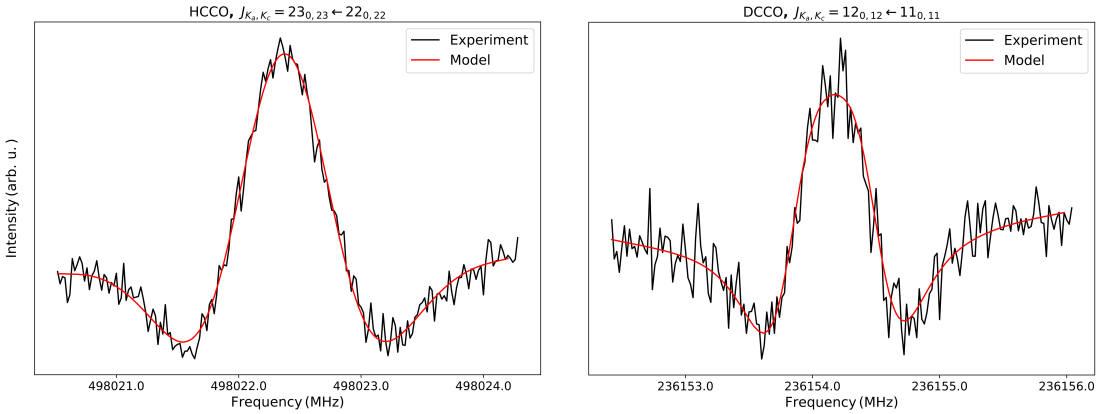

Figure 3.1: (*Left panel*) Recording of the $J_{K_a,K_c} = 23_{0,23} - 22_{0,22}$ transition of HCCO. Total integration time is 309 s with a time constant of 3 ms. (*Right panel*) Recording of the $J_{K_a,K_c} = 12_{0,12} - 11_{0,11}$ transition of DCCO. Total integration time is 127 s with a 3 ms time constant. The red curves represent our modeled $2f$ Voigt profiles (see text).

The initial prediction for new rotational transitions of HCCO and DCCO was done based on the spectroscopic constants determined previously by Endo and Hirota [1987]. The spectral analysis was done using the Pickett SPFIT/SPCAT suit of programs [Pickett, 1991], applying a S-reduced, asymmetric rotor Hamiltonian [Watson, 1977]:

$$\mathrm{H} = \mathrm{H_{rot}} + \mathrm{H_{sr}} + \mathrm{H_{hfs}}, \tag{3.3}$$

where H_{rot} describes the rotational energy of the molecule, H_{sr} the spin-rotation interaction and H_{hfs} the hyperfine coupling. The spin-rotation interaction arises from the spin dipole moment of the unpaired electron that interacts with the magnetic field generated by the rotation of the molecule. The hyperfine coupling was only included for HCCO, since its hyperfine splitting was already resolved in Ohshima and Endo [1993], unlike DCCO. The hyperfine coupling involves two constants: the Fermi contact interaction b_F and the dipolar interaction c. The Fermi contact interaction describes the magnetic coupling between the unpaired electron and the hydrogen nucleus, indicating the overlap of the unpaired spin on the nucleus. The dipolar coupling depends only on the orientation of the unpaired electron with respect to the hydrogen nucleus, meaning that constant c is structure dependent [Ohshima and Endo, 1993].

The previous study by Endo and Hirota [1987] had shown that the observed spin splittings of the $K_a = 2$ and $K_a = 3$ lines are much smaller than those expected from the

Table 3.1: Spectroscopic parameters determined for HCCO and DCCO.

Constants (MHz)	HCCO[b]	HCCO[c]	DCCO[b]	DCCO[c]
A	1046955.(1682)	1243000.(45000)	652933.(410)	652100.(3600)
B	10896.7954(16)	10896.788(41)	9926.7979(12)	9926.8008(104)
C	10766.0154(23)	10766.466(39)	9755.2295(11)	9755.2316(126)
D_N	0.0038207(13)	0.003861(21)	0.0035141(15)	0.0035088(34)
D_{NK}	-0.2536(24)	0.2376(26)	-1.67334(82)	-1.6724(123)
D_K	30475.(528)	18480.(1200)	3952.(264)	5000.
d_1	-0.00008151(65)	-0.000119(34)	-0.00024091(40)	-0.0002431(73)
d_2	-0.00004013(90)	0.0000201(101)	-0.00005828(90)	-0.0000649(43)
H_{KN}	-0.191900(924)	-0.01185(24)	0.037735(302)	0.0375(45)
H_K	352.(14)	-	-	-
L_{KKN}	0.020538(108)	-	-0.0106543(349)	-0.01059(52)
P_{KKKN}	-0.00069701(376)	-	0.00039998(121)	0.0003971(176)
ϵ_{aa}	-247917.6(69)	-247827.(74)	-112219.2(33)	-112201.(34)
ϵ_{bb}	-43.128(60)	-43.1(27)	-30.655(74)	-30.62(85)
ϵ_{cc}	13.322(60)	13.8(27)	10.225(65)	10.20(69)
$(\epsilon_{ab}+\epsilon_{ba})/2$	529.4(77)	1619.(53)	276.28(99)	275.(31)
D_N^S	-0.000086(60)	-0.00920(178)	0.000519(31)	0.00041(65)
D_{NK}^S	2.405(36)	1.52(36)	-1.698(18)	-1.589(191)
D_{KN}^S	-17.66(31)	-4.68(141)	5.180(76)	4.71(65)
D_K^S	-53.61(66)	953.1(53)	1.75(34)	826.7(21)
d_1^S	-0.000056(44)	-0.00520(141)	0.000316(23)	0.00025(44)
H_K^S	-23.320(60)	-27.386(169)	-21.6652(164)	-21.628(89)
H_{KNK}^S	0.1425(41)	-	-	-
b_F	-54.0304(46)	-54.030(24)[d]	-	-
c	16.029(18)	16.041(92)[d]	-	-
σ	0.059	0.125	0.064	0.029
σ_w	1.15	-	1.18	-
No. of lines	168	54	193	55

[a] Values in parentheses are 1σ uncertainties, expressed in units of the last quoted digit. σ_w denotes the weighted root mean square deviation.
[b] This work
[c] Endo and Hirota [1987]
[d] Ohshima and Endo [1993]

Table 3.2: Spin-rotation constants $\epsilon_{aa}(K)$ determined for HCCO and DCCO.

Constants (MHz)	HCCO	DCCO
$\epsilon_{aa}(K=0)$	-247917.6(69)	-112219.2(33)
$\epsilon_{aa}(K=1)$	-157486.3(22)	-89141.7(18)
$\epsilon_{aa}(K=2)$[a]	-112607.9(31)	-71781.2(21)
$\epsilon_{aa}(K=3)$[a]	-83405.9(23)	-56987.9(16)
$\epsilon_{aa}(K=4)$[a]	-60804.3(16)	-43191.0(12)

[a] Computed from the $\epsilon_{aa}(K=0)$ value. See text for explanation.

$K_a = 1$ lines. This peculiar behaviour is caused by the Renner-Teller coupling (see Appendix B.1.1), whereby a special case of vibronic coupling is cancelling the degeneracy of the electronic state $^2\Pi_u$, which subsequently splits to an excited, linear component, $1^2A'(1^2\Pi)$, and a ground, bent component, $1^2A''(1^2\Pi)$. The low lying excited state interacts with the ground state, which leads to a non-negligible perturbation of the rotational levels. As a result, a conventional power series of the spin-rotation constant $\epsilon_{aa}(K)$ is not sufficient to reproduce the anomalous K-dependence. In order to include this distortion in the analysis, Endo and Hirota [1987] adopted a Pade-type formula given by:

$$\epsilon_{aa}(K) = \epsilon_{aa}(K=0)/(1 + t \cdot K), \tag{3.4}$$

allowing the prediction and assignment of transitions with K_a up to 4. The parameter t corresponds to $\omega/\Delta E$, where ω describes the bending vibration frequency and ΔE the electronic energy of the excited state (see work from Endo and Hirota [1987] for further explanation). In order to take into account the energy perturbation mentioned above, we calculated one effective spin-rotation constant $\epsilon_{aa}(K)$ for every K transition according to Equation 3.4, using the t value inferred by Endo and Hirota [1987]. Thus, we defined five separate ϵ_{aa} constants in the input file of the fitting program, where $\epsilon_{aa}(K=0)$ is applied to all transitions with $K_a = 0$, $\epsilon_{aa}(K=1)$ is applied to all transitions with $K_a = 1$, and so on. After including all the lines, we were able to fit $\epsilon_{aa}(K=0)$ and $\epsilon_{aa}(K=1)$ while keeping the remaining epsilon parameters fixed. We also set the relation between $\epsilon_{aa}(K=0)$ and the other epsilon parameters for $K = 2, 3, 4$ constant. This means that $\epsilon_{aa}(K=2,3,4)$ are changed with respect to the fitted $\epsilon_{aa}(K=0)$ parameter, following Equation 3.4. The application of the Pade-type expansion for $\epsilon_{aa}(K)$ allows us to fit and predict rest frequencies for transitions with K_a up to 4 and an accuracy well suited for astrophysical needs. Without this approach we were only able to predict lines up to $K_a = 2$.

The final fits include our new measured lines as well as those measured in the previous studies mentioned above. In case of HCCO, there were two transitions, $J_{K_a,K_c} = 15_{3,12} - 14_{3,11}$ and $J_{K_a,K_c} = 16_{3,13} - 15_{3,12}$, measured by Endo and Hirota [1987], which were

considerably deviating from the predicted frequencies ($\sim$ 300 kHz). For this reason, we have re-measured these two lines in the laboratory to search for possible misassignments. However, since the discharge of acetylene and oxygen leads to the production of numerous species (other than HCCO), the resulting spectra had various lines, that were partially blended with the HCCO features, making the line assignment rather difficult. In the end, we were able to measure and assign the $J_{K_a,K_c} = 16_{3,13} - 15_{3,12}$ transition, which is in better agreement with the prediction than the one measured by Endo and Hirota [1987].

For both species, the final fits allowed us to determine all the quartic centrifugal distortion constants, one sextic parameter, H_{KN}, as well as all the quartic and one sextic spin-rotation constant, H_K^S [2]. The resulting parameters are listed in Table 1. For the HCCO spectral analysis we additionally included one sextic constant H_K, one octic, L_{KKN}, and one decadic constant, P_{KKKN}, along with one sextic spin-rotation parameter, H_{KNK}^S, compared to the previous fit done by Endo and Hirota [1987]. Adding these extra parameters has considerably improved the fit, resulting in a root mean square (rms) deviation of 59 kHz, which is an improvement of a factor $\sim$ 2 compared to the previous fit by Endo and Hirota [1987] (rms =125 kHz).

Strong correlations between H_K, L_{KKN}, P_{KKKN} and other constants modify the final values of some rotational parameters with respect to Endo and Hirota [1987]. In particular, the introduction of L_{KKN}, P_{KKKN} has a significant impact on the constants d_1^S, $(\epsilon_{ab}+\epsilon_{ba})/2$, D_N^S, H_{KN} and D_{NK}, with correlation coefficients ranging from 82% to 99%. This also results in a sign change for D_{NK}, d_2 and D_K^S compared to the previous published results [Endo and Hirota, 1987]. Nevertheless, these high-order centrifugal distortion corrections are critical to reproduce our spectral data within the experimental accuracy: by using a smaller set of constants the obtained rms is increased up to several MHz. An accurate determination of the rotational constants would require a full analysis of both interacting states ($1^2A'(1^2\Pi)$ and $1^2A''(1^2\Pi)$), which is beyond the scope of this work.

The spectral analysis of DCCO resulted to a root mean square deviation of 64 kHz. Also here the rotational parameters are more strongly constrained in our fit (see for example constants $(\epsilon_{ab}+\epsilon_{ba})/2$ and D_N^S) compared to Endo and Hirota [1987]. In addition, we were able to determine D_K, unlike Endo and Hirota [1987], where the constant had previously been kept fixed to 5000 MHz. In case of D_K^S we note a considerable difference of a factor of $\sim$ 500 between our and the previous study. Since there is a correlation between the constants D_K and D_K^S of $\sim$ 50%, we do expect a change in D_K^S by fitting D_K.

Table 2 shows a summary of the $\epsilon_{aa}(K)$ constants for HCCO and DCCO determined in this work. A list with all the experimental frequencies is available at the CDS as supplementary data.

3.5 Astrochemical Relevance

In cold environments with a gas temperature of 10 K or lower (such as Lupus-1A and L483, where HCCO has been detected), the Boltzmann distribution for HCCO and

[2]The order of the rotational constant refers to which power of J the energy contributions depend on.

Table 3.3: Spin-rotation constants $\epsilon_{aa}(K)$ determined for HCCO and DCCO.

Constants (MHz)	HCCO	DCCO
$\epsilon_{aa}(K=0)$	-247917.6(69)	-112219.2(33)
$\epsilon_{aa}(K=1)$	-157486.3(22)	-89141.7(18)
$\epsilon_{aa}(K=2)$[a]	-112607.9(31)	-71781.2(21)
$\epsilon_{aa}(K=3)$[a]	-83405.9(23)	-56987.9(16)
$\epsilon_{aa}(K=4)$[a]	-60804.3(16)	-43191.0(12)

[a] Computed from the $\epsilon_{aa}(K=0)$ value. See text for explanation.

DCCO peaks at around 100 GHz. With the present results we are able to reduce the predicted uncertainties down to 5-14 kHz at this frequency range (for HCCO and DCCO, respectively), opening the possibility for astronomical observations towards cold sources, such as starless and pre-stellar cores, which are characterized by narrow emission lines. Table 3.4 lists five DCCO transitions with $K_a = 0$ that could be relevant for observations of cold sources in the 3 mm range.

Table 3.4: Spectroscopic parameters of DCCO transitions relevant at low temperatures ($\sim$ 10 K).

Transitions J_{K_a,K_c}	Frequency (MHz)	Accuracy (kHz)	$E_{\rm up}$[a] (K)	A_{ul}[a] (10^{-5}s^{-1})	g_u[a]
$4_{0,4} - 3_{0,3}$	78721.6685	14.4	9.45	0.71	10
$5_{0,5} - 4_{0,4}$	98402.4782	14.4	14.18	1.42	12
$6_{0,6} - 5_{0,5}$	118082.6947	14.4	19.85	2.50	14
$7_{0,7} - 6_{0,6}$	137762.1984	14.4	26.46	4.01	16
$8_{0,8} - 7_{0,7}$	157440.8700	14.4	34.03	6.03	18

[a] $E_{\rm up}$ is the upper state energy, A_{ul} is the Einstein coefficient of the corresponding transition and the upper state degeneracy is given by g_u.

Further HCCO detections towards cold sources will help us clarify the gas-grain chemistry of this species in the early phase of star formation. As already mentioned in the introduction, HCCO is believed to be formed mainly in the gas-phase, via the reaction of C_2H with OH. A first step towards understanding the HCCO interstellar chemistry would be to search for a correlation between HCCO and its main precursor C_2H. An ideal candidate for this purpose is the well-studied, evolved pre-stellar core, L1544. The chemical structure

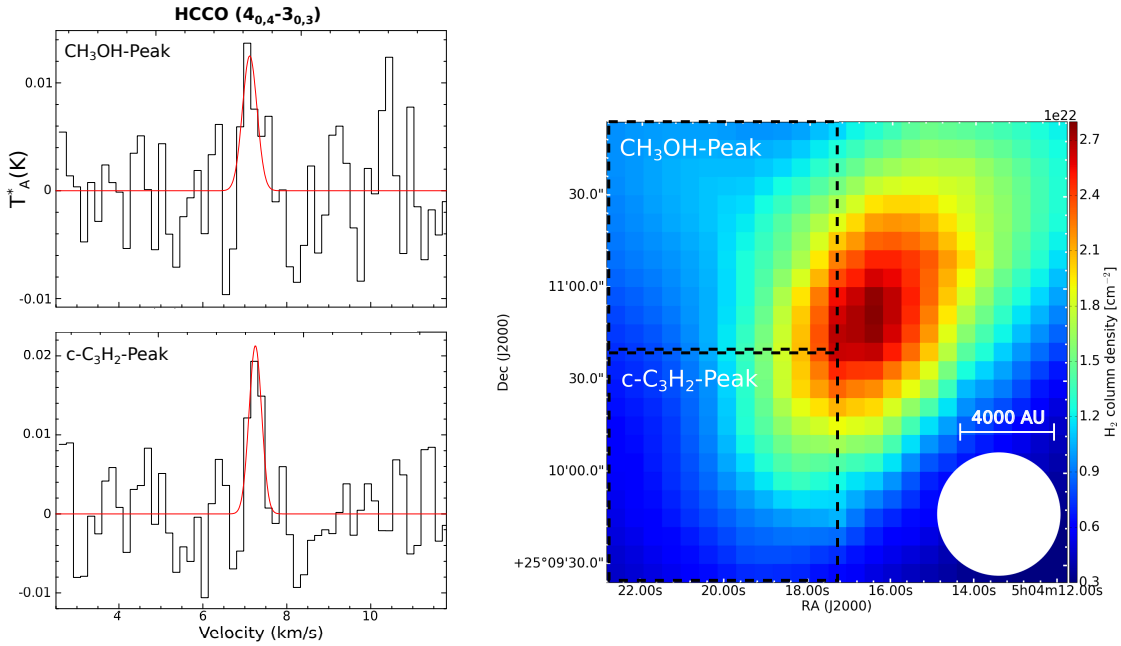

Figure 3.2: Map of the H_2 column density derived from far-infrared images taken by *Herschel* [Spezzano et al., 2016]. The dashed squares cover 40″ in the x- and y- direction and indicate the regions where the molecules *c*-C_3H_2 and CH_3OH peak. The white circle represents the beam of the *Herschel*/SPIRE instrument. On the left part of the figure we show the resulting spectra of the $J_{K_a,K_c} = 4_{0,4} - 3_{0,3}$ transition of HCCO averaged over the dashed squares. The red line plots the CLASS Gaussian fit.

of the source L1544 was studied in Spezzano et al. [2017] through molecular maps. In particular, the authors investigated the spatial distribution of 22 different molecules, and came to the conclusion that different parts of the source favour the formation of either carbon-, nitrogen or oxygen-bearing molecules. *c*-C_3H_2 and other carbon-chain molecules like H_2CCC and C_3H, have their emission peak in the south-east part of the core, while oxygen-bearing species, such as CH_3OH, HCO and SO peak towards the north-east part of the dust continuum peak. In addition, HNCO (as well as CH_3CCH, CH_2DCCH and CH_3CCD) peaks towards the north-west part of the core. The right part of Figure 3.2 shows the H_2 column density map in L1544, which was derived by the far-infrared images taken with *Herschel*/SPIRE [Spezzano et al., 2016]. We used the data by Spezzano et al. [2017] to search for an HCCO line at 86.6 GHz. For the data processing we employed the software CLASS from the GILDAS[3] package [Pety, 2005]. Since the HCCO detections are very weak ($\sim$ 10 mK), we chose to average its spectrum over two large regions that contain either the *c*-C_3H_2 or CH_3OH peak, and cover 40″ in the x- and y-direction, respectively. These regions are marked by the dashed squares in Figure 3.2. The center of the map is positioned at the 1.3 mm dust peak [Ward-Thompson et al., 1999].

[3]http://www.iram.fr/IRAMFR/GILDAS

As it can be seen on the left part of Figure 3.2, HCCO peaks towards the region where c-C_3H_2 peaks, while the line intensity decreases by almost a factor of 2 towards the CH_3OH peak.This is a clear evidence that HCCO follows a different chemistry than other oxygen-bearing species, showing instead a predominant hydrocarbon chemistry. This favours the fact that C_2H is chemically related to HCCO. However, higher-sensitivity observations are needed to prove this point and constrain the gas-grain chemical models.

3.6 Chemical Model

The chemical model that we apply is based on the model developed by Vasyunin and Herbst [2013a] with several minor updates in grain-surface chemistry (Vasyunin et al. 2019, in prep.), and includes a gas-grain chemical network with 6000 gas-phase reactions, 200 surface reactions and 660 species. The gas-phase and grain surface chemistry are connected by accretion and desorption processes. The code numerically integrates chemical rate equations and gives a set of time dependent abundances of all chemical species for a time span that the user chooses. We use typical conditions of a cold dark cloud with a gas and dust temperature of 10 K, a visual extinction of 30 magnitudes, a proton density of $2 \cdot 10^4\,\mathrm{cm}^{-3}$ and a cosmic ionization rate of $1.3 \cdot 10^{-17}\,\mathrm{s}^{-1}$. As initial atomic abundances we use the ones reported in Wakelam et al. [2015b]. In addition, we include all the known formation and destruction reactions for HCCO available in the literature and the KIDA (KInetic Database for Astrochemistry) online database [Wakelam et al., 2015a]. In order to simulate the HCCO chemistry, the model is run with steady physical conditions and integrated over 10^7 years. As already reported in previous studies [Agúndez et al., 2015, Wakelam et al., 2015b], we find that the main formation pathway of HCCO in the gas-phase is the reaction of C_2H with OH, while the most effective reaction on grain surfaces is $\mathrm{s-H + s-CCO \rightarrow s-HCCO}$. For the reaction $\mathrm{OH + C_2H \rightarrow HCCO + H}$ we use a rate coefficient of $2 \cdot 10^{-10}\,\mathrm{cm}^3\,\mathrm{s}^{-1}$, as proposed in Wakelam et al. [2015b].

In the end, our simulations are able to reproduce the observed abundance of HCCO for times between 10^5 and 10^6 yr, reaching a maximum abundance of $5.6 \cdot 10^{-11}$. Nevertheless, a theoretical and/or an experimental study of the main formation pathway $\mathrm{OH + C_2H \rightarrow HCCO + H}$ is still needed for a better interpretation of the chemical simulations.

3.7 Conclusions

This work describes a rotational analysis of the ketenyl radical, HCCO, and its deuterated counterpart DCCO. For each isotopologue we measured and assigned more than 100 lines. We extended the measurements up to $\sim$ 650 GHz, which helped us improve the determination of the spectroscopic parameters with respect to the previous study by Endo and Hirota [1987]. In particular, we measured the rotational transitions with N ranging from 8 to 27 for HCCO and with $N = 9 - 33$ for DCCO with a maximum K_a of 4.

- For both species we were able to determine all the quartic centrifugal distortion constants, one sextic parameter, H_{KN}, as well as all the quartic and one sextic spin-rotation constant, H_K^S.

- We expanded the centrifugal distortion analysis of HCCO by including a sextic constant H_K, an octic, L_{KKN}, and one decadic constant, P_{KKKN}, along with one sextic spin-rotation parameter, H_{KNK}^S. This extended set of parameters reduced the rms deviation by a factor of ~ 2 with respect to the previous fit by Endo and Hirota [1987]. We also decreased the uncertainty on the rotational constants up to a factor of ~ 40.

- We show that towards the pre-stellar core L1544, HCCO peaks within the region where c-C_3H_2 peaks, suggesting that the ketenyl formation is based predominantly on hydrocarbon chemistry.

- The spectral analysis of DCCO resulted to a rms deviation of 64 kHz. The rotational parameters are more strongly constrained in our fit with respect to Endo and Hirota [1987]. We provide for the first time a catalog of highly accurate frequencies for DCCO (uncertainties at 3 mm $\sim$ 15 kHz), which allows a future DCCO detection in cold sources, like starless and pre-stellar cores.

Chapter 4

The Supersonic Jet Experiment

The Supersonic Jet Experiment is a new spectrometer that has been developed at the Center of Astrochemical Studies in Garching with the aim of studying unstable species in the millimeter and submillimeter range. The supersonic expansion of a selected gas mixture into a vacuum chamber results in strong rotational cooling of the molecular species, reaching very low temperatures (down to ~ 5 K), which are typical for interstellar environments. Isolated in a collision-free molecular beam, ions and radicals are stabilized and become available for spectroscopic studies.

4.1 Introduction

In this experiment a gas sample is injected with a high pressure ($P_0 > 1$ bar) through a pulsed valve into a vacuum chamber where it experiences very low pressures down to $P_b \sim 10^{-8}$ bar. At such large pressure gradients there is almost no heat transfer taking place, meaning that the thermal/internal energy of the species inside the mechanical valve almost entirely converts into the expansion energy of the molecular gas. Thus, the gas flow can be treated as an adiabatic expansion, which leads to a dramatic rotational cooling of the molecular species down to a few Kelvin. This process is illustrated in Fig. 4.1. The molecular thermal motion within the valve transforms into a strongly confined translational movement, leading to very narrow velocity distibutions and therefore substantially decreasing the Doppler broadening. The resulting cooling effect leads to a significant decrease of the local speed of sound v_s of the expanding gas, since $v_s \sim \sqrt{T}$. The Mach number, M, on the other hand, which is given by the ratio of the flow velocity v_f to the local speed of sound v_s, is increasing, and thus the expanding gas reaches locally supersonic velocity. In particular, there is a region within the jet expansion, where the density reduces to such a low level, that molecules are stabilised in a nearly collision-free environment called the *zone of silence*. Here, the molecular flow is travelling with supersonic velocity ($M \gg 1$), without being influenced by the warm background gas.

The interaction of the molecular jet with the background gas is, however, disturbing the gas expansion in vertical and horizontal direction to the centerline of the beam, causing

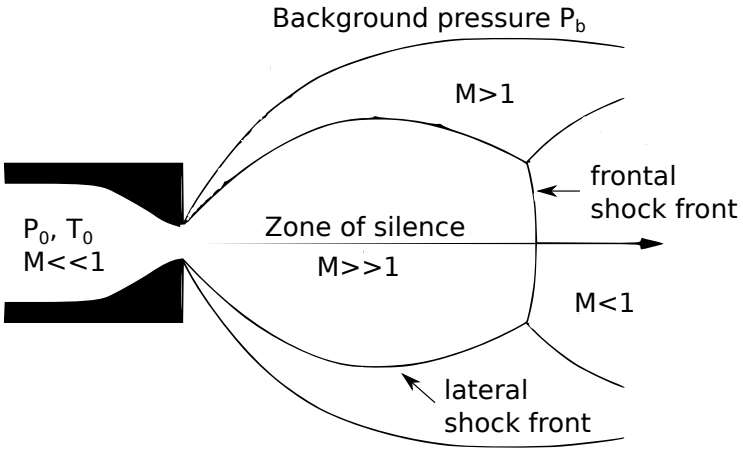

Figure 4.1: The supersonic jet expansion. In the so-called zone of silence the molecular flow is nearly collision-free and travels with supersonic velocity. The interaction of the jet with the background gas leads to the formation of lateral and frontal shock fronts with respect to the centerline of the beam [Scoles, 1988].

a rapid deceleration of the molecules. Expansion waves are reflected at the jet boundary, forming a lateral shock zone, also called barrel shock, as well as a frontal shock front, known as the Mach disk. The location of the Mach disk determines the expansion length x_m of the jet and is given by the following relation:

$$\frac{x_m}{d} = 0.67 \cdot \sqrt{\frac{P_0}{P_b}}, \tag{4.1}$$

with d being the diameter of the valve's orifice, P_0 the source pressure and P_b the background pressure inside the vacuum chamber. The above formula indicates that a high pressure ratio results in an elongated jet expansion, which means a larger absorption length and thus a stronger molecular signal. The relation for an adiabatic thermodynamic process of the expanding gas is described as:

$$\frac{T}{T_0} = \left(\frac{P_b}{P_0}\right)^{\frac{\gamma-1}{\gamma}} \quad \text{with} \quad \gamma = \frac{c_P}{c_V} = \frac{f+2}{f}, \tag{4.2}$$

where $c_{P,V}$ is the specific heat capacity at constant pressure and volume, respectively, and f the degree of freedoms of the investigated gas. For all gases with $\gamma = \frac{5}{3}$ and with $\frac{x_m}{d} \gg 1$, the Mach number M is given by [Scoles, 1988]:

$$M = 3.232 \cdot \left(\frac{x_m}{d}\right)^2. \tag{4.3}$$

This relation is only valid in the *zone of silence* with $M \gg 1$. Using Eq. 4.2 we obtain for the jet temperature T according to Scoles [1988] the following expression:

$$\frac{T}{T_0} = \left(1 + \frac{\gamma-1}{2}M^2\right)^{-1}. \tag{4.4}$$

The production and spectroscopic study of interstellar COMs in a cold molecular beam has proven to be beneficial for several reasons. The resulting low temperatures lead to the population of the lowest rotational levels, which simplifies dense and complex rotational spectra and subsequently makes spectral assignment easier. In addition, the collisions between molecules in a cold molecular beam are minimized, thus stabilizing sensitive and highly reactive molecules. In other words, once the molecules of interest are formed they are frozen-out within the jet, without being able to further react. Finally, the reduced Doppler broadening is significantly enhancing the achieved spectral resolution.

4.2 Experimental set up

In this section I will discuss the experimental set up of our supersonic jet experiment and show in greater detail the main components of the instrumentation. A simple schematic figure of our experiment is illustrated in Fig. 4.2.

As a radiation source we use a frequency synthesizer (Keysight E8257D), which generates a maximum signal frequency of 67 GHz and is synchronized to a 10 MHz rubidium frequency clock (Standford Research Systems), that provides a high frequency and phase stability of the electrical signal. The output signal of the synthesizer is then coupled into an amplifier multiplier chain (AMC, Virginia Diodes Inc.) that covers a frequency range of 75-1100 GHz. The (sub)mm radiation is subsequently focused through a high density polyethelen (HDPE) lens onto a wire-grid polarizer, which in turn reflects the radiation onto a so-called rooftop reflector, placed within the vacuum chamber. In the center of the rooftop reflector we have mounted the mechanical pulsed valve that ejects a selected gas mixture into the chamber. The chamber is sealed on the radiation side with a teflon window. The application of teflon and HDPE components allows for a high transmission of the radiation in the mm- and (sub)mm range and thus minimizes the power losses. The rooftop reflector consists out of two flat rectangular mirrors, that are placed perpendicularly to each other. The reflector has a inclination angle of 45° with respect to the beam direction, which in turn causes a 90° shift in the polarisation of the incoming light. This polarisation shift enables the reflected radiation to simply pass through the wire-grid polarizer and be focused with the help of a second HDPE lens on the detector. With the above geometry the radiation propagates coaxially to the jet, probing the molecular beam twice. This arrangement reduces the Doppler broadening, as it removes the Doppler effect caused by the molecular velocity component, that is perpendicular to the beam direction [Park et al., 2011]. In addition, since the molecular beam is probed twice, we increase the absorption length, and thus the signal intensity. The parallel and antiparallel propagation of the radiation to the jet leads to two lines in our spectrum, resulting from the positive and negative frequency shift caused by the Doppler effect (see Fig. 4.2). The actual transition frequency of the molecule corresponds to the average value of the two Doppler-shifted frequencies.

For the preparation of our gas mixture we use four mass flow controllers (MKS Instruments), each of them being connected to a sample bottle. The flow controller units keep

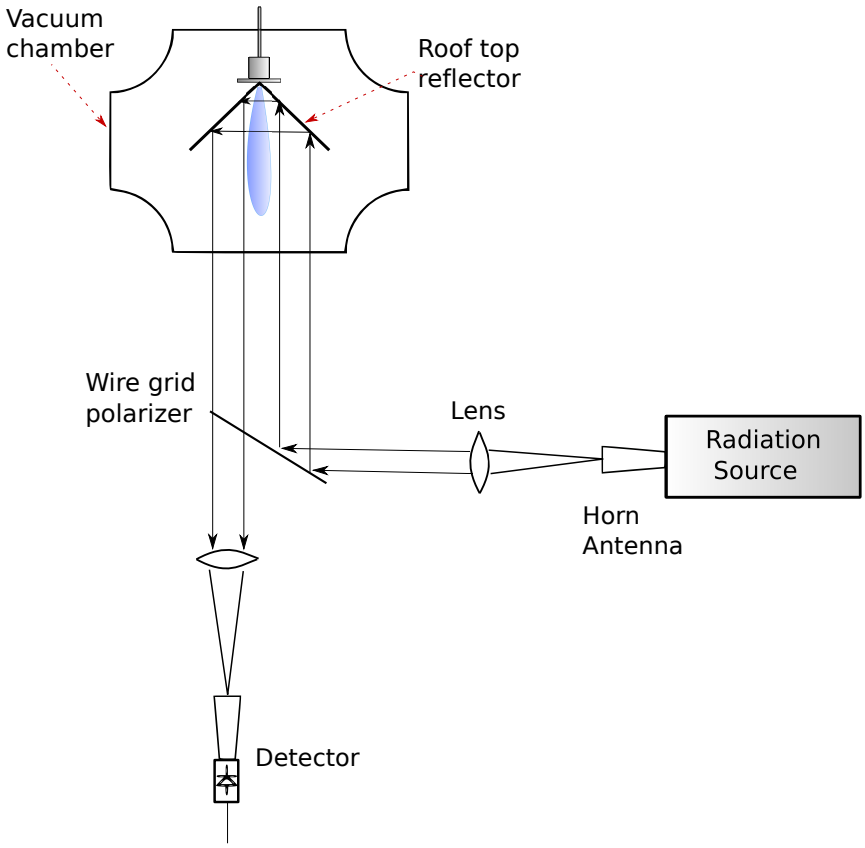

Figure 4.2: A schematic figure of the experimental set up. The experiment is arranged in a double-pass coaxial geometry.

the gas mixing ratios during measurements constant and thus provide us with stable flow conditions, that are easy to reproduce. The individual gas components are mixed at the output of the flow controllers and subsequently injected into the vacuum chamber through a pulsed valve (Series 9, Parker Hannifin), which is fixed centrally to the rooftop mirror, as shown in Fig. 4.2. The high vacuum of 10^{-7} Torr/10^{-10} bar inside the chamber is achieved by using an effective pumping system, that consists of a diffusion pump (DIP 8000, Oerlikon Leybold) combined with two mechanical pumps used as backing pumps (roots blower and rotary-vane pump, Oerlikon Leybold).

For the spectral acquisition we apply the frequency modulation method (see Section 1.5.6). After interacting with the molecular beam the modulated signal is detected by a liquid-He cooled InSb hot electron Bolometer (QMC Instruments Ltd.). Finally, the detected signal is demodulated at twice the modulation frequency ($2f$ modulation) by a lock-in amplifier (MFLI, Zurich Instruments), which means that we record the second derivative of the absorption line profile. The lock-in demodulation and the frequency stepping are synchronised to the repetition rate of the pulsed valve. During the time that the valve is switched off the background is substracted, decreasing that way the noise level and correcting for any strong baselines.

Fig. 4.3 shows construction drawings of our instrumentation. The left panel illustrates the vacuum chamber on top of the diffusion pump as well as the optical bench, which is used for the radiation source, the optical components (lenses and wire-grid polarizer) and the detector. The right panel shows the rooftop reflector within the chamber, where it is placed on top of a rail system, allowing it to move and be adjusted along two dimensions.

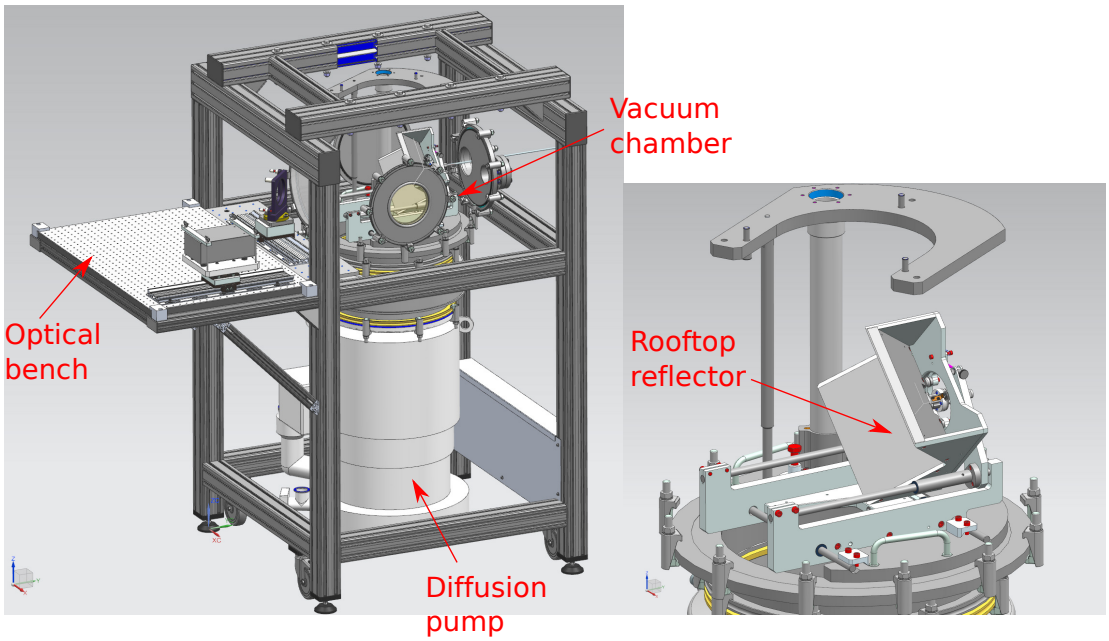

Figure 4.3: Construction drawings *(credit: Christian Deysenroth)* of the supersonic jet experiment. The left panel shows the vacuum chamber, the diffusion pump and the optical bench. The right panel illustrates the inner part of the chamber (rooftop reflector on top of a rail system).

Due to the Earth's magnetic field and the one caused by the mechanical valve (during operation), the spectral lines of open-shell molecules are split into several components as a result of the Zeeman effect. This splitting makes the line assignment hard, especially with the coaxial geometry of our experiment, that already produces two Doppler components of the same transition. Furthermore, such an effect dilutes the intensity of a single transition in several, and eventually no longer detectable, lines. In order to suppress the rotational Zeeman effect of open-shell molecular species we have arranged three pairs of Helmholtz coils around the vacuum chamber, as it is illustrated in Fig. 4.4. Placing two circular coils symmetrically on the same axis, in a distance that equals their radius, generates a homogeneous magnetic field in the center between the two coils. With three pairs of such coils surrounding the chamber, we are able to generate a magnetic field in every spatial direction, and thus compensate for all the components of the terrestrial magnetic field.

The compensation of the magnetic field at the center of the chamber was tested on molecules like SO and O_2, that have a large g factor and thus show an observable Zeeman effect [Cazzoli et al., 2017].

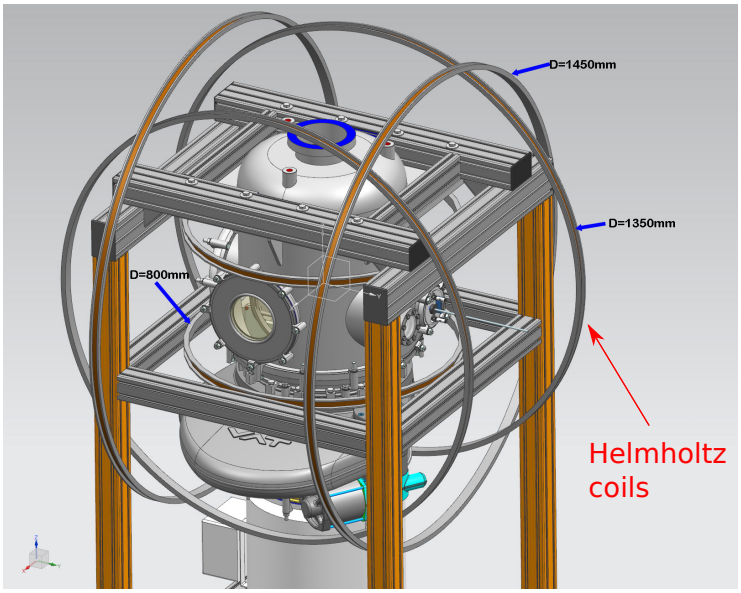

Figure 4.4: Application of Helmholtz coils around the vacuum chamber *(credit: Christian Deysenroth)*.

4.2.1 Mechanical valve and discharge nozzle

The mechanical valve that we are using for the injection of the molecular sample into the vacuum chamber is an electro-magnetic driven device. It consists of a tube containing a metallic spring, which is wrapped by six layers of copper coil with an inductance of just 4 μH. The required voltage for the operation of the nozzle is 28 V, which results in a current of 400 mA flowing through the coils. Switching on an electrical current induces a strong magnetic field, that forces the spring to move. A small poppet located on top of the spring pushes the gas outside of the valve through a 1 mm-orifice. The pulse controller (IOTA ONE, Parker Hannifin) provides the valve with the needed voltage and allows the system to deliver repeatable pulses with very high repetition rates (up to 250 Hz).

Since we are studying molecules of astrophysical relevance, that are formed in the ISM under extreme environments, we have to apply unique conditions (specific range of temperatures, pressures, voltages, certain reactants, etc.) in the lab in order to produce and stabilize these species and finally measure their rotational spectra. One prominent production method of reactive species is the gas discharge (see Section 1.5.5). For this implementation, we extend our beam source with a DC-discharge nozzle, which consists of alternating copper electrodes and teflon spacers (see Fig. 4.5). When the gas mixture flows through the mechanical valve, we apply a high voltage (up to 2 kV) simultaneously with the jet pulse, prior to free expansion. The high voltage produces a hot plasma between the two electrodes in which the precursor gases are either being excited, ionized or dissociated and subsequently react with each other to form new (reactive) species. In order to obtain the strongest possible signal, we have implemented a high voltage pulsing box for the discharge

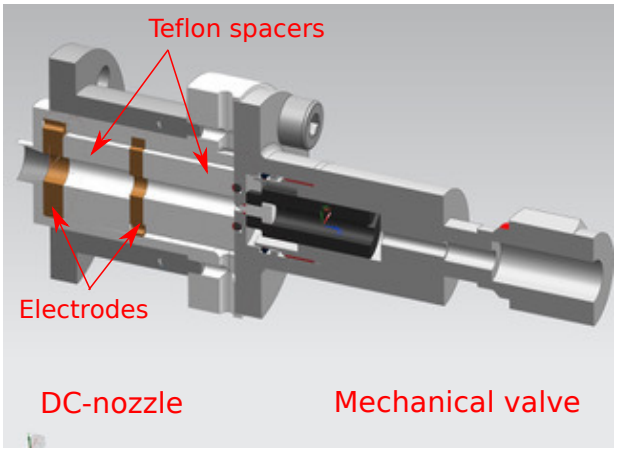

Figure 4.5: Design of our discharge nozzle (left part) attached to the mechanical valve (right part) *(credit: Christian Deysenroth)*.

nozzle, that helps us adjust the time length of the discharge pulse as well as its time delay with respect to the gas pulse.

4.3 Measurements of $HSCO^+$

Our first measurements with the supersonic jet experiment were performed on the protonated species $HSCO^+$. Protonated species are astrophysically relevant because they are good indicators of important physical parameters in the ISM, such as the gas ionisation fraction and dissociative electron recombination rates of ions, which in turn is useful information for chemical models. Furthermore, they can also serve as tracers for non-polar (and thus not directly observable) species.

The (sub)mm measurements on $HSCO^+$ and the corresponding spectral analysis is discussed in detail in the work done by Lattanzi et al. [2018]. Here, I will report a brief summary of the above study, in order to emphasize the capabilities of the jet experiment.

The molecule $HSCO^+$ is a nearly-prolate asymmetric top, that shows both a-type and b-type rotational spectra with dipole moments of $\mu_a = 1.57$ D and $\mu_b = 1.18$ D [McCarthy and Thaddeus, 2007]. The OCS backbone is almost linear with an angle of 175°. Three a-type transitions with $K_a = 0$ of $HSCO^+$ had been previously measured in McCarthy and Thaddeus [2007] in the microwave range, allowing to constrain the effective rotational constant $B_{eff} = (B+C)/2$. The uncertainty on the A rotational constant was nevertheless still large and the predicted frequencies in the mm- and (sub)mm range were not accurate enough to perform reliable astronomical observations of this species.

For this reason the spectroscopic study of $HSCO^+$ was substantially extended up to 400 GHz that led to an improved spectral fit. In particular, additional a-type lines (up to $J = 36, K_a = 6$) were obtained in the millimiter band with the CASAC (see Chapter 3), which helped constrain even further the constant B_{eff}. In order to also constrain the A

constant, which still remained highly uncertain (accuracy of ~ 20 MHz), it was important to measure b-type transitions, starting with the fundamental one $J_{K_a,K_c} = 1_{1,1} - 0_{0,0}$. Fig. 4.6 shows the simulated spectra of protonated OCS at a temperature of 15 K (top panel) and 130 K (bottom panel). The low-energy b-type transitions around 250-300 GHz are strongly populated at low temperatures, while at 130 K, the population of higher energy lines (higher K-transitions) considerably increases, making the rotational b-type spectrum rather complex and the line assignment difficult. Hence, in order to address the colder part of the spectrum it was necessary to switch from the warm plasma present in the CASAC to the cool molecular beam in the jet experiment. Decreasing the temperature of the absorption cell in the CASAC proved to be unsuccessful due to the freeze-out of the precursor gas, OCS.

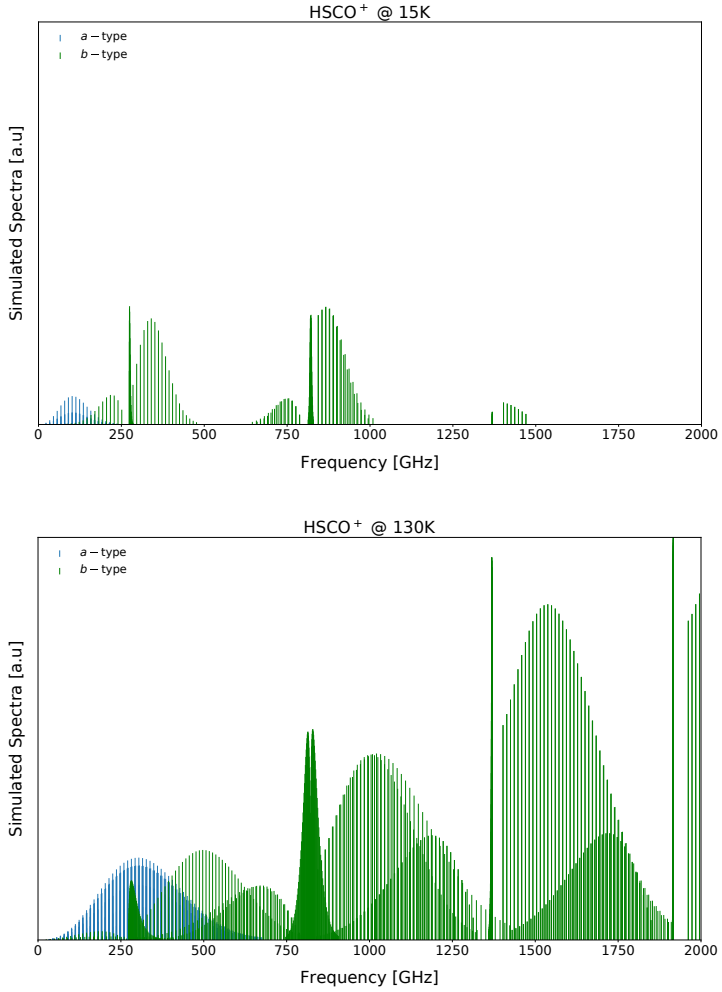

Figure 4.6: Simulated spectra of $HSCO^+$ at typical temperatures for the Jet (15 K) and the CASAC (130 K) experiment. The intensity axis is the same for both panels [Lattanzi et al., 2018].

For the production of $HSCO^+$ in the jet, we used as precursor gases a mixture of OCS highly diluted in H_2 (0.3%), that was injected through the pulsed valve with a backing pressure of 2 bar and a repetition rate of 15 Hz (opening time was 1 ms). The discharge nozzle was operated at 1.5 kV and the discharge pulse was 1.5 ms long. The signal was frequency modulated at 30 kHz and the time constant of the lock-in amplifier was 30 μs. With the above experimental conditions we were able in the end to detect 16 b-type transitions of $HSCO^+$ between 274 and 373 GHz, that helped us determine precisely the A constant with an uncertainty of just 10 kHz and a deviation of only 0.07% from the ab initio value. In Fig. 4.7 we show as an example a recorded line ($4_{1,4} - 3_{0,3}$) of $HSCO^+$ at $\sim$ 318 GHz, after integrating for $\sim$ 15 minutes.

For the spectral analysis of the rotational spectrum of $HSCO^+$ we applied a Watson S-reduced Hamiltonian, which included all the quartic centrifugal distortion terms and two sextic terms, H_{JK} and H_{KJ}. After including all the available lines measured in [Lattanzi et al., 2018] and in previous work [McCarthy and Thaddeus, 2007], the theoretical model was able to reproduce very well the measurements with a final rms uncertainty of 39 kHz. With this new improved fit, the rest frequencies of the astronomically relevant lines $HSCO^+$ are predicted with an accuracy of less than 100 kHz up to 500 GHz.

This work emphasizes the fact that the CASAC and the supersonic jet experiment are complementary techniques, that address different parts of the molecular spectrum; the combination of the two experiments provides us with a complete spectroscopic study of astronomically relevant molecules.

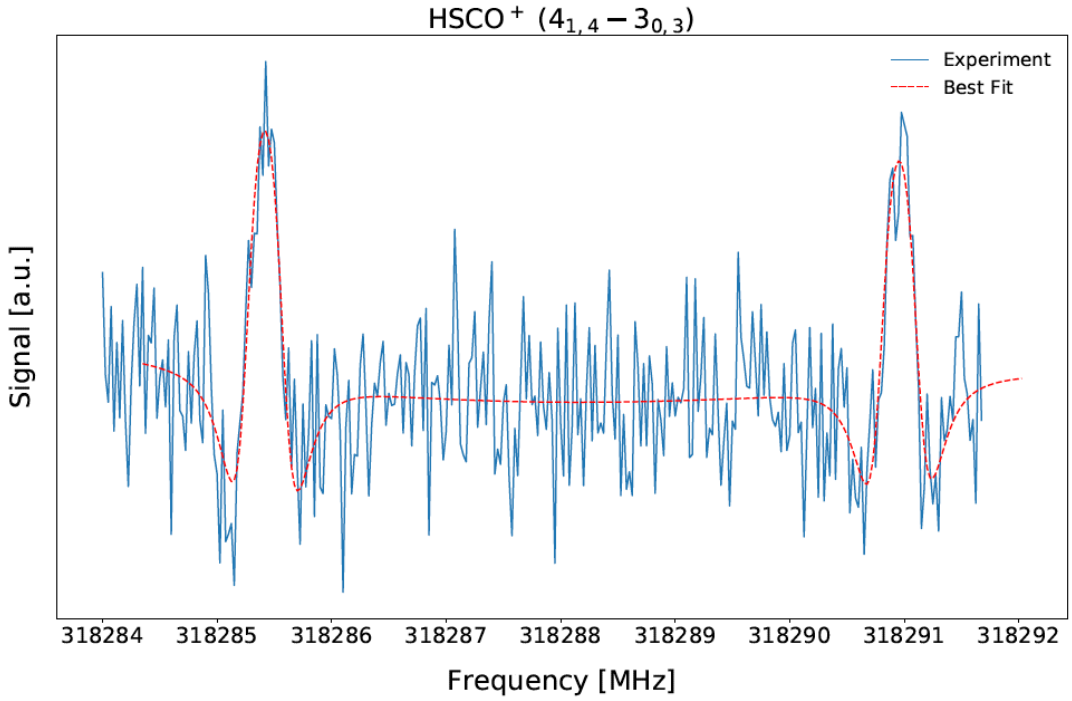

Figure 4.7: The $J_{K_a,K_c} = 4_{1,4} - 3_{0,3}$ transition of $HSCO^+$ at $\sim$ 318 GHz, recorded with our supersonic jet experiment. The red line represents the best fit described by a Voigt profile. The transition shows two components, as a result of the Dopper effect, which is caused by the radiation propagating parallel and anti-parallel to the molecular beam [Lattanzi et al., 2018].

Chapter 5

The first steps of interstellar phosphorus chemistry

The content of this chapter was published in *Astronomy & Astrophysics Journal*.

5.1 Abstract

Phosphorus-bearing species are essential to the formation of life on Earth, however they have barely been detected in the interstellar medium. In particular, towards star-forming regions only PN and PO have been identified so far. Since only a small number of detections of P-bearing molecules are available, their chemical formation pathways are not easy to constrain and are thus highly debatable. An important factor still missing in the chemical models is the initial elemental abundance of phosphorus, that is, the depletion level of P at the start of chemical models of dense clouds. In order to overcome this problem, we study P-bearing species in diffuse and translucent clouds. In these objects phosphorus is expected to be mainly in the gas phase and therefore the elemental initial abundance needed in our chemical simulations corresponds to the cosmic one and is well constrained. For the study of P-bearing chemistry we used an advanced chemical model. We updated and significantly extended the P-chemistry network based on chemical databases and previous literature. We performed single-pointing observations with the IRAM 30m telescope in the 3 mm range towards the line of sight to the strong continuum source B0355+508 aiming for the (2-1) transitions of PN, PO, HCP, and CP. This line of sight incorporates five diffuse and/or translucent clouds. The (2-1) transitions of the PN, PO, HCP, and CP were not detected. We report high signal-to-noise-ratio detections of the (1-0) lines of ^{13}CO, HNC, and CN along with a first detection of C^{34}S towards this line of sight. We have attempted to reproduce the observations of HNC, CN, CS, and CO in every cloud with our model by applying typical physical conditions for diffuse or translucent clouds. We find that towards the densest clouds with $v_{\rm LSR} = -10$, $-17\,{\rm km\,s^{-1}}$ the best-fit model is given by the parameters $(n({\rm H}), A_V, T_{\rm gas}) = (300\,{\rm cm^{-3}}, 3\,{\rm mag}, 40\,{\rm K})$. According to our best-fit model,

the most abundant P-bearing species are HCP and CP ($\sim 10^{-10}$). The molecules PN, PO, and PH_3 also show relatively high predicted abundances of $\sim 10^{-11}$. We show that the abundances of these species are sensitive to visual extinction, cosmic-ray ionization rate, and the diffusion-to-desorption energy ratio on dust grains. The production of P-bearing species is favored towards translucent rather than diffuse clouds, where the environment provides a stronger shielding from the interstellar radiation. Based on our improved model, we show that the (1-0) transitions of HCP, CP, PN, and PO are expected to be detectable with estimated intensities of up to ~ 200 mK.

5.2 Introduction

Phosphorus is essential for biotic chemistry, since it is a fundamental component of many important biological molecules, such as nucleic acids and phospholipids. Phosphorus is therefore vital to life on Earth and can consequently play an important role in exoplanets [Schaefer and Fegley, 2011]. Despite its importance, the chemistry of P-bearing molecules is in its infancy and remains poorly understood. The aim of this work is to add an important missing piece to the puzzle: unveiling the first steps of P chemistry via observations and chemical simulations of simple P-bearing molecules in diffuse clouds.
The ion P^+ was detected in several diffuse clouds by Jura and York [1978], where an elemental abundance of $\sim 2 \times 10^{-7}$ with a low P depletion factor of between approximately two and three was derived. However, a more recent study by Lebouteiller et al. [2006] showed that phosphorus remains mostly undepleted towards diffuse clouds. In addition, P has been identified towards dwarf and giant stars [Maas et al., 2017, Caffau et al., 2016], while detections of simple P-bearing molecules (PN, PO, HCP, CP, CCP, NCCP, PH_3) have been done towards the circumstellar material of carbon- and oxygen-rich stars [Agúndez et al., 2007, 2014a,b, Tenenbaum et al., 2007, De Beck et al., 2013, Ziurys et al., 2018]. The species PN and only very recently PO are the only P-bearing molecules to have been discovered towards dense star-forming regions [Turner and Bally, 1987, Fontani et al., 2016, Rivilla et al., 2016, Lefloch et al., 2016, Mininni et al., 2018, Fontani et al., 2019] and molecular clouds in the Galactic Center [Rivilla et al., 2018]. The limited number of available observations hinders our understanding of the chemical pathways involved in P chemistry. The main uncertainty in P chemistry is the unknown depletion factor of P in molecular clouds. In general, chemical models of dark clouds start with the so-called "low-metal abundances", where the elemental abundances of heavy elements (such as P, S, Fe, Mg) are reduced by orders of magnitude to reproduce molecular observations [e.g., Agúndez and Wakelam, 2013], but with poor understanding of the chemical processes at the base of such depletions. In the case of P, the level of depletion is still very uncertain. While Turner et al. [1990] and Wakelam et al. [2015b] used high depletion factors of 600-10^4 with respect to cosmic P abundance, recent works have shown that it could be as low as ~ 100 [Rivilla et al., 2016, Lefloch et al., 2016].

As only a very limited number of P-bearing molecules have been detected in star-forming regions, it is very hard to put constraints on the elemental abundance of P in

the gas phase and on the major chemical pathways. In order to elucidate the interstellar P chemistry we focus on diffuse clouds, which represent the first steps of molecular-cloud evolution. Diffuse clouds can provide important constraints on P chemistry, since P in these objects is not strongly affected by depletion, meaning that the initial P abundance that can be used for chemical simulations is well constrained [Lebouteiller et al., 2006]. With this approach we are able to remove an important uncertainty in our model and use a reliable starting point for our chemical simulations.

The existing chemical and physical models focus solely on diffuse clouds [e.g., Dalgarno, 1988, Le Petit et al., 2004, Cecchi-Pestellini et al., 2012, Godard et al., 2014]. For example, in Godard et al. [2014], a model including dissipation of turbulence was applied to reproduce the observed molecular abundances in the diffuse interstellar medium (ISM). The main results showed that chemical complexity is strongly linked to turbulent dissipation, which was able to reproduce the high abundances of CO and other species (such as C^+ and HCO^+) observed towards Galactic diffuse clouds. Le Petit et al. [2004] describe the development of a chemical model of the diffuse cloud towards ζ Persei that was able to reproduce the abundance of H_3^+ and other species, like CN and CO. This was achieved by modeling two phases, namely a small dense phase ($\sim 100\,\mathrm{au}$) with a density of $n(\mathrm{H}) = 2 \times 10^4\,\mathrm{cm}^{-3}$ and a larger diffuse region (4 pc) with $n(\mathrm{H}) = 100\,\mathrm{cm}^{-3}$. In addition, the reproduction of the CH^+ abundance and that of the rotationally excited H_2 required the inclusion of shocks into the model. Similar results were achieved by Cecchi-Pestellini et al. [2012] when including the injection of hot H_2 into the model.

Previous observations [Corby et al., 2018, Liszt et al., 2018, Thiel et al., 2019] prove the chemical complexity and the wide range of densities, temperatures, and visual extinctions of diffuse and translucent clouds, making them promising targets for observations of P-bearing molecules. Diffuse clouds are characterized by low densities with $n(\mathrm{H}) = 100 - 500\,\mathrm{cm}^{-3}$ and are therefore more exposed to interstellar radiation, which can destroy molecules. Translucent clouds on the other hand are an intermediate state between diffuse and dense molecular clouds, being more protected from UV radiation ($1\,\mathrm{mag} < A_V < 5\,\mathrm{mag}$). They are denser with typical densities of $n(\mathrm{H}) = 500 - 5000\,\mathrm{cm}^{-3}$ and are consequently cooler ($T_{\mathrm{gas}} = 15 - 50\,\mathrm{K}$), showing higher chemical complexity [Snow and McCall, 2006, Thiel et al., 2019]. One prominent candidate that has been widely studied in previous works [e.g., Liszt et al., 2018, and references therein] is the gas that lies along the line of sight to the compact extragalactic continuum source B0355+508. This strong blazar is located at a very low latitude in the outer Galaxy ($b = -1.6037°$), meaning that the way through the Galactic disk is long and therefore gathers a significant amount of distributed Galactic diffuse gas [Pety et al., 2008]. Indeed, the line of sight towards B0355+508 shows a complex kinematic structure which incorporates several diffuse and translucent clouds. The detections of numerous molecules like S- and CN-bearing species as well as small hydrocarbons towards B0355+508 also indicate the rich chemistry present in this diffuse and translucent gas [e.g., Liszt et al., 2018, and references therein]. The substantial velocity structure coupled with a high chemical complexity of this line of sight enables us to adjust our chemical and physical model to every cloud component and find which physical conditions most favor the abundances of P-bearing molecules. Other background sources

that have previously been studied are either lacking the chemical (like B0224+671) or the velocity (such as B0415+479) features which are essential for the present work.

In this paper, we present single-pointing observations of the (2-1) transitions of HCP, CP, PN, and PO and chemical simulations of their molecular abundances towards the line of sight to B0355+508 in order to investigate P-bearing chemistry within diffuse and translucent clouds, the precursors of molecular clouds. In Section 5.3 we describe the observational details. Section 5.4 summarizes the results of the observations. In Section 5.5 we describe our updated phosphorus chemical network as well as the grid of models that we apply in order to reproduce the observations of HNC, CN, CS, and CO towards every cloud component along the line of sight. Furthermore, in Section 5.6 we focus on the P-bearing chemistry based on our best-fit model (which was determined in Section 5.5). In particular, we report the predicted molecular abundances of HCP, CP, PN, PO, and PH_3 and we study their dependence on visual extinction, cosmic-ray ionization rate, and diffusion-to-desorption energy ratio on dust grains. A future outlook and conclusions are summarized in Sections 5.7 and 5.8.

5.3 Observations

The observations of the HCP (2-1), CP (2-1), PN (2-1), and PO (2-1) transitions in the 3 mm range were carried out at the IRAM 30m telescope located at Pico Veleta (Spain) towards the line of sight to the compact extragalactic quasar B0355+508. Table 5.1 lists the observed transitions, the spectroscopic constants, and the telescope settings at the targeted frequencies: the upper state energy is described by $E_{\rm up}$, the upper state degeneracy is given by g_u, while A_{ul} stands for the Einstein coefficient of the transition $u \rightarrow l$. The main beam efficiency and the main beam size of the telescope at a given frequency are denoted by the parameters $B_{\rm eff}$ and $\theta_{\rm MB}$, respectively. For our observations we used the EMIR receiver with the E090 configuration (3 mm atmospheric window). We applied three observational setups, in which every setup covered a total spectral coverage of 7.2 GHz (each sub-band covered 1.8 GHz). As a backend we used the Fast Fourier Transform Spectrometer with a frequency resolution of 50 kHz ($0.15\,{\rm km\,s^{-1}}$ at 100 GHz). In addition, we applied the wobbler switching mode with an amplitude offset of $\pm 90''$. Pointing and focus of the telescope was performed every 2 hr on the background source B0355+508 itself and was found to be accurate to within $2''$.

The intensity of the obtained spectra was converted from antenna ($T_{\rm A}^*$) to main beam temperature ($T_{\rm mb}$) units, using the following relation: $T_{\rm mb} = \frac{F_{\rm eff}}{B_{\rm eff}} \times T_{\rm A}^*$, where $F_{\rm eff}$ is the forward efficiency. $F_{\rm eff}$ is equal to 95% in the targeted frequency range.

5.4 Results

The compact extragalactic source B0355+508 is located at $\alpha = 3{\rm h}\,59{\rm m}\,29.73{\rm s}$, $\delta = 50°57'\,50.2''$ with a low galactic latitude of $b = -1.6037°$, incorporating a large amount of Galac-

Table 5.1: Spectroscopic parameters of the observed species and telescope settings

Species	Transitions	$E_{\rm up}$ (K)	Frequency (GHz)	$A_{\rm ul}$ ($10^{-5}\,{\rm s}^{-1}$)	g_u	B_{eff} (%)	$\theta_{\rm MB}$ ($''$)	References[a]
HCP	J=2-1	5.8	79.90329	0.04	5	83	31	1
PN	J=2-1	6.8	93.97977	2.92	5	80	26	2
CP	N =2-1, J=3/2-1/2, F = 2-1	6.8	95.16416	0.33	5	80	26	3
PO	J=5/2-3/2, $\Omega = 1/2$, F=3-2, e	8.4	108.99845	2.13	7	78	23	4
PO	J=5/2-3/2, $\Omega = 1/2$, F=2-1, e	8.4	109.04540	1.92	5	78	23	4
PO	J=5/2-3/2, $\Omega = 1/2$, F=3-2, f	8.4	109.20620	2.14	7	78	23	4
PO	J=5/2-3/2, $\Omega = 1/2$, F=2-1, f	8.4	109.28119	1.93	5	78	23	4

[a] (1) Bizzocchi et al. [2005]; (2) Cazzoli et al. [2006]; (3) Saito et al. [1989]; (4) Bailleux et al. [2002].

tic gas along the line of sight that harbors up to five diffuse and/or translucent clouds at velocities of -4, -8, -10, -14 and $-17\,{\rm km\,s^{-1}}$ [e.g., Liszt et al., 2018, and references therein]. The flux of the blazar B0355+508 is variable over time and has been measured at ~ 3 mm to be on average equal to (4.62 ± 1.02) Jy, after averaging the flux of 76 different observations [Agudo, 2017]. This corresponds to a temperature $T_{\rm c}$ of (0.96 ± 0.21) K at a beam size of $27''$ by taking into account the Rayleigh-Jeans-Approximation. The obtained spectra were reduced and analyzed by the GILDAS software [Pety, 2005]. Every detected line was fitted via the standard CLASS Gaussian fitting method. For the derivation of the peak opacity we use the radiative transfer equation

$$\begin{aligned} T_{\rm mb} &= (J_\nu(T_{\rm ex}) - J_\nu(T_{\rm bg}) - J_\nu(T_{\rm c})) \times (1 - \exp(-\tau)) \Rightarrow \\ \tau &= -\ln\Big(1 - \frac{T_{\rm mb}}{J_\nu(T_{\rm ex}) - J_\nu(T_{\rm bg}) - J_\nu(T_{\rm c})}\Big), \end{aligned} \tag{5.1}$$

where $T_{\rm ex}$ is the excitation temperature, $T_{\rm bg}$ is the cosmic background temperature, and $J(T) = (\frac{h\nu}{k_B})(e^{\frac{h\nu}{k_B T}} - 1)^{-1}$ describes the Rayleigh-Jeans temperature in Kelvin [1]. After obtaining the peak opacity τ, the column density N is then estimated by following the relation:

$$N = \tau \sqrt{\frac{16\pi^3}{\ln 2}} \frac{\nu^3 Q_{\rm rot}(T_{\rm ex}) \Delta v \, e^{E_u/k_B T_{\rm ex}}}{c^3 A_{ul}\, g_u \, (e^{h\nu/k_B T_{\rm ex}} - 1)}, \tag{5.2}$$

with k_B being the Boltzmann constant, Δv the line width (FWHM), ν the transition frequency, c the speed of light, and h the Planck constant. $Q_{\rm rot}(T_{\rm ex})$ gives the partition function of a molecule at a given excitation temperature $T_{\rm ex}$.

The (2-1) transitions of HCP, CP, PN, and PO were not detected within our observations (see Figure 5.1). We derive 3σ upper limits for the opacities and column densities

[1] When considering emission lines, $J_\nu(T_{\rm c})$ is neglected because $J_\nu(T_{\rm ex}) \gg J_\nu(T_{\rm c})$.

of the P-bearing species using Eqs. (5.1) and (5.2). Due to the low densities in diffuse clouds, molecules are expected to show no collisional excitation. The column densities were calculated assuming $T_{\rm ex} = T_{\rm bg} = 2.7\,{\rm K}$, which simplifies Eq. (5.1) to:

$$\tau \;=\; -\ln\Big(1 + \frac{T_{\rm mb}}{J_\nu(T_{\rm c})}\Big). \tag{5.3}$$

The results are summarized in Table 5.2.

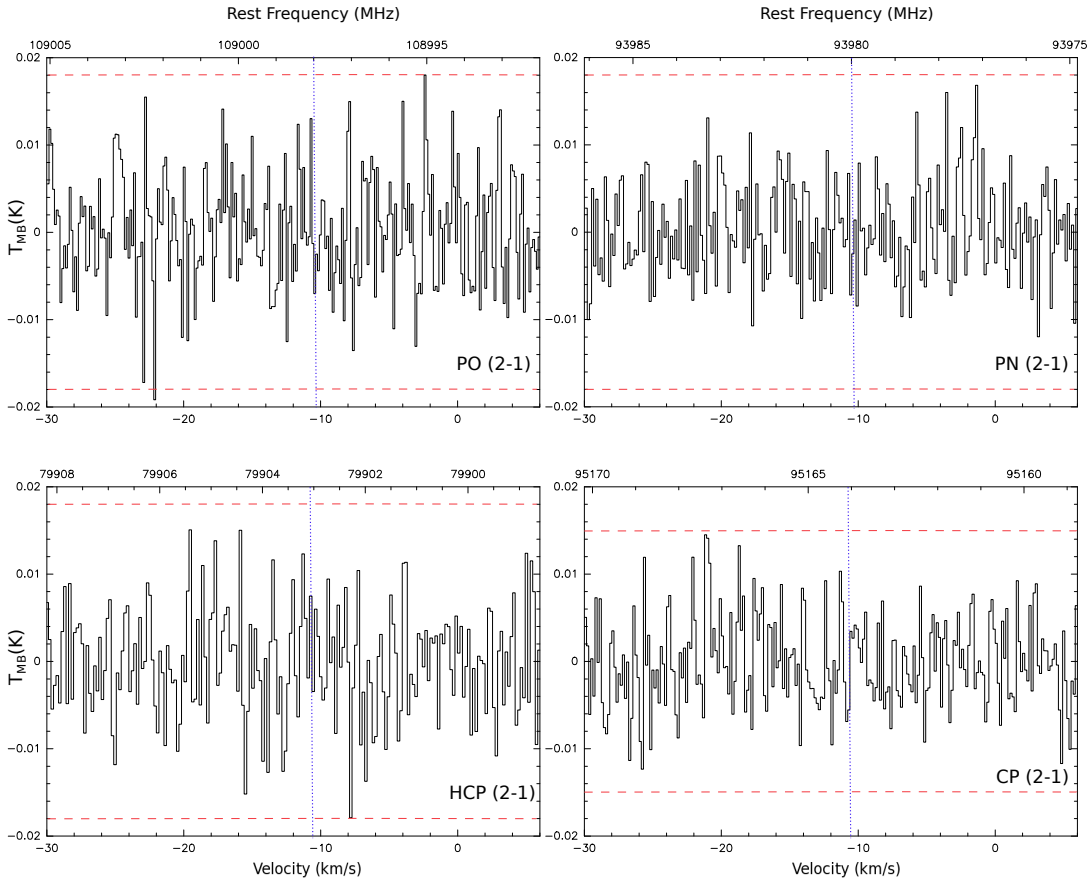

Figure 5.1: Spectra of the nondetected (2-1) transitions of PO, PN, HCP, and CP. The upper x-axis shows the rest frequency (in MHz) and the lower one is a velocity axis (in $\mathrm{km\,s^{-1}}$). The red dashed line indicates the 3σ level and the blue dashed line shows the transition frequency of the corresponding molecule. In the case of PO, we show as an example one of the observed transitions at 108.998 GHz.

We detected the HNC (1-0), CN (1-0), and $C^{34}S$ (2-1) transitions in absorption as well as the ^{13}CO (1-0) in emission at the 3 mm range with a high signal-to-noise ratio

Table 5.2: Derived upper limits for the opacity and the column density of HCP, CP, PN, and PO. The upper limits are 3σ.

Species	Frequency (GHz)	τ	N ($10^{11}\,\mathrm{cm}^{-2}$)	T_{MB} (K)	rms (mK)
HCP	79.90329	< 0.02	< 22.7	< 0.02	6
CP	95.16416	< 0.02	< 12.6	< 0.02	5
PN	93.97977	< 0.02	< 0.42	< 0.02	6
PO	108.99845	< 0.02	< 4.29	< 0.02	6
	109.04540	< 0.02	< 6.70	< 0.02	6
	109.20620	< 0.02	< 4.34	< 0.02	6
	109.28119	< 0.02	< 6.69	< 0.02	6

(S/N), ranging from 6 to 80 [2]. Figure 5.2 shows all the detected spectra towards the line of sight to B0355+508. In the case of CN we were able to detect and resolve four hyperfine components from 113.123 GHz to 113.191 GHz (see Figure 5.3). Every hyperfine component was detected in the three velocity components at -8, -10, and $-17\,\mathrm{km\,s^{-1}}$ except for the one weak transition at 113.123 GHz, which was identified only in two clouds (at -10, $-17\,\mathrm{km\,s^{-1}}$). The molecule HNC was identified in all five cloud components, while $C^{34}S$ (in absorption) and ^{13}CO (in emission) were detected solely towards the densest features, at $-10\,\mathrm{km\,s^{-1}}$ and $-17\,\mathrm{km\,s^{-1}}$. Table 5.3 lists the identified species and the corresponding spectroscopic parameters.

For estimating the CN column density we use the hyperfine component at 113.170 GHz. Our derived opacities and column densities of CN agree within a factor of two to three with previous results [Liszt and Lucas, 2001], while the HNC results are well reproduced within a factor of 1.5. Table 5.4 summarizes the derived opacities and column densities of the detected species, as well as the obtained line intensities and rms levels.

[2] The rms levels are lying between 4 and 13 mK.

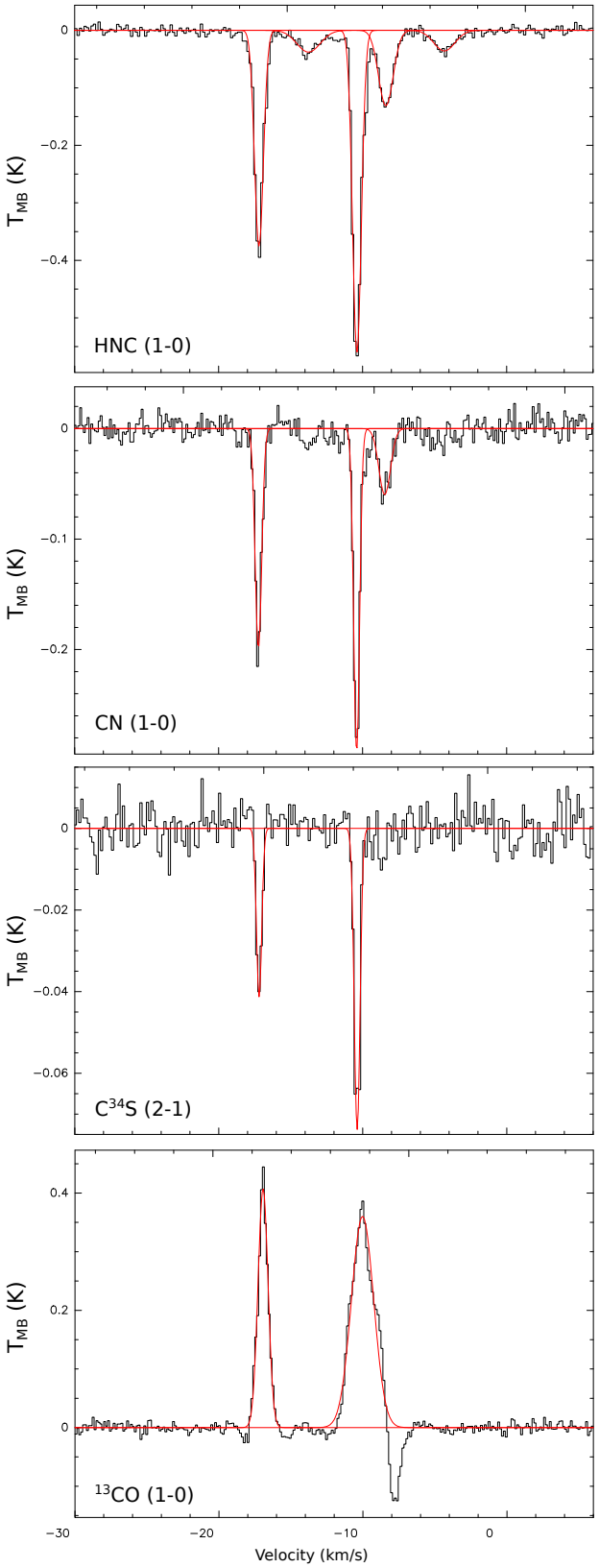

Figure 5.2: Spectra of the detected species HNC, CN, $C^{34}S$, and^{13}CO in the 3 mm range towards the line of sight to the extragalactitc source B0355+508. The red line represents the CLASS Gaussian fit.

Table 5.3: Spectroscopic parameters of the detected species and telescope settings

Species	Transitions	$E_{\rm up}$ (K)	Frequency (GHz)	$A_{\rm ul}$ $10^{-5}\,{\rm s}^{-1}$	g_u	B_{eff} (%)	$\theta_{\rm MB}$ ($''$)	References[a]
HNC	J=1-0	4.4	90.66357	2.69	3	81	27	1
CN	N= 1-0, F = 3/2-1/2	5.5	113.17049	0.51	4	78	22	2
$C^{34}S$	J= 2-1	6.9	96.41295	1.60	5	80	26	3
^{13}CO	J=1-0	5.3	110.20135	0.006	6	78	22	4

[a] (1) Saykally et al. [1976]; (2) Dixon and Woods [1977]; (3) Gottlieb et al. [2003]; (4) Klapper et al. [2000], Cazzoli et al. [2004].

Lucas and Liszt [2002] reported the detection of the main isotopolog $C^{32}S$ with the IRAM Plateau de Bure interferometer (PdBI) and estimated a column density of $(4.27 \pm 0.16) \times 10^{12}\,{\rm cm}^{-2}$ at the $-10\,{\rm kms}^{-1}$ component and $(3.06 \pm 0.32) \times 10^{12}\,{\rm cm}^{-2}$ at $-17\,{\rm kms}^{-1}$. With the above values and the column densities of $C^{34}S$ calculated in this work, we derive a sulfur isotopic ratio $^{32}S/^{34}S$ of 12.8 ± 4.8 and 18.7 ± 9.5 for the components at $-10\,{\rm kms}^{-1}$ and $-17\,{\rm kms}^{-1}$, respectively. The latter value is in good agreement with the $^{32}S/^{34}S$ ratio for the local ISM of 24 ± 5 [Chin et al., 1996]. However, the isotopic ratio determined for $v = -10\,{\rm kms}^{-1}$ is significantly lower than the local interstellar value, which could be the result of opacity effects of the $C^{32}S$ line. In addition, the determination of the sulphur isotopic ratio was based on just one spectral line of the main species $C^{32}S$ and its isotopolog, which also yields a high uncertainty. To our knowledge this is the first detection of $C^{34}S$ towards this line of sight, owing to the high spectral resolution of $\sim$ 50 kHz and high sensitivity (rms of ~ 4 mK) achieved with our observations.

In Liszt and Lucas [1998], detections of the main species ^{12}CO and its isotopolog ^{13}CO are reported, which were obtained with the PdBI as well as the NRAO 12m telescope. The single-dish observations covered a large beam of $60''$, thus seeing CO and its isotopolog in emission, while the interferometric observations were sensitive only to the very narrow column of gas towards the strong background blazar, giving rise to absorption lines. For deriving the excitation temperatures and the column densities, both emission (single-dish data) and absorption lines (interferometric data) were considered.

In Figure 5.2 it is clearly visible that the strong ^{13}CO emission line at $-10\,{\rm kms}^{-1}$ overlaps with an absorption feature at around $-8\,{\rm kms}^{-1}$. This is probably due to the fact that absorption is present close to the background source, meaning that emission and absorption lines are merged together in our observations with the IRAM 30m telescope. This contamination effect is influencing the line profile at $-10\,{\rm kms}^{-1}$ which subsequently results in an unreliable fit. This could possibly explain why the ^{13}CO column density derived at $-10\,{\rm kms}^{-1}$ deviates by a factor of about four from previous results [Liszt and Lucas, 1998], while towards $-17\,{\rm kms}^{-1}$, $N(^{13}CO)$ is well reproduced within 10% (see Table

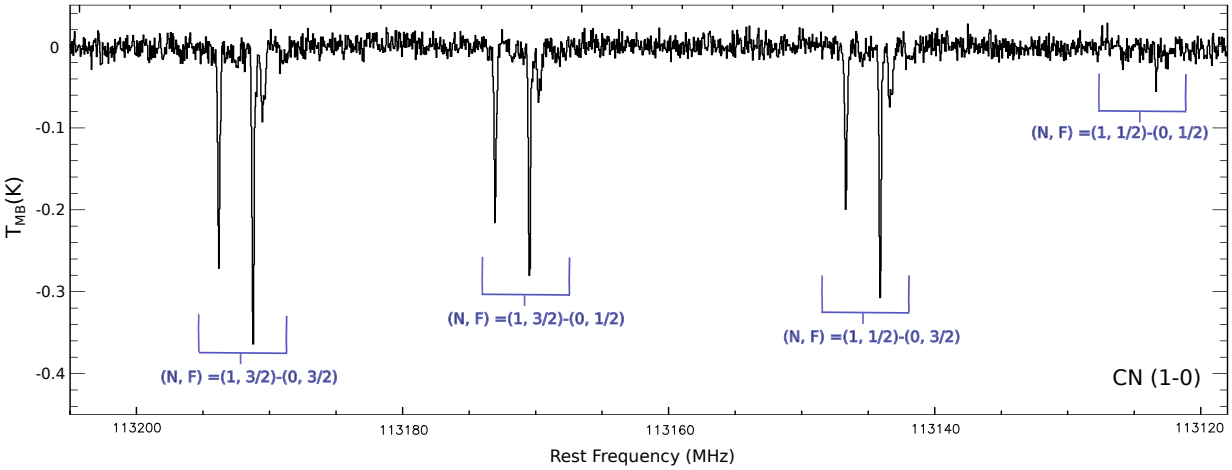

Figure 5.3: Detected hyperfine components of the CN (1-0) transition between 113.12 and 113.20 GHz. The three strongest hyperfine components were detected in the three clouds with $v_{\rm LSR} = -8, -10, -17\,{\rm km\,s^{-1}}$ except for the one weak transition $({\rm N, F}) = (1, 1/2) - (0, 1/2)$, which was identified only in the two densest clouds (at $-10, -17\,{\rm km\,s^{-1}}$).

5.4)[3]. Our derived isotopic ratio $^{12}{\rm CO}/^{13}{\rm CO}$ at $-17\,{\rm kms^{-1}}$ is equal to 16.7 ± 1.4. For this calculation, we used the column density of ^{12}CO derived in Liszt and Lucas [1998] with $N(^{12}{\rm CO}) = (6.64 \pm 0.47) \times 10^{15}\,{\rm cm^{-2}}$. The resulting CO isotopic ratio is almost a factor of four lower than the local interstellar ratio $^{12}{\rm C}/^{13}{\rm C} = 60$ [Lucas and Liszt, 1998]. This was already confirmed by previous studies [Liszt, 2007, 2017] that show an increased insertion of ^{13}C into CO towards clouds in the translucent regime with elevated densities and/or smaller radiation fields, which lead to an enhanced abundance of ^{13}CO by a factor of two to four. Under these conditions isotope exchange fractionation ($^{13}{\rm C}^+ + {}^{12}{\rm CO} \rightarrow {}^{12}{\rm C}^+ + {}^{13}{\rm CO} + 35\,{\rm K}$) is more dominant than selective photodissociation.

[3]We used a $T_{\rm ex}$ of 6 K for deriving $N(^{13}{\rm CO})$, as it was inferred in Liszt and Lucas [1998].

Table 5.4: Gaussian fitting results of CN, HNC, $C^{34}S$, ^{13}CO.

Species	Velocity ($km\,s^{-1}$)	Δv ($km\,s^{-1}$)	τ	T_{MB} (K)	rms (mK)	Spectral resolution ($km\,s^{-1}$)	N (cm^{-2}) (this work)	N (cm^{-2}) (previous work) [a]
CN								
	-17.23 ± 0.01	0.54 ± 0.02	0.23 ± 0.07	0.20 ± 0.02	9	0.13	$(0.87 \pm 0.28) \times 10^{13}$	$(2.14 \pm 0.24) \times 10^{13}$
	-10.41 ± 0.01	0.49 ± 0.01	0.36 ± 0.09	0.29 ± 0.02	9	0.13	$(1.23 \pm 0.34) \times 10^{13}$	$(3.34 \pm 0.37) \times 10^{13}$
	-8.47 ± 0.04	0.97 ± 0.09	0.06 ± 0.03	0.06 ± 0.01	9	0.13	$(0.43 \pm 0.20) \times 10^{13}$	$(0.76 \pm 0.21) \times 10^{13}$
HNC								
	-17.197 ± 0.004	0.73 ± 0.01	0.50 ± 0.10	0.37 ± 0.01	6	0.17	$(0.69 \pm 0.16) \times 10^{12}$	$(0.74 \pm 0.02) \times 10^{12}$
	-10.392 ± 0.003	0.73 ± 0.01	0.87 ± 0.16	0.56 ± 0.01	7	0.17	$(1.20 \pm 0.23) \times 10^{12}$	$(1.14 \pm 0.04) \times 10^{12}$
	-8.37 ± 0.01	1.14 ± 0.04	0.15 ± 0.04	0.13 ± 0.01	6	0.17	$(0.32 \pm 0.15) \times 10^{12}$	$(0.39 \pm 0.02) \times 10^{12}$
	-13.68 ± 0.07	2.30 ± 0.23	0.04 ± 0.01	0.04 ± 0.01	6	0.17	$(0.16 \pm 0.08) \times 10^{12}$	$(0.10 \pm 0.02) \times 10^{12}$
	-4.32 ± 0.06	1.71 ± 0.15	0.04 ± 0.02	0.04 ± 0.01	6	0.17	$(0.12 \pm 0.06) \times 10^{12}$	$(0.14 \pm 0.01) \times 10^{12}$
$C^{34}S$								
	-17.20 ± 0.02	0.43 ± 0.04	0.04 ± 0.02	0.04 ± 0.01	4	0.16	$(1.64 \pm 0.82) \times 10^{11}$	$< 3.2 \times 10^{11}$ [b]
	-10.39 ± 0.01	0.48 ± 0.02	0.08 ± 0.03	0.07 ± 0.01	4	0.16	$(3.33 \pm 1.23) \times 10^{11}$	$< 4.4 \times 10^{11}$ [b]
^{13}CO								
	-16.935 ± 0.004	0.82 ± 0.01	0.154 ± 0.004	0.41 ± 0.01	8	0.14	$(3.98 \pm 0.16) \times 10^{14}$	$(4.34 \pm 0.51) \times 10^{14}$ [c]
	-10.03 ± 0.01	1.82 ± 0.03	0.135 ± 0.004	0.36 ± 0.01	13	0.14	$(7.73 \pm 0.38) \times 10^{14}$	$(1.79 \pm 0.26) \times 10^{14}$ [c]

[a] Liszt and Lucas [2001]
[b] Lucas and Liszt [1998]
[c] Liszt and Lucas [1998]

5.5 Chemical modeling

The goal of the present study is to constrain and improve our model of diffuse and translucent clouds to make reliable predictions regarding the abundances of P-bearing species (and also others). For this reason, we used the observations of HNC, CN, CS, and CO in order to constrain the physical parameters in our model. The chemical code that we applied was developed by Vasyunin and Herbst [2013a] with an updated grain-surface chemistry (Vasyunin et al. 2019, in prep.). The model includes a gas-grain chemical network with 6000 gas-phase reactions, 200 surface reactions, and 660 species. Accretion and desorption processes regulate and connect the gas-phase and grain surface chemistry. The code numerically solves coupled differential equations (chemical rate equations) and computes a set of time-dependent molecular abundances. Since the observations were carried out towards diffuse and translucent clouds, we considered as initial elemental abundances the standard Solar elemental composition (see Table 5.5). We note that our initial elemental abundances are significantly different compared to the low metal abundances used in Wakelam et al. [2015b] for dark clouds (200 times more abundant S and up to 10^4 more abundant Fe, Cl, P, and F). In particular, the initial abundance of P is 2.6×10^{-7} and is therefore well constrained unlike in dense molecular clouds. This approach will help us better elucidate the chemistry of P since a key parameter for the chemical model is well determined. In addition, we begin our chemical simulations with the entirety of hydrogen being in its atomic form in order to start with pure atomic diffuse cloud conditions.

Table 5.5: Assumed solar initial elemental abundances [Asplund et al., 2006]

Species	Abundances
H	1.0
He	8.5×10^{-2}
N	6.8×10^{-5}
O	4.9×10^{-4}
C^+	2.7×10^{-4}
S^+	1.3×10^{-5}
Si^+	3.2×10^{-5}
Fe^+	3.2×10^{-5}
Na^+	1.7×10^{-6}
Mg^+	3.9×10^{-5}
Cl^+	3.2×10^{-7}
P^+	2.6×10^{-7}
F^+	3.6×10^{-8}

5.5.1 The chemical network of phosphorus

The phosphorus chemical network that has been used in previous studies [Fontani et al., 2016, Rivilla et al., 2016] has been extended with new available information in the literature (new reactions, updated reaction rates, desorption energies, etc.). In particular, chemical reactions of several P-bearing species, such as PN, PO, HCP, CP, and PH_3, were included and/or updated in our chemical network. The reaction rates were taken from the online chemical databases KInetic Database for Astrochemistry [Wakelam et al., 2015a, KIDA][4] and the UMIST Database for Astrochemistry [McElroy et al., 2013, UDfA][5], as well as from numerous previous papers [Thorne et al., 1984, Adams et al., 1990, Millar, 1991, Anicich, 1993, Charnley and Millar, 1994, Jiménez-Serra et al., 2018]. In particular we included several reactions involving the formation and destruction of PH_n ($n = 1, 2, 3$) and their cationic species from Charnley and Millar [1994] and Anicich [1993], along with the chemical network proposed by Thorne et al. [1984] that contains production and loss routes for P, PO, P^+, PO^+, PH^+, HPO^+ and H_2PO^+. In addition, we extended the PN chemical network based on the work by Millar et al. [1987], and we took into account the gas-phase reaction $P + OH \rightarrow PO + H$ proposed by Jiménez-Serra et al. [2018], as well as two formation routes of PN in the gas phase, $N + CP \rightarrow PN + C$ and $P + CN \rightarrow PN + C$, by Agúndez et al. [2007]. Finally, we included the photodissociation reactions of PN, PO, HCP, and PH_n ($n = 1, 2, 3$) based on the reaction rates given in KIDA and UDfA. The reaction rates of the photodissociation of PH_n were assumed to be equal to the analogous reactions for NH_n.

Concerning the chemistry taking place on grain surfaces, we took into account the hydrogenation reactions of P-bearing species (where the letter "g" denotes a grain surface species) as well as their corresponding desorption reactions:

- $gH + gP \rightarrow gPH$,
- $gH + gPH \rightarrow gPH_2$,
- $gH + gPH_2 \rightarrow gPH_3$.

The desorption energy of PH_3 was calculated based on that of NH_3 and amounts to ~ 5800 K. This corresponds to an evaporation temperature of ~ 100 K, which is in good agreement with the value of ~ 90 K proposed by Turner et al. [1990] [6]. The reactive desorption efficiency in our chemical model is set equal to 1%. An increased reactive desorption of 10% changes the predicted abundances of the aforementioned P-bearing molecules by less

[4] http://kida.obs.u-bordeaux1.fr

[5] http://udfa.ajmarkwick.net/index.php?mode=species

[6] The evaporation temperature describes the temperature at which a given species starts to desorb thermally.

than a factor of two. Another nonthermal desorption mechanism included in our model is the cosmic-ray desorption, which is fully described in Hasegawa and Herbst [1993]. Based on this study, dust grains are heated upon impact with cosmic rays reaching a peak temperature $T_{\rm dust}$ of 70 K, which subsequently leads to preferential desorption of molecules from grain surfaces. This type of desorption is however negligible in diffuse clouds, where photodesorption dominates. In our model we adopt for all species a photodesorption rate of 3×10^{-3} molecules per incident UV photon, as was determined in Öberg et al. [2007] based on laboratory measurements of pure CO ice. This stands in good agreement with the photodesorption yield of $\sim 10^{-3}$ molecules per UV photon found for other species, such as H_2O, O_2 and CH_4 [Öberg et al., 2009, Fayolle et al., 2013, Dupuy et al., 2017].

5.5.2 Comparison to observations

In order to reproduce the observed abundances of HNC, CN, CS, and CO in every cloud towards the line of sight to B0355+508 we produce a grid of models applying typical physical conditions for diffuse or translucent gas [Snow and McCall, 2006, Thiel et al., 2019]. We note here that, since our chemical model is not treating isotopic species, we are using as a reference for our comparison the main species ^{12}CO and C^{32}S instead of ^{13}CO and C^{34}S. For the fractional abundances of ^{12}CO and C^{32}S, we are adopting the column densities determined in Liszt and Lucas [1998] and Lucas and Liszt [2002]. In addition, for the clouds at $-14\,\mathrm{km\,s^{-1}}$ and $-4\,\mathrm{km\,s^{-1}}$ we use for CN and CS the upper limits derived in this work ($N(\mathrm{CN}) < 10^{12}\,\mathrm{cm^{-2}}$) and in Lucas and Liszt [2002]. The parameter space that we investigate is listed below:

- $n(\mathrm{H}) = 100 - 1000\,\mathrm{cm^{-3}}$, spacing of $100\,\mathrm{cm^{-3}}$,
- $A_V = 1 - 5\,\mathrm{mag}$, spacing of $1\,\mathrm{mag}$,
- $T_{\rm gas} = 20 - 100\,\mathrm{K}$, spacing of $10\,\mathrm{K}$.

The chemical evolution in each model is simulated over 10^7 yr (100 time steps) assuming static physical conditions. For the cosmic-ray ionization rate $\zeta(\mathrm{CR})$ we use a value of $1.7 \times 10^{-16}\,\mathrm{s^{-1}}$ [Indriolo and McCall, 2012, see Section 5.6 for further explanation]. This also corresponds to the values applied in Godard et al. [2014] and Le Petit et al. [2004], where the best-fit models provided a $\zeta(\mathrm{CR})$ of $10^{-16}\,\mathrm{s^{-1}}$ and $2.5 \times 10^{-16}\,\mathrm{s^{-1}}$, respectively.

Given the above parameter space, we calculate the level of disagreement $D(t, r)$ between modeled and observed abundances (for the species HNC, CN, CS and CO), which, following Wakelam et al. [2010] and Vasyunin et al. [2017], we define as

$$D(t,r) = \sum_{j=1}^{N_{\rm species}} |\log\big(x^j_{\rm mod}(t,r)\big) - \log\big(x^j_{\rm obs}\big)|, \tag{5.4}$$

with $r = (n(\mathrm{H}), A_V, T_{\mathrm{gas}})$ and $x^j_{\mathrm{obs,\,mod}}$ is the observed or modeled abundance of species j, respectively. We then determine the minimal value of $D(t,r)$, (noted as $D_{\mathrm{min}}(t,r)$), that corresponds to the best-fit model; the parameters (t,r) provided by the best-fit model are the ones giving the smallest deviation between observations and predictions. The smaller the $D_{\mathrm{min}}(t,r)$, the better the agreement.

According to Pety et al. [2008] and references therein, the clouds with $v_{\mathrm{LSR}} = -10\,\mathrm{km\,s^{-1}}$ and $-17\,\mathrm{km\,s^{-1}}$ towards B0355+508 show strong ^{12}CO emission lines that originate from dense regions (with $n(\mathrm{H}) = 300 - 500\,\mathrm{cm^{-3}}$ and $N(\mathrm{H_2}) > 10^{21}\,\mathrm{cm^{-2}}$) which are just outside the synthesized beam (combination of the 30m and PdBI telescopes), but still within the IRAM 30m beam [Pety et al., 2008]. Based on the CO (2-1) maps shown in Pety et al. [2008] with $22''$ and $5.8''$ resolutions, respectively, the cloud at $v_{\mathrm{LSR}} = -10\,\mathrm{km\,s^{-1}}$ shows the most pronounced, dense substructure. This is confirmed by the fact that this particular cloud component produces the most detectable amounts of observed species in the data presented in this work and previous works by Liszt and Lucas [2001] and Lucas and Liszt [2000], and is therefore chemically the most complex one. The component at $v_{\mathrm{LSR}} = -8\,\mathrm{km\,s^{-1}}$ shows a similar structure to the one at $v_{\mathrm{LSR}} = -10\,\mathrm{km\,s^{-1}}$, incorporating a dense region as well. Pety et al. [2008] suggest that the two components are part of the same cloud, even though they are distinguishable in absorption and show different levels of chemical complexity. With a higher spatial resolution of $5.8''$, the CO emission at $v_{\mathrm{LSR}} = -8\,\mathrm{km\,s^{-1}}$ is separated from the one at $v_{\mathrm{LSR}} = -10\,\mathrm{km\,s^{-1}}$ and is clearly visible. The diffuse gas seen at velocities $-14\,\mathrm{km\,s^{-1}}$ and $-4\,\mathrm{km\,s^{-1}}$ shows barely any ^{13}CO [Liszt and Lucas, 1998, and this work] or ^{12}CO [Pety et al., 2008, Liszt and Lucas, 1998] in emission, which suggests that the density of these clouds is too low to sufficiently excite CO. Pety et al. [2008] estimated a low to moderate density of these clouds to be $\sim 64-256\,\mathrm{cm^{-3}}$ with $A_V < 2$ mag.

Since we are performing single-dish observations with a beam of $\sim 22''$, we also cover the high-density regions that produce significant ^{12}CO emission [Pety et al., 2008]. For this reason we constrain our grid of models to high densities of $\geq 300\,\mathrm{cm^{-3}}$ for the denser clouds (-8, -10, $-17\,\mathrm{km\,s^{-1}}$), while for the low-density objects at $-14\,\mathrm{km\,s^{-1}}$ and $-4\,\mathrm{km\,s^{-1}}$ we restrict our input parameters to $n(\mathrm{H}) \leq 200\,\mathrm{cm^{-3}}$ and $A_V < 2$ mag. The calculation of the molecular abundances was done with respect to the $\mathrm{H_2}$ column densities ($N(\mathrm{H_2}) \sim 4 - 5 \times 10^{20}\,\mathrm{cm^{-2}}$) that were derived towards every cloud by Liszt et al. [2018]. However, our model provides the fractional abundance of a species X with respect to the total number of hydrogen nuclei, as in $n(\mathrm{X})/n(\mathrm{H})$, with the total volume density of hydrogen defined as $n(\mathrm{H}) = n(\mathrm{H\,I} + 2 \cdot \mathrm{H_2})$. The surface mobility parameters that we set as default values in our model (see Section 5.6.3) enable fast and effective formation of $\mathrm{H_2}$ on the surfaces of grains. At the end of our simulations (at $t = 10^7$ yr), the $\mathrm{H_2}$ abundance reaches a value of $40 - 50\%$ (depending on the set of parameters). This means that almost the entire hydrogen is predicted to be in its molecular form at the late phases of the chemical evolution. Following this consideration, we divide all the observed abundances and their upper limits mentioned in this paper by a factor of two, since $n(\mathrm{X})/n(\mathrm{H\,I} + 2 \cdot \mathrm{H_2}) \simeq n(\mathrm{X})/2 \cdot n(\mathrm{H_2}) = 0.5 \cdot n(\mathrm{X})/n(\mathrm{H_2})$. We note that this expression applies to the high-density parts of the clouds and does not account for the low-density (and H I rich) gas along the

line of sight.

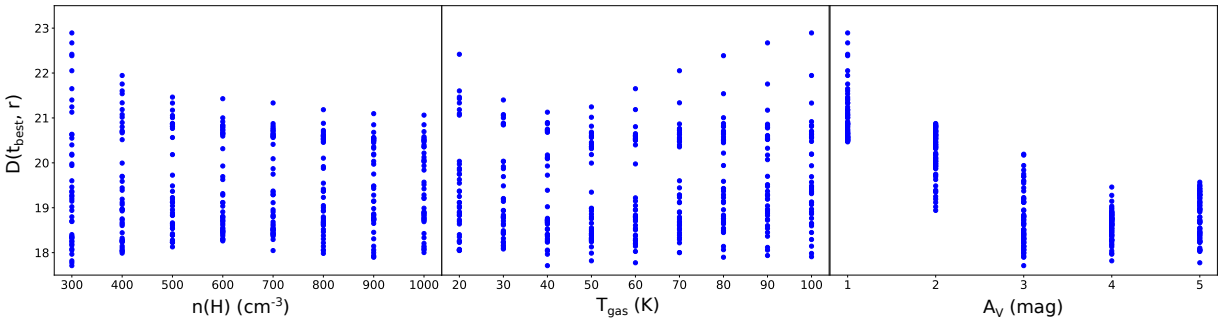

Figure 5.4: Results of the grid of models applying typical conditions for diffuse or translucent clouds in order to reproduce the observations towards the cloud at $v_{\rm LSR} = -17\,{\rm km\,s^{-1}}$. The deviation between observations and model at the time of best agreement $t_{\rm best}$ is given by $D(t_{\rm best}, r)$, which is plotted versus density, temperature, and visual extinction. The best-fit model is given at a time $t_{\rm best} = 6.2 \times 10^6\,{\rm yr}$ and has the following parameters: $(n({\rm H}), A_V, T_{\rm gas}) = (300\,{\rm cm^{-3}},\, 3\,{\rm mag},\, 40\,{\rm K})$.

Figure 5.4 shows the results of the grid of models that was applied to reproduce the observations towards $v_{\rm LSR} = -17\,{\rm km\,s^{-1}}$. In particular, we plot $D(t_{\rm best}, r)$, which describes the deviation between observed and modeled abundances at the time of best agreement $t_{\rm best}$, versus the density, temperature, and visual extinction. Between an A_V of 1 and 3 mag the smallest level of disagreement $D(t_{\rm best}, r)$ reduces by 13%. The main discrepancy between observed and modeled abundances at low A_V comes from the fact that a high visual extinction results in higher molecular abundances and is therefore able to reproduce the chemical complexity seen towards the translucent clouds. For models with $A_V > 3\,{\rm mag}$ the minimal $D(t_{\rm best}, r)$ barely changes (less than 1% of increase). The smallest $D(t_{\rm best}, r)$ increases with respect to the density and temperature up to 3% and 2%, respectively. This is a clear indication that the most influential physical parameter in our analysis is the visual extinction.

For the cloud component at $v_{\rm LSR} = -17\,{\rm km\,s^{-1}}$ the best-fit model with $D_{\rm min}(t, r)$ is reached at a time $t_{\rm best} = 6.2 \times 10^6\,{\rm yr}$ and has the parameters: $r_{\rm best} = (n({\rm H}), A_V, T_{\rm gas}) = (300\,{\rm cm^{-3}},\, 3\,{\rm mag},\, 40\,{\rm K})$. At $t_{\rm best} = 6.2 \times 10^6\,{\rm yr}$ we also fulfill the assumption of having most of the hydrogen in molecular form, as the H_2 abundance reaches a value of 0.45. Based on this model, we show in Figure 5.5 the time dependent abundances of CO, CN, CS and HNC over 10^7 yr as well as the corresponding observed abundances towards $v_{\rm LSR} = -17\,{\rm km\,s^{-1}}$. Our chemical model reproduces the observed species CO, CN, and CS very well within a factor of $\sim 1 - 1.4$ at $t_{\rm best} = 6.2 \times 10^6$ yr. As can be seen in Figure 5.5, the predicted abundances follow the order of the observed quantities. The most significant discrepancy is found in case of HNC, where the chemical model underestimates the observed abundance by a factor of four at the time of best agreement (see Table 5.6). According to the model, one of the main destruction mechanisms of HNC is: $C^+ + HNC \rightarrow C_2N^+ + H$; based on

the online chemical databases, its reaction rate remains uncertain. In UDfA the given reaction rate was determined theoretically [Leung et al., 1984] and therefore entails a high uncertainty. Experimental studies of the above chemical route are still needed to make reliable predictions of the HNC abundance.

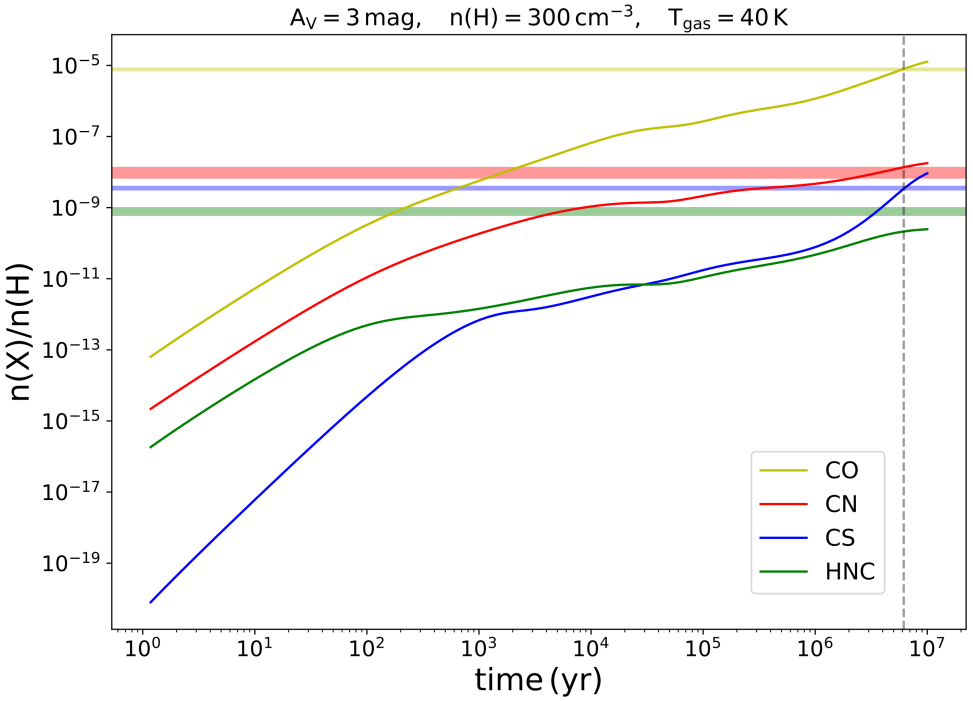

Figure 5.5: Chemical evolution of the abundances of CO, CN, CS and HNC over 10^7 yr predicted by our best-fit model with the parameters $(n(\mathrm{H}), A_V, T_{\mathrm{gas}}) = (300\,\mathrm{cm}^{-3}, 3\,\mathrm{mag}, 40\,\mathrm{K})$. The colored horizontal bands correspond to the observed abundances towards the cloud with $v_{\mathrm{LSR}} = -17\,\mathrm{km\,s}^{-1}$, including the inferred uncertainties. The vertical dashed line indicates the time of best agreement ($t = 6.2 \times 10^6$ yr) between observations and model results.

The smallest deviation with the observations towards the cloud with $v_{\mathrm{LSR}} = -10\,\mathrm{km\,s}^{-1}$ was produced by the same set of parameters: $r_{\mathrm{best}} = (n(\mathrm{H}), A_V, T_{\mathrm{gas}}) = (300\,\mathrm{cm}^{-3}, 3\,\mathrm{mag}, 40\,\mathrm{K})$. However, in this case the best-fit model gives a $D_{\mathrm{min}}(t, r)$ that is slightly larger by a factor of approximately 1.4. The molecular abundances observed towards $v_{\mathrm{LSR}} = -8\,\mathrm{km\,s}^{-1}$ are best reproduced with an A_V of 5 mag, a density of $400\,\mathrm{cm}^{-3}$ and a gas temperature of 40 K. The smallest level of disagreement between an A_V of 3 and 5 mag differs by less than 1%.

For the two remaining clouds with $v_{\mathrm{LSR}} = -4\,\mathrm{km\,s}^{-1}$ and $v_{\mathrm{LSR}} = -14\,\mathrm{km\,s}^{-1}$ the best-fit model in both cases is given by the parameters: $(n(\mathrm{H}), A_V, T_{\mathrm{gas}}) = (200\,\mathrm{cm}^{-3}, 1\,\mathrm{mag}, 30\,\mathrm{K})$ at $t_{\mathrm{best}} = 10^7\,\mathrm{yr}$. Here, the discrepancy in both clouds arises mostly from the fact that

Table 5.6: Observed abundances for the cloud component with $v_{\rm LSR} = -17\,{\rm km\,s^{-1}}$ and predictions of the species HNC, CO, CS and CN based on our best-fit model at the time of best agreement $t = 6.2 \times 10^6\,{\rm yr}$. The last column lists the ratio of observed to predicted abundances.

Species	Observed Abundance[a]	Predicted Abundance	Ratio (Observed/Predicted)
HNC	$8.0(1.9) \times 10^{-10}$	2.1×10^{-10}	3.8
CN	$1.0(0.3) \times 10^{-8}$	1.4×10^{-8}	0.7
CS	$3.6(0.4) \times 10^{-9}$	3.4×10^{-9}	1.1
CO	$7.7(0.6) \times 10^{-6}$	8.0×10^{-6}	1.0

[a] For the calculation of the observed abundances we used an $N(H_2)$ value of $4.30 \times 10^{20}\,{\rm cm^{-2}}$, as determined in Liszt et al. [2018].

the model underestimates the CS abundance by a factor of between approximately six and nine. In our model, CS is being effectively destroyed via photodissociation due to the low A_V. Table 5.7 lists the best-fit parameters that were determined towards every cloud component.

We note that towards the same line of sight there have been detections of several other molecules, as reported in Liszt et al. [2008]. The best-fit model determined towards $v_{\rm LSR} = -17\,{\rm km\,s^{-1}}$ and $v_{\rm LSR} = -10\,{\rm km\,s^{-1}}$ is able to reproduce within one order of magnitude the species OH, C_2H, H_2CO, NH_3 and CH, while other species such as HCN, SO, H_2S and C_3H_2 are strongly underestimated by up to two orders of magnitude. This is a clear indication that the chemical network of certain molecules (other than P-bearing ones) still needs to be extended and updated. This however will be addressed in future work, as the present paper focuses mainly on P chemistry.

Table 5.7: Set of physical parameters that give the best agreement between model results and observations towards every cloud component

Velocity (${\rm km\,s^{-1}}$)	n(H) (${\rm cm^{-3}}$)	A_V (mag)	$T_{\rm gas}$ (K)	$t_{\rm best}$ (10^6 yr)
-17	300	3	40	6.2
-14	200	1	30	10
-10	300	3	40	6.2
-8	400	5	40	2.3
-4	200	1	30	10

5.6 Discussion: the chemistry of phosphorus

Based on the above results we can conclude that the molecular abundances observed at $v_{\mathrm{LSR}} = -8,\ -10,\ -17\,\mathrm{km\,s^{-1}}$ can be best reproduced by a more "shielded" ($A_V > 1\,\mathrm{mag}$) interstellar medium that allows the build-up of molecules to occur more efficiently. The resulting visual extinction A_V of 3 mag should be viewed as an average value over the region covered by our beam ($\sim 22''$). Within this region the denser clumps are most likely translucent in nature. Hence, the observed cloud components are probably heterogeneous clouds, incorporating diffuse and translucent material, filled with relatively abundant molecules. This result stands in good agreement with a study by Liszt [2017], which involved modeling the CO formation and fractionation towards diffuse clouds. One of the main results of this latter study was that strong ^{13}CO absorption lines observed in the millimeter- and UV-range can be explained by higher densities ($\geq 256\,\mathrm{cm^{-3}}$) and weaker radiation (and thus higher visual extinction), as already mentioned in Section 5.4. Our conclusions also agree well with the work done by Thiel et al. [2019] in which the physical and chemical structure of the gas along the line of sight to SgrB2(N) was studied; here, complex organic molecules such as NH_2CHO and CH_3CHO were detected in the majority of the clouds, which at the same time proved to have relatively high visual extinctions ($A_V = 2.5 - 5\,\mathrm{mag}$ with $N(\mathrm{H_2}) > 10^{21}\,\mathrm{cm^{-2}}$), thus consisting mainly of translucent gas. According to Thiel et al. [2019] the column density of H_2 that corresponds to an A_V of 3 mag is $\sim 3 \times 10^{21}\,\mathrm{cm^{-2}}$. This is also consistent with the study by Pety et al. [2008], which states that the bright ^{12}CO emission originates from dense regions with $N(\mathrm{H_2}) > 10^{21}\,\mathrm{cm^{-2}}$. The gas observed at velocities of $-14\,\mathrm{km\,s^{-1}}$ and $-4\,\mathrm{km\,s^{-1}}$ on the other hand, corresponds mainly to a "classical" diffuse cloud with a visual extinction of ~ 1 mag according to the above analysis. These clouds also yielded the smallest amounts of the detected molecular abundances. Since chemical complexity seems to be favored towards translucent rather than diffuse gas, for the following discussion we use the model that provided the best fit towards the dense clouds with $v_{\mathrm{LSR}} = -17\,\mathrm{km\,s^{-1}}$ and $v_{\mathrm{LSR}} = -10\,\mathrm{km\,s^{-1}}$ as a reference.

According to our best-fit model, P^+ has a gas-phase abundance of 1.8×10^{-7} at the end of our simulations, being a factor of approximately 1.4 lower than its cosmic value, which indicates that little depletion takes place. The main reservoir of phosphorus other than P^+ is atomic P, having an abundance of 7.4×10^{-8} at 10^7 yr. Atomic P is formed mainly through the electronic recombination of P^+. For our models with elevated densities ($10^3\,\mathrm{cm^{-3}}$) we reach high elemental depletion (such as for C^+, S^+ and P^+) after running the code for 10^7 yr. This is consistent with the results presented by Fuente et al. [2019], which show significant depletion of C, O, and S happening already towards translucent material at the edge of molecular clouds (3-10 mag) with $1 - 5 \times 10^3\,\mathrm{cm^{-3}}$. In Appendix C.1 we investigate further the expected depletion of phosphorus when transitioning from diffuse- to dense-cloud conditions. We find that there is a significant depletion of atomic P on dust grains after the final density of $10^5\,\mathrm{cm^{-3}}$ is reached. This in turn leads to a strong increase of gPH_3, that becomes the main carrier of phosphorus in the dense phase. We also find a considerable decrease of the molecules HCP, CP, PN, PO and PH_3 due to freeze-out on grains and their destruction route with H_3^+ after the final density is attained

at $t \sim 10^6 - 10^7$ yr.

The most abundant P-bearing molecules in the gas phase are HCP and CP, with maximal abundances of 3.4×10^{-10} and 2.1×10^{-10}, respectively[7]. The formation and destruction pathways of both HCP and CP are strongly related to the electron fraction, as they are mainly produced (throughout the entire chemical evolution) by dissociative recombination of the protonated species PCH_2^+ and destroyed by reacting with C^+, the main carrier of positive charge in diffuse clouds. Two additional P-bearing species that are predicted by our model to have "observable" abundances in the gas phase are PN and PO, with respective maximal abundances of 4.8×10^{-11} and 1.4×10^{-11}. The most productive formation pathways for PN start with $P + CN \rightarrow PN + C$, $N + PH \rightarrow PN + H$ and end with $N + CP \rightarrow PN + C$. In the late stage of evolution ($\sim 0.5 \times 10^6 - 10^7$ yr) PN is primarily being destroyed by $He^+ + PN \rightarrow P^+ + N + He$. The species PO is mainly produced over the entire chemical evolution of 10^7 yr by the dissociative recombination of HPO^+: $HPO^+ + e^- \rightarrow PO + H$, and is mostly destroyed by reactions with C^+ and H^+. On the other hand, HPO^+ is efficiently formed via $P^+ + H_2O \rightarrow HPO^+ + H$[8]. An additional reaction that becomes relevant at progressive times ($\sim 10^6 - 10^7$ yr) is $O + PH \rightarrow PO + H$ with a $\sim 10\%$ reaction significance.

Another relatively abundant P-bearing species in the gas-phase based on our best-fit model is phosphine, PH_3, with a maximal abundance of $\sim 1.6 \times 10^{-11}$ at a late time of 10^7 yr. We note here that the species PH is also predicted to be detectable with a maximal abundance of $\sim 3.6 \times 10^{-11}$. Unlike PH however, PH_3 has already been detected in circumstellar envelopes of evolved stars [Agúndez et al., 2014a], indicating that it could be an important P-bearing species in interstellar environments such as diffuse and translucent clouds. We therefore focus in the following sections on the PH_3 rather than the PH chemistry. Based on our chemical model, PH_3 is formed most efficiently on dust grains in the early phase, being released to the gas-phase via reactive desorption: $gH + gPH_2 \rightarrow PH_3$. Its formation proceeds after 1.4×10^3 yr with the photodesorption process $gPH_3 \rightarrow PH_3$ being the most effective reaction. Since the evaporation temperature of PH_3 lies at ~ 100 K, the main mechanism driving the desorption of PH_3 at low temperatures is photodesorption (instead of thermal desorption). Switching off the photodesorption in our model leads to a decrease of the PH_3 gas-phase abundance of two orders of magnitude. Once in the gas phase, PH_3 is mostly destroyed by reactions with C^+ and H^+ as well as through the photodissociation reaction: $PH_3 + h\nu \rightarrow PH_2 + H$. The most abundant species on grains is gPH_3, with a maximal abundance of 7.2×10^{-10}. Almost all the atomic P that depletes onto the dust grains reacts with gH and forms gPH ($gP + gH \rightarrow gPH$), which subsequently forms gPH_3 through further hydrogenation. Table 5.8 summarizes all the main formation and destruction pathways for the molecules PN, PO, HCP, CP and PH_3 at three different

[7]The maximal abundances of the P-bearing species are reached at the end of our chemical simulations, at $t = 10^7$ yr. These abundances barely differ from the abundances at $t = 6.2 \times 10^6$ yr, which is the time of the best agreement with the observations.

[8]The species H_2O is formed efficiently on dust grains ($gH + gOH \rightarrow H_2O$) in the first 10^3 yr, while it is effectively produced via desorption $gH_2O \rightarrow H_2O$ at late times. Our best-fit model produces a maximal H_2O abundance in the gas phase of 2.3×10^{-8}.

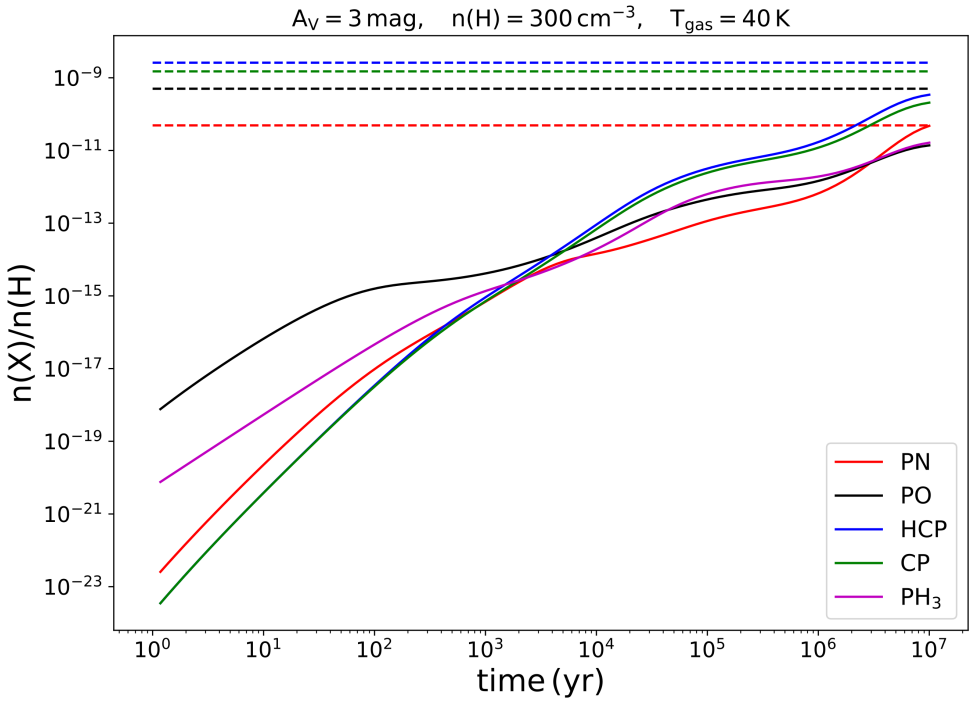

Figure 5.6: Variation of the predicted abundances of PN, PO, HCP, CP and PH_3 over 10^7 yr in our best-fit model. The dashed lines represent the 3σ upper limits derived from the observations at $v_{LSR} = -17\,km\,s^{-1}$. In the case of PO we use 5×10^{-10} as an upper limit (see Table 5.9 and text for explanation).

times ($t = 10^3, 10^5, 10^7$ yr). The last column shows the significance of the given reaction in the total formation or destruction rate of the species of interest.

Figure 5.6 depicts the time-dependent abundances of PN, PO, HCP, CP and PH_3 over 10^7 yr predicted by the best-fit model along with the computed 3σ upper limits. The predicted abundance for PO lies a factor of about 40 below the observational upper limit at $t = 10^7$ yr, while the current upper limits of HCP and CP are about one order of magnitude higher than the model predictions. Finally, for PN the modeled abundance almost reaches the observed value at the end of our simulations. This means that in all cases the predicted abundances of P-bearing species are lower than the derived upper limits. Future observations of the ground-energy transitions (1-0) will help us to constrain these upper limits even more (see Section 5.7 for further justification). Table 5.9 lists the predicted abundances of the above species given by our chemical model at $t = 10^7$ yr along with the corresponding upper limits. In the case of PO we show only the lowest value of the four upper limits that were derived for each transition.

Table 5.8: Main formation and destruction mechanisms for the species PN, PO, HCP, CP and PH_3 based on the best-fit chemical model at times: $t = 10^3$, 10^5, 10^7 yr. The last column represents the share of the given reaction in the total formation or destruction rate of the corresponding species.

Species	Time (yr)	Reaction type	Reaction	Reaction importance (%)
PN	10^3	Formation	$P + CN \rightarrow PN + C$	47
		Formation	$N + PH \rightarrow PN + H$	25
		Formation	$N + PO \rightarrow PN + O$	17
	10^5	Formation	$N + CP \rightarrow PN + C$	27
		Destruction	$H^+ + PN \rightarrow PN^+ + H$	-27
		Destruction	$He^+ + PN \rightarrow P^+ + N + He$	-23
		Formation	$N + PH \rightarrow PN + H$	10
	10^7	Destruction	$He^+ + PN \rightarrow P^+ + N + He$	-41
		Formation	$N + CP \rightarrow PN + C$	38
		Destruction	$H^+ + PN \rightarrow PN^+ + H$	-8
PO	10^3	Formation	$HPO^+ + e^- \rightarrow PO + H$	48
		Destruction	$C^+ + PO \rightarrow PO^+ + C$	-44
	10^5	Formation	$HPO^+ + e^- \rightarrow PO + H$	47
		Destruction	$H^+ + PO \rightarrow PO^+ + H$	-37
		Destruction	$C^+ + PO \rightarrow PO^+ + C$	-9
	10^7	Formation	$HPO^+ + e^- \rightarrow PO + H$	36
		Destruction	$C^+ + PO \rightarrow PO^+ + C$	-26
		Formation	$O + PH \rightarrow PO + H$	13
HCP	10^3	Formation	$PCH_2^+ + e^- \rightarrow HCP + H$	55
		Destruction	$C^+ + HCP \rightarrow CCP^+ + H$	-22
		Destruction	$C^+ + HCP \rightarrow HCP^+ + C$	-22
	10^5	Formation	$PCH_2^+ + e^- \rightarrow HCP + H$	50
		Destruction	$H^+ + HCP \rightarrow HCP^+ + H$	-39
	10^7	Formation	$PCH_2^+ + e^- \rightarrow HCP + H$	50
		Destruction	$C^+ + HCP \rightarrow CCP^+ + H$	-17
		Destruction	$C^+ + HCP \rightarrow HCP^+ + C$	-17
CP	10^3	Destruction	$C^+ + CP \rightarrow CP^+ + C$	-45
		Formation	$PCH_2^+ + e^- \rightarrow CP + H_2$	34
	10^5	Destruction	$H^+ + CP \rightarrow CP^+ + H$	-38
		Formation	$PCH_2^+ + e^- \rightarrow CP + H_2$	29
		Formation	$HCP^+ + e^- \rightarrow CP + H$	18
	10^7	Formation	$PCH_2^+ + e^- \rightarrow CP + H_2$	35
		Destruction	$C^+ + CP \rightarrow CP^+ + C$	-32
		Destruction	$H^+ + CP \rightarrow CP^+ + H$	-9
PH_3	10^3	Destruction	$C^+ + PH_3 \rightarrow PH_3^+ + C$	-45
		Formation	$gH + gPH_2 \rightarrow PH_3$	31
		Formation	$gPH_3 \rightarrow PH_3$	23
	10^5	Formation	$gPH_3 \rightarrow PH_3$	49
		Destruction	$H^+ + PH_3 \rightarrow PH_3^+ + H$	-26
		Destruction	$C^+ + PH_3 \rightarrow PH_3^+ + C$	-20
	10^7	Formation	$gPH_3 \rightarrow PH_3$	49
		Destruction	$C^+ + PH_3 \rightarrow PH_3^+ + C$	-36
		Destruction	$PH_3 + h\nu \rightarrow PH_2 + H$	-6

Table 5.9: Observed and predicted abundances at time $t = 10^7$ yr for the species PO, PN, HCP, CP and PH_3 given by our best-fit model. The upper limits are 3σ.

Species	Observed Abundance[a]	Predicted Abundance
PN	$< 4.9 \times 10^{-11}$	4.8×10^{-11}
PO	$< 5.0 \times 10^{-10}$	1.4×10^{-11}
HCP	$< 2.6 \times 10^{-9}$	3.4×10^{-10}
CP	$< 1.5 \times 10^{-9}$	2.1×10^{-10}
PH_3	-	1.6×10^{-11}

[a] For the calculation of the upper-limit-abundances we used an $N(H_2)$ value of $4.30 \times 10^{20}\,cm^{-2}$ [Liszt et al., 2018]. There are no observed data available for PH_3.

In the following discussion we focus on how deviations from our best-fit model can affect the chemistry of P-bearing species. In particular, we examine the dependence of the abundances of HCP, CP, PN, PO and PH_3 on increasing visual extinction A_V, increasing cosmic-ray ionization rate ζ(CR), and alternating the surface mobility constants (diffusion-to-desorption ratio E_b/E_D and possibility of quantum tunneling for light species).

5.6.1 Effects of visual extinction on the P-bearing chemistry

In this section we analyze how an increase of A_V is affecting the predicted abundances of P-bearing species. For this purpose we consider the parameters of the best-fit model with $n(H) = 300\,cm^{-3}$ and $T_{gas} = 40\,K$, while varying the A_V from 1 to 10 mag. By keeping the density constant, we avoid high levels of elemental depletion. The increase in visual extinction can then be explained by a figurative increase of the size of the source. Figure 5.7 (left panel) shows the predicted abundances of P-bearing species at the end of our simulations ($t = 10^7$ yr) under the effect of varying the visual extinction. All species reach a maximal abundance at an A_V of 4 mag. The abundances of HCP, CP, and PN barely change for $A_V > 4$ mag, while for the rest of the molecules the abundances drop; especially in the case of PH_3 where we see a substantial decrease of almost two orders of magnitude. As already mentioned in Section 5.6, the most effective formation process of PH_3 is the photodesorption $gPH_3 \rightarrow PH_3$. Thus, a high visual extinction attenuates the incoming UV-field and therefore the desorption of gPH_3.

In order to better understand the A_V dependence of the remaining molecular abundances, we plotted in Figure 5.7 the predicted abundances of the species that mainly form and destroy HCP, CP, PN, and PO (see Table 5.8) as a function of the visual extinction.

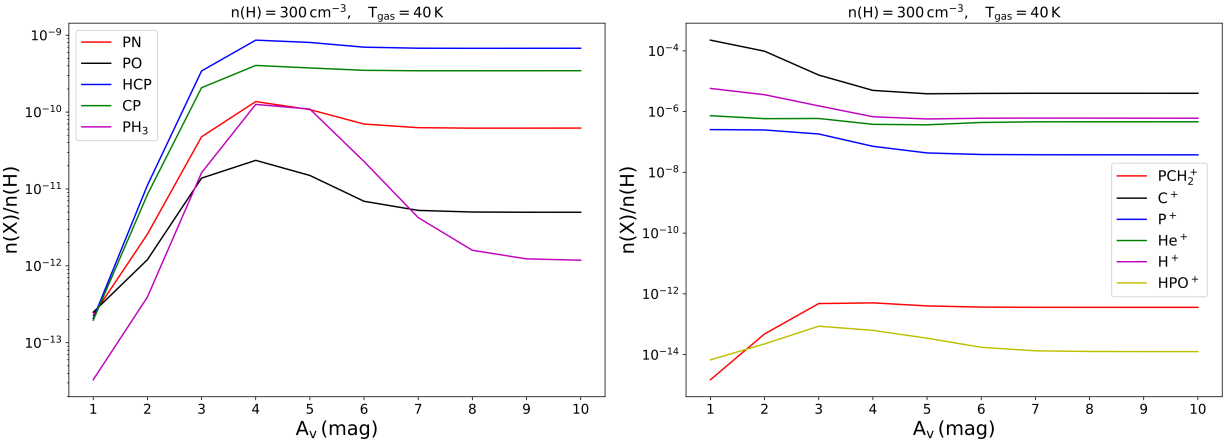

Figure 5.7: Predicted abundances of P-bearing molecules as a function of visual extinction A_V. The molecular abundances shown here are computed at $t = 10^7$ yr. The right panel illustrates the predicted abundances of PCH_2^+, C^+, P^+, He^+, H^+, and HPO^+ as they are contributing the most to the formation and destruction of HCP, CP, PN, PO and PH_3 (left panel).

In particular, we simulated the abundances of PCH_2^+, C^+, P^+, He^+, and H^+ as well as HPO^+. In the case of HCP (and also CP) its abundance increases up to an A_V of 4 mag and then remains constant above that value. This behavior is correlated with the increase of the PCH_2^+ abundance up to an A_V of 3 mag as well as the decrease of C^+ up to a visual extinction of 4 mag. The species PO seems to be more strongly affected by the increasing A_V. Its abundance will also increase for $A_V \leq 4$ mag which again stands in correlation with the decrease of the C^+ abundance (the main "destroyer" of PO), followed by a drop in abundance up to 7 mag. This on the other hand results from the decrease in HPO^+ abundance (the main precursor of PO) in the same A_V range. An increase in A_V will decrease the P^+ abundance (due to the decrease of the total ionization rate), as can be seen in Figure 5.7. In addition, an enhanced A_V slightly decreases the H_2O abundance (by a factor of two), since the most effective formation for H_2O at late times is the photodesorption $gH_2O \rightarrow H_2O$ (see footnote 7). Therefore, for higher A_V, both P^+ and H_2O decrease, meaning that HPO^+ and subsequently PO reduce in abundance as well.

5.6.2 Effects of the cosmic-ray ionization rate on the chemistry of P-bearing species

As already mentioned in Section 5.5.2, for all the applied models we use a value of $1.7 \times 10^{-16}\,s^{-1}$ for the cosmic-ray ionization rate ζ(CR), as was derived by Indriolo and McCall [2012]. This is also consistent with previous work in which diffuse and translucent clouds were studied as well [Fuente et al., 2019, Godard et al., 2014, Le Petit et al., 2004]. However, we should note here that in Indriolo and McCall [2012] several cosmic-ray

ionization rates were derived towards 50 diffuse lines of sight, ranging from $1.7 \times 10^{-16}\,\mathrm{s}^{-1}$ to $10.6 \times 10^{-16}\,\mathrm{s}^{-1}$ with a mean value of $3.5 \times 10^{-16}\,\mathrm{s}^{-1}$. Due to the complex and not yet fully understood nature of our observed clouds, we test our chemical model by also applying the elevated values of $\zeta(\mathrm{CR}) = 3.5 \times 10^{-16}\,\mathrm{s}^{-1}$ and $10.6 \times 10^{-16}\,\mathrm{s}^{-1}$ in order to examine the influence of the cosmic-ray ionization rate on P-bearing chemistry. As for the remaining parameters of the code (such as A_V and T_{gas}) we use the values given by our best-fit model (see Section 5.5.2). Figure 5.8 shows the chemical evolution of the species PN, PO, HCP, CP and PH_3 over 10^7 yr for $\zeta(\mathrm{CR}) = 1.7 \times 10^{-16}\,\mathrm{s}^{-1}$ and $10.6 \times 10^{-16}\,\mathrm{s}^{-1}$ in the left and right panels, respectively.

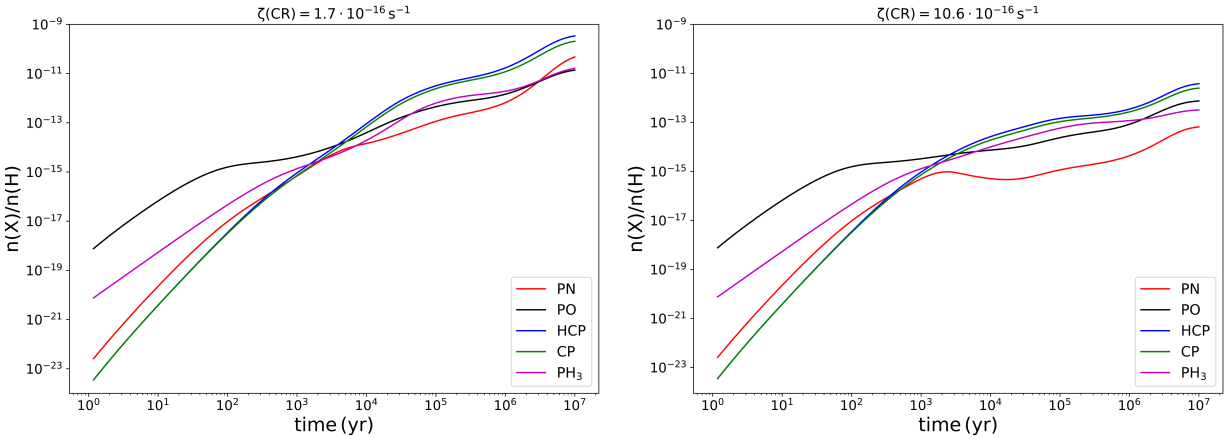

Figure 5.8: Chemical evolution of P-bearing molecules as a function of time under the effects of cosmic-ray ionization rates of $\zeta(\mathrm{CR}) = 1.7 \times 10^{-16}\,\mathrm{s}^{-1}$ (left panel) and $10.6 \times 10^{-16}\,\mathrm{s}^{-1}$ (right panel).

Table 5.10: Predicted abundances of the species PN, PO, HCP, CP and PH_3 at $t = 10^7$ yr for three different cosmic-ray ionization rates (see text for explanation).

Species	Predicted Abundances ($\zeta(\mathrm{CR}) = 1.7 \times 10^{-16}\,\mathrm{s}^{-1}$)	Predicted Abundances ($\zeta(\mathrm{CR}) = 3.5 \times 10^{-16}\,\mathrm{s}^{-1}$)	Predicted Abundances ($\zeta(\mathrm{CR}) = 10.6 \times 10^{-16}\,\mathrm{s}^{-1}$)
PN	4.8×10^{-11}	2.9×10^{-12}	6.6×10^{-14}
PO	1.4×10^{-11}	4.4×10^{-12}	7.5×10^{-13}
HCP	3.4×10^{-10}	6.7×10^{-11}	3.8×10^{-12}
CP	2.1×10^{-10}	4.2×10^{-11}	2.5×10^{-12}
PH_3	1.6×10^{-11}	2.7×10^{-12}	3.2×10^{-13}

Table 5.10 summarizes the predicted abundances of P-bearing species for the three different cosmic-ray ionization rates given in Indriolo and McCall [2012]. As one can see that PN shows the most substantial decrease in abundance with increasing $\zeta(\mathrm{CR})$. From

the lowest ($\zeta(\mathrm{CR}) = 1.7 \times 10^{-16}\,\mathrm{s}^{-1}$) to the highest ($\zeta(\mathrm{CR}) = 10.6 \times 10^{-16}\,\mathrm{s}^{-1}$) cosmic-ray ionization rate, the PN abundance decreases by a factor of approximately 730, while for HCP, CP, and PH_3 we see a drop by a factor of about 85 and 50, respectively. As already mentioned, PN is heavily destroyed by He^+ with a $\sim 40\%$ reaction significance. An increase of $\zeta(\mathrm{CR})$ up to a value of $10.6 \times 10^{-16}\,\mathrm{s}^{-1}$ significantly enhances the ionization of He and H by a factor of about 20 and 30, respectively, via cosmic-ray-induced secondary UV photons: $\mathrm{He} + \mathrm{CRP} \rightarrow \mathrm{He}^+ + \mathrm{e}^-$ and $\mathrm{H} + \mathrm{CRP} \rightarrow \mathrm{H}^+ + \mathrm{e}^-$ (the abundance of C^+ increases by a factor of ~ 6). Therefore, the destruction path with H^+ becomes relevant for all P-bearing species showing a 10-40% loss efficiency. The effect is the strongest in the case of PN, because PN is mainly formed through CP which drastically decreases and is also efficiently destroyed by both He^+ and H^+. The PO abundance is only reduced by a factor of about 20 after increasing $\zeta(\mathrm{CR})$ up to $10.6 \times 10^{-16}\,\mathrm{s}^{-1}$, despite being heavily destroyed by H^+. On the other hand, the significance of the dissociative recombination of HPO^+ increases up to 50% which in turn counterbalances the loss through H^+. An increased $\zeta(\mathrm{CR})$ of $10.6 \times 10^{-16}\,\mathrm{s}^{-1}$ enhances the abundance of P^+ up to $\sim 2.5 \times 10^{-7}$, nearly reaching its cosmic value of $\sim 2.6 \times 10^{-7}$ [Asplund et al., 2006], while the abundance of atomic P decreases down to $\sim 9.5 \times 10^{-9}$ via the enhanced reaction with C^+ and H^+.

5.6.3 Effects of the diffusion-to-desorption ratio on the chemistry of P-bearing species

The chemistry in the ISM is heavily influenced by the presence of dust grains [Caselli and Ceccarelli, 2012]. The mobility of the depleted species on the surface of dust grains depends on two mechanisms: thermal hopping and quantum tunneling for the lightest species H and H_2 through potential barriers between surface sites [Hasegawa et al., 1992]. Without the possibility of tunneling, the species are not able to scan the grain surface quickly at low temperatures and the total mobility decreases. The parameters that strongly determine the surface chemistry are the diffusion-to-desorption energy ratio E_b/E_D as well as the thickness of the potential barrier between adjacent sites. Based on previous studies [Hasegawa et al., 1992, Ruffle and Herbst, 2000, Garrod and Herbst, 2006], Vasyunin and Herbst [2013a] proposed three different values for the E_b/E_D ratio: 0.3, 0.5, and 0.77. In the case of low ratios ($E_b/E_D = 0.3$) we activate in our model the possibility of quantum tunneling for light species, while for the other two cases, surface mobility is only controlled by thermal hopping (and quantum tunneling is deactivated). The potential barriers are assumed to have rectangular shape and a thickness of 1 Å [Vasyunin and Herbst, 2013a]. In our model we utilize the first set of parameters ($E_b/E_D = 0.3$, with tunneling), nevertheless, since the chemistry of P-bearing species is still highly uncertain, we examine how the remaining two sets of parameters ($E_b/E_D = 0.5$, 0.77, no tunneling) influence the predicted abundances. Table 5.11 lists the predictions for PN, PO, HCP, CP, and PH_3 as well as H_2 at $t = 10^7$ yr for the three different sets of surface mobility parameters proposed in Vasyunin and Herbst [2013a]. As Table 5.11 shows, the H_2 abundance decreases by a factor of four by switching from setup 1 ($E_b/E_D = 0.3$ with tunneling) to setup 2 ($E_b/E_D = 0.5$ no tunneling), and

finally experiences a dramatic drop of a factor 50 when increasing the E_b/E_D up to 0.77 (overall change of a factor 200 between setups 1 and 3).

Table 5.11: Predicted abundances of the species PN, PO, HCP, CP and PH_3 as well as H_2 at $t = 10^7$ yr for three different sets of surface mobility parameters (see text for explanation).

Species	Predicted Abundances ($E_b/E_D = 0.3$ with tunneling)	Predicted Abundances ($E_b/E_D = 0.5$ no tunneling)	Predicted Abundances ($E_b/E_D = 0.77$ no tunneling)
PN	4.8×10^{-11}	5.0×10^{-13}	1.6×10^{-13}
PO	1.4×10^{-11}	1.2×10^{-12}	6.7×10^{-13}
HCP	3.4×10^{-10}	1.3×10^{-11}	4.6×10^{-12}
CP	2.1×10^{-10}	9.5×10^{-12}	3.2×10^{-12}
PH_3	1.6×10^{-11}	1.8×10^{-12}	1.2×10^{-12}
H_2	4.8×10^{-1}	1.3×10^{-1}	2.4×10^{-3}

The reduction of the H_2 abundance has a significant impact on the formation of PCH_2^+ and PH, which affects the PN, PO, HCP and CP abundances through the following reactions:

PN

- $P^+ + H_2 \rightarrow PH_2^+$
- $PH_2^+ + e^- \rightarrow PH + H$
- $N + PH \rightarrow PN + H$

PO

- $P^+ + H_2 \rightarrow PH_2^+$
- $PH_2^+ + e^- \rightarrow PH + H$
- $O + PH \rightarrow PO + H$

HCP

- $HCP^+ + H_2 \rightarrow PCH_2^+$
- $PCH_2^+ + e^- \rightarrow HCP + H$

CP

- $HCP^+ + H_2 \rightarrow PCH_2^+$
- $PCH_2^+ + e^- \rightarrow CP + H_2$

Both PH and PCH_2^+ decrease by a factor of approximately 20 when increasing the E_b/E_D up to 0.77. In addition, the abundance of H^+ is increased by a factor of about 25, since the reduction of H_2 formation leads to more atomic hydrogen and subsequently more H^+. The enhanced H^+ abundance results in a stronger destruction of all P-bearing species through their reaction with H^+. The species HCP and CP are also strongly affected by changing the surface mobility parameters, with an overall decrease by a factor of about 70 and 65 in abundance, respectively. In both cases the dissociative recombination of PCH_2^+ is essential during the whole chemical evolution for the formation of HCP and CP showing a reaction significance of 30 to 99%. A decrease of PCH_2^+ due to lower H_2 abundance therefore results in reduced HCP and CP formation. The largest effect is seen for PN, where a diffusion-to-desorption ratio of 0.77 and no quantum tunneling of light species reduces the PN abundance by a factor of 300 (see Figure 5.9).

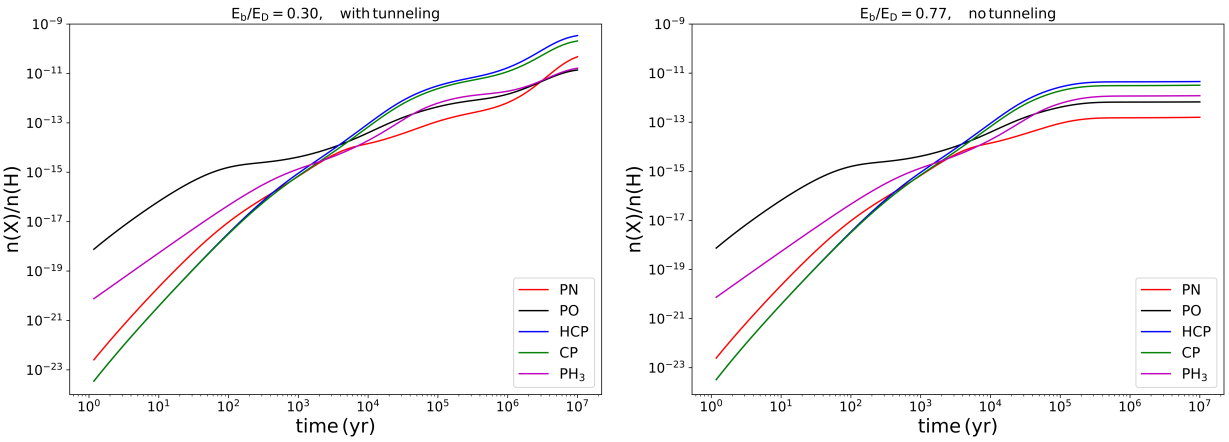

Figure 5.9: Chemical evolution of P-bearing molecules as a function of time for a diffusion-to-desorption ratio E_b/E_D of 0.3 (with quantum tunneling) shown in the left panel and for a E_b/E_D of 0.77 (without quantum tunneling) in the right panel.

Besides the effective loss through H^+, the substantial decrease in PN is also related to the reduction of CP, which is the main precursor of PN at late times. In addition, the reaction $N + PH \rightarrow PN + H$ is important for PN formation over the entire chemical evolution of 10^7 yr with a 10-50% formation efficiency (for $E_b/E_D = 0.77$ and no tunneling). This means that the reduction of the H_2 abundance decreases PH, which in turn produces less PN. In the case of PO however, the change in abundance between the two extreme cases is only a factor of about 20. Here, the route $O + PH \rightarrow PO + H$ increases in significance only up to 3% at late times ($4 \times 10^6 - 10^7$ yr), indicating that the decrease of PH will not considerably affect PO production. Furthermore, the reduction of PO due to H^+ is compensated through its effective formation via the dissociative recombination of HPO^+. Finally, the abundance of PH_3 decreases only by a factor of 13 in total when changing the surface chemistry constants. Despite being heavily destroyed by H^+, PH_3 is still sufficiently

formed through the photodesorption of gPH_3.

5.7 Future observations

Thanks to the sensitive observations (rms of ~ 6 mK) of the (2-1) transitions of HCP, CP, PN and PO we were able to obtain good upper limits for the column densities and abundances of the above species (see Tables 5.2 and 5.9) and thus constrain P chemistry. The observations of HNC, CN, CS, and CO helped us to put important constraints on the main physical parameters of the targeted diffuse and translucent clouds, that is, the visual extinction, the density, and the gas temperature. For the prospect of future observations we want to estimate the expected line intensities of the (1-0) transitions of HCP, CP, PN and PO (at $\sim 40 - 65$ GHz) based on our new and improved diffuse-cloud model. Since the densities present in diffuse and translucent clouds are too low to show any collisional excitation ($T_{\rm ex} = T_{\rm bg} = 2.7\,{\rm K}$), the (1-0) transitions are expected to be more strongly populated than the higher-energy transition levels. For these calculations, we take into account the nonthermal nature of the blazar emission, meaning that the flux increases with decreasing frequency. In particular, we apply a power law to the emission of the blazar with $\frac{F}{F_0} = (\frac{\nu}{\nu_0})^{-\alpha}$, where F is the flux, ν is the corresponding frequency, and α is the spectral index. By using the fluxes determined in Agudo [2017] at 3 and 1.3 mm we infer a spectral index of $\alpha \sim 1.06$. Following this, we determine the flux at 7 mm to be ~ 11 Jy, which in turn corresponds to a temperature of ~ 26 K with a beam size of $17''$ (at 7 mm with the Green Bank Telescope). As Table 5.12 shows, the derived peak intensities of the species PN, PO, HCP and CP vary from 10 to 200 mK, making these lines "detectable" with radio telescopes, such as the Green Bank Telescope (GBT) and the Effelsberg Telescope. The capabilities of these instruments will allow us to reach rms levels down to 4 mK and enable possible detections up to the 50σ level. The only exception is PH_3 with a (1-0) transition at 266.944 GHz. The flux of the background source at that frequency based on the above power law is equal to 1.91 Jy. This corresponds to a background temperature $T_{\rm c}$ of 0.4 K with a beam size of $9''$ (with the IRAM telescope), which in the end results in a very weak, nondetectable absorption line.

Table 5.12: Estimated absorption line intensities for the (1-0) transitions of HCP, CP, PN and PO towards B0355+508 for $T_{\rm ex} = 2.73\,{\rm K}$, a FWHM line width of $\Delta v = 0.5\,{\rm km\,s^{-1}}$ and based on the predicted abundances given by our best-fit model at $t = 10^7$ yr.

Species	Transitions	$E_{\rm up}$ (K)	Frequency (GHz)	$A_{\rm ul}$ ($10^{-6}\,{\rm s^{-1}}$)	g_u	Estimated Intensities (mK)	References[a]
HCP	J=1-0	1.9	39.95190	0.04	3	23	1
PN	J=1-0	2.3	46.99028	3.04	3	214	2
CP	N= 1-0, J=3/2-1/2, F=2-1	2.3	47.98288	0.43	5	51	3
PO	J=3/2-1/2, Ω=1/2, F= 2-1, e	3.2	65.31224	3.83	5	12	4

[a] (1) Bizzocchi et al. [2005]; (2) Cazzoli et al. [2006]; (3) Saito et al. [1989]; (4) Bailleux et al. [2002].

5.8 Conclusions

The aim of this work is to understand through observations and chemical simulations which physical conditions favor the production of P-bearing molecules in the diffuse ISM and to what degree. Observing diffuse clouds offers us the opportunity to constrain an important parameter in our chemical simulations, namely the depletion level of phosphorus (and in general the initial elemental abundances).

We performed single-pointing observations (IRAM 30m telescope) of the (2-1) transitions of the species PN, PO, HCP and CP at 3 mm towards the line of sight to the bright continuum source B0355+508. None of the above transitions were detected. Nevertheless, the sensitive observations yielding an rms level of ~ 6 mK allowed us to obtain reliable upper limits (see Tables 5.2 and 5.9).

We have obtained high S/N detections of the (1-0) lines of HNC, CN, and ^{13}CO between 80 and 110 GHz. We also show a first detection of C^{34}S (2-1) at 96 GHz towards the two densest cloud components at $-10\,\mathrm{km\,s^{-1}}$ and $-17\,\mathrm{km\,s^{-1}}$. Following this, we were able to derive a sulfur isotopic ratio ^{32}S/^{34}S of 12.8 ± 4.8 and 18.7 ± 9.5 towards the $-10\,\mathrm{km\,s^{-1}}$ and $-17\,\mathrm{km\,s^{-1}}$ features, with the latter being close to the local interstellar value of 24 ± 5 [Chin et al., 1996]. The detected molecular species show the highest abundances towards the two components at $-10\,\mathrm{km\,s^{-1}}$ and $-17\,\mathrm{km\,s^{-1}}$, as already shown in previous studies [e.g., Liszt et al., 2018, and references therein].

Based on the detected molecular abundances, we updated our chemical model in order to provide reliable predictions of abundances and line intensities of P-containing molecules that will serve as a guide for future observations. For this purpose we ran a grid of chemical models, with typical physical conditions of diffuse or translucent clouds, trying to reproduce the observed abundances and upper limits of HNC, CN, CO, and CS in every cloud component along the line of sight (at -4, -8, -10, -14 and $-17\,\mathrm{km\,s^{-1}}$). For the clouds with $v_{\mathrm{LSR}} = -10\,\mathrm{km\,s^{-1}}$ and $-17\,\mathrm{km\,s^{-1}}$, the best agreement between observed and modeled abundances is reached at a time $t_{\mathrm{best}} = 6.2 \times 10^6$ yr and at $r_{\mathrm{best}} = (n(\mathrm{H}), A_V, T_{\mathrm{gas}}) = (300\,\mathrm{cm^{-3}}, 3\,\mathrm{mag}, 40\,\mathrm{K})$. We chose this set of parameters as a reference for modeling the phosphorus chemistry.

According to our best-fit model mentioned above, the most abundant P-bearing species are HCP and CP ($\sim 10^{-10}$) at a time of $t = 10^7$ yr. The species PN, PO, and PH_3 also show relatively high predicted abundances of 4.8×10^{-11} to 1.4×10^{-11} at the end of our simulations. All species are effectively destroyed through reactions with C^+, H^+, and He^+. The molecules HCP, CP, and PO are efficiently formed throughout the entire chemical evolution via the dissociative electron recombination of the protonated species PCH_2^+ and HPO^+, respectively. In addition, the species PH_3 is mainly formed on dust grains through subsequent hydrogenation reactions of P, PH, and PH_2 and then released to the gas-phase via photodesorption. Finally, PN is formed at late times ($10^5 - 10^7$ yr) mainly through the reaction $\mathrm{N + CP \rightarrow PN + C}$.

We also examined how the visual extinction A_V, the cosmic-ray ionization rate ζ(CR), and the surface mobility on dust grains affect the chemistry of P-bearing species. We found that all P-bearing species are strongly sensitive to the visual extinction: low A_V values of 1

and 2 mag lead to very low P-bearing molecular abundances of $\sim 10^{-14} - 10^{-12}$, indicating that a translucent region rather than a diffuse one is needed to produce observable amounts of P-containing species. All examined species in our study are influenced by the cosmic-ray ionization rate as well. An increasing ζ(CR) enhances the abundance of He^+, H^+ and C^+, which in turn are effectively destroying all P-bearing species. A similar conclusion was found when changing the diffusion-to-desorption ratio to $E_b/E_D = 0.77$ and deactivating the possibility of quantum tunneling of light species on grain surfaces. This setup increases the H^+ abundance, which in turn efficiently reacts with and destroys PN, PO, HCP, CP, and PH_3. Finally, we performed a study of the P-depletion level by tracing the phosphorus chemistry from a diffuse to a dense cloud with the application of a dynamical model that varies the density, the gas and dust temperature, the cosmic-ray ionization rate, and the visual extinction with time (see Appendix C.1). We came to the main conclusion that at high densities of $\sim 10^5\,\mathrm{cm}^{-3}$, atomic P is strongly depleted through freeze-out on dust grains, resulting in a significant increase of the gPH_3 abundance. The molecules PN, PO, HCP, CP, and PH_3 are also affected by freeze-out on grains and are destroyed by their reaction with H_3^+ when reaching the dense phase at timescales of $\sim 10^6 - 10^7$ yr.

Based on the predictions of our improved diffuse-cloud model, the (1-0) transitions of HCP, CP, PN, and PO are expected to be detectable with estimated intensities ranging from 10 to 200 mK. A possible detection of the above species will help us to further constrain the physical and chemical properties of our model and help us to better understand interstellar phosphorus chemistry.

Chapter 6

Conclusions and future prospects

6.1 Summary of this thesis

This thesis presented a comprehensive study of molecular deuteration towards dense cores, using radioastronomical observations, as well as an extended laboratory investigation in the (sub)mm range of the transient species, HCCO, DCCO, and the molecular ion $HSCO^+$ by applying two complementary experimental techniques. Finally, this work explored the interstellar phosphorus chemistry towards diffuse and translucent clouds, mostly by means of chemical modeling. The main results are summarized below:

A study of the c-C_3HD/c-C_3H_2 ratio in low-mass star forming regions. I presented the study on the c-C_3H_2 deuteration towards 10 starless/pre-stellar cores and 5 protostars in the Taurus and Perseus Complexes. I showed that the deuterium fraction of c-C_3H_2 correlates with the dust temperature, i.e. decreasing towards the warmest protostars, as predicted by theory and previous studies. The $N(c\text{-}C_3HD)/N(c\text{-}C_3H_2)$ ratio towards the starless cores is not changing significantly and is equal to $\sim 10\%$ within the error bars for all cores. I obtained the same deuteration level within the protostellar sample, except for the protostar HH211, which is the youngest protostar in our sample; for this source we retrieved the highest deuterium fraction of 23%. This indicates that c-C_3H_2 is additionally deuterated while being frozen onto dust grains during the pre-stellar core phase, right before the ignition of a protostar. The deuteration of c-C_3H_2 is comparable to that of N_2H^+, except towards the evolved pre-stellar core L1544, where c-C_3H_2 is heavily affected by depletion.

Rotational spectroscopy of the HCCO and DCCO radicals in the millimeter and submillimeter range. I presented our spectroscopic study on ketenyl (HCCO) and its deuterated counterpart DCCO in the millimeter and submillimeter range. The rotational spectra of the above radicals were recorded with our frequency modulation absorption spectrometer (CAS Absorption Cell, CASAC) in the frequency range between 170 and 650 GHz. The new set of measured lines significantly improved the spectral fit, allow-

ing the determination of high-order rotational constants. The improved set of spectroscopic parameters provides us with highly accurate rest-frequencies for both HCCO and DCCO, allowing reliable future astronomical observations in the (sub)mm range. Furthermore, I reported an HCCO detection towards the prestellar core L1544 and showed that ketenyl peaks towards the region where c-C_3H_2 peaks. This stands in good agreement with our gas-grain model, which shows that the main precursor of ketenyl is C_2H, indicating that the HCCO formation is based mostly on hydrocarbon chemistry.

The Supersonic Jet Experiment. I presented the development and implementation of a new spectrometer called Supersonic Jet Experiment, which is used to study reactive species in the (sub)mm range. This experiment is based on the production of a cold, molecular beam through an adiabatic supersonic expansion of a selected gas mixture into a high-vacuum chamber. The resulting low temperatures ($\sim 5 - 10\,\mathrm{K}$) and the nearly collision-free environment within the jet, gives us the perfect conditions for studying transient molecules, like radicals and ions. Apart from the technical realization of the experiment I reported new measurements in the (sub)mm range (between 274 and 373 GHz) of the protonated species $HSCO^+$, which was produced within an electric DC gas discharge. I show that the Supersonic Jet Experiment is complementary to the CASAC, as every experiment helps us study different parts of the molecular spectrum.

The first steps of interstellar phosphorus chemistry. I studied the interstellar phosphorus chemistry towards diffuse and translucent clouds, through chemical modeling and observations. I performed observations towards the diffuse/translucent clouds along the line of sight to the strong quasar B0355+508. The detections of HNC, CN, $C^{34}S$ and ^{13}CO were used to constrain the physical properties of the observed sources. Based on the best-fit parameters I make reliable predictions for the abundances of the P-bearing species. I show that the most abundant P-bearing molecules are HCP and CP ($\sim 10^{-10}$) followed by PN, PO and PH_3 ($\sim 10^{-11}$). Parameters such as the visual extinction A_V and the cosmic-ray ionization rate ζ(CR), have a significant effect on the abundances of all P-bearing molecules. The new model-results indicate that P-chemistry is more favoured towards translucent rather than diffuse clouds, where there is a higher shielding from the interstellar radiation.

6.2 Prospective work

This thesis has drawn important conclusions on astrochemical processes towards the early phases of low-mass star formation through astronomical observations and chemical modeling, while also contributing to the spectroscopic investigation of transient molecules in the laboratory. Based on these conclusions I will discuss in the following paragraphs future perspectives of the projects presented in this work:

Observations and Model. The study of the *c*-C_3H_2 deuteration towards dense cores was based on single pointing observations. However, for a full picture of the chemical differentiation of a pre-stellar and protostellar core, detailed molecular maps are needed, as was done in Spezzano et al. [2016]. Thus, a future step for this project would be to obtain maps of *c*-C_3H_2 and *c*-C_3HD in order to explore the deuterium fraction as a function of the physical properties of the core. In fact, these maps would reveal the depletion zone of *c*-C_3H_2 and its deuterated counterpart and therefore show up to which extent the *c*-C_3H_2 deuteration is comparable to that of N_2H^+. As already suggested in Chapter 2, the fact that the highest deuteration level is seen towards the youngest protostar HH211 indicates that *c*-C_3H_2 is additionally deuterated on dust grains, most likely through hydrogen-deuterium exchange reactions. Current chemical models [Sipilä et al., 2016] are unable to reproduce the present results, which suggests that the chemical network of dust-grain reactions involving *c*-C_3H_2 and *c*-C_3HD is still incomplete and/or the reaction rates should be re-evaluated.

The interstellar phosphorus chemistry still remains a mystery among astrochemists. So far there have been detections of only PN and PO towards molecular clouds, which makes it hard for astronomers to unveil their chemistry. In this work we focused on the very early phases of star formation, i.e. diffuse and translucent clouds, where we do not expect any high levels of elemental depletion. The (2-1) transitions of the molecules HCP, CP, PN and PO which we targeted in this thesis were not detected in the observed sources. Based on the new physical constraints, our current model predicts the corresponding (1-0) transitions to be detectable towards the two translucent clouds along the line of sight towards B0355+508. Nevertheless, both model and observations can still be improved in several ways. First of all, one could explore even further the possible formation and destruction routes of P-bearing species. In fact, many of these found in the literature and databases were either scientific guesses or based on the equivalent nitrogen-bearing reactions, which naturally introduces some level of uncertainty. Testing various new reactions and their reaction rates in the laboratory will help us to further elucidate the chemical network of phosphorus and make predictions for the molecular abundances with greater confidence. Furthermore, this work and previous studies have shown that the observed sources are highly heterogeneous, which makes the determination of their physical conditions (density, temperature and visual extinction) rather difficult. New observations of additional nitrogen-, oxygen- and sulfur-bearing species towards these clouds would help us benchmark the model and put additional constraints on their physical properties.

Maps of the ^{12}CO (1-0) emission shown in Pety et al. [2008] reveal that dense clumps

are located just 4″ away from the continuum source B0355+508 that lead to remarkably strong CO emission lines. These dense regions could probably cause collisional excitation (and thus emission) of the targeted (1-0) lines of HCP, CP, PN and PO that in turn could compensate for any absorption seen along the line of sight to the quasar. For this reason, we propose to perform future observations with interferometers (such as the JVLA) instead, which, thanks to their high angular resolution, will only be sensitive to the very narrow column of gas in front of the quasar, giving rise to pure absorption lines rather than showing any contamination effects from emission.

Laboratory. Since the Supersonic Jet Experiment has only been recently built we are considering several new technical implementations that can extend and improve its capabilities. One of these is the application of a quadrupole mass spectrometer (QMS), that could help us explore the chemistry within the jet expansion. The QMS is ionising any entering gas species, that subsequently pass through a quadrupole field, which is generated between 4 parallel rods. The entering ions are then selected based on their mass-to-charge ratio (m/q): for each interval of the applied AC voltage, there is one m/q ratio that resonates with the oscillating electric fields inside of the QMS and the corresponding ions can simply pass through without being deflected from their original trajectory. Such an aperture would help us discover what species are produced in our gas-discharge within the nozzle, and more importantly if the molecules of interest have also been produced with the given discharge conditions.

In addition, we are planning to further extend the frequency coverage of our radiation source, by using a new, active multiplier chain that will cover frequencies up to 1.6 THz. This will allow us to access a much larger part of the molecular spectrum and measure, in addition to pure rotational, also ro-vibrational transitions of astrochemically relevant species.

Another possible implementation that will introduce several new advantages is the so-called chirped-pulse technique. Traditional frequency-domain spectrometers can scan one frequency element at a time, which makes the acquisition of broadband spectra expensive and very time-consuming. The new generation of frequency generators called arbitrary waveform generators (AWG) can produce very short frequency pulses, with a frequency bandwidth of several gigahertz and a pulse duration of a few microseconds (or less). This could offer us the possibility of covering the entire molecular spectrum in a single jet pulse. Apart from much shorter acquisition times, this technique is helpful especially if we are searching for new lines with a large uncertainty and if we want to study large molecules with a rich rotational spectrum.

Finally, we are currently introducing a new production method of reactive species, in which precursor molecules are heated up to pyrolytic temperatures just before their adiabatic expansion into the vacuum chamber. The strong heating can lead to fragmentation of large molecules into smaller reactive compounds that are then stabilized under cryogenic and collision-free conditions within the jet. Technically this is done by extending our beam source with a high-temperature heating nozzle, where a small resevoir will allow molecules to briefly heat up. The nozzle is made out of robust material that can reach high temperatures of up to ~ 530 K and also maintain this temperature for several hours. Apart from

the right nozzle material, the design of this new beam source involves technical challenges like adjustable heating via an appropriate power supply and exact temperature monitoring via temperature sensors. This pyrolytic nozzle has proven to be highly beneficial when it comes to using non-gaseous probes as precursor molecules and producing reactive species that are mostly free of contamination [Jahn et al., 2017, McNaughton et al., 2011].

Appendix A

A study of the *c*-C_3HD/*c*-C_3H_2 ratio in low-mass star forming regions

A.1 Observed Spectra of *c*-C_3H_2 and its isotopologues toward the starless and protostellar core samples

In Figures A.1-A.16 we show the observed spectra toward all sources.

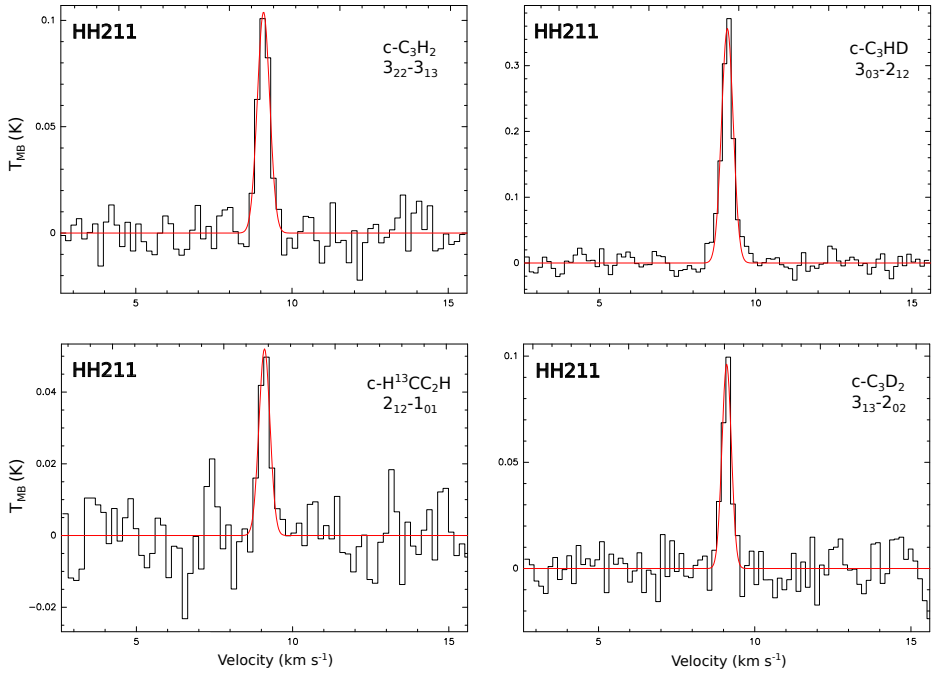

Figure A.1: Spectra of several isotopologues of *c*-C_3H_2 toward the protostellar core HH211. The red line plots the CLASS Gaussian fit.

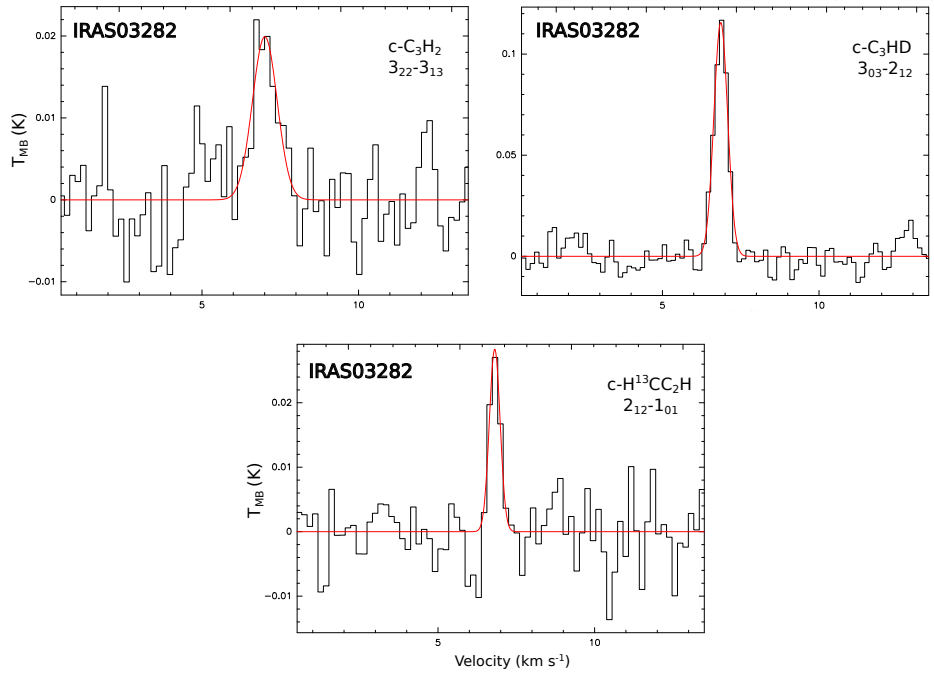

Figure A.2: Spectra of the isotopologues of c-C_3H_2 observed toward the protostellar core IRAS03282. The red line plots the CLASS Gaussian fit.

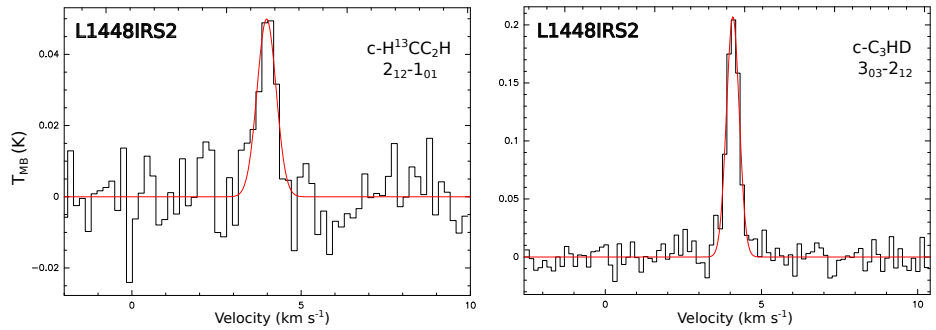

Figure A.3: Spectra of the isotopologues of c-C_3H_2 observed toward the protostellar core L1448IRS2. The red line plots the CLASS Gaussian fit.

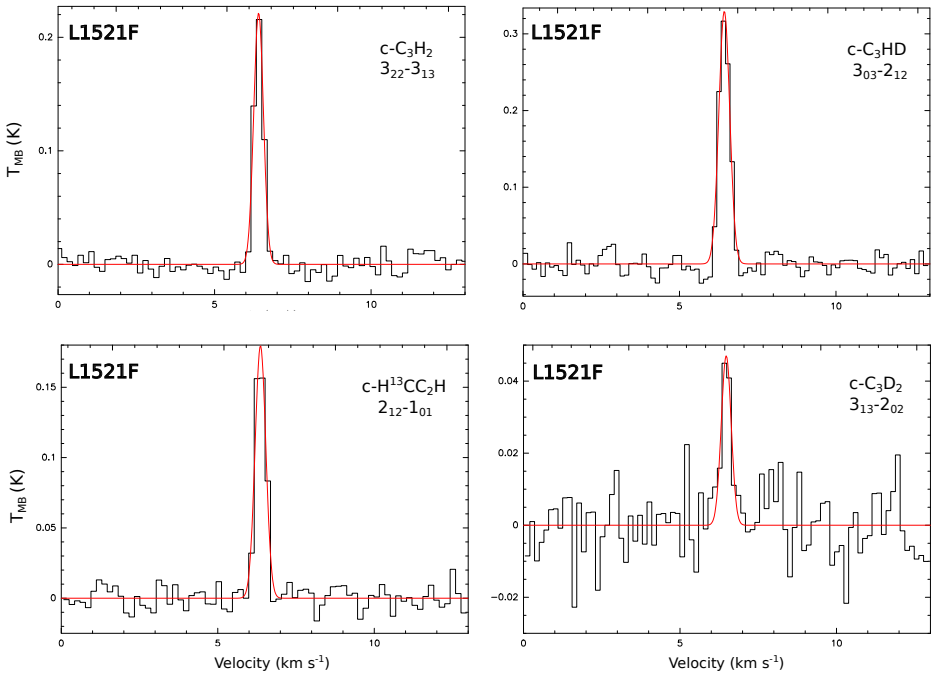

Figure A.4: Spectra of the isotopologues of c-C_3H_2 observed toward the protostellar core L1521F. The red line plots the CLASS Gaussian fit.

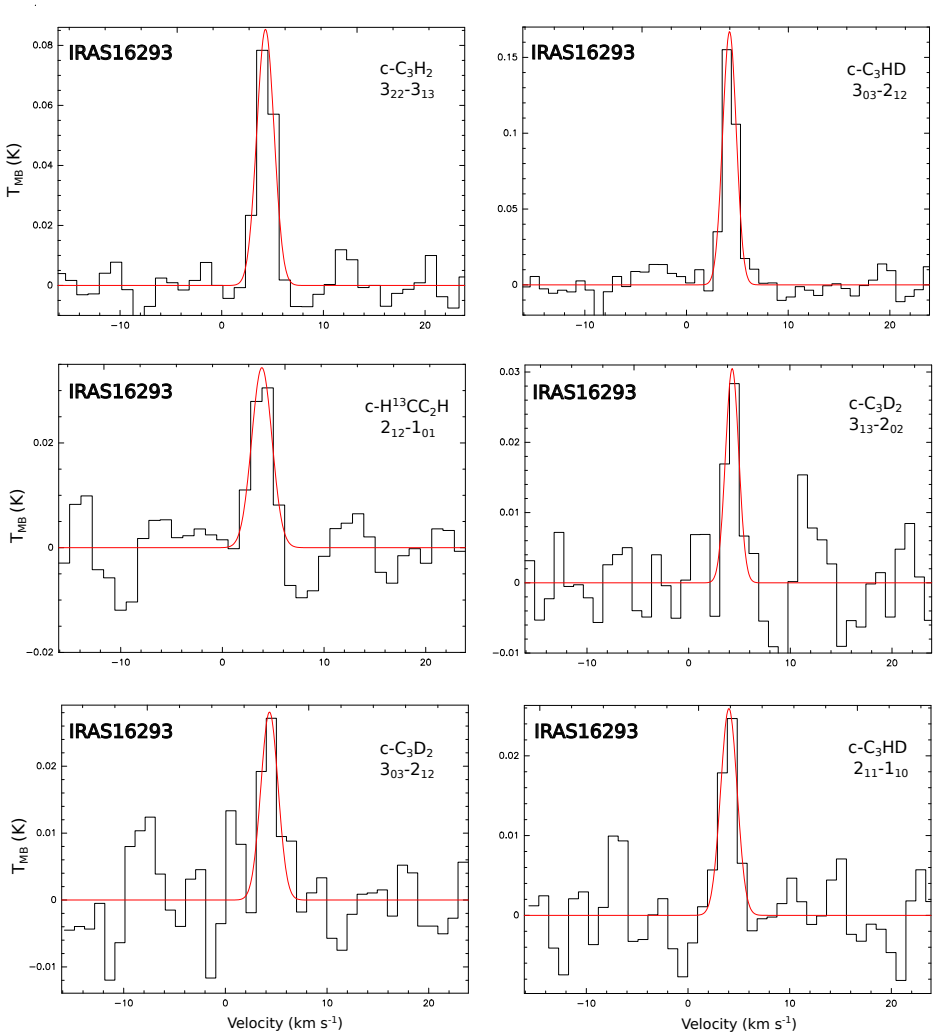

Figure A.5: Spectra of the isotopologues of c-C_3H_2 observed toward the protostellar core IRAS16293. The red line plots the CLASS Gaussian fit.

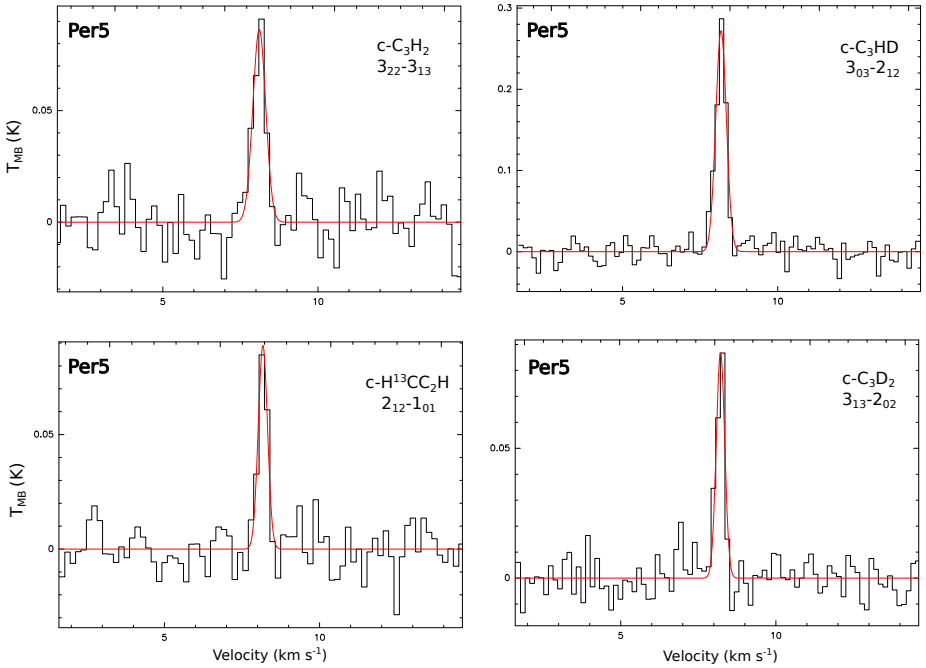

Figure A.6: Spectra of the isotopologues of c-C_3H_2 observed toward the protostellar core Per5. The red line plots the CLASS Gaussian fit.

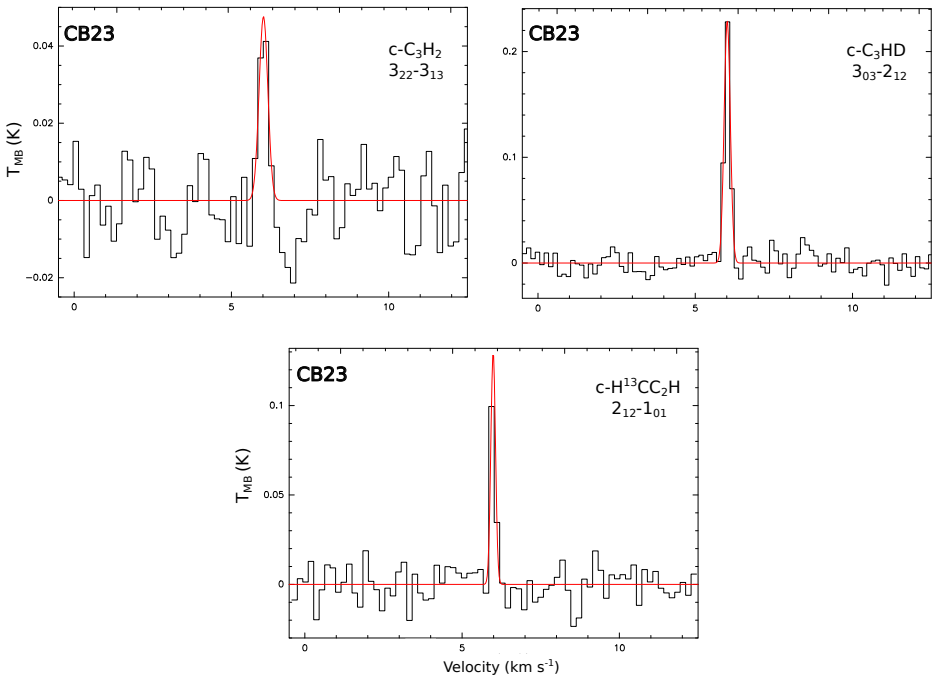

Figure A.7: Spectra of the isotopologues of c-C_3H_2 observed toward the starless core CB23. The red line plots the CLASS Gaussian fit.

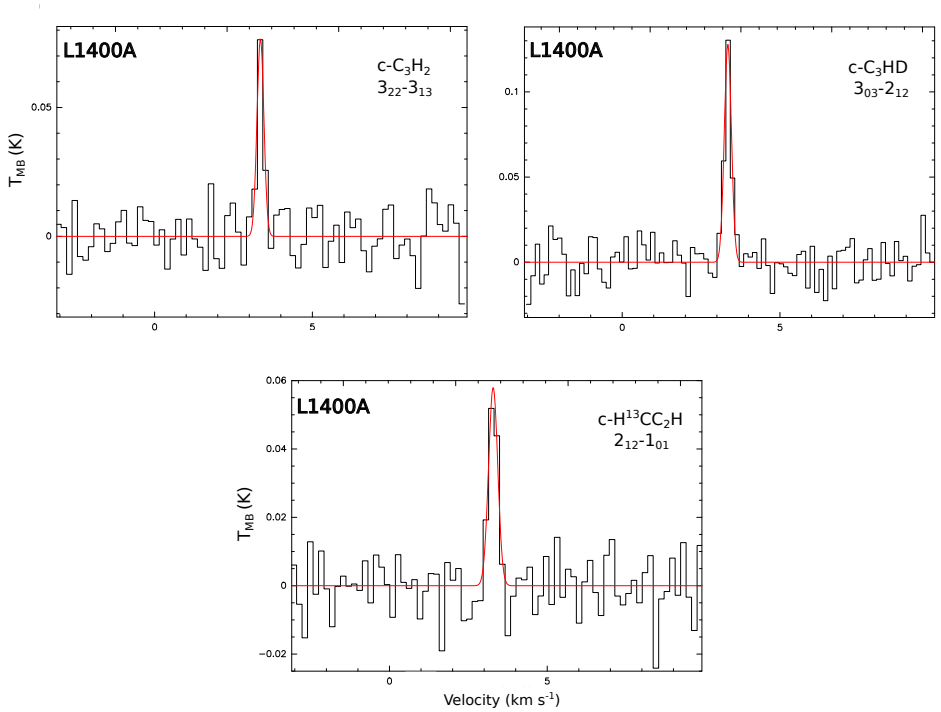

Figure A.8: Spectra of the isotopologues of c-C_3H_2 observed toward the starless core L1400A. The red line plots the CLASS Gaussian fit.

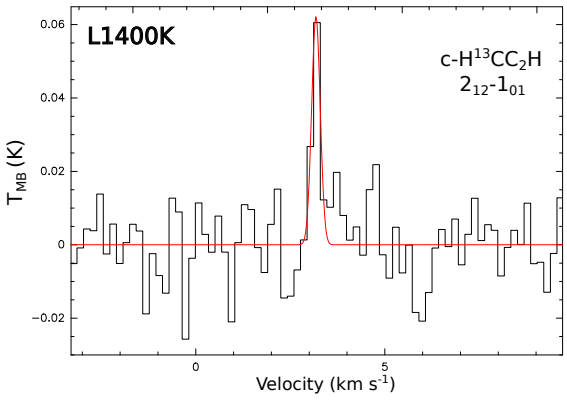

Figure A.9: Spectrum of the main species c-C_3H_2 observed toward the starless core L1400K. The red line plots the CLASS Gaussian fit.

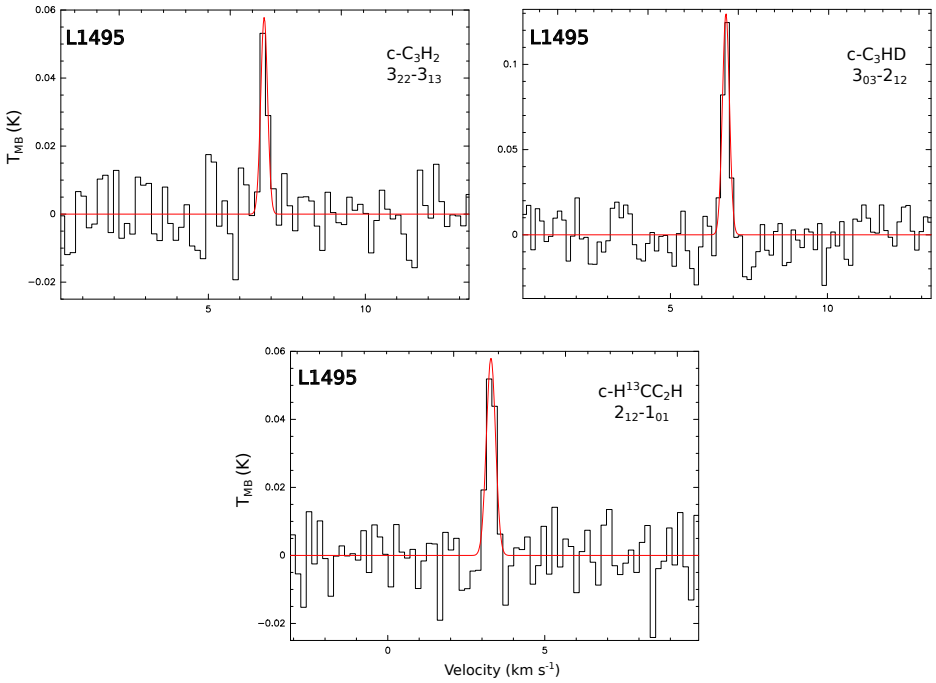

Figure A.10: Spectra of the isotopologues of c-C_3H_2 observed toward the starless core L1495. The red line plots the CLASS Gaussian fit.

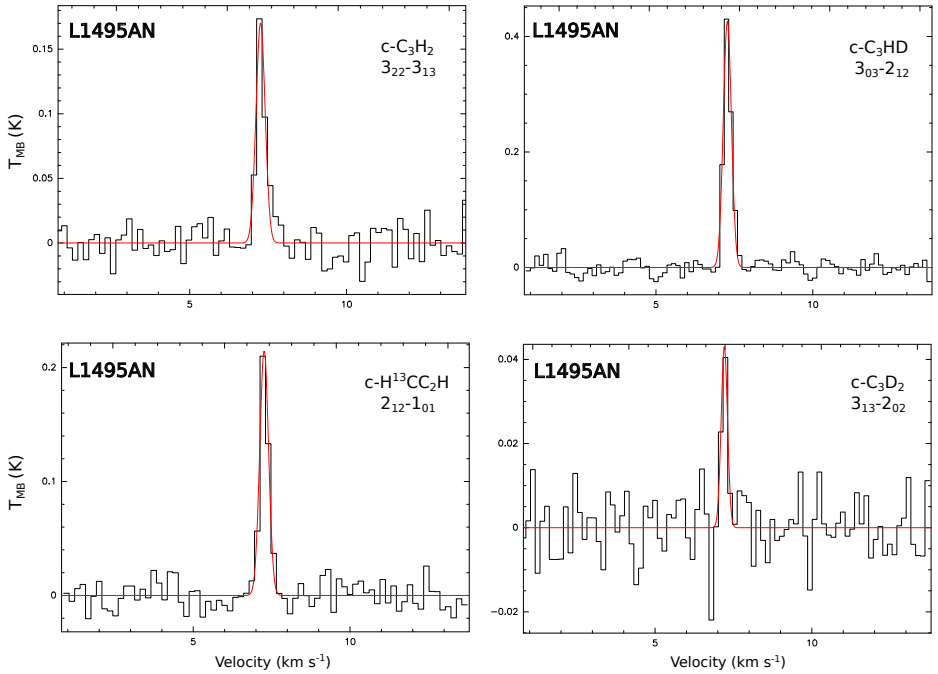

Figure A.11: Spectra of the isotopologues of c-C_3H_2 observed toward the starless core L1495AN. The red line plots the CLASS Gaussian fit.

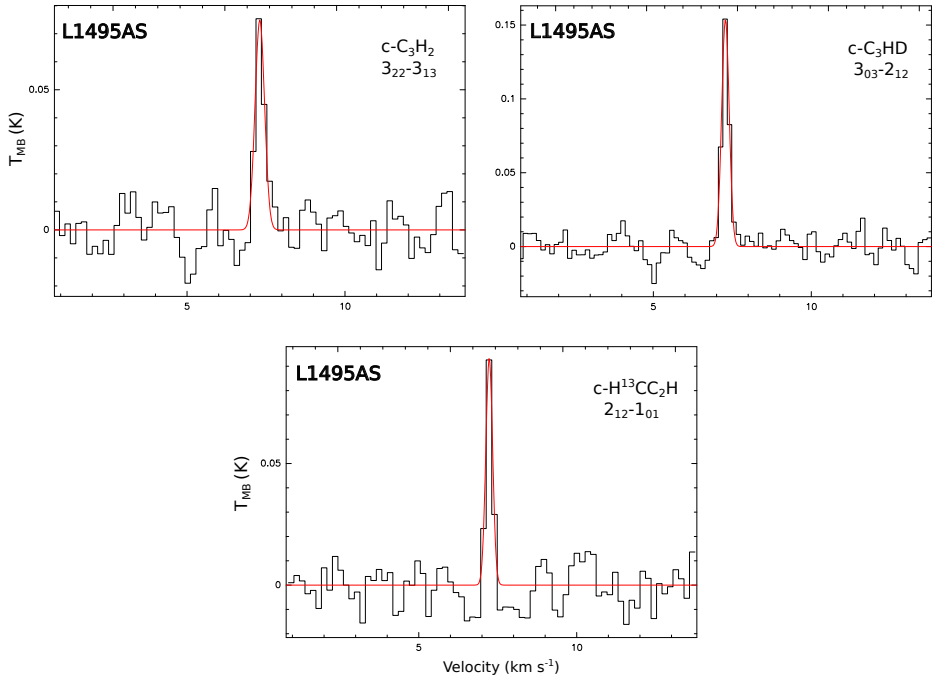

Figure A.12: Spectra of the isotopologues of c-C_3H_2 observed toward the starless core L1495AS. The red line plots the CLASS Gaussian fit.

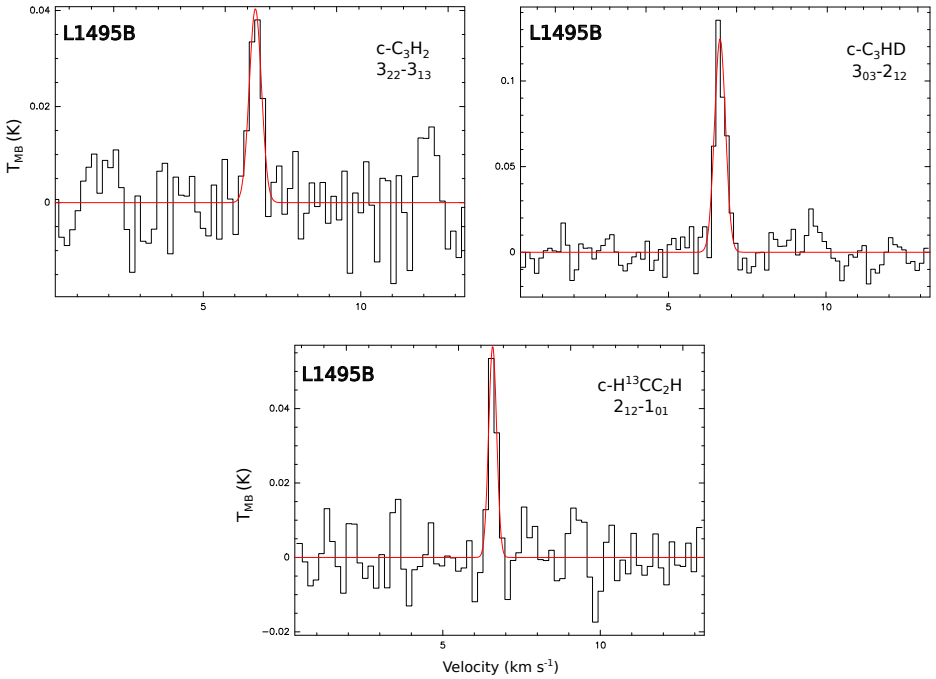

Figure A.13: Spectra of the isotopologues of c-C_3H_2 observed toward the starless core L1495B. The red line plots the CLASS Gaussian fit.

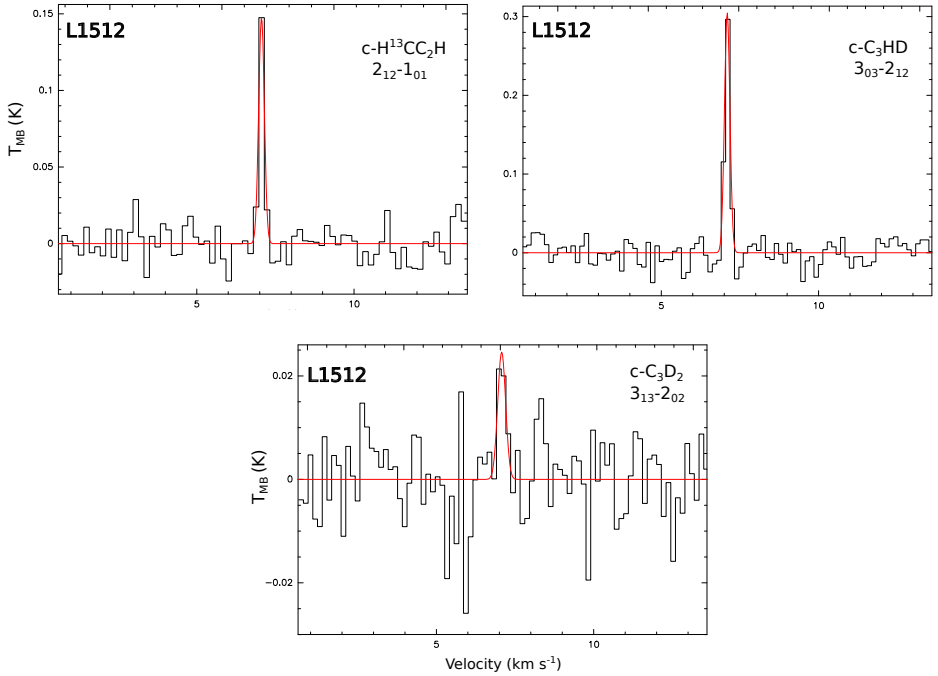

Figure A.14: Spectra of the isotopologues of c-C_3H_2 observed toward the starless core L1512. The red line plots the CLASS Gaussian fit.

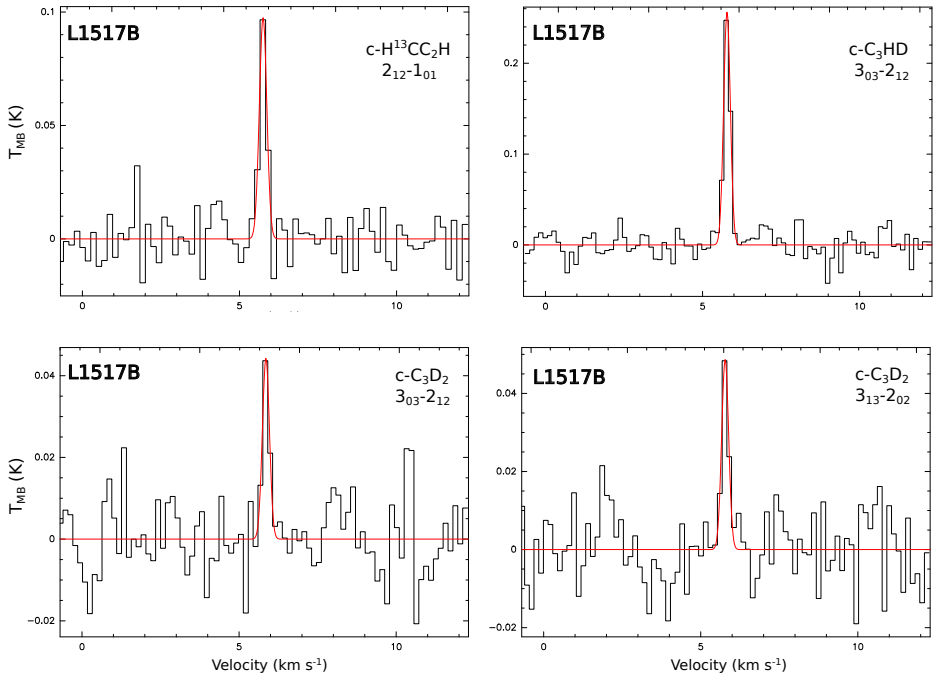

Figure A.15: Spectra of the isotopologues of c-C_3H_2 observed toward the starless core L1517B. The red line plots the CLASS Gaussian fit.

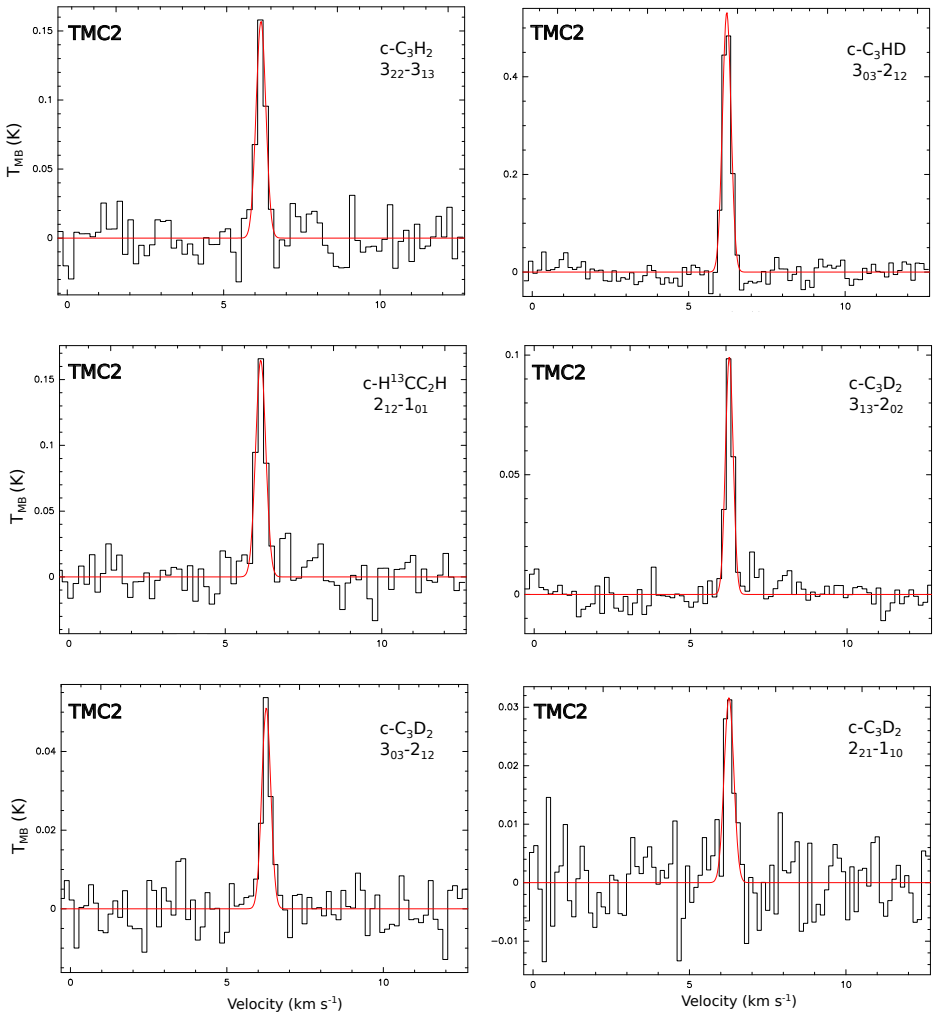

Figure A.16: Spectra of the isotopologues of c-C_3H_2 observed toward the pre-stellar core TMC2. The red line plots the CLASS Gaussian fit.

A.2 The c-C_3H_2 and c-C_3HD distribution across the pre-stellar core L1544

We use the chemical/physical model for L1544 described in Sipilä et al. [2016] to simulate the abundances of gaseous and solid c-C_3H_2, c-C_3HD and the ratio c-C_3HD/c-C_3H_2 as functions of distance from the core centre, defined by the position of the millimeter dust continuum peak. Figure A.17 shows the abundances of the gaseous and solid species as well as the deuteration level c-C_3HD/c-C_3H_2 at three different times: 10^4, 10^5 and 10^6 yr. The depletion of c-C_3H_2 and c-C_3HD toward the center increases with the evolution of the core, as expected. At $t = 10^6$ yr the depletion zone of both species reaches a few 1000 AU. Here we confirm the fact that c-C_3H_2 as well as its deuterated counterpart stop tracing the zone where high levels of deuterium fraction are present, as already suggested in §2.4.2. The right panel of Figure A.17 shows that the total deuteration level of gaseous and solid c-C_3H_2 is less than 20% at $t = 10^6$ yr. This means that one of the most advanced gas-grain chemical codes including deuterium fractionation is not able to reproduce the large deuterium fraction of 23% observed in c-C_3H_2 toward the young protostar HH211 (which represents the next evolutionary state after the evolved pre-stellar core L1544), suggesting either that some important surface processes are missing in the current chemical scheme, or that the relative rates of the currently-included processes need to be modified.

A.3 Error estimation of the H_2 column density

One source of uncertainty in the estimation of $N(H_2)$, which is derived from the SPIRE images at (250, 350, 500) μm, is the flux uncertainty. The flux calibration of the SPIRE photometer is based on Neptune. Being a bright source, Neptune produces high SNR spectra and has a well understood submillimeter spectrum. The calibration flux densities for Neptune at (250, 350, 500) μm are (160, 100, 60) Jy and the absolute flux uncertainty for Neptune is estimated to be 4%, which corresponds to the absolute calibration uncertainty. Considering also the relative calibration and the extended source calibration uncertainty, the total flux uncertainty for the SPIRE bands amounts to 7% according to the SPIRE Handbook.

The column density of H_2 and its total error are estimated by applying a Monte Carlo fitting procedure with 1000 iterations. After every iteration, the noise level $\epsilon_{\rm noise}$ is added to every map, pixel by pixel, following the equation:

$$\epsilon_{\rm noise} = \epsilon_1 \cdot 0.07 \cdot I_\nu + \delta I_\nu \cdot \epsilon_2,$$

where I_ν is the detected intensity at a frequency ν, $\epsilon_{1,2}$ describes a random number taken from a standard normal distribution and δI_ν is the statistical error on the flux density value in each pixel, produced by the pipeline. The fitting method gives a cube of $N = 1000$ maps. The fist map with $\epsilon_{\rm noise}$=0 gives the resulting $N(H_2)$, while its uncertainty is given by the standard deviation of the remaining maps.

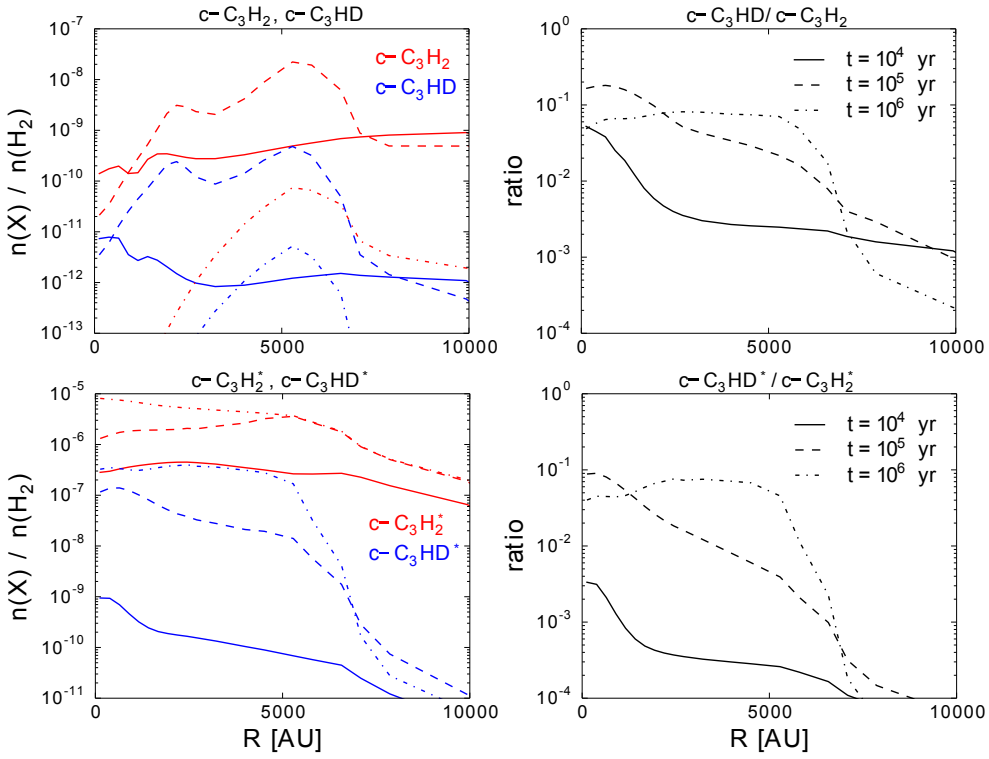

Figure A.17: Abundance profiles of gaseous and solid c-C_3H_2 (red), c-C_3HD (blue) and the ratio c-C_3HD/c-C_3H_2 toward L1544, as functions of distance, from the core center to a radius of 10^4AU. The solid species are marked with an asterisk. The abundances and abundance ratios are plotted at three different times: 10^4, 10^5 and 10^6 yr.

Appendix B

Rotational spectroscopy of the HCCO and DCCO radicals in the millimeter and submillimeter range

B.1 Theoretical considerations

B.1.1 Renner-Teller Effect

The coupling between the vibrational angular and the electron orbital momenta (with $\Lambda > 0$) in a linear molecule is known as the Renner-Teller interaction [Herzberg and Teller, 1933, Renner, 1934]. This effect occurs when the nuclei are displaced within a bending vibration and a vibrational angular momentum with the projection number $l = 0, 1, 2, ...$ is induced. The resulting vibronic angular momentum K around the molecular axis is then equal to $K = | \pm \Lambda \pm l |$, meaning that a doubly degenerate electronic state (with $\Lambda > 0$) is split into two components [Brown, 1977, Lee et al., 1984]. In the case of the ketenyl radical, the unpaired electron occupies a Π orbital that lies perpendicular to the molecular plane. When the H-atom is bent away from the linear molecular axis, the $1^2\Pi_u$ degeneracy is cancelled and split into two components: a $1^2A''(1^2\Pi)$ bent component described by an attractive potential with respect to the bending coordinate, and a $1^2A'(1^2\Pi)$ linear component described by a repulsive potential [Szalay et al., 1996, Aarts, 1978]. The anomalous features observed in the spectrum are ascribed to the fact that $^2A'$ is a low-lying excited state that interacts with the ground state $^2A''$ resulting to a non-negligible perturbation of the rotational levels. A small energy splitting between these two states would mean a stronger interaction of the systems, and thus a stronger perturbation. Using the spin-rotation coupling obtained from the submillimeter spectrum, Endo and Hirota [1987] predicted that the excited electronic state $1^2A'$ lies only 777 K above the ground state $1^2A''$, assuming that the unpaired electron is mostly localized at the carbon atom. However, Szalay et al. [1992] showed that the unpaired electron has a considerable density on both the oxygen and the carbon atom, which led finally to an energy splitting of 1727 K [Szalay et al., 1996].

Appendix C

The first steps of interstellar phosphorus chemistry

C.1 The depletion of Phosphorus

The main advantage of studying the early phases of star formation is to avoid high levels of elemental depletion and thus to constrain the initial abundances used in our model to their cosmic values. This is crucial especially for phosphorus, as the small number of detections of P-bearing species in the ISM makes the determination of the P-depletion level quite difficult. In order to obtain an approximate estimation of the expected depletion level, we apply a dynamical model with time-dependent physical conditions that allows us to follow the chemical evolution of P-bearing species from a diffuse to a dense cloud. In particular we simulate a "cold" stage in which a free-fall collapse takes place within 10^6 yr [Vasyunin and Herbst, 2013a, Garrod and Herbst, 2006]. During that time the density increases from $n(\mathrm{H}) = 300\,\mathrm{cm}^{-3}$ to $10^5\,\mathrm{cm}^{-3}$ and the visual extinction rises from 1 to 40 mag. The gas temperature decreases from 40 to 10 K, while the dust temperature drops slightly, from 20 to 10 K. Finally, the cosmic-ray ionization rate also changes from $1.7 \times 10^{-16}\,\mathrm{s}^{-1}$ to $1.3 \times 10^{-17}\,\mathrm{s}^{-1}$. We note here that the changes in the above-mentioned physical constants happen within 10^6 yr, while the total chemical evolution is over 10^7 yr. This means that between 10^6 and 10^7 yr the model becomes static with the above parameters retaining the values they reached at 10^6 yr. That way, we simulate a long-lived collapse that provides enough time for chemical processes such as depletion to evolve.

As a first step, we plot the chemical evolution of the sum of abundances of gas-phase and solid-phase P-bearing species separately (see lower left panel of Figure C.1). It is clearly visible how at late times, the gas-phase species decrease, and in return the grain species increase in abundance due to depletion. In particular, the sum of the gas-phase abundances of P-bearing species reduces by a factor of ~ 3000 at $t = 10^7$ yr. This does not correspond to the elemental depletion, but it indicates the redistribution of phosphorus between the gas phase and the dust grains. The right-hand panel of Figure C.1 shows the time-dependent abundances of the main carriers of phosphorus in the gas phase and on

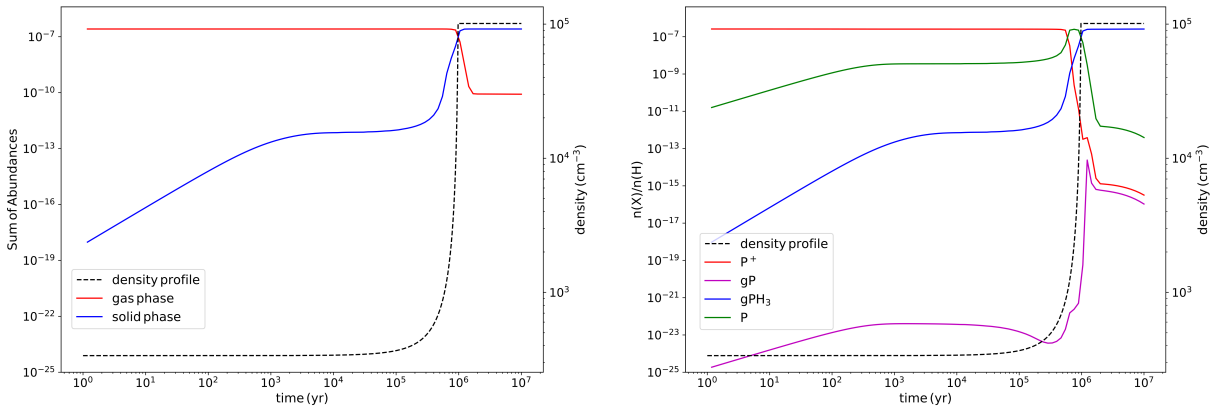

Figure C.1: Results of our dynamical model that simulates the transition from a diffuse to a dense cloud. The left panel shows the sum of abundances of all P-bearing species in the gas phase (red line) and the solid phase (blue line) as a function of time. The right panel illustrates the chemical evolution of the main carriers of phosphorus in the gas and solid phase: P^+, P, gP and gPH_3. In both figures the density profile of the free-fall collapse is depicted as a black dashed line.

grains. The species that experience the largest change during the transition from diffuse to dense cloud are P^+ and gPH_3. The P^+ abundance strongly decreases down to $\sim 10^{-16}$, mainly through its destruction reactions with OH, CH_4, S, and H_2. Atomic P decreases significantly because of freeze-out on dust grains, which is also evident through the increase in gP. According to the model almost all P that freezes out, quickly reacts with hydrogen on grains, and finally forms gPH_3 (after successive hydrogenation), which reaches a high abundance of $\sim 2.5 \times 10^{-7}$ at the end of our simulations.

Finally, Figure C.2 shows the time-dependent abundances of PN, PO, HCP, CP, PH_3 in the gas phase (left panel) and the corresponding grain species (right panel). All species reach their peak abundances at around 10^6 yr, followed by a strong decrease due to freeze-out on dust grains as well as through their reaction with H_3^+ (at $t = 10^6 - 10^7$ yr). The species PN, PH_3, and HCP show a more significant freeze-out than CP and PO, as they are the most abundant molecules in the gas-phase at $t = 10^6$ yr. The freeze-out process is also clearly evident from the substantial increase of the corresponding grain species once high densities of $\sim 10^4 - 10^5\,\mathrm{cm}^{-3}$ are reached (see right panel of Figure C.2.)

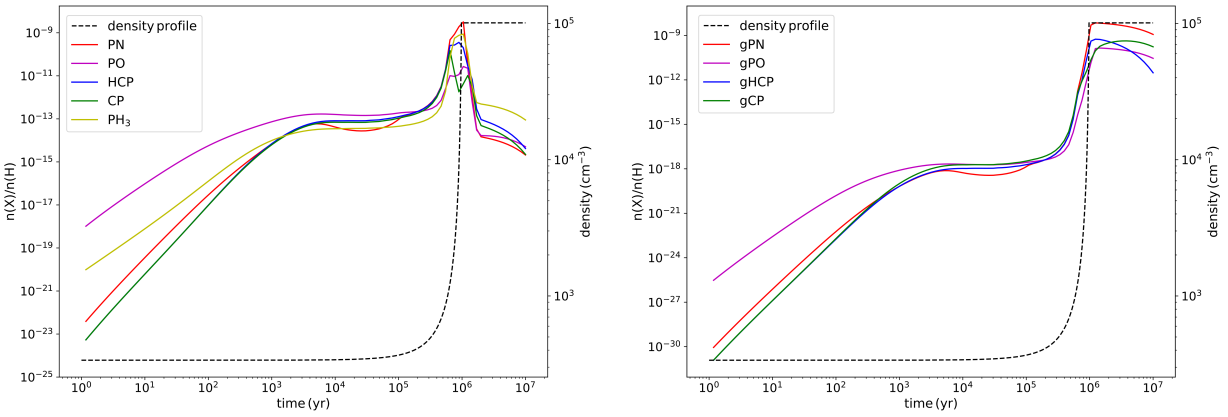

Figure C.2: Chemical evolution of PN, PO, HCP, CP and PH_3 (left panel) and the corresponding grain species (right panel) as a function of time based on our dynamical model (diffuse to dense cloud). The black dashed line illustrates the density profile of the free-fall collapse. The gPH_3 abundance is shown in Figure C.1.

Bibliography

J. F. M. Aarts. The renner effect in 2Π electronic states of linear triatomic molecules. *Molecular Physics*, 35(6):1785–1803, 1978. doi: 10.1080/00268977800101351. URL `https://doi.org/10.1080/00268977800101351`.

N. G. Adams, B. J. McIntosh, and D. Smith. Production of phosphorus-containing molecules in interstellar clouds. *A&A*, 232:443, Jun 1990.

I. Agudo. Polami: Full-Polarization Monitoring Of Agn At Millimeter Wavelengths With The Iram 30M Telescope. In *Submm/mm/cm QUESO Workshop 2017 (QUESO2017)*, page 1, Oct 2017. doi: 10.5281/zenodo.1038049.

M. Agúndez and V. Wakelam. Chemistry of Dark Clouds: Databases, Networks, and Models. *Chemical Reviews*, 113:8710–8737, December 2013. doi: 10.1021/cr4001176.

M. Agúndez, J. Cernicharo, and M. Guélin. Discovery of Phosphaethyne (HCP) in Space: Phosphorus Chemistry in Circumstellar Envelopes. *ApJL*, 662(2):L91–L94, Jun 2007. doi: 10.1086/519561.

M. Agúndez, J. Cernicharo, L. Decin, P. Encrenaz, and D. Teyssier. Confirmation of Circumstellar Phosphine. *ApJL*, 790:L27, August 2014a. doi: 10.1088/2041-8205/790/2/L27.

M. Agúndez, J. Cernicharo, and M. Guélin. New molecules in IRC +10216: confirmation of C_5S and tentative identification of MgCCH, NCCP, and SiH_3CN. *A&A*, 570:A45, Oct 2014b. doi: 10.1051/0004-6361/201424542.

M. Agúndez, J. Cernicharo, and M. Guélin. Discovery of interstellar ketenyl (HCCO), a surprisingly abundant radical. *A&A*, 577:L5, May 2015. doi: 10.1051/0004-6361/201526317.

Y. Aikawa, V. Wakelam, F. Hersant, R. T. Garrod, and E. Herbst. From Prestellar to Protostellar Cores. II. Time Dependence and Deuterium Fractionation. *ApJ*, 760:40, November 2012. doi: 10.1088/0004-637X/760/1/40.

P. André, A. Men'shchikov, S. Bontemps, V. Könyves, F. Motte, N. Schneider, P. Didelon, V. Minier, P. Saraceno, D. Ward-Thompson, J. di Francesco, G. White, S. Molinari,

L. Testi, A. Abergel, M. Griffin, T. Henning, P. Royer, B. Merín, R. Vavrek, M. Attard, D. Arzoumanian, C. D. Wilson, P. Ade, H. Aussel, J.-P. Baluteau, M. Benedettini, J.-P. Bernard, J. A. D. L. Blommaert, L. Cambrésy, P. Cox, A. di Giorgio, P. Hargrave, M. Hennemann, M. Huang, J. Kirk, O. Krause, R. Launhardt, S. Leeks, J. Le Pennec, J. Z. Li, P. G. Martin, A. Maury, G. Olofsson, A. Omont, N. Peretto, S. Pezzuto, T. Prusti, H. Roussel, D. Russeil, M. Sauvage, B. Sibthorpe, A. Sicilia-Aguilar, L. Spinoglio, C. Waelkens, A. Woodcraft, and A. Zavagno. From filamentary clouds to prestellar cores to the stellar IMF: Initial highlights from the Herschel Gould Belt Survey. *A&A*, 518:L102, July 2010. doi: 10.1051/0004-6361/201014666.

V. G. Anicich. A Survey of Bimolecular Ion-Molecule Reactions for Use in Modeling the Chemistry of Planetary Atmospheres, Cometary Comae, and Interstellar Clouds: 1993 Supplement. *ApJS*, 84:215, Feb 1993. doi: 10.1086/191752.

M. Asplund, N. Grevesse, and A. Jacques Sauval. The solar chemical composition. *Nuclear Physics A*, 777:1–4, October 2006. doi: 10.1016/j.nuclphysa.2005.06.010.

A. Bacmann, B. Lefloch, C. Ceccarelli, J. Steinacker, A. Castets, and L. Loinard. CO Depletion and Deuterium Fractionation in Prestellar Cores. *ApJL*, 585:L55–L58, March 2003. doi: 10.1086/374263.

A. Bacmann, V. Taquet, A. Faure, C. Kahane, and C. Ceccarelli. Detection of complex organic molecules in a prestellar core: a new challenge for astrochemical models. *A&A*, 541:L12, May 2012. doi: 10.1051/0004-6361/201219207.

S. Bailleux, M. Bogey, C. Demuynck, Y. Liu, and A. Walters. Millimeter-Wave Spectroscopy of PO in Excited Vibrational States up to v=7. *Journal of Molecular Spectroscopy*, 216(2):465–471, Dec 2002. doi: 10.1006/jmsp.2002.8665.

M. B. Bell, L. W. Avery, H. E. Matthews, P. A. Feldman, J. K. G. Watson, S. C. Madden, and W. M. Irvine. A study of C3HD in cold interstellar clouds. *ApJ*, 326:924–930, March 1988. doi: 10.1086/166150.

P. J. Benson, P. Caselli, and P. C. Myers. Dense Cores in Dark Clouds. XI. A Survey for N_2H^+, C_3H_2, and CCS. *ApJ*, 506:743–757, October 1998. doi: 10.1086/306276.

E. A. Bergin, D. R. Ciardi, C. J. Lada, J. Alves, and E. A. Lada. Molecular Excitation and Differential Gas-Phase Depletions in the IC 5146 Dark Cloud. *ApJ*, 557:209–225, August 2001. doi: 10.1086/321625.

O. Biham, I. Furman, V. Pirronello, and G. Vidali. Master Equation for Hydrogen Recombination on Grain Surfaces. *ApJ*, 553(2):595–603, Jun 2001. doi: 10.1086/320975.

L. Bizzocchi, C. Degli Esposti, L. Dore, and C. Puzzarini. Lamb-dip millimeter-wave spectroscopy of HCP: Experimental and theoretical determination of ^{31}P nuclear spin-rotation coupling constant and magnetic shielding. *Chemical Physics Letters*, 408(1): 13–18, Jun 2005. doi: 10.1016/j.cplett.2005.03.134.

L. Bizzocchi, V. Lattanzi, J. Laas, S. Spezzano, B. M. Giuliano, D. Prudenzano, C. Endres, O. Sipilä, and P. Caselli. Accurate sub-millimetre rest frequencies for $HOCO^+$ and $DOCO^+$ ions. *A&A*, 602:A34, June 2017. doi: 10.1051/0004-6361/201730638.

G. A. Blake, E. C. Sutton, C. R. Masson, and T. G. Phillips. Molecular abundances in OMC-1 - The chemical composition of interstellar molecular clouds and the influence of massive star formation. *ApJ*, 315:621–645, April 1987. doi: 10.1086/165165.

M. Bogey, C. Demuynck, J. L. Destombes, and H. Dubus. Molecular structure of cyclopropenylidene, H#58872 overlineCCC#58872H from the millimeter wave spectra of its isotopomers. *Journal of Molecular Spectroscopy*, 122:313–324, April 1987. doi: 10.1016/0022-2852(87)90007-5.

S. Bottinelli, C. Ceccarelli, B. Lefloch, J. P. Williams, A. Castets, E. Caux, S. Cazaux, S. Maret, B. Parise, and A. G. G. M. Tielens. Complex Molecules in the Hot Core of the Low-Mass Protostar NGC 1333 IRAS 4A. *ApJ*, 615:354–358, November 2004. doi: 10.1086/423952.

T. L. Bourke, P. C. Myers, N. J. Evans, II, M. M. Dunham, J. Kauffmann, Y. L. Shirley, A. Crapsi, C. H. Young, T. L. Huard, T. Y. Brooke, N. Chapman, L. Cieza, C. W. Lee, P. Teuben, and Z. Wahhaj. The Spitzer c2d Survey of Nearby Dense Cores. II. Discovery of a Low-Luminosity Object in the "Evolved Starless Core" L1521F. *ApJL*, 649:L37–L40, September 2006. doi: 10.1086/508161.

J. M. Brown. The effective hamiltonian for the renner-teller effect. *Journal of Molecular Spectroscopy*, 68:412–422, December 1977. doi: 10.1016/0022-2852(77)90245-4.

J. M. Brown and T. J. Sears. A reduced form of the spin-rotation hamiltonian for asymmetric-top molecules, with applications to ho2 and nh2. *Journal of Molecular Spectroscopy*, 75(1):111 – 133, 1979. doi: https://doi.org/10.1016/0022-2852(79)90153-X. URL `http://www.sciencedirect.com/science/article/pii/002228527990153X`.

S. Brünken, H. Gupta, C. A. Gottlieb, M. C. McCarthy, and P. Thaddeus. Detection of the Carbon Chain Negative Ion C_8H^- in TMC-1. *ApJL*, 664(1):L43–L46, Jul 2007. doi: 10.1086/520703.

S. Brünken, O. Sipilä, E. T. Chambers, J. Harju, P. Caselli, O. Asvany, C. E. Honingh, T. Kamiński, K. M. Menten, J. Stutzki, and S. Schlemmer. H_2D^+ observations give an age of at least one million years for a cloud core forming Sun-like stars. *Nature*, 516: 219–221, December 2014. doi: 10.1038/nature13924.

E. Caffau, S. Andrievsky, S. Korotin, L. Origlia, E. Oliva, N. Sanna, H.-G. Ludwig, and P. Bonifacio. GIANO Y-band spectroscopy of dwarf stars: Phosphorus, sulphur, and strontium abundances. *A&A*, 585:A16, January 2016. doi: 10.1051/0004-6361/201527272.

P. Caselli and C. Ceccarelli. Our astrochemical heritage. *A&A Rev.*, 20:56, October 2012. doi: 10.1007/s00159-012-0056-x.

P. Caselli, T. W. Hartquist, and O. Havnes. Grain-grain collisions and sputtering in oblique C-type shocks. *A&A*, 322:296–301, June 1997.

P. Caselli, C. M. Walmsley, M. Tafalla, L. Dore, and P. C. Myers. CO Depletion in the Starless Cloud Core L1544. *ApJL*, 523:L165–L169, October 1999. doi: 10.1086/312280.

P. Caselli, C. M. Walmsley, A. Zucconi, M. Tafalla, L. Dore, and P. C. Myers. Molecular Ions in L1544. II. The Ionization Degree. *ApJ*, 565:344–358, January 2002. doi: 10.1086/324302.

E. Caux, C. Kahane, A. Castets, A. Coutens, C. Ceccarelli, A. Bacmann, S. Bisschop, S. Bottinelli, C. Comito, F. P. Helmich, B. Lefloch, B. Parise, P. Schilke, A. G. G. M. Tielens, E. van Dishoeck, C. Vastel, V. Wakelam, and A. Walters. TIMASSS: the IRAS 16293-2422 millimeter and submillimeter spectral survey. I. Observations, calibration, and analysis of the line kinematics. *A&A*, 532:A23, August 2011. doi: 10.1051/0004-6361/201015399.

S. Cazaux, A. G. G. M. Tielens, C. Ceccarelli, A. Castets, V. Wakelam, E. Caux, B. Parise, and D. Teyssier. The Hot Core around the Low-mass Protostar IRAS 16293-2422: Scoundrels Rule! *ApJL*, 593:L51–L55, August 2003. doi: 10.1086/378038.

G. Cazzoli, C. Puzzarini, and A. V. Lapinov. Precise Laboratory Frequencies for the J<–J-1 (J=1, 2, 3, 4) Rotational Transitions of ^{13}CO. *ApJ*, 611(1):615–620, Aug 2004. doi: 10.1086/421992.

G. Cazzoli, L. Cludi, and C. Puzzarini. Microwave spectrum of P ^{14}N and P ^{15}N: Spectroscopic constants and molecular structure. *Journal of Molecular Structure*, 780:260–267, Jan 2006. doi: 10.1016/j.molstruc.2005.07.010.

G. Cazzoli, V. Lattanzi, S. Coriani, J. Gauss, C. Codella, A. A. Ramos, J. Cernicharo, and C. Puzzarini. Zeeman effect in sulfur monoxide. A tool to probe magnetic fields in star forming regions. *A&A*, 605:A20, Sep 2017. doi: 10.1051/0004-6361/201730858.

C. Ceccarelli, P. Caselli, D. Bockelée-Morvan, O. Mousis, S. Pizzarello, F. Robert, and D. Semenov. Deuterium Fractionation: The Ariadne's Thread from the Precollapse Phase to Meteorites and Comets Today. In Henrik Beuther, Ralf S. Klessen, Cornelis P. Dullemond, and Thomas Henning, editors, *Protostars and Planets VI*, page 859, Jan 2014. doi: 10.2458/azu_uapress_9780816531240-ch037.

C. Cecchi-Pestellini, W. W. Duley, and D. A. Williams. Hot Hydrogen in Diffuse Clouds. *ApJ*, 755(2):119, Aug 2012. doi: 10.1088/0004-637X/755/2/119.

J. Cernicharo, N. Marcelino, E. Roueff, M. Gerin, A. Jiménez-Escobar, and G. M. Muñoz Caro. Discovery of the Methoxy Radical, CH_3O, toward B1: Dust Grain and Gas-phase Chemistry in Cold Dark Clouds. *ApJL*, 759:L43, November 2012. doi: 10.1088/2041-8205/759/2/L43.

K. Cernis. Interstellar extinction in the vicinity of the reflection nebula NGC 1333 in Perseus. *Ap&SS*, 166:315–330, April 1990. doi: 10.1007/BF01094902.

S. Chandra and W. H. Kegel. Collisional rates for asymmetrical top molecules. *A&AS*, 142:113–118, February 2000. doi: 10.1051/aas:2000142.

Q. Chang and E. Herbst. Unified Microscopic-Macroscopic Monte Carlo Simulations of Complex Organic Molecule Chemistry in Cold Cores. *ApJ*, 819:145, March 2016. doi: 10.3847/0004-637X/819/2/145.

S. B. Charnley and T. J. Millar. The Chemistry of Phosphorus in Hot Molecular Cores. *MNRAS*, 270:570, Oct 1994. doi: 10.1093/mnras/270.3.570.

Y. N. Chin, C. Henkel, J. B. Whiteoak, N. Langer, and E. B. Churchwell. Interstellar sulfur isotopes and stellar oxygen burning. *A&A*, 305:960, Jan 1996.

J. F. Corby, B. A. McGuire, E. Herbst, and A. J. Remijan. The molecular chemistry of diffuse and translucent clouds in the line-of-sight to Sgr B2: Absorption by simple organic and inorganic molecules in the GBT PRIMOS survey. *A&A*, 610:A10, Feb 2018. doi: 10.1051/0004-6361/201730988.

A. Crapsi, P. Caselli, C. M. Walmsley, M. Tafalla, C. W. Lee, T. L. Bourke, and P. C. Myers. Observations of L1521F: A highly evolved starless core. *A&A*, 420:957–974, June 2004. doi: 10.1051/0004-6361:20035915.

A. Crapsi, P. Caselli, C. M. Walmsley, P. C. Myers, M. Tafalla, C. W. Lee, and T. L. Bourke. Probing the Evolutionary Status of Starless Cores through N_2H^+ and N_2D^+ Observations. *ApJ*, 619:379–406, January 2005. doi: 10.1086/426472.

S. E. Cummins, R. A. Linke, and P. Thaddeus. A survey of the millimeter-wave spectrum of Sagittarius B2. *ApJS*, 60:819–878, March 1986. doi: 10.1086/191102.

A. Dalgarno. The Chemistry of Diffuse Clouds. *Astrophysical Letters and Communications*, 26:153, Jan 1988.

A. Dalgarno and S. Lepp. Deuterium fractionation mechanisms in interstellar clouds. *ApJL*, 287:L47–L50, December 1984. doi: 10.1086/184395.

E. De Beck, T. Kamiński, N. A. Patel, K. H. Young, C. A. Gottlieb, K. M. Menten, and L. Decin. PO and PN in the wind of the oxygen-rich AGB star IK Tauri. *A&A*, 558: A132, October 2013. doi: 10.1051/0004-6361/201321349.

F. C. De Lucia, E. Herbst, G. M. Plummer, and G. A. Blake. The production of large concentrations of molecular ions in the lengthened negative glow region of a discharge. *J. Chem. Phys.*, 78(5):2312–2316, Mar 1983. doi: 10.1063/1.445004.

W. Demtröder. *Experimentalphysik III: Atome, Moleküle und Festkörper*. Springer-Verlag Berlin Heidelberg New York, 3. edition, 2010.

T. A. Dixon and R. C. Woods. The laboratory microwave spectrum of the cyanide radical in its X ^{2}Sigma $^+$ ground state. *J. Chem. Phys.*, 67(9):3956–3964, Nov 1977. doi: 10.1063/1.435412.

L. Dore. Using Fast Fourier Transform to compute the line shape of frequency-modulated spectral profiles. *Journal of Molecular Spectroscopy*, 221:93–98, September 2003. doi: 10.1016/S0022-2852(03)00203-0.

B. T. Draine. Photoelectric heating of interstellar gas. *ApJS*, 36:595–619, Apr 1978. doi: 10.1086/190513.

R. Dupuy, M. Bertin, G. Féraud, X. Michaut, P. Jeseck, M. Doronin, L. Philippe, C. Romanzin, and J. H. Fillion. Spectrally-resolved UV photodesorption of CH_4 in pure and layered ices. *A&A*, 603:A61, Jul 2017. doi: 10.1051/0004-6361/201730772.

M. Emprechtinger, P. Caselli, N. H. Volgenau, J. Stutzki, and M. C. Wiedner. The N{2}D^+/N{2}H$^+$ ratio as an evolutionary tracer of Class 0 protostars. *A&A*, 493: 89–105, January 2009. doi: 10.1051/0004-6361:200810324.

Y. Endo and E. Hirota. The submillimeter-wave spectrum of the HCCO radical. *J. Chem. Phys.*, 86:4319–4326, April 1987. doi: 10.1063/1.451892.

C. P. Endres, S. Schlemmer, P. Schilke, J. Stutzki, and H. S. P. Müller. The Cologne Database for Molecular Spectroscopy, CDMS, in the Virtual Atomic and Molecular Data Centre, VAMDC. *Journal of Molecular Spectroscopy*, 327:95–104, Sep 2016. doi: 10.1016/j.jms.2016.03.005.

A. Faure, M. Faure, P. Theulé, E. Quirico, and B. Schmitt. Hydrogen isotope exchanges between water and methanol in interstellar ices. *A&A*, 584:A98, December 2015. doi: 10.1051/0004-6361/201526499.

E. C. Fayolle, M. Bertin, C. Romanzin, H. A. M. Poderoso, L. Philippe, X. Michaut, P. Jeseck, H. Linnartz, K. I. Öberg, and J. H. Fillion. Wavelength-dependent UV photodesorption of pure N_2 and O_2 ices. *A&A*, 556:A122, Aug 2013. doi: 10.1051/0004-6361/201321533.

D. R. Flower, G. Pineau Des Forêts, and C. M. Walmsley. The abundances of nitrogen-containing molecules during pre-protostellar collapse. *A&A*, 456:215–223, September 2006. doi: 10.1051/0004-6361:20065375.

F. Fontani, A. Palau, P. Caselli, Á. Sánchez-Monge, M. J. Butler, J. C. Tan, I. Jiménez-Serra, G. Busquet, S. Leurini, and M. Audard. Deuteration as an evolutionary tracer in massive-star formation. *A&A*, 529:L7, May 2011. doi: 10.1051/0004-6361/201116631.

F. Fontani, V. M. Rivilla, P. Caselli, A. Vasyunin, and A. Palau. Phosphorus-bearing Molecules in Massive Dense Cores. *ApJL*, 822:L30, May 2016. doi: 10.3847/2041-8205/822/2/L30.

F. Fontani, V. M. Rivilla, F. F. S. van der Tak, C. Mininni, M. T. Beltrán, and P. Caselli. Origin of the PN molecule in star-forming regions: the enlarged sample. *MNRAS*, 489 (4):4530–4542, Nov 2019. doi: 10.1093/mnras/stz2446.

M. A. Frerking, W. D. Langer, and R. W. Wilson. The relationship between carbon monoxide abundance and visual extinction in interstellar clouds. *ApJ*, 262:590–605, November 1982. doi: 10.1086/160451.

R. K. Friesen, H. M. Kirk, and Y. L. Shirley. An Analysis of the Deuterium Fractionation of Star-forming Cores in the Perseus Molecular Cloud. *ApJ*, 765:59, March 2013. doi: 10.1088/0004-637X/765/1/59.

A. Fuente, D. G. Navarro, P. Caselli, M. Gerin, C. Kramer, E. Roueff, T. Alonso-Albi, R. Bachiller, S. Cazaux, and B. Commercon. Gas phase Elemental abundances in Molecular cloudS (GEMS). I. The prototypical dark cloud TMC 1. *A&A*, 624:A105, Apr 2019. doi: 10.1051/0004-6361/201834654.

R. T. Garrod. A new modified-rate approach for gas-grain chemical simulations. *A&A*, 491:239–251, November 2008. doi: 10.1051/0004-6361:200810518.

R. T. Garrod and E. Herbst. Formation of methyl formate and other organic species in the warm-up phase of hot molecular cores. *A&A*, 457:927–936, October 2006. doi: 10.1051/0004-6361:20065560.

R. T. Garrod, V. Wakelam, and E. Herbst. Non-thermal desorption from interstellar dust grains via exothermic surface reactions. *A&A*, 467(3):1103–1115, Jun 2007. doi: 10.1051/0004-6361:20066704.

M. Gerin, H. A. Wootten, F. Combes, F. Boulanger, W. L. Peters, III, T. B. H. Kuiper, P. J. Encrenaz, and M. Bogey. Deuterated C3H2 as a clue to deuterium chemistry. *A&A*, 173:L1–L4, February 1987.

E. L. Gibb, D. C. B. Whittet, W. A. Schutte, A. C. A. Boogert, J. E. Chiar, P. Ehrenfreund, P. A. Gerakines, J. V. Keane, A. G. G. M. Tielens, E. F. van Dishoeck, and O. Kerkhof. An Inventory of Interstellar Ices toward the Embedded Protostar W33A. *ApJ*, 536(1): 347–356, Jun 2000. doi: 10.1086/308940.

B. M. Giuliano, A. A. Gavdush, B. Müller, K. I. Zaytsev, T. Grassi, A. V. Ivlev, M. E. Palumbo, G. A. Baratta, C. Scirè, G. A. Komand in, S. O. Yurchenko, and P. Caselli. Broadband spectroscopy of astrophysical ice analogues. I. Direct measurement of the complex refractive index of CO ice using terahertz time-domain spectroscopy. *A&A*, 629:A112, Sep 2019. doi: 10.1051/0004-6361/201935619.

B. Godard, E. Falgarone, and G. Pineau des Forêts. Chemical probes of turbulence in the diffuse medium: the TDR model. *A&A*, 570:A27, Oct 2014. doi: 10.1051/0004-6361/201423526.

C. A. Gottlieb, P. C. Myers, and P. Thaddeus. Precise Millimeter-Wave Laboratory Frequencies for CS and $C^{34}S$. *ApJ*, 588(1):655–661, May 2003. doi: 10.1086/368378.

H. J. Habing. The interstellar radiation density between 912 A and 2400 A. *Bull. Astron. Inst. Netherlands*, 19:421, Jan 1968.

T. I. Hasegawa and E. Herbst. New gas-grain chemical models of quiscent dense interstellar clouds :the effects of H2 tunnelling reactions and cosmic ray induced desorption. *MNRAS*, 261:83–102, Mar 1993. doi: 10.1093/mnras/261.1.83.

T. I. Hasegawa, E. Herbst, and C. M. Leung. Models of Gas-Grain Chemistry in Dense Interstellar Clouds with Complex Organic Molecules. *ApJS*, 82:167, Sep 1992. doi: 10.1086/191713.

A. N. Heays, A. D. Bosman, and E. F. van Dishoeck. Photodissociation and photoionisation of atoms and molecules of astrophysical interest. *A&A*, 602:A105, Jun 2017. doi: 10.1051/0004-6361/201628742.

E. Herbst and C. M. Leung. Gas-phase production of complex hydrocarbons, cyanopolyynes, and related compounds in dense interstellar clouds. *ApJS*, 69:271–300, February 1989. doi: 10.1086/191314.

E. Herbst and E. F. van Dishoeck. Complex Organic Interstellar Molecules. *ARA&A*, 47:427–480, September 2009. doi: 10.1146/annurev-astro-082708-101654.

C. Herzberg and E. Teller. Schwingungsstruktur der elektronenübergänge bei mehratomigen molekülen. *Z. Physik. Chem.*, 21:410, 1933.

R. H. Hildebrand. The Determination of Cloud Masses and Dust Characteristics from Submillimetre Thermal Emission. *QJRAS*, 24:267, September 1983.

E. Hirota. *High-Resolution spectroscopy of Transient Molecules*. Springer-Verlag Berlin Heidelberg, 1985.

R. L. Hudson and M. J. Loeffler. Ketene Formation in Interstellar Ices: A Laboratory Study. *ApJ*, 773:109, August 2013. doi: 10.1088/0004-637X/773/2/109.

N. Indriolo and B. J. McCall. Investigating the Cosmic-Ray Ionization Rate in the Galactic Diffuse Interstellar Medium through Observations of H^+_3. *ApJ*, 745:91, January 2012. doi: 10.1088/0004-637X/745/1/91.

M. K. Jahn, J.-U. Grabow, M. J. Travers, D. Wachsmuth, P. D. Godfrey, and D. McNaughton. The radio spectra of planar aromatic heterocycles: how to quantify and predict the negative inertial defects. *Physical Chemistry Chemical Physics (Incorporating Faraday Transactions)*, 19(13):8970–8976, Jan 2017. doi: 10.1039/C6CP07487A.

S. V. Jerosimić. Calculation of the magnetic hyperfine structure in the ground electronic state of HCCO. *Journal of Molecular Spectroscopy*, 242:139–149, April 2007. doi: 10.1016/j.jms.2007.02.026.

I. Jiménez-Serra, P. Caselli, J. Martín-Pintado, and T. W. Hartquist. Parametrization of C-shocks. Evolution of the sputtering of grains. *A&A*, 482:549–559, May 2008. doi: 10.1051/0004-6361:20078054.

I. Jiménez-Serra, A. I. Vasyunin, P. Caselli, N. Marcelino, N. Billot, S. Viti, L. Testi, C. Vastel, B. Lefloch, and R. Bachiller. The Spatial Distribution of Complex Organic Molecules in the L1544 Pre-stellar Core. *ApJL*, 830:L6, October 2016. doi: 10.3847/2041-8205/830/1/L6.

I. Jiménez-Serra, S. Viti, D. Quénard, and J. Holdship. The Chemistry of Phosphorus-bearing Molecules under Energetic Phenomena. *ApJ*, 862(2):128, Aug 2018. doi: 10.3847/1538-4357/aacdf2.

I. T. N. Jones and Kyle D. Bayes. Detection of steady-state free-radical concentrations by photoionization. *Journal of the American Chemical Society*, 94(19):6869–6871, 1972. doi: 10.1021/ja00774a057. URL `https://doi.org/10.1021/ja00774a057`.

M. Jura and D. G. York. Observations of interstellar chlorine and phosphorus. *ApJ*, 219:861–869, February 1978. doi: 10.1086/155847.

N. Katz, I. Furman, O. Biham, V. Pirronello, and G. Vidali. Molecular Hydrogen Formation on Astrophysically Relevant Surfaces. *ApJ*, 522(1):305–312, Sep 1999. doi: 10.1086/307642.

E. Keto and P. Caselli. Dynamics and depletion in thermally supercritical starless cores. *MNRAS*, 402:1625–1634, March 2010. doi: 10.1111/j.1365-2966.2009.16033.x.

J. M. Kirk, D. Ward-Thompson, and P. André. The initial conditions of isolated star formation - VI. SCUBA mappingof pre-stellar cores. *MNRAS*, 360:1506–1526, July 2005. doi: 10.1111/j.1365-2966.2005.09145.x.

G. Klapper, F. Lewen, R. Gendriesch, S. P. Belov, and G. Winnewisser. Sub-Doppler Measurements of the Rotational Spectrum of $^{13}C\ ^{16}O$. *Journal of Molecular Spectroscopy*, 201(1):124–127, May 2000. doi: 10.1006/jmsp.2000.8071.

R. S. Klessen and S. C. O. Glover. Physical Processes in the Interstellar Medium. *Saas-Fee Advanced Course*, 43:85, Jan 2016. doi: 10.1007/978-3-662-47890-5_2.

S. Kong, J. C. Tan, P. Caselli, and F. Fontani. The Deuteration Clock for Massive Starless Cores. 75:337–341, May 2015. doi: 10.1051/eas/1575068.

J. H. Lacy, R. Knacke, T. R. Geballe, and A. T. Tokunaga. Detection of absorption by H2 in molecular clouds: A direct measurement of the H2:CO ratio. *ApJL*, 428:L69–L72, June 1994. doi: 10.1086/187395.

E. F. Ladd, F. C. Adams, S. Casey, J. A. Davidson, G. A. Fuller, D. A. Harper, P. C. Myers, and R. Padman. Far-infrared and submillimeter-wavelength observations of star-forming dense cores. I - Spectra. *ApJ*, 366:203–220, January 1991. doi: 10.1086/169553.

R. B. Larson. Numerical calculations of the dynamics of collapsing proto-star. *MNRAS*, 145:271, Jan 1969. doi: 10.1093/mnras/145.3.271.

V. Lattanzi, S. Spezzano, J. C. Laas, J. Chantzos, L. Bizzocchi, K. L. K. Lee, M. C. McCarthy, and P. Caselli. $HSCO^+$ and $DSCO^+$: a multi-technique approach in the laboratory for the spectroscopy of interstellar ions. *A&A*, 620:A184, Dec 2018. doi: 10.1051/0004-6361/201834340.

R. Le Gal, P. Hily-Blant, A. Faure, G. Pineau des Forêts, C. Rist, and S. Maret. Interstellar chemistry of nitrogen hydrides in dark clouds. *A&A*, 562:A83, February 2014. doi: 10.1051/0004-6361/201322386.

F. Le Petit, E. Roueff, and E. Herbst. H_3^+ and other species in the diffuse cloud towards ζ Persei: A new detailed model. *A&A*, 417:993–1002, Apr 2004. doi: 10.1051/0004-6361:20035629.

V. Lebouteiller, Kuassivi, and R. Ferlet. *Phosphorus in the diffuse ISM*, volume 348 of *Astronomical Society of the Pacific Conference Series*. 2006.

C. W. Lee, P. C. Myers, and M. Tafalla. A Survey for Infall Motions toward Starless Cores. II. CS (2-1) and N_2H^+ (1-0) Mapping Observations. *ApJS*, 136:703–734, October 2001. doi: 10.1086/322534.

T. J. Lee, D. J. Fox, H. F. Schaefer, III, and R. M. Pitzer. Analytic second derivatives for Renner-Teller potential energy surfaces. Examples of the five distinct cases. *J. Chem. Phys.*, 81:356–361, July 1984. doi: 10.1063/1.447313.

B. Lefloch, C. Vastel, S. Viti, I. Jimenez-Serra, C. Codella, L. Podio, C. Ceccarelli, E. Mendoza, J. R. D. Lepine, and R. Bachiller. Phosphorus-bearing molecules in solar-type star-forming regions: first PO detection. *MNRAS*, 462:3937–3944, November 2016. doi: 10.1093/mnras/stw1918.

C. M. Leung, E. Herbst, and W. F. Huebner. Synthesis of complex molecules in dense interstellar clouds via gas-phase chemistry - A pseudo time-dependent calculation. *ApJS*, 56:231–256, October 1984. doi: 10.1086/190982.

H. Liszt and R. Lucas. Comparative chemistry of diffuse clouds. II. CN, HCN, HNC, CH_3CN & N_2H^+. *A&A*, 370:576–585, May 2001. doi: 10.1051/0004-6361:20010260.

H. Liszt, M. Gerin, A. Beasley, and J. Pety. Chemical Complexity in Local Diffuse and Translucent Clouds: Ubiquitous Linear C_3H and CH_3CN, a Detection of HC_3N and an Upper Limit on the Abundance of CH_2CN. *ApJ*, 856:151, April 2018. doi: 10.3847/1538-4357/aab208.

H. S. Liszt. Formation, fractionation, and excitation of carbon monoxide in diffuse clouds. *A&A*, 476(1):291–300, Dec 2007. doi: 10.1051/0004-6361:20078502.

H. S. Liszt. Formation and Fractionation of CO (Carbon Monoxide) in Diffuse Clouds Observed at Optical and Radio Wavelengths. *ApJ*, 835(2):138, Feb 2017. doi: 10.3847/1538-4357/835/2/138.

H. S. Liszt and R. Lucas. CO in absorption and emission toward compact extragalactic radio continuum sources. *A&A*, 339:561–574, Nov 1998.

H. S. Liszt, J. Pety, and R. Lucas. Limits on chemical complexity in diffuse clouds: search for CH_3OH and HC_5N absorption. *A&A*, 486(2):493–496, Aug 2008. doi: 10.1051/0004-6361:200809851.

R. Lucas and H. Liszt. Interstellar isotope ratios from mm-wave molecular absorption spectra. *A&A*, 337:246–252, Sep 1998.

R. Lucas and H. S. Liszt. Comparative chemistry of diffuse clouds. I. C_2H and C_3H_2. *A&A*, 358:1069–1076, June 2000.

R. Lucas and H. S. Liszt. Comparative chemistry of diffuse clouds. III. Sulfur-bearing molecules. *A&A*, 384:1054–1061, Mar 2002. doi: 10.1051/0004-6361:20020043.

Z. G. Maas, C. A. Pilachowski, and G. Cescutti. Phosphorus Abundances in FGK Stars. *ApJ*, 841:108, June 2017. doi: 10.3847/1538-4357/aa7050.

S. Maity, R. I. Kaiser, and B. M. Jones. Formation of Ketene (H_2CCO) in Interstellar Analogous Methane (CH_4)-Carbon Monoxide (CO) Ices: A Combined Ftir and Reflectron Time-of-Flight Mass Spectroscopic Study. *ApJ*, 789:36, July 2014. doi: 10.1088/0004-637X/789/1/36.

L. Majumdar, P. Gratier, I. Andron, V. Wakelam, and E. Caux. A study of singly deuterated cyclopropenylidene c-C_3HD in the protostar IRAS 16293-2422. *MNRAS*, 467:3525–3532, May 2017. doi: 10.1093/mnras/stx259.

J. G. Mangum and Y. L. Shirley. How to Calculate Molecular Column Density. *PASP*, 127(949):266, Mar 2015. doi: 10.1086/680323.

J. S. Mathis, W. Rumpl, and K. H. Nordsieck. The size distribution of interstellar grains. *ApJ*, 217:425–433, Oct 1977. doi: 10.1086/155591.

M. C. McCarthy and P. Thaddeus. Laboratory detection of the elusive $HSCO^+$ isomer. *J. Chem. Phys.*, 127(22):221104–221104, Dec 2007. doi: 10.1063/1.2822042.

M. C. McCarthy, C. A. Gottlieb, H. Gupta, and P. Thaddeus. Laboratory and Astronomical Identification of the Negative Molecular Ion C_6H^-. *ApJL*, 652(2):L141–L144, Dec 2006. doi: 10.1086/510238.

M. C. McCarthy, K. N. Crabtree, M.-A. Martin-Drumel, Jr. Martinez, O., B. A. McGuire, and C. A. Gottlieb. A Laboratory Study of C_3H^+ and the C_3H Radical in Three New Vibrationally Excited $^2\Sigma$ States Using a Pin-Hole Nozzle Discharge Source. *ApJS*, 217 (1):10, Mar 2015. doi: 10.1088/0067-0049/217/1/10.

D. McElroy, C. Walsh, A. J. Markwick, M. A. Cordiner, K. Smith, and T. J. Millar. The UMIST database for astrochemistry 2012. *A&A*, 550:A36, Feb 2013. doi: 10.1051/0004-6361/201220465.

D. McNaughton, P. D. Godfrey, M. K. Jahn, D. A. Dewald, and J.-U. Grabow. Fourier transform microwave and millimeter wave spectroscopy of quinazoline, quinoxaline, and phthalazine. *J. Chem. Phys.*, 134(15):154305, Apr 2011. doi: 10.1063/1.3580770.

J. V. Michael and A. F. Wagner. Rate constants for the reactions o + c2h2 and o + c2d2 .fwdarw. products, over the temperature range .apprx.850-1950 k, by the flash photolysis-shock tube technique. determination of the branching ratio and a further theoretical analysis. *The Journal of Physical Chemistry*, 94(6):2453–2464, 1990. doi: 10.1021/j100369a047. URL `https://doi.org/10.1021/j100369a047`.

T. J. Millar. Phosphorus chemistry in dense interstellar clouds. *A&A*, 242:241, Feb 1991.

T. J. Millar, A. Bennett, and E. Herbst. An efficient gas phase synthesis for interstellar planetary nebulae. *MNRAS*, 229:41P–44, Dec 1987. doi: 10.1093/mnras/229.1.41P.

T. J. Millar, A. Bennett, and E. Herbst. Deuterium fractionation in dense interstellar clouds. *ApJ*, 340:906–920, May 1989. doi: 10.1086/167444.

C. Mininni, F. Fontani, V. M. Rivilla, M. T. Beltrán, P. Caselli, and A. Vasyunin. On the origin of phosphorus nitride in star-forming regions. *MNRAS*, 476(1):L39–L44, May 2018. doi: 10.1093/mnrasl/sly026.

M. Minissale, F. Dulieu, S. Cazaux, and S. Hocuk. Dust as interstellar catalyst. I. Quantifying the chemical desorption process. *A&A*, 585:A24, January 2016. doi: 10.1051/0004-6361/201525981.

P. C. Myers and E. F. Ladd. Bolometric temperatures of young stellar objects. *ApJL*, 413: L47–L50, August 1993. doi: 10.1086/186956.

K. I. Öberg. Photochemistry and astrochemistry: Photochemical pathways to interstellar complex organic molecules. *Chemical Reviews*, 116(17):9631–9663, 2016. doi: 10.1021/acs.chemrev.5b00694. URL `https://doi.org/10.1021/acs.chemrev.5b00694`. PMID: 27099922.

K. I. Öberg, G. W. Fuchs, Z. Awad, H. J. Fraser, S. Schlemmer, E. F. van Dishoeck, and H. Linnartz. Photodesorption of CO Ice. *ApJL*, 662(1):L23–L26, Jun 2007. doi: 10.1086/519281.

K. I. Öberg, H. Linnartz, R. Visser, and E. F. van Dishoeck. Photodesorption of Ices. II. H_2O and D_2O. *ApJ*, 693(2):1209–1218, Mar 2009. doi: 10.1088/0004-637X/693/2/1209.

Y. Ohshima and Y. Endo. Determination of the Hyperfine Constants for HCCO by Pulsed-Discharge-Nozzle Fourier-Transform Microwave Spectroscopy. *Journal of Molecular Spectroscopy*, 159:458–467, June 1993. doi: 10.1006/jmsp.1993.1142.

L. Pagani, M. Salez, and P. G. Wannier. The chemistry of H2D(+) in cold clouds. *A&A*, 258:479–488, May 1992.

L. Pagani, A. Bacmann, S. Cabrit, and C. Vastel. L183 (=L134N) revisited : the physical conditions in the main prestellar core. In *Molecules in Space and Laboratory*, page 32, December 2007.

B. Parise, C. Ceccarelli, A. G. G. M. Tielens, A. Castets, E. Caux, B. Lefloch, and S. Maret. Testing grain surface chemistry: a survey of deuterated formaldehyde and methanol in low-mass class 0 protostars. *A&A*, 453:949–958, July 2006. doi: 10.1051/0004-6361:20054476.

G. B. Park, A. H. Steeves, K. Kuyanov-Prozument, J. L. Neill, and R. W. Field. Design and evaluation of a pulsed-jet chirped-pulse millmeter-wave spectrometer for the 70-102 ghz region. *J. Chem. Phys.*, 135:024202, 2011. doi: doi.org/10.1063/1.3597774.

J. Pety. Successes of and Challenges to GILDAS, a State-of-the-Art Radioastronomy Toolkit. In F. Casoli, T. Contini, J. M. Hameury, and L. Pagani, editors, *SF2A-2005: Semaine de l'Astrophysique Francaise*, page 721, December 2005.

J. Pety, R. Lucas, and H. S. Liszt. Imaging galactic diffuse gas: bright, turbulent CO surrounding the line of sight to NRAO150. *A&A*, 489:217–228, October 2008. doi: 10.1051/0004-6361:200809803.

H. M. Pickett. The fitting and prediction of vibration-rotation spectra with spin interactions. *Journal of Molecular Spectroscopy*, 148(2):371–377, Aug 1991. doi: 10.1016/0022-2852(91)90393-O.

H. M. Pickett, R. L. Poynter, E. A. Cohen, M. L. Delitsky, J. C. Pearson, and H. S. P. Müller. Submillimeter, millimeter and microwave spectral line catalog. *J. Quant. Spec. and Radiative Transfer*, 60(5):883–890, Nov 1998. doi: 10.1016/S0022-4073(98)00091-0.

A. Piel. *Plasma Physics: An Introduction to Laboratory, Space, and Fusion Plasmas*. Springer-Verlag Berlin Heidelberg, 2010. doi: 10.1007/978-3-642-10491-6.

G. Pineau des Forets, E. Roueff, and D. R. Flower. The formation of nitrogen-bearing species in dark interstellar clouds. *MNRAS*, 244:668–674, June 1990.

A. Punanova, P. Caselli, A. Pon, A. Belloche, and P. André. Deuterium fractionation in the Ophiuchus molecular cloud. *A&A*, 587:A118, March 2016. doi: 10.1051/0004-6361/201527592.

L. Reboussin, V. Wakelam, S. Guilloteau, and F. Hersant. Grain-surface reactions in molecular clouds: the effect of cosmic rays and quantum tunnelling. *MNRAS*, 440: 3557–3567, June 2014. doi: 10.1093/mnras/stu462.

R. Renner. Zur theorie der wechselwirkung zwischen elektronen- und kernbewegung bei dreiatomigen, stabförmigen molekülen. *Z. Physik.*, 92:172, 1934.

V. M. Rivilla, F. Fontani, M. T. Beltrán, A. Vasyunin, P. Caselli, J. Martín-Pintado, and R. Cesaroni. The First Detections of the Key Prebiotic Molecule PO in Star-forming Regions. *ApJ*, 826:161, August 2016. doi: 10.3847/0004-637X/826/2/161.

V. M. Rivilla, I. Jiménez-Serra, S. Zeng, S. Martín, J. Martín-Pintado, J. Armijos-Abendaño, S. Viti, R. Aladro, D. Riquelme, M. Requena-Torres, D. Quénard, F. Fontani, and M. T. Beltrán. Phosphorus-bearing molecules in the Galactic Center. *MNRAS*, 475 (1):L30–L34, Mar 2018. doi: 10.1093/mnrasl/slx208.

L. S. Rothman, I. E. Gordon, A. Barbe, D. Chris Benner, P. F. Bernath, M. Birk, V. Boudon, L. R. Brown, A. Campargue, J. P. Champion, K. Chance, L. H. Coudert, V. Dana, V. M. Devi, S. Fally, J. M. Flaud, R. R. Gamache, A. Goldman, D. Jacquemart, I. Kleiner, N. Lacome, W. J. Lafferty, J. Y. Mand in, S. T. Massie, S. N. Mikhailenko, C. E. Miller, N. Moazzen-Ahmadi, O. V. Naumenko, A. V. Nikitin, J. Orphal, V. I. Perevalov, A. Perrin, A. Predoi-Cross, C. P. Rinsland, M. Rotger, M. Šimečková, M. A. H. Smith, K. Sung, S. A. Tashkun, J. Tennyson, R. A. Toth, A. C. Vandaele, and J. Vander Auwera. The HITRAN 2008 molecular spectroscopic database. *J. Quant. Spec. and Radiative Transfer*, 110(9-10):533–572, Jun 2009. doi: 10.1016/j.jqsrt.2009.02.013.

M. Ruaud, J. C. Loison, K. M. Hickson, P. Gratier, F. Hersant, and V. Wakelam. Modelling complex organic molecules in dense regions: Eley-Rideal and complex induced reaction. *MNRAS*, 447:4004–4017, March 2015. doi: 10.1093/mnras/stu2709.

D. P. Ruffle and E. Herbst. New models of interstellar gas-grain chemistry - I. Surface diffusion rates. *MNRAS*, 319(3):837–850, Dec 2000. doi: 10.1046/j.1365-8711.2000.03911.x.

S. Saito, S. Yamamoto, K. Kawaguchi, M. Ohishi, H. Suzuki, S.-I. Ishikawa, and N. Kaifu. The Microwave Spectrum of the CP Radical and Related Astronomical Search. *ApJ*, 341:1114, Jun 1989. doi: 10.1086/167570.

N. Sakai, T. Shiino, T. Hirota, T. Sakai, and S. Yamamoto. Long Carbon-chain Molecules and Their Anions in the Starless Core, Lupus-1A. *ApJL*, 718(2):L49–L52, Aug 2010. doi: 10.1088/2041-8205/718/2/L49.

R. J. Saykally, P. G. Szanto, T. G. Anderson, and R. C. Woods. The microwave spectrum of hydrogen isocyanide. *ApJL*, 204:L143–L145, Mar 1976. doi: 10.1086/182074.

L. Schaefer and B. Fegley, Jr. Atmospheric Chemistry of Venus-like Exoplanets. *ApJ*, 729: 6, March 2011. doi: 10.1088/0004-637X/729/1/6.

S. Schnee and A. Goodman. Density and Temperature Structure of TMC-1C from 450 and 850 Micron Maps. *ApJ*, 624(1):254–266, May 2005. doi: 10.1086/429156.

F. L. Schöier, J. K. Jørgensen, E. F. van Dishoeck, and G. A. Blake. Does IRAS 16293-2422 have a hot core? Chemical inventory and abundance changes in its protostellar environment. *A&A*, 390:1001–1021, August 2002. doi: 10.1051/0004-6361:20020756.

F. L. Schöier, F. F. S. van der Tak, E. F. van Dishoeck, and J. H. Black. An atomic and molecular database for analysis of submillimetre line observations. *A&A*, 432:369–379, March 2005. doi: 10.1051/0004-6361:20041729.

G. Scoles. *Atomic and Molecular Beam Methods*. Oxford University Press, Vol. 1., 1. edition, 1988.

R. J. Shannon, M. A. Blitz, A. Goddard, and D. E. Heard. Accelerated chemistry in the reaction between the hydroxyl radical and methanol at interstellar temperatures facilitated by tunnelling. *Nature Chemistry*, 5(9):745–749, Sep 2013. doi: 10.1038/nchem.1692.

C. J. Shen, J. M. Greenberg, W. A. Schutte, and E. F. van Dishoeck. Cosmic ray induced explosive chemical desorption in dense clouds. *A&A*, 415:203–215, Feb 2004. doi: 10.1051/0004-6361:20031669.

C. N. Shingledecker, J. Tennis, R. Le Gal, and E. Herbst. On Cosmic-Ray-driven Grain Chemistry in Cold Core Models. *ApJ*, 861(1):20, Jul 2018. doi: 10.3847/1538-4357/aac5ee.

O. Sipilä, P. Caselli, and J. Harju. HD depletion in starless cores. *A&A*, 554:A92, June 2013. doi: 10.1051/0004-6361/201220922.

O. Sipilä, S. Spezzano, and P. Caselli. Understanding the C_3H_2 cyclic-to-linear ratio in L1544. *A&A*, 591:L1, June 2016. doi: 10.1051/0004-6361/201628689.

T. P. Snow and B. J. McCall. Diffuse Atomic and Molecular Clouds. *ARA&A*, 44(1): 367–414, Sep 2006. doi: 10.1146/annurev.astro.43.072103.150624.

S. Spezzano, F. Tamassia, S. Thorwirth, P. Thaddeus, C. A. Gottlieb, and M. C. McCarthy. A High-resolution Isotopic Study of the Rotational Spectrum of c-C_3H_2. *ApJS*, 200:1, May 2012. doi: 10.1088/0067-0049/200/1/1.

S. Spezzano, S. Brünken, P. Schilke, P. Caselli, K. M. Menten, M. C. McCarthy, L. Bizzocchi, S. P. Trevinõ-Morales, Y. Aikawa, and S. Schlemmer. Interstellar Detection of c-C_3D_2. *ApJL*, 769:L19, June 2013. doi: 10.1088/2041-8205/769/2/L19.

S. Spezzano, L. Bizzocchi, P. Caselli, J. Harju, and S. Brünken. Chemical differentiation in a prestellar core traces non-uniform illumination. *A&A*, 592:L11, August 2016. doi: 10.1051/0004-6361/201628652.

S. Spezzano, P. Caselli, L. Bizzocchi, B. M. Giuliano, and V. Lattanzi. The observed chemical structure of L1544. *A&A*, 606:A82, October 2017. doi: 10.1051/0004-6361/201731262.

S. W. Stahler and F. Palla. *The Formation of Stars*. John Wiley and Sons, Ltd, 2008. ISBN 9783527618675. URL `https://onlinelibrary.wiley.com/doi/abs/10.1002/9783527618675.ch2`.

P. G. Szalay, J. F. Stanton, and R. J. Bartlett. A systematic coupled-cluster investigation of structure and vibrational frequencies of the lowest electronic states of ketenyl radical. *Chemical Physics Letters*, 193:573–579, June 1992. doi: 10.1016/0009-2614(92)85850-A.

P. G. Szalay, G. Fogarasi, and L. Nemes. Quantum chemical coupled cluster study of the structure and spectra of the ground and first excited states of the ketenyl radical. *Chemical Physics Letters*, 263:91–99, December 1996. doi: 10.1016/S0009-2614(96)01173-6.

M. Tafalla, P. C. Myers, P. Caselli, C. M. Walmsley, and C. Comito. Systematic Molecular Differentiation in Starless Cores. *ApJ*, 569:815–835, April 2002. doi: 10.1086/339321.

S. Takahashi, N. Ohashi, and T. L. Bourke. Direct Imaging of a Compact Molecular Outflow from a Very Low Luminosity Object: L1521F-IRS. *ApJ*, 774:20, September 2013. doi: 10.1088/0004-637X/774/1/20.

E. D. Tenenbaum, N. J. Woolf, and L. M. Ziurys. Identification of Phosphorus Monoxide ($X^2\Pi_r$) in VY Canis Majoris: Detection of the First PO Bond in Space. *ApJL*, 666: L29–L32, September 2007. doi: 10.1086/521361.

J. Tennyson, S. N. Yurchenko, A. F. Al-Refaie, E. J. Barton, K. L. Chubb, P. A. Coles, S. Diamantopoulou, M. N. Gorman, C. Hill, A. Z. Lam, L. Lodi, L. K. McKemmish, Y. Na, A. Owens, O. L. Polyansky, T. Rivlin, C. Sousa-Silva, D. S. Underwood, A. Yachmenev, and E. Zak. The ExoMol database: Molecular line lists for exoplanet

and other hot atmospheres. *Journal of Molecular Spectroscopy*, 327:73–94, Sep 2016. doi: 10.1016/j.jms.2016.05.002.

P. Thaddeus, M. Guelin, and R. A. Linke. Three new 'nonterrestrial' molecules. *ApJL*, 246:L41–L45, May 1981. doi: 10.1086/183549.

P. Thaddeus, J. M. Vrtilek, and C. A. Gottlieb. Laboratory and astronomical identification of cyclopropenylidene, C3H2. *ApJL*, 299:L63–L66, December 1985. doi: 10.1086/184581.

V. Thiel, A. Belloche, K. M. Menten, A. Giannetti, H. Wiesemeyer, B. Winkel, P. Gratier, H. S. P. Müller, D. Colombo, and R. T. Garrod. Small-scale physical and chemical structure of diffuse and translucent molecular clouds along the line of sight to Sgr B2. *A&A*, 623:A68, Mar 2019. doi: 10.1051/0004-6361/201834467.

L. R. Thorne, V. G. Anicich, S. S. Prasad, and Jr. Huntress, W. T. The chemistry of phosphorus in dense interstellar clouds. *ApJ*, 280:139–143, May 1984. doi: 10.1086/161977.

A. G. G. M. Tielens. *The Physics and Chemistry of the Interstellar Medium*. Cambridge University Press, 2005.

C. H. Townes and A. L. Schawlow. *Microwave Spectroscopy*. McGraw-Hill Book Company, Inc., 1955.

B. E. Turner. Deuterated molecules in translucent and dark clouds. *The Astrophysical Journal Supplement Series*, 136(2):579, 2001. URL `http://stacks.iop.org/0067-0049/136/i=2/a=579`.

B. E. Turner and J. Bally. Detection of interstellar PN - The first identified phosphorus compound in the interstellar medium. *ApJL*, 321:L75–L79, October 1987. doi: 10.1086/185009.

B. E. Turner, T. Tsuji, J. Bally, M. Guelin, and J. Cernicharo. Phosphorus in the dense interstellar medium. *ApJ*, 365:569–585, December 1990. doi: 10.1086/169511.

E. F. van Dishoeck. Astrochemistry: overview and challenges. *Proceedings of the International Astronomical Union*, 13(S332):3–22, 2017. doi: 10.1017/S1743921317011528.

C. Vastel, C. Ceccarelli, B. Lefloch, and R. Bachiller. The Origin of Complex Organic Molecules in Prestellar Cores. *ApJL*, 795:L2, November 2014. doi: 10.1088/2041-8205/795/1/L2.

A. I. Vasyunin and E. Herbst. A Unified Monte Carlo Treatment of Gas-Grain Chemistry for Large Reaction Networks. II. A Multiphase Gas-surface-layered Bulk Model. *ApJ*, 762:86, January 2013a. doi: 10.1088/0004-637X/762/2/86.

A. I. Vasyunin and E. Herbst. Reactive Desorption and Radiative Association as Possible Drivers of Complex Molecule Formation in the Cold Interstellar Medium. *ApJ*, 769:34, May 2013b. doi: 10.1088/0004-637X/769/1/34.

A. I. Vasyunin, D. A. Semenov, D. S. Wiebe, and T. Henning. A Unified Monte Carlo Treatment of Gas-Grain Chemistry for Large Reaction Networks. I. Testing Validity of Rate Equations in Molecular Clouds. *ApJ*, 691:1459–1469, February 2009. doi: 10.1088/0004-637X/691/2/1459.

A. I. Vasyunin, P. Caselli, F. Dulieu, and I. Jiménez-Serra. Formation of Complex Molecules in Prestellar Cores: A Multilayer Approach. *ApJ*, 842:33, June 2017. doi: 10.3847/1538-4357/aa72ec.

R. Visser, E. A. Bergin, and J. K. Jørgensen. Chemical tracers of episodic accretion in low-mass protostars. *A&A*, 577:A102, May 2015. doi: 10.1051/0004-6361/201425365.

V. Wakelam, E. Herbst, J. Le Bourlot, F. Hersant, F. Selsis, and S. Guilloteau. Sensitivity analyses of dense cloud chemical models. *A&A*, 517:A21, Jul 2010. doi: 10.1051/0004-6361/200913856.

V. Wakelam, J.-C. Loison, E. Herbst, B. Pavone, A. Bergeat, K. Béroff, M. Chabot, A. Faure, D. Galli, W. D. Geppert, D. Gerlich, P. Gratier, N. Harada, K. M. Hickson, P. Honvault, S. J. Klippenstein, S. D. Le Picard, G. Nyman, M. Ruaud, S. Schlemmer, I. R. Sims, D. Talbi, J. Tennyson, and R. Wester. The 2014 KIDA Network for Interstellar Chemistry. *ApJS*, 217:20, April 2015a. doi: 10.1088/0067-0049/217/2/20.

V. Wakelam, J.-C. Loison, K. M. Hickson, and M. Ruaud. A proposed chemical scheme for HCCO formation in cold dense clouds. *MNRAS*, 453:L48–L52, October 2015b. doi: 10.1093/mnrasl/slv097.

P. G. Wannier. Nuclear abundances and evolution of the interstellar medium. *ARA&A*, 18:399–437, 1980. doi: 10.1146/annurev.aa.18.090180.002151.

D. Ward-Thompson, F. Motte, and P. Andre. The initial conditions of isolated star formation - III. Millimetre continuum mapping of pre-stellar cores. *MNRAS*, 305:143–150, May 1999. doi: 10.1046/j.1365-8711.1999.02412.x.

J. K. G. Watson. A planarity relation for sextic centrifugal distortion constants. *Journal of Molecular Spectroscopy*, 65(1):123–133, Apr 1977. doi: 10.1016/0022-2852(77)90364-2.

K. Willacy, W. D. Langer, and T. Velusamy. Dust Emission and Molecular Depletion in L1498. *ApJL*, 507:L171–L175, November 1998. doi: 10.1086/311695.

T. L. Wilson and R. Rood. Abundances in the Interstellar Medium. *ARA&A*, 32:191–226, 1994. doi: 10.1146/annurev.aa.32.090194.001203.

K. M. T. Yamada and G. Winnerwisser. *Interstellar Molecules: Their Laboratory and Interstellar Habitat.* Springer-Verlag Berlin Heidelberg, 2011. doi: 10.1007/978-3-642-16268-8.

S. Yamamoto. *Introduction to Astrochemistry: Chemical Evolution from Interstellar Clouds to Star and Planet Formation.* Springer-Verlag Berlin Heidelberg, 2017. doi: 10.1007/978-4-431-54171-4.

L. M. Ziurys, D. R. Schmidt, and J. J. Bernal. New Circumstellar Sources of PO and PN: The Increasing Role of Phosphorus Chemistry in Oxygen-rich Stars. *ApJ*, 856:169, April 2018. doi: 10.3847/1538-4357/aaafc6.

Acknowledgements

First of all I want to sincerely thank Paola Caselli for being an excellent supervisor and for always finding the time and patience to guide me through all my projects.

I would also like to thank Silvia Spezzano and Valerio Lattanzi for being the best supervisors any PhD student could ever wish for! Silvia, I am endlessly grateful to you for believing in me from the very beginning and giving me this huge opportunity to work at the MPE and start a new life in Munich. Valerio, thank you for all the great time we spent together in the lab (despite listening to your Jazz music!), your honest advice and your friendship. Thanks to both of you for all the fun, the jokes, and the support when I needed it the most!

I also want to thank my collaborators Victor Rivilla and Anton Vasyunin, whose valuable guidance (despite the distance) helped me finish my third paper in time!

A very big thank you goes to my wonderful office mates Elena, Carolina and Domenico for the amazing three years we spent together, with all the ups and downs. I will never forget our IMPRS parties, our funny chats, our coffee breaks and our nights out. I will miss you and I will think back to our time together with a smile on my face and a tear in my eye.

I would also like to thank my dearest friends Elena (again) and Matteo, for all our astonishing adventures, for "kidnapping me" to Italy when I needed an escape and for always having a couch free for me at your place!

Thank you Luca and Michela for our pleasant "merenda" afternoons and for introducing me to the magnificent world of italian cuisine and italian language. Luca, I will also miss our long scientific discussions, that always helped me see clearly through a complex problem. Grazie mille!

Da Mütter oft nicht genug Anerkennung bekommen, möchte ich mich an dieser Stelle ganz herzlich bei meiner Mutter Andrea bedanken. Dass ich soweit gekommen bin in meinem Leben und zu der Person geworden bin, die ich heute bin, habe ich dir zu verdanken. Du hast mir beigebracht nie den Mut zu verlieren und mir selbst treu zu bleiben. Danke Mama.

Θέλω επίσης να ευχαριστήσω τον πατέρα μου, Κώστα, που από μικρό παιδί μού έδειξε την ομορφιά των γραμμάτων και μού κίνησε το ενδιαφέρον για τις φυσικές επιστήμες. Σε ευχαριστώ που δούλευες τόσο σκλήρα όλα αυτά τα χρόνια για να μπορέσω να τελειώσω τις σπουδές μου στο εξωτερικό και να εκπληρώσω τα όνειρά μου. Επιπλέον, θα ήθελα να ευχαριστήσω τα αδέλφια μου, Δημήτρη και Λουκά, που παρά τις μεγάλες αποστάσεις μεταξύ

μας, πάντα μού προσφέρουν υποστήριξη και δύναμη.

Last and definitely not least, I would like to thank Jake for his infinite support during the last years of my PhD. I feel so lucky to have met you and I am looking forward to a fun, exciting and loving future with you!